Technical Report

DNA-TR-94-187

CHARACTERIZATION OF ROCKS AND GROUTS TO SUPPORT DNA'S VERIFICATION PROGRAM

Approved for public release; distribution is unlimited.

September 2000

DEPARTMENT OF DEFENSE
UNITED STATES OF AMERICA

Prepared for:
Defense Threat Reduction Agency
45045 Aviation Drive
Dulles, VA 20166-7517

DNA001-93-C-0040

J. Wesley Martin
Sherri Heroux

Prepared by: TerraTek, Inc.
P.O. Box 8275
Salt Lake City, UT 84108-8275

20010426 024

CUT HERE AND RETURN

DISTRIBUTION LIST UPDATE

This mailer is provided to enable DTRA to maintain current distribution lists for reports. (We would appreciate you providing the requested information.)

Note:
Please return the mailing label from the document so that any additions, changes, corrections or deletions can be made easily. For distribution cancellation or more information call DTRA/ADM (703) 325-1036.

- ☐ Add the individual listed to your distribution list.
- ☐ Delete the cited organization/individual.
- ☐ Change of address.

NAME: ______________________________

ORGANIZATION: ______________________________

OLD ADDRESS	**NEW ADDRESS**
____________________	____________________
____________________	____________________
____________________	____________________

TELEPHONE NUMBER: ( ) ______________________________

DTRA PUBLICATION NUMBER/TITLE	**CHANGES/DELETIONS/ADDITIONS, etc.)** *(Attach Sheet if more Space is Required)*
____________________	____________________
____________________	____________________
____________________	____________________

DTRA or other GOVERNMENT CONTRACT NUMBER: ______________________________

CERTIFICATION of NEED-TO-KNOW BY GOVERNMENT SPONSOR (if other than DTRA):

SPONSORING ORGANIZATION: ______________________________

CONTRACTING OFFICER or REPRESENTATIVE: ______________________________

SIGNATURE: ______________________________

DEFENSE THREAT REDUCTION AGENCY
ATTN: ADM
45045 AVIATION DRIVE
DULLES, VA 20156-7517

DEFENSE THREAT REDUCTION AGENCY
ATTN: ADM
6801 TELEGRAPH ROAD
ALEXANDRIA, VA 22310-3398

REPORT DOCUMENTATION PAGE	*Form Approved* *OMB No. 0704-0188*

1. AGENCY USE ONLY (*Leave blank*)	2. REPORT DATE	3. REPORT TYPE AND DATES COVERED Technical 930301 - 941231

4. TITLE AND SUBTITLE Characterization of Rocks and Grout to Support DNA's Verification Program	5. FUNDING NUMBERS C - DNA 001-93-C-0040 PE - 63711H PR - CD TA - CD WU - DH600090
6. AUTHOR(S) J. Wesley Martin and Sherri A. Heroux	
7. PERFORMING ORGANIZATION NAME(S) AND ADDRESS(ES) Terra Tek, Inc. P. O. Box 8275 Salt Lake City, UT 87108-8275	8. PERFORMING ORGANIZATION REPORT TR 95-36
9. SPONSORING/MONITORING AGENCY NAME(S) AND ADDRESS(ES) Defense Threat Reduction Agency 45045 Aviation Drive Dulles, VA 20166-7517 CPTP/Martinez	10. SPONSORING/MONITORING AGENCY REPORT NUMBER DNA-TR-94-187

11. SUPPLEMENTARY NOTES

This work was sponsored by the Defense Threat Reduction Agency under RDT&E RMC code T 4662 D CD CD 60009 5900 A 25904D.

12a. DISTRIBUTION/AVAILABILITY STATEMENT Approved for public release; distribution is unlimited.	12B. DISTRIBUTION CODE

13. ABSTRACT (Maximum 200 words)

The mechanical and physical properties of various geologic materials and man-made grouts have been determined. The testing was in support of the Defense Nuclear Agency's (DNA) Treaty Verification program. Specifically, test data was generated for use with DNA's HYDROPLUS program. The tests performed included unconfined compression tests, uniaxial strain tests, physical properties, ultrasonic velocities, XRD mineralogy, and lithologic descriptions. In some instances, gas gun samples were prepared and shipped to DNA's gas gun experimentalists.

14. SUBJECT TERMS

Uniaxial Strain	Physical Properties	Granite
Unconfined Compression	Grout	Limestone
XRD	Thin Sections	Ultrasonic Velocities

15. NUMBER OF PAGES

16. PRICE CODE

17. SECURITY CLASSIFICATION OF THIS PAGE UNCLASSIFIED	18. SECURITY CLASSIFICATION OF REPORT UNCLASSIFIED	19. SECURITY CLASSIFICATION OF ABSTRACT UNCLASSIFIED	20. LIMITATION OF ABSTRACT SAR

NSN 7540-01-280-5500

Standard Form 298 (Rev. 2-89)
Prescribed by ANSI Sta. 239-18, 298-102

UNCLASSIFIED
SECURITY CLASSIFICATION OF THIS PAGE

CLASSIFIED BY:	N/A since Unclassified
DECLASSIFY ON:	N/A since Unclassified

14. SUBJECT TERMS (Continued)

Gas Gun Preparation

PREFACE

The authors would like to acknowledge the substantial contribution of many other TerraTek personnel. In particular, special thanks are given to Mark Grazier for performing the mechanical, physical and ultrasonic velocity tests, and for the preparation of samples, and Barbara Marin for lithological descriptions.

The authors would also like to express their appreciation for the contributions and guidance provided by Audrey Martinez and Bob Reinke of DNA throughout the course of this contract.

The Contracting Officer's Technical Representative (COTR) for this effort was Audrey Martinez (FCDNA/FCTT). Dr. George Baladi was the Assistant Director for FCTT, Col Harland A. Lawson was the Director, Test Operations Directorate (FCT), and Col Darrell W. Singleton was the Commander, FCDNA.

CONVERSION TABLE

Quantity	SI → English	English → SI
Area	1 m^2 = 10.764 ft^2 1 m^2 = 1550.0 in^2	1 ft^2 = 0.0929 m^2 1 in^2 = 6.452 x 10^{-4} m^2
Density	1 kg/m^3 = 0.06243 lb_m/ft^3	1 lb_m/ft^3 = 16,018 kg/m^3 1 slug/ft^3 = 515.38 kg/m^3
Force	1 N = 0.22481 lb_f	1 lb_f = 4.448 N
Length	1 m = 3.281 ft 1 m = 39.37 in	1 ft = 0.3048 m 1 in = 0.0254 m
Mass	1 kg = 2.2046 lb_m	1 lb_m = 0.4536 kg 1 slug = 14.594 kg
Pressure and Stress (Note: 1 Pa = 1 N/m^2)	1 N/m^2 = 0.02089 lb_f/ft^2 1 N/m^2 = 1.4504 x 10^{-4} lb_f/in^2 1 N/m^2 = 4.015 x 10^{-3} in H_2O 1 N/m^2 = 2.953 x 10^{-4} in Hg	lb_f/ft^2 = 47.88 N/m^2 1 psi = lb_f/in^2 = 6894.8 N/m^2 1 std. atm. = 1.0133 x 10^5 N/m^2 1 bar = 1 x 10^5 N/m^2
Volume	1 m^3 = 35.3134 ft^3	1 ft^3 = 0.02832 m^3 1 in^3 = 1.6387 x 10^{-5} 1 gal (U.S. liq.) = 0.003785 m^3

TABLE OF CONTENTS

Section Page

Appendix

FIGURES

FIGURES (Continued)

FIGURES (Continued)

Figure | Page

FIGURES (Continued)

Figure **Page**

FIGURES (Continued)

TABLES

SECTION 1

INTRODUCTION

Characterization of the mechanical and physical properties of the test bed geologic medium are important parameters in the development and evaluation of the material models used for the determination of yield calculations of nuclear tests. To this end, TerraTek has been performing laboratory tests on geologic materials and man-made grouts in support of the HYDROPLUS method. These tests are designed to characterize physical and mechanical properties which help model the in-situ behavior of the host rock and calculate responses resulting from an underground nuclear explosion.

This report summarizes the efforts of TerraTek during the period from March 1993 to December 1994. In the laboratory test program, uniaxial strain tests, uniaxial/triaxial compression tests, ultrasonic velocity (both longitudinal and shear wave velocity) measurements, physical property measurements and other material characterization tests were performed. The physical property measurements included as-received, dry and grain densities. From these measured values, effective porosity, total porosity, and occluded voids were calculated.

This report contains four Appendices. Each Appendix groups data from a particular drill hole or material type. Also, each Appendix contains a technical report documenting test results from a particular location. Table 1-1 presents a summary of the types of tests conducted for each of the drill holes and material types.

Table 1-1. Summary of technical reports.

Appen.	Drill Hole/ Project ID	Report Number	Footage (ft)	Physical Properties	Ultrasonic Velocities	Uniaxial Strain	Triaxial Compression	Unconfined Compression	Other Tests and Evaluations
A	SHIST	TR94-16	104.2-170	X	X			X	XRD, Gas Gun Sample Preparation
B	SHIST	TR94-37	18.7-119.0	X	X			X	Gas Gun Sample Preparation
C	SHI Mix #1 SHI Mix #2	TR94-53	Grout	X	X	X		X	Drying Temp. of 60° and 105°C
D	Linchburg Mine	TR95-17	NA	X	X	X		X	XRD, Thin Section Descriptions

SECTION 2

TEST PROCEDURES

The mechanical compression tests were conducted on right-circular cylinders with a length-to-diameter ratio of approximately 2:1; sample diameter was as-received, unless there was a specific reason for coring to a smaller size. The specimens were cut with a diamond saw and end ground flat and parallel to 0.001 inch per inch length using water coolant. For moisture sensitive material, care was taken during sample cutting and end grinding to ensure a minimum loss of moisture.

All mechanical tests were conducted using a servo-controlled triaxial testing apparatus to subject samples to desired stress states at controlled strain rates. The samples were isolated from the pressure-vessel confining fluid by an impermeable jacket, which was sealed at the sample ends against steel endcaps. Axial and radial strains were measured using transducers which measured changes in the external sample dimensions. Stress difference was determined using a load cell within the vessel. Confining pressure was measured using a calibrated pressure data acquisition system and analog X-Y recorders.

2.1 UNIAXIAL/TRIAXIAL COMPRESSION TESTS.

Samples subjected to triaxial compression were initially loaded hydrostatically to the specified target confining pressure (unconfined (uniaxial) compression test had zero confining pressure). The axial stress was increased at a strain rate of approximately 10^{-5} s^{-1}. Axial loading was continued until either a decrease in the stress difference occurred or an axial strain of at least 5% was reached. Triaxial compression tests were performed undrained. Measurements obtained during these tests included axial and radial strains, maximum axial stress difference[1], and the target confining pressure during triaxial compression.

---

[1] Axial stress difference is the stress above the confining pressure. Confining pressure acts on all sides of the sample, including the ends. To fail a material, an additional stress, known as the axial stress difference, must be applied along the axis of the core. The effective compressive strength of a sample is the maximum axial stress difference plus the effective confining pressure.

In some cases, the test material was exceptionally dense and competent (e.g., the Linchburg mine material). For several of these samples, it was anticipated that brittle catastrophic failure would ensue once reaching the maximum compressive strength of the material under unconfined conditions (zero confining pressure). Hence, two loading cycles were performed to protect the transducers that measure axial and radial deformation. During the first cycle, axial and radial deformation was recorded up to an axial stress of 100 MPa. Prior to the second cycle, the axial stress was reduced to zero and the radial transducers (cantilevers) were removed. The sample was then loaded to failure. In most cases, the test sample unexpectedly failed prior to 100 MPa. Hence, stress-strain data exists to failure for these samples. Axial stress for both loading cycles was increased using an axial strain rate of 1 x 10^{-5}/sec. Axial strain, radial strain and axial stress were recorded continuously (where applicable) through both loading cycles using a digital data acquisition system.

Poisson's ratio, and static Young's modulus, Bulk modulus and Shear modulus were calculated using the following relationships:

$$E_s = \frac{\Delta\sigma_a}{\Delta\varepsilon_a} \tag{2.1}$$

$$\nu_s = \frac{\Delta\varepsilon_r}{\Delta\varepsilon_a} \tag{2.2}$$

$$K_s = \frac{E_s}{3(1-2\nu_s)} \tag{2.3}$$

$$G_s = \frac{Es}{2(1+\nu)} \tag{2.4}$$

where E_s, K_s, and G_s are the static Young's modulus, Bulk modulus, and Shear modulus, respectively; ν_s is the static Poisson's ratio; and ε_a and ε_r are the axial and radial strains, respectively.

2.2 UNIAXIAL STRAIN TESTS.

The objective of the uniaxial strain test is to subject a sample to axial loading and unloading while preventing any measurable radial deformation of the material. In order to accomplish this, both stress difference and confining pressure are simultaneously increased from the initial zero stress state. The stress difference is applied at a strain rate of approximately 10^{-5} s^{-1}; the confining pressure is increased as needed to prevent radial deformation of the sample. After reaching the maximum confining pressure of 4 kb (400 MPa), the stress difference and confining pressures are decreased simultaneously while maintaining zero radial strains. After reaching zero stress difference (i.e., a hydrostatic state of stress), the confining pressure is further reduced to zero. All uniaxial strain tests are conducted under undrained conditions, with "as-received" samples. Measurements made during the tests included axial and radial strains, stress difference and confining pressure.

2.2.1 Uniaxial strain definitions.

Specific parameters are referred to from the uniaxial strain tests. For completeness, some of the more common terms are defined as follows (slopes from graphical presentations of the data are needed to generate the various moduli).

Maximum volumetric strain. The maximum volumetric strain seen during a uniaxial strain test usually occurs at the maximum mean normal stress level (confining pressure of about 400 MPa), shown as point D in Figure 2-la. For the uniaxial strain condition, the volumetric strain is represented by the axial deformation since the radial strains are held constant.

Measured permanent compaction (MPC). The "permanent" volumetric strain that occurs after a load-unload cycle of a uniaxial strain test to a maximum lateral stress of 400 MPa. This is also known as the non-recoverable deformation following a uniaxial strain test and is directly related to the amount of air-filled voids (void collapse due to shear enhanced compaction) occurring in the sample prior to testing. Point F corresponds to the MPC in Figure 2-1a.

Loading bulk modulus. The slope of the line on the mean normal stress versus volumetric strain curve which is vertically above the measured permanent compaction and extending to the maximum mean normal stress. This region of the loading curve is primarily influenced by the intrinsic properties of the material (most of the air-filled voids are presumably crushed). This corresponds to line C-D in Figure 2-1a.

Unloading bulk modulus. The slope of the line on the mean normal stress versus volumetric strain curve extending from the maximum mean normal stress to a point at which hydrostatic unloading begins (removal of the axial stress difference), shown as line D-E in Figure 2-la.

Loading apparent constrained modulus. The slope of the line on the axial stress versus axial strain curve extending from a point on the loading curve that occurs vertically above where the axial stress equals zero on the unloading curve to the maximum axial stress (see line J-K in Figure 2-1c).

Unloading apparent constrained modulus. The slope of the line on the axial stress versus axial strain curve extending from the maximum axial stress, point K, to point L on the unloading curve (Figure 2-1c).

Loading shear modulus. The slope of the line on the axial stress difference versus strain difference curve extending from approximately 50% of the loading curve to the maximum stress difference, shown as line M-N in Figure 2-1d.

Unloading shear modulus. The slope of the line on the axial stress difference versus strain difference curve extending from the maximum stress difference to approximately 50% of the unloading curve, shown as line N-O in Figure 2-1d.

Maximum axial stress difference. The maximum stress difference usually occurs at the peak lateral stress (400 MPa) during a uniaxial strain test. It is denoted as point H in Figure 2-lb. The parameter is commonly referred as the "strength" of the material at 400 MPa confining pressure.

In addition to the above definitions, other definitions are commonly used for highly compressible materials (e.g. grouts, tufts, porous materials with high gas-filled voids). The following are definitions typically applied to highly compressible/deformable materials.

Stress difference intercept. The stress difference intercept is obtained by extrapolating a representative straight line to the ordinate through the stress difference versus confining pressure curve ranging from 200 to 400 MPa, where inelastic response dominates. In Figure 2-lb, points G and H are the limits for straight line representation. The intercept of the ordinate is called the stress difference intercept.

Initial bulk modulus. The stiffness of a material is defined by the bulk modulus in the region of interest. Because of the variation in stress-strain response of compressible material, several different moduli are defined and calculated. The initial bulk modulus is defined as the slope of the line on the mean normal stress versus volumetric strain curve from point A to point B (Figure 2-la).

Low pressure bulk modulus. The slope of the line which extends from the origin to a point on the loading portion of the curve, which is vertically above the measured permanent compaction, shown as A-C in Figure 2-1a. Point F is the measured permanent compaction.

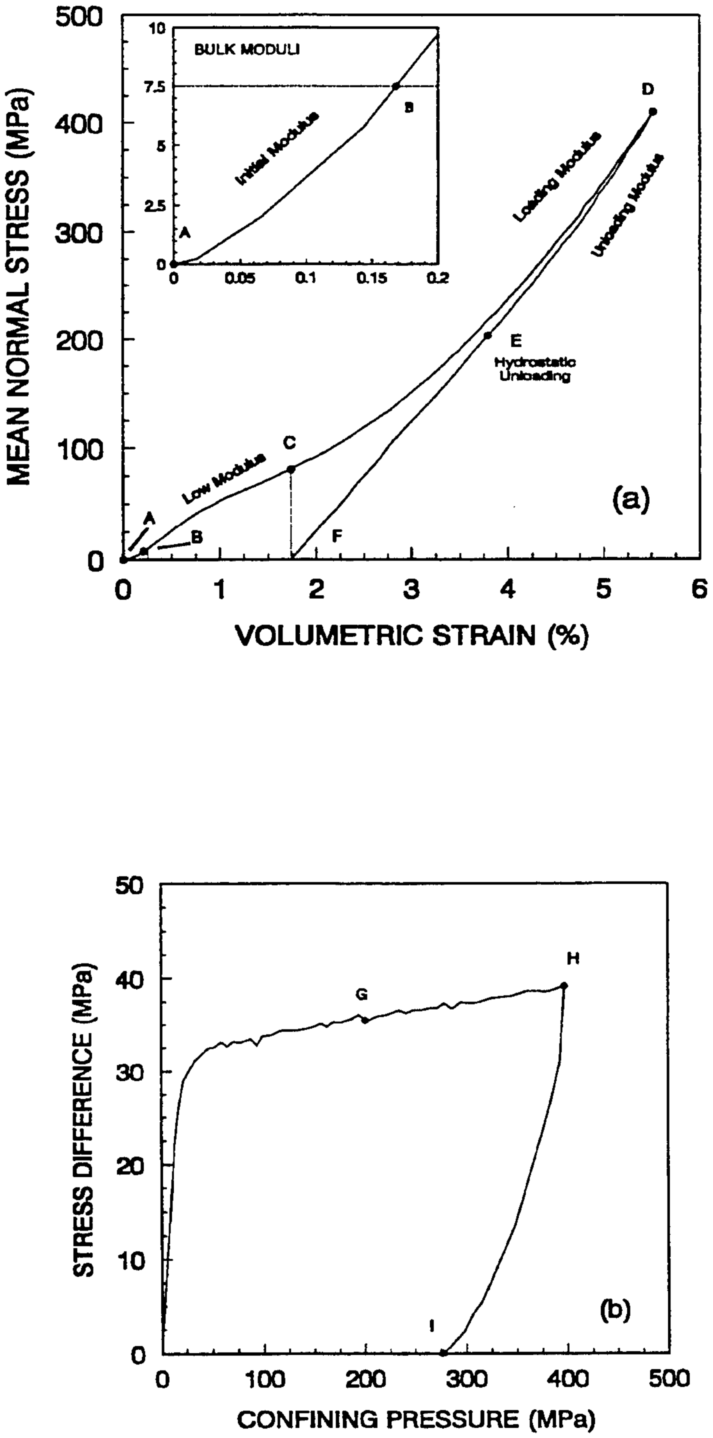

Figure 2-1. Material properties and bulk moduli definitions.

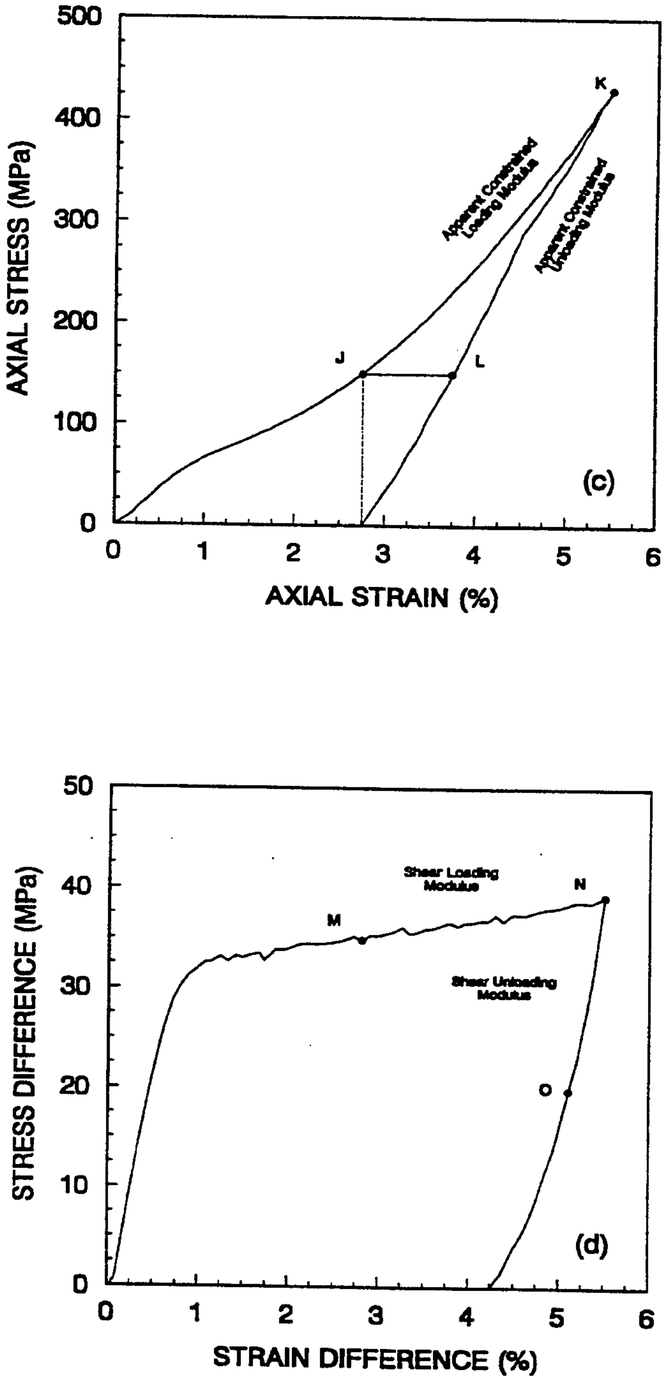

Figure 2-1. Apparent constrained and shear moduli definitions . (Continued)

2.3 PHYSICAL PROPERTY MEASUREMENT PROCEDURES.

Physical properties consisted of as-received weight in air, dry weight and effective and true grain volume for each test sample. Each set of physical property measurements was performed on a sample weighing between 50 and 70 gm cut immediately adjacent to the mechanical test sample. In many instances, physical properties were measured directly on the mechanical test samples. From these direct measurements, calculations were made to determine the as-received density, dry density, the effective porosity, and the total porosity (matrix porosity).

The bulk volume of regularly shaped specimens (usually right-circular cylinders) may be calculated from micrometer or caliper measurements. In some cases, bulk volume was determined using the mercury immersion technique. For cylindrical samples, an average of six diameter and four length readings, each accurate to 0.025 mm, are used for calculation of bulk volume. To measure the mass of the sample, a digital balance with a resolution of 0.001 gm was used. As-received bulk density was determined by simply dividing the as-received mass by the bulk volume. Dry density was similarly determined by dividing the dry mass (sample dried at either 105°C or 60°C) by it's bulk volume. A 60°C drying temperature was used for material containing moisture sensitive mineral phases (e.g., clays, zeolites, hydrated salts, etc.).

Grain density was measured on test plugs and powders using the gas pycnometry technique. After the dry density measurement, the test plugs were inserted into a porosimeter, and the effective grain volume determined using Boyle's Law. Gas pycnometry is based on Boyle's Law, which holds that, at constant temperature, the volume of an ideal gas will vary inversely with the pressure:

$$\frac{P_1}{P_2} = \frac{V_2}{V_1} \tag{2.5}$$

where P_1, is the initial pressure in V_1, P_2 is the final pressure in V_2, V_1, is the initial volume and V_2 is the final volume.

The pressure in a reference vessel of known volume, V_1, is communicated with a vessel containing the sample. The porosimeter vessel is calibrated using a series of steel billets of known volume. V_1, is constant. By using different billets, V_2 increases by a known increment at each step of the calibration. As V_2 increases, the ratio P_1/P_2 also increases. From pressure volume relationships with various billets of different, known volumes, linear regression is used to generate a relevant proportionality factor. This is used in subsequent calculations of grain volume:

$$V_g = \alpha\left(\frac{P_1}{P_2}\right) + b \tag{2.6}$$

where V_g is the grain volume, α is a proportionality factor between grain volume and pressure ratio, and b is a constant (representing a zero offset due to "dead volume" in the porosimeter). The grain density is calculated as follows:

$$\rho_g = \frac{W}{V_g} \tag{2.7}$$

where ρ_g is the grain density (gm/cm^3), W is the pre-test weight (gm), and V_g is the grain volume determined from the porosimeter (cm^3).

Gas pycnometry can be used to measure grain density on powdered (destructive) or plug (nondestructive) specimens, assuming all porosity is connected. With plug specimens, the interconnected pores are flooded with gas and an effective grain density is determined. The measurement is generally performed on an oven dried sample using a low to no sorptive gas (normally helium).

The dry density and the effective and true grain densities were used to calculate the effective porosity and total (matrix) porosity using the relation:

$$\text{Porosity} = 1 - \left(\frac{\rho_d}{\rho_g} \right) \tag{2.8}$$

where ρ_d is the dry density and ρ_g is either the effective or true grain density.

2.4 ULTRASONIC VELOCITY MEASUREMENT PROCEDURES.

Ultrasonic velocities were measured using the "Pulse-Propagation Technique" shown in block diagram form in Figure 2-2. This is an adaptation of the technique introduced by Mattaboni and Schreiber[2] which is capable of measuring small elapsed times to a high degree of accuracy. Time measurements were obtained from the frequency synthesizer data (stability ±l part in 10^7/month, accuracy ±0.0001 percent).

Compressional (P) and shear (S) wave velocities were measured on all the mechanical test specimens at bench conditions. Bench conditions involved applying a nominal axial stress of approximately 1 MPa. To measure the P and S-wave velocities, two piezoelectric (1MHz) crystals were placed in mechanical contact with the sample, one at each end. A high voltage pulse of short duration was then applied to one of the crystals, using a pulse generator. This pulse was received by the crystal at the opposite end of the specimen. Based on the time required for the pulse to travel through the length of the specimen, the P and S-wave velocities were calculated. The formula for calculating the dynamic properties are as follows[3]:

$$E = \frac{C_s^2 \rho \left[3 (C_p / C_s)^2 - 4 \right]}{\left[(C_p / C_s)^2 - 1 \right]} \tag{2.9}$$

---

[2] Mattaboni, P., and Schreiber, E., "Methods of Pulse Transmission Measurements for Determining Sound Velocities," Journal of Geophysical Research, Vol. 70, No. 20, pp. 5160-5163, 1967.

[3] Jaegar, J.C. and Cook, N.G.W., *Fundamentals of Rock Mechanics,* Chapman and Hall, pp. 183-187, 1979.

$$\nu = \frac{\frac{1}{2}\left[\left(\frac{C_p}{C_s}\right)^2 - 2\right]}{\left[\left(\frac{C_p}{C_s}\right)^2 - 1\right]} \tag{2.10}$$

$$K = \rho\left(C_p^2 - \frac{4C_s^2}{3}\right) \tag{2.11}$$

$$G = C_s^2(\rho) \tag{2.12}$$

where:

E = Young's modulus,

ν = Poisson's ratio,

K = Bulk modulus,

G = Shear modulus,

ρ = Bulk density,

C_p = Compressional velocity, and

C_s = Shear velocity.

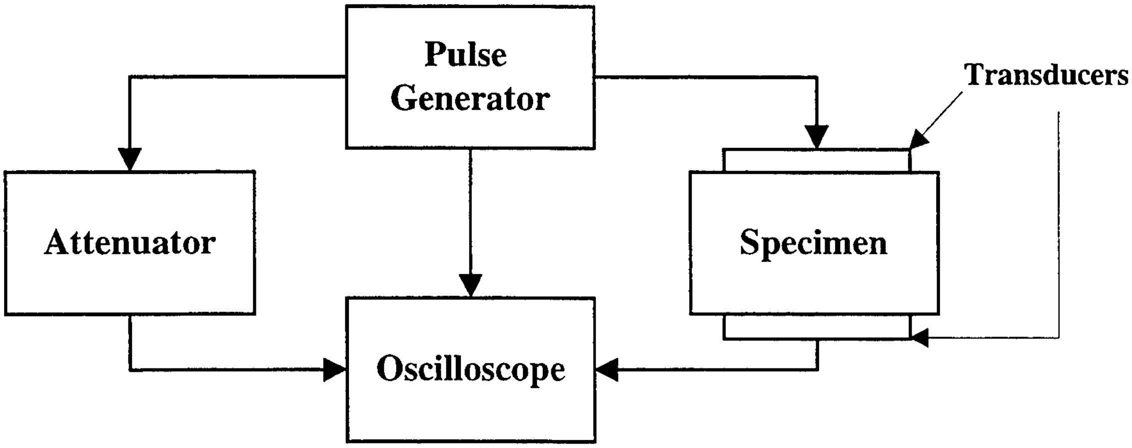

Figure 2-2. Pulse propagation system.

2.5 SEMI-QUANTITATIVE MINERALOGIC ANALYSIS BY X-RAY DIFFRACTION

Bulk-Analysis: Representative one-gram splits of bulk samples were ground in acetone in an agate mortar to <325 mesh (<45 μ) then scanned at 2°2θ per minute from 2-65°2θ. Diagnostic peaks of minerals identified on resulting diffractograms were rescanned on duplicate samples. Approximate weight percentages of the minerals were determined by comparing diagnostic peak intensities with those generated by standard pure phases mixed in various known proportions.

Clay Analysis: Bulk samples, at least 35 grams if possible, were sonically disaggregated in deionized water, allowed to settle sufficiently to yield the desired particle size fraction (generally <2 μ or <5 μ), decanted and centrifuged. The resulting slurries were smeared on glass slides and X-rayed at 1°2θ per minute following air-drying (2-37°) vapor glycolation for 24 hours at 60°C (2-22°), heating to 250°C for one hour (2-15°), and/or heating to 550°C for one hour (2-15°). Approximate weight percentages of the layer silicates identified on diffractograms corresponding to these treatments were determined by comparison of diagnostic peak intensities with those generated by pure reference clays in appropriate mixtures.

APPENDIX A
LABORATORY STUDY OF SAMPLES SELECTED FROM THE SHIST SITE

A.1 PREPARATION.

Nominal 1 inch diameter plugs with lengths varying from 1.4 to 2 inches were cut from selected cores. Short lengths (lengths between 1.40 and 1.53 inches) were obtained for the perpendicular samples due to the size restrictions of the whole core (1.865 inches). A total of twelve test plugs were cut, four from each core box (two parallel and two perpendicular with respect to the whole core axis). The test plugs were identified by their depth and orientation with respect to the whole core axis (|| or ⊥). Water was used as the circulating/cooling fluid during all cutting, coring, and grinding activities. In addition to the test plugs cut for material properties testing at TerraTek, gas gun samples were prepared from Core Hole #1 for dynamic testing at Ktech. A total of five in-situ stress samples and four visar samples were prepared and sent to Ktech in two shipments. A list of the gas gun samples shipped is provided in Tables A-1 and A-2.

A.2 PROCEDURES.

Physical properties consisted of bulk density (dry), effective and true grain density, and effective and total porosity. The core was received in an unpreserved dry state. Hence, moisture content and saturation was not determined. Following preparation, the test plugs were placed in an oven set at 105°C for a period of 24 hours to drive off any residual water imbibed in the samples during preparation. The dried samples were then weighed and the bulk volume measured employing the mercury immersion technique. The bulk density was calculated by dividing the mass of the test sample by its bulk volume. Effective grain density was determined using Boyle's Law helium porosimetry on the intact plug sample. Following the unconfined compression tests, each plug was pulverized to minus 100μm, and the true grain density measured using the water pycnometry method. From the bulk density and effective and true grain densities, the porosity (effective or total) was calculated using the relation:

$$\phi = 1 - \frac{\rho_d}{\rho_g} \qquad \text{(A.1)}$$

where ϕ is the porosity, ρ_d is the dry bulk density, and ρ_g is the grain density.

Ultrasonic velocities (P- and S-waves) were measured on each plug at bench conditions prior to unconfined compression testing. Dynamic properties were calculated from the measured velocities and the test sample bulk density. Unconfined compression tests were conducted using an axial strain rate of $10^{-5}s^{-1}$ until catastrophic failure occurred. Both axial and radial deformation was measured during unconfined compressive loading. Static properties were calculated from the measured strains and axial stress.

A.3 RESULTS.

Tables A-3 through A-6 present the XRD mineralogy, physical properties, ultrasonic velocities, and unconfined compressive strengths. Included in Table A-4 (physical properties) is the estimated occluded voids, which is the difference between the total and effective porosities. Stress-strain curves generated from the unconfined compression tests are provided in Annex 1.

As indicated in Table A-3, the material from the SHIST site has a granite composition (quartz >20%, K-spar 35-90% of feldspars, plagioclase 10-65% of feldspars, and mafics 5-20%). Two samples were analyzed using XRD; one sample from Core Hole #1, depth 163.2 ft., and the other from Core Hole #2, depth 104.9 ft. Both samples have essentially the same mineralogy. This limited data set suggests that the SHIST site is compositionally similar.

Consistent bulk, effective grain and true grain densities were measured for this material. Bulk densities ranged from 2.587 to 2.606 gm/cc and averaged 2.599 gm/cc (±0.007 gm/cc). Effective grain and total grain densities ranged from 2.611 to 2.622 gm/cc and 2.633 to 2.639 gm/cc, and averaged 2.616 gm/cc (±0.003 gm/cc) and 2.636 gm/cc (±0.002 gm/cc), respectively. The effective, total, and occluded porosities averaged 0.65% (±0.3), 1.4% (±0.2), and 0.8% (±0.2%), respectively. It is interesting to note that the effective and occluded porosities are nearly equal.

Ultrasonic velocities were more variable as shown in Table A-5. P-wave and S-wave velocities ranged from 4.323 to 5.356 km/sec and 2.771 to 3.343 km/sec, respectively. The P-wave velocities measured parallel to the axis of the whole core are consistently faster then P-wave velocities measured perpendicular to the core axis. This slight anisotropic behavior is illustrated in Figure A-1.

Compressive strengths were also variable with values ranging from 75.9 to 132.4 MPa. The lowest strength of 75.9 MPa was measured for sample 105.0 ft. (||), which contained a healed joint oriented at approximately 30° with respect to the plug axis. This structural feature undoubtedly contributed to the lower strength determined for sample 105.0 ft. (||). The average strength for the SHIST samples tested was 106.2 MPa (±15.8 MPa). There is a slight indication of anisotropic behavior based on compressive strength. As shown in Figure A-2, the perpendicular plugs are consistently stronger then the parallel samples with one exception. The samples tested from a depth of 115 ft. had similar strengths (86.3 and 93.1 MPa).

Table A-1. SHIST site gas gun samples shipped to Ktech on September 29, 1993.

Sample ID	Core Hole	Depth (ft)	Length (in)	Diameter (in)	Weight (gm)
In-Situ Stress Samples					
1A	#1	165.73-.76	0.194	1.872	22.632
1B	#1	165.76-.79	0.193	1.872	22.581
1C	#1	165.79-.85	0.390	1.872	45.653
2A	#1	165.85-.91	0.395	1.872	46.186
2B	#1	165.91-.94	0.199	1.872	23.284
2C	#1	165.94-.97	0.199	1.872	23.283
3A	#1	165.70-.73	0.196	1.872	22.894
3B	#1	165.33-.36	0.197	1.871	22.824
3C	#1	164.98-65.04	0.393	1.872	46.010
Visar Samples					
1	#1	163.02-.04	0.198	1.871	23.099
2	#1	162.75-.77	0.199	1.871	23.177
3	#1	162.77-.80	0.199	1.871	23.134

Table A-2. SHIST gas gun samples shipped to Ktech on October 6, 1993.

Sample ID	Core Hole	Depth (ft)	Length (in)	Diameter (in)	Weight (gm)
In-Situ Stress Samples					
4A	#1	164.95-.98	0.193	1.872	22.679
4B	#1	164.91-.95	0.194	1.872	22.773
4C	#1	164.86-.91	0.395	1.872	46.335
5A	#1	164.83-.86	0.197	1.872	23.164
5B	#1	164.80-.83	0.196	1.872	23.056
5C	#1	164.75-.80	0.395	1.872	46.322
Visar Samples					
4	#1	164.72-.75	0.199	1.872	23.395

Table A-3. XRD semi-quantitative mineralogy of selected samples from the SHIST site.

Core Hole	Depth (ft)	Mineralogy, Approximate Weight Percent					
		Quartz	Plagioclase	K-Feldspar	Calcite	Chlorite	Illite/Mica*
#2	104.9-104.95	32	22	34	2	4	6
#1	163.2-163.25	28	26	36	3	3	4

*Illite/mica is probably biotite (dark micaceous mineral) - verified from thin section.

Table A-4. Summary of Physical Properties for SHIST Test Plugs.

Sample ID (ft)	Core Hole	Length (in)	Diameter (in)	Weight (gm)	Bulk Density (gm/cc)	Effective Grain Density (gm/cc)	Effective Porosity (%)	True Grain Density (gm/cc)	Total Porosity (%)	Occluded Porosity (%)
104.9-105.0 (⊥)	#2	1.445	0.995	48.014	2.596	2.619	0.9	2.633	1.4	0.5
105.0-105.2 (‖)	#2	1.991	0.994	64.934	2.587	2.611	0.9	2.637	1.9	1.0
115.6-115.7 (⊥)	#2	1.421	0.996	47.327	2.592	2.618	1.0	2.635	1.6	0.6
115.3-115.5 (‖)	#2	1.996	0.996	66.435	2.602	2.614	0.5	2.637	1.3	0.8
124.2-124.3 (⊥)	#2	1.400	0.996	46.239	2.601	2.612	0.4	2.633	1.2	0.8
123.9-124.1 (‖)	#2	1.999	0.995	66.375	2.605	2.614	0.3	2.638	1.3	1.0
128.6-128.7 (⊥)	#2	1.485	0.996	49.256	2.604	2.615	0.4	2.635	1.2	0.8
128.7-128.9 (‖)	#2	1.993	0.995	66.283	2.603	2.622	0.6	2.636	1.3	0.7
163.2-163.3 (⊥)	#1	1.531	0.995	50.361	2.587	2.618	1.2	2.634	1.8	0.6
162.9-163.1 (‖)	#1	1.996	0.994	66.116	2.603	2.613	0.4	2.634	1.2	0.8
166.2-166.3 (⊥)	#1	1.526	0.996	50.123	2.596	2.618	0.9	2.639	1.6	0.7
166.3-166.5 (‖)	#1	1.994	0.994	66.070	2.606	2.616	0.3	2.639	1.3	1.0

⊥designates perpendicular test plug - plug drilled perpendicular to the axis of the whole core.
‖ designates parallel test plug - plug drilled parallel to the axis of the whole core.

Table A-5. Summary of Ultrasonic Velocities and Calculated Dynamic Properties for the SHIST Test Plugs.

Sample ID (ft)	Core Hole	Length (in)	Bulk Density (gm/cc)	P-Wave Velocity (km/sec)	S-Wave Velocity (km/sec)	Dynamic Properties			
						Poisson's Ratio	Young's Modulus (Gpa)	Bulk Modulus (Gpa)	Shear Modulus (Gpa)
104.9-105.0 (⊥)	#2	1.445	2.596	4.729	3.008	0.16	54.5	26.7	23.5
105.0-105.2 (‖)	#2	1.991	2.587	4.812	2.771	0.25	49.7	33.1	19.9
115.6-115.7 (⊥)	#2	1.423	2.592	4.323	2.812	0.13	46.4	20.9	20.5
115.3-115.5 (‖)	#2	1.997	2.602	4.565	2.980	0.13	52.1	23.5	23.1
124.2-124.3 (⊥)	#2	1.398	2.601	5.025	3.126	0.18	60.2	31.3	25.5
123.9-124.1 (‖)	#2	1.999	2.605	5.097	3.105	0.20	60.5	33.6	25.2
128.6-128.7 (⊥)	#2	1.487	2.604	5.029	3.242	0.14	62.6	29.0	27.5
128.7-128.9 (‖)	#2	1.994	2.603	5.189	3.278	0.17	65.3	33.0	27.9
163.2-163.3 (⊥)	#1	1.532	2.587	5.147	3.297	0.15	64.8	30.8	28.2
162.9-163.1 (‖)	#1	1.994	2.603	5.326	3.343	0.17	68.3	34.5	29.2
166.2-166.3 (⊥)	#1	1.526	2.596	4.900	3.177	0.14	59.6	27.6	26.1
166.3-166.5 (‖)	#1	1.995	2.606	5.356	3.290	0.20	67.5	37.5	28.1

⊥ designates perpendicular test plug - plug drilled perpendicular to the axis of the whole core.

‖ designates parallel test plug - plug drilled parallel to the axis of the whole core.

Table A-6. Summary of Static Mechanical Properties determined from Unconfined Compression Tests for the SHIST Test Plugs.

Sample ID (ft)	Core Hole	Compressive Strength (MPa)	Poisson's Ratio	Young's Modulus (GPa)	Bulk Modulus (GPa)	Shear Modulus (GPa)
104.9-105.0 (⊥)	#2	109.2	0.35	35.5	39.6	13.1
105.0-105.2 (‖)	#2	75.9	0.34	22.3	23.0	8.3
115.6-115.7 (⊥)	#2	86.3	0.37	25.9	33.3	9.5
115.3-115.5 (‖)	#2	93.1	0.25	30.5	20.3	12.2
124.2-124.3 (⊥)	#2	119.7	0.33	50.8	50.1	19.1
123.9-124.1 (‖)	#2	95.0	0.21	38.6	22.3	15.9
128.6-128.7 (⊥)	#2	114.4	0.26	42.7	29.8	16.9
128.7-128.9 (‖)	#2	106.8	0.36	52.0	60.5	19.2
163.2-163.3 (⊥)	#1	132.4	0.44 0.37*	50.9 48.6*	146.5 63.5*	17.7 17.7*
162.9-163.1 (‖)	#1	116.9	0.22	43.7	25.8	18.0
166.2-166.3 (⊥)	#1	114.2	0.43 0.34*	38.2 38.5*	93.5 39.4*	13.3 14.4*
166.3-166.5 (‖)	#1	110.5	0.22	45.0	27.1	18.4

⊥ designates perpendicular test plug - plug drilled perpendicular to the axis of the whole core.
‖ designates parallel test plug - plug drilled parallel to the axis of the whole core.

*Static properties calculated between 10 and 40% of the maximum axial stress. All other static properties determined between 10 and 50% of the maximum axial stress.

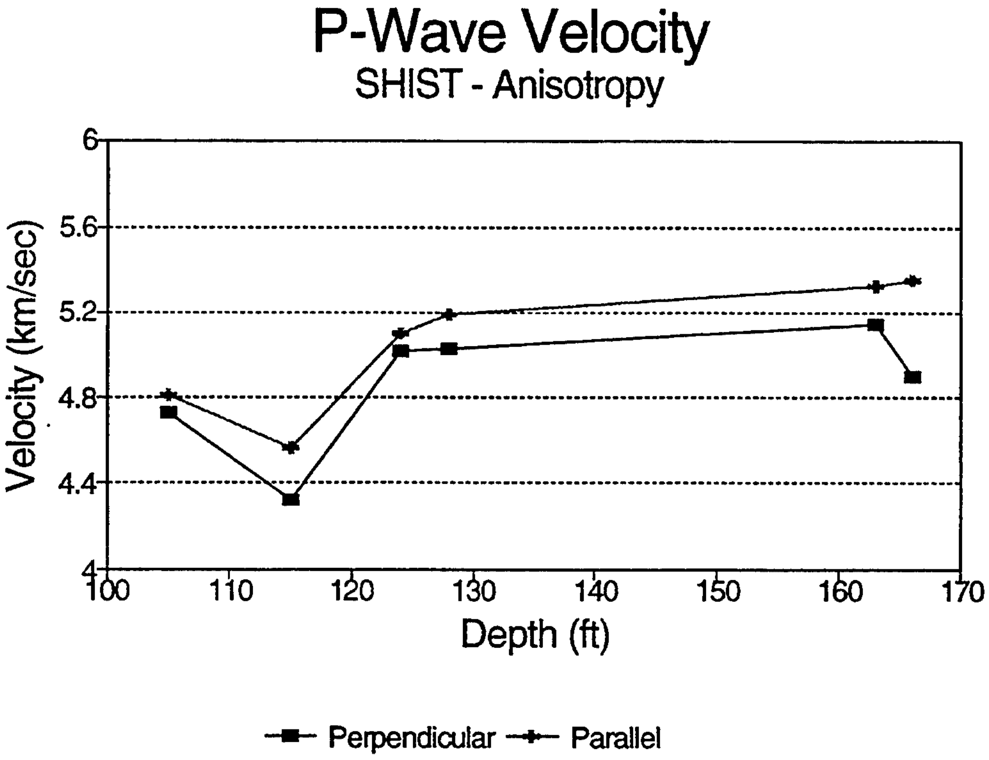

Figure A-1. P-wave velocity comparisons for selected samples from the SHIST site.

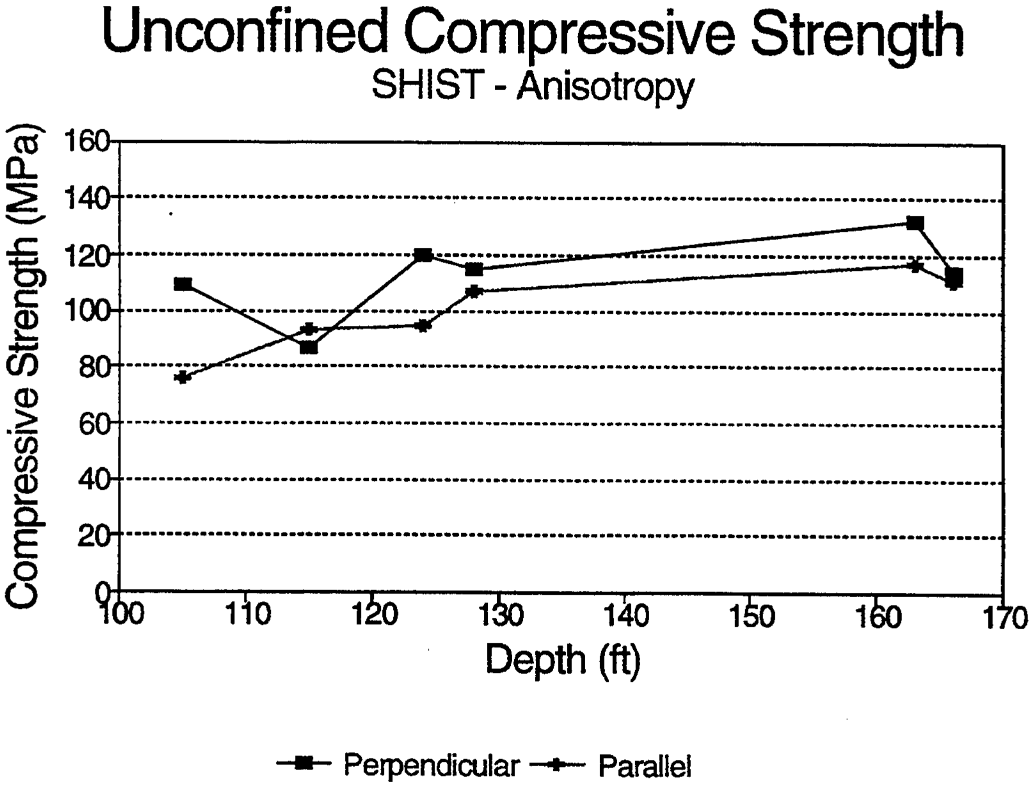

Figure A-2. Unconfined compressive strength comparisons for selected samples from the SHIST site.

Annex 1
Stress-Strain Plots - Unconfined Compression Tests

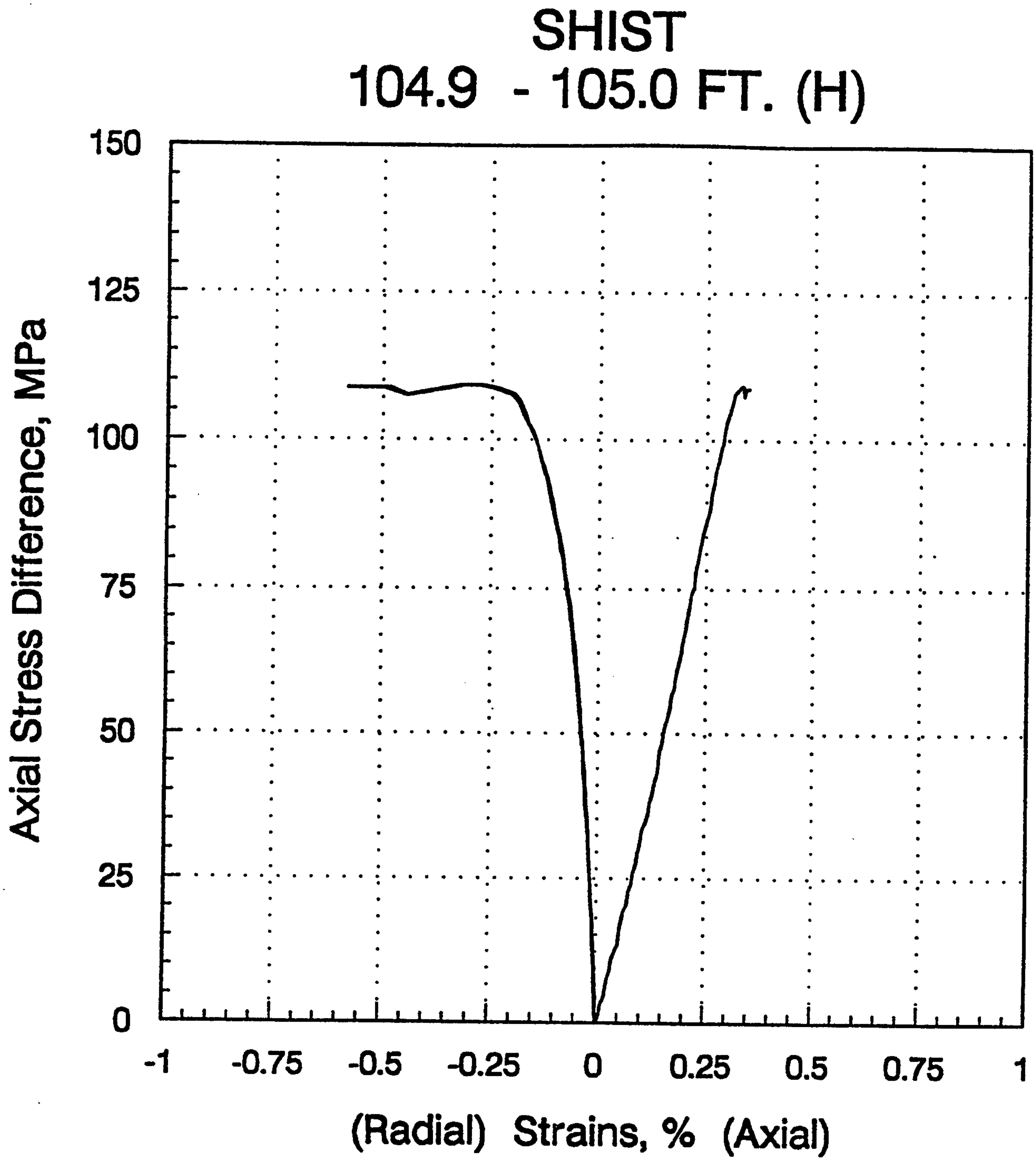

Figure A-3. Stress versus strain for sample 104.9 - 105.0 ft. (H).

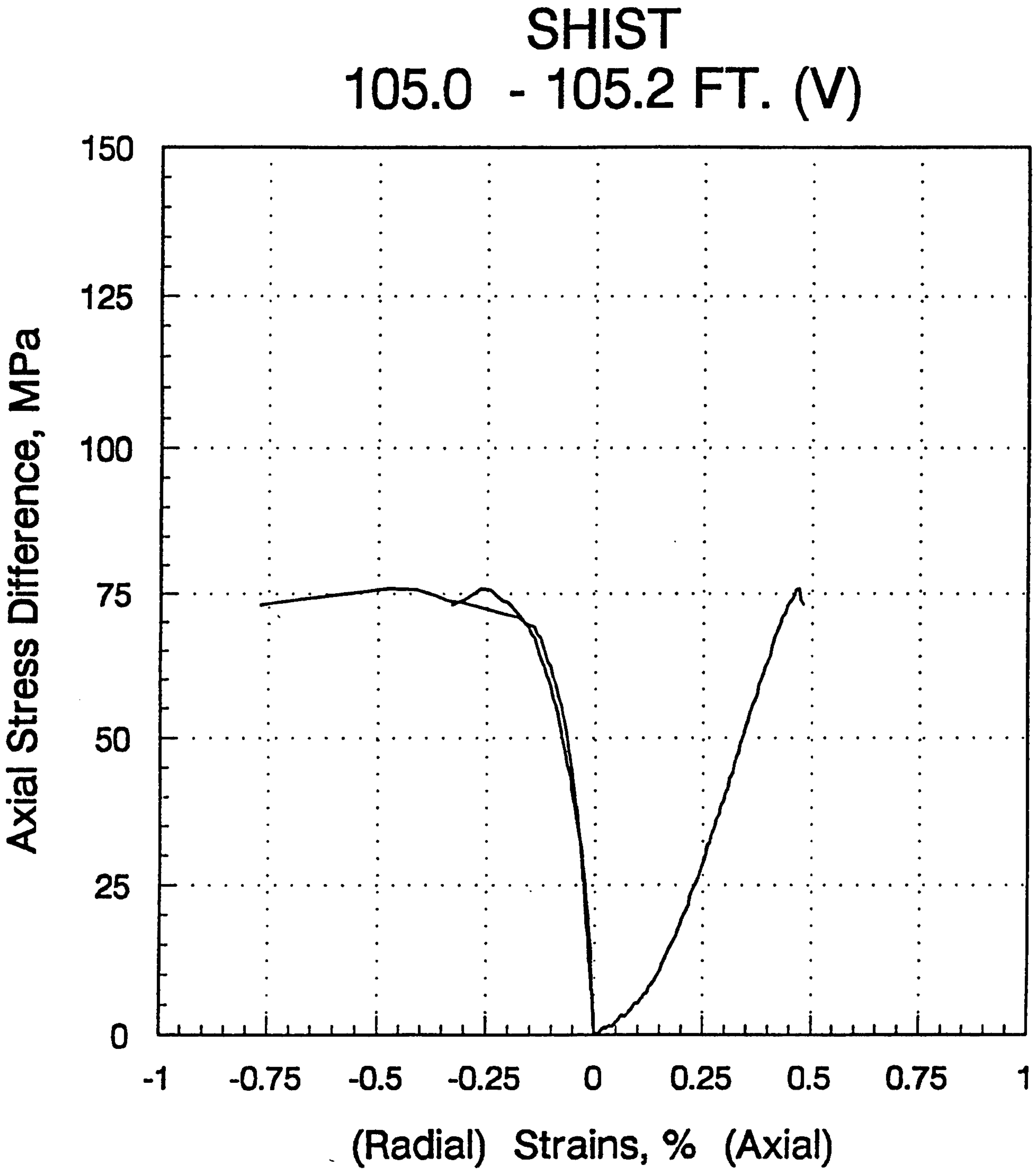

Figure A-4. Stress versus strain for sample 105.0 - 105.2 ft. (V).

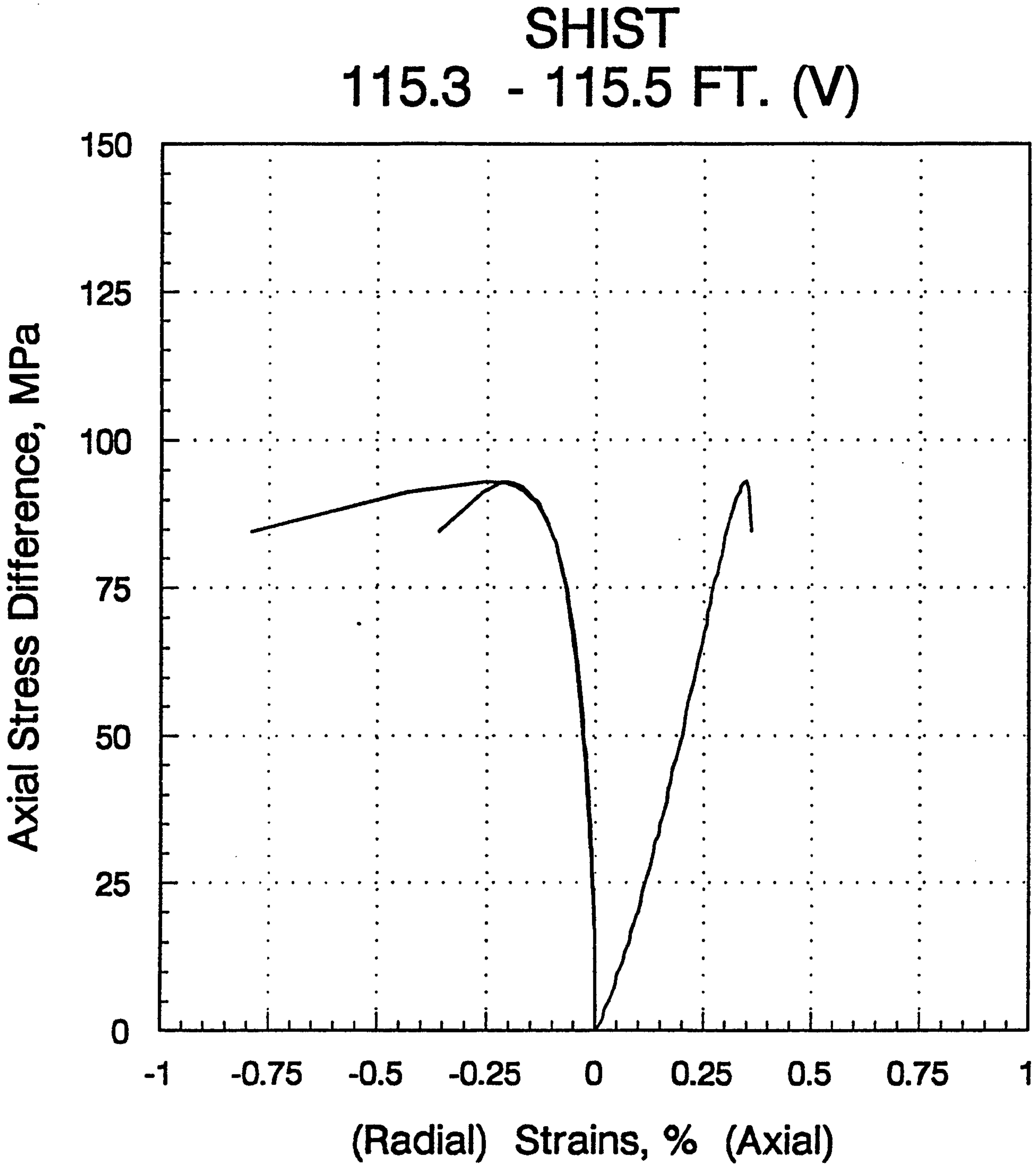

Figure A-5. Stress versus strain for sample 115.3 - 115.5 ft. (V).

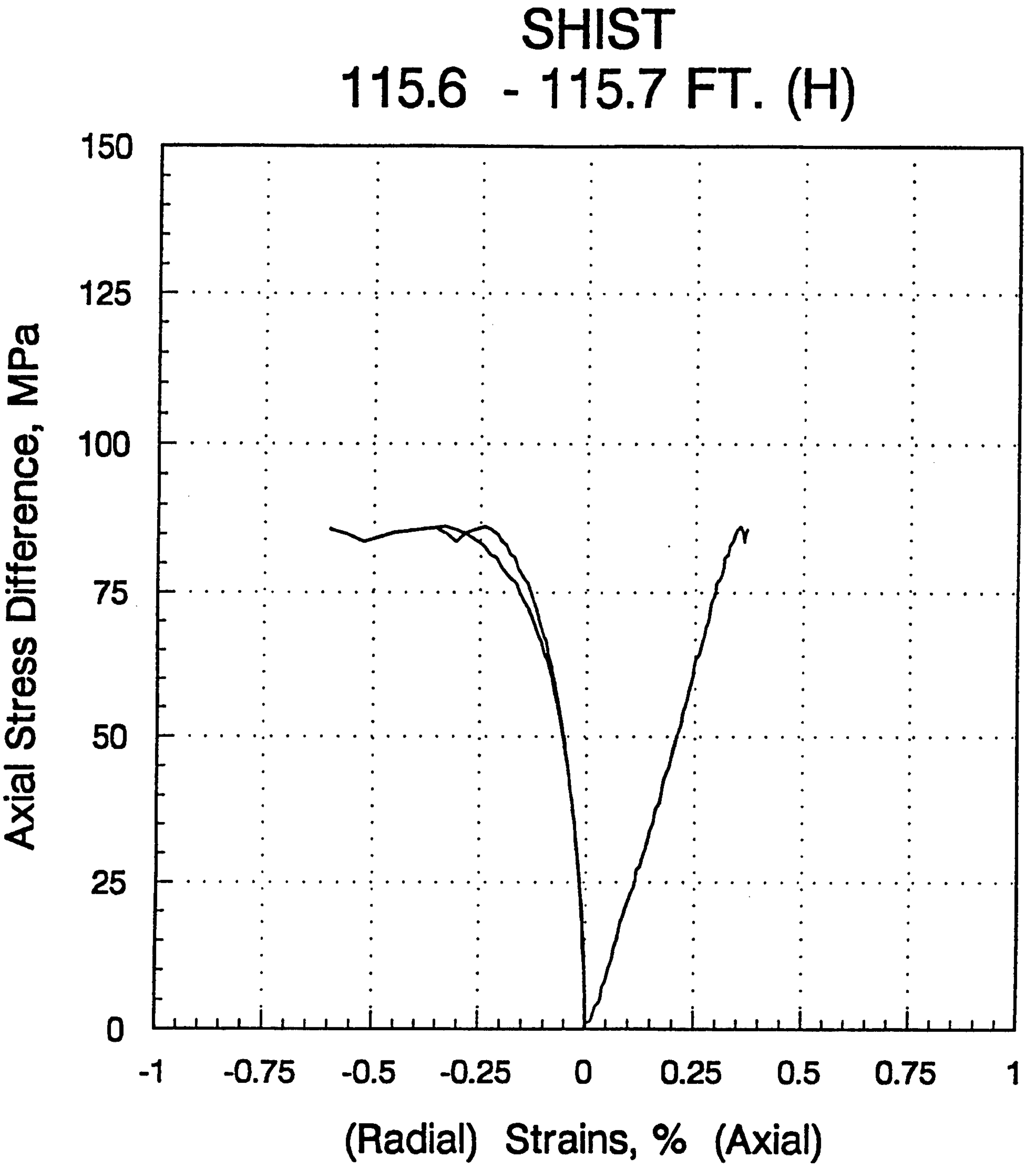

Figure A-6. Stress versus strain for sample 115.6 - 115.7 ft. (H).

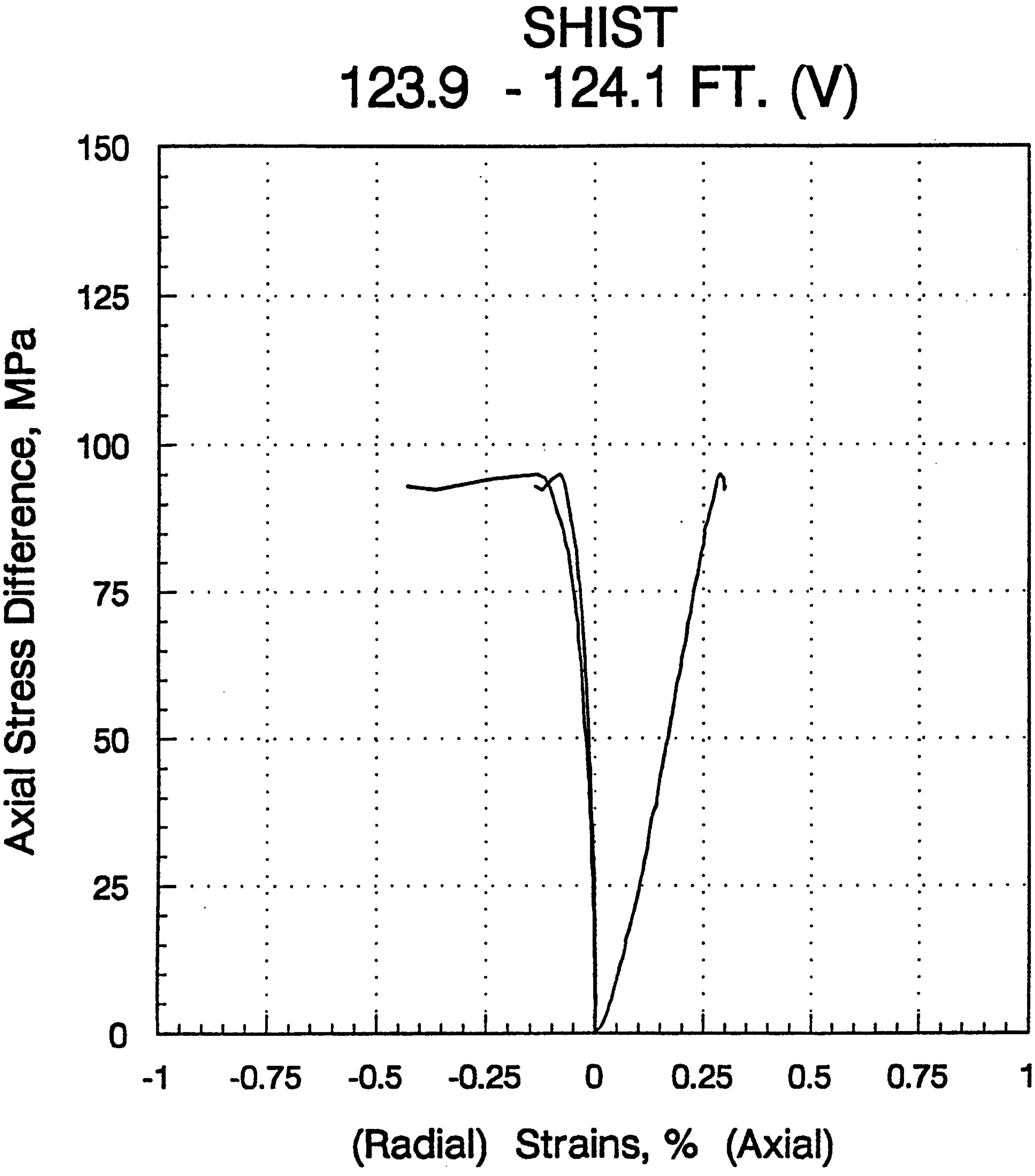

Figure A-7. Stress versus strain for sample 123.9 - 124.1 ft. (V).

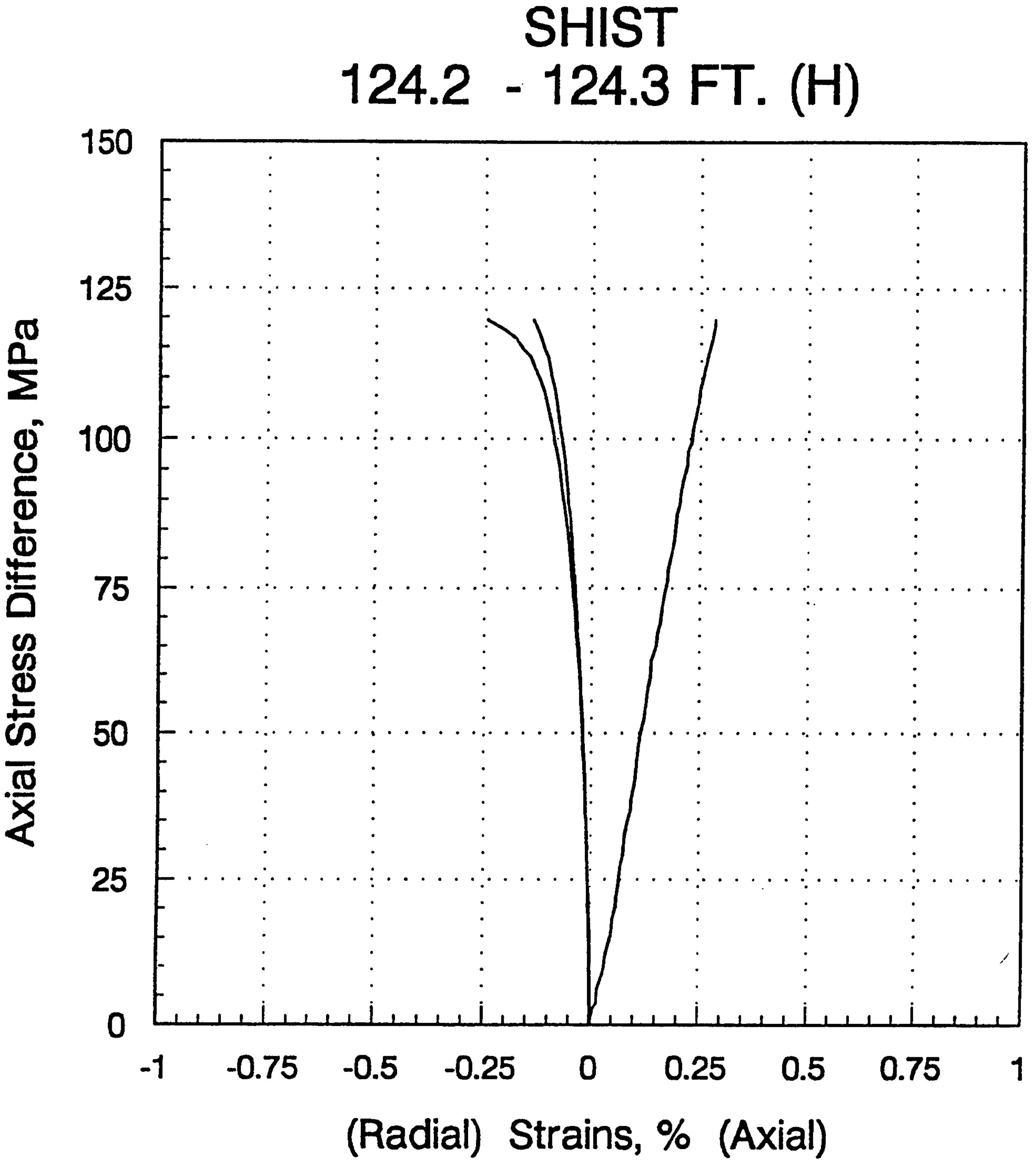

Figure A-8. Stress versus strain for sample 124.2 - 124.3 ft. (H).

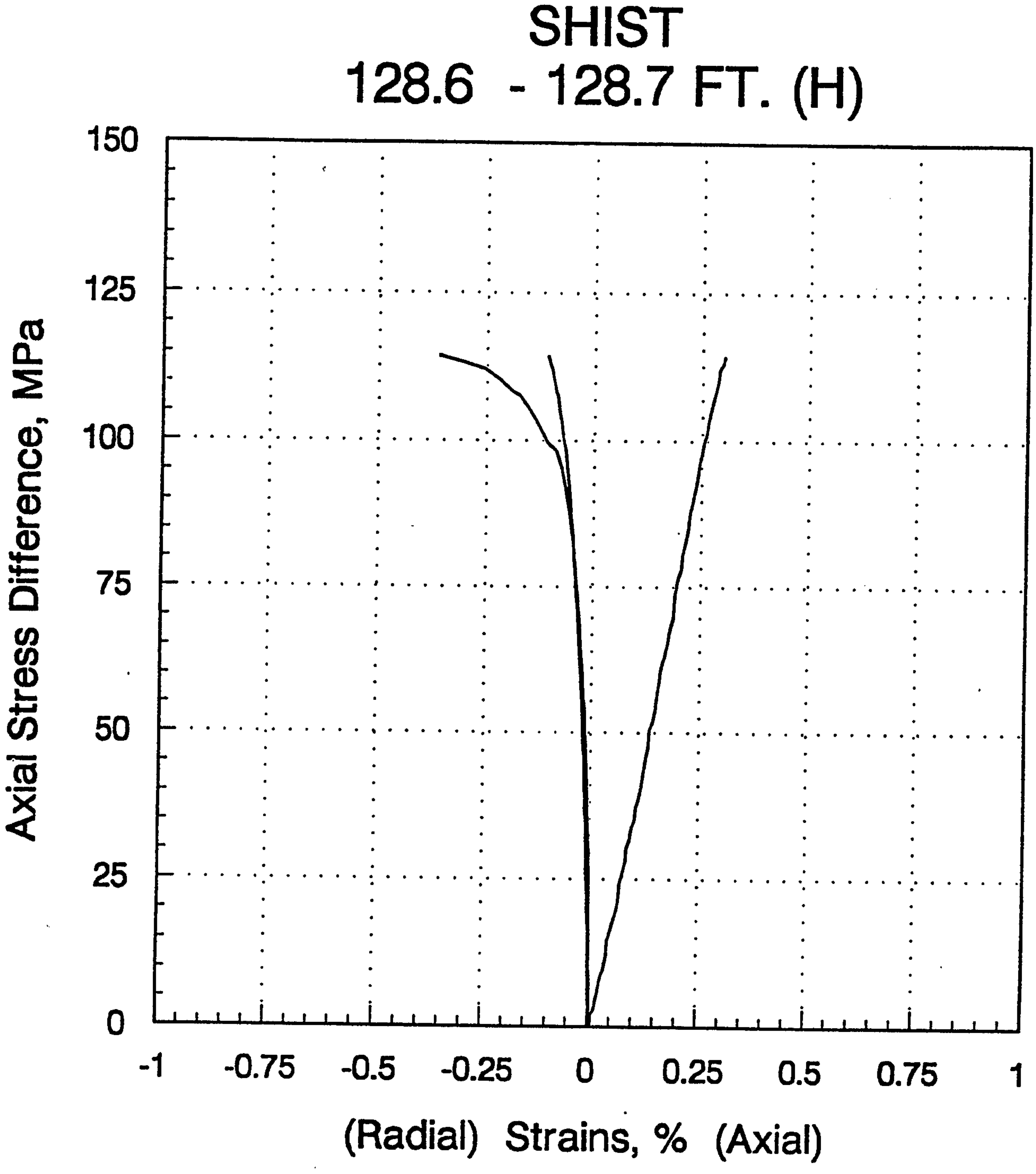

Figure A-9. Stress versus strain for sample 128.6 - 128.7 ft. (H).

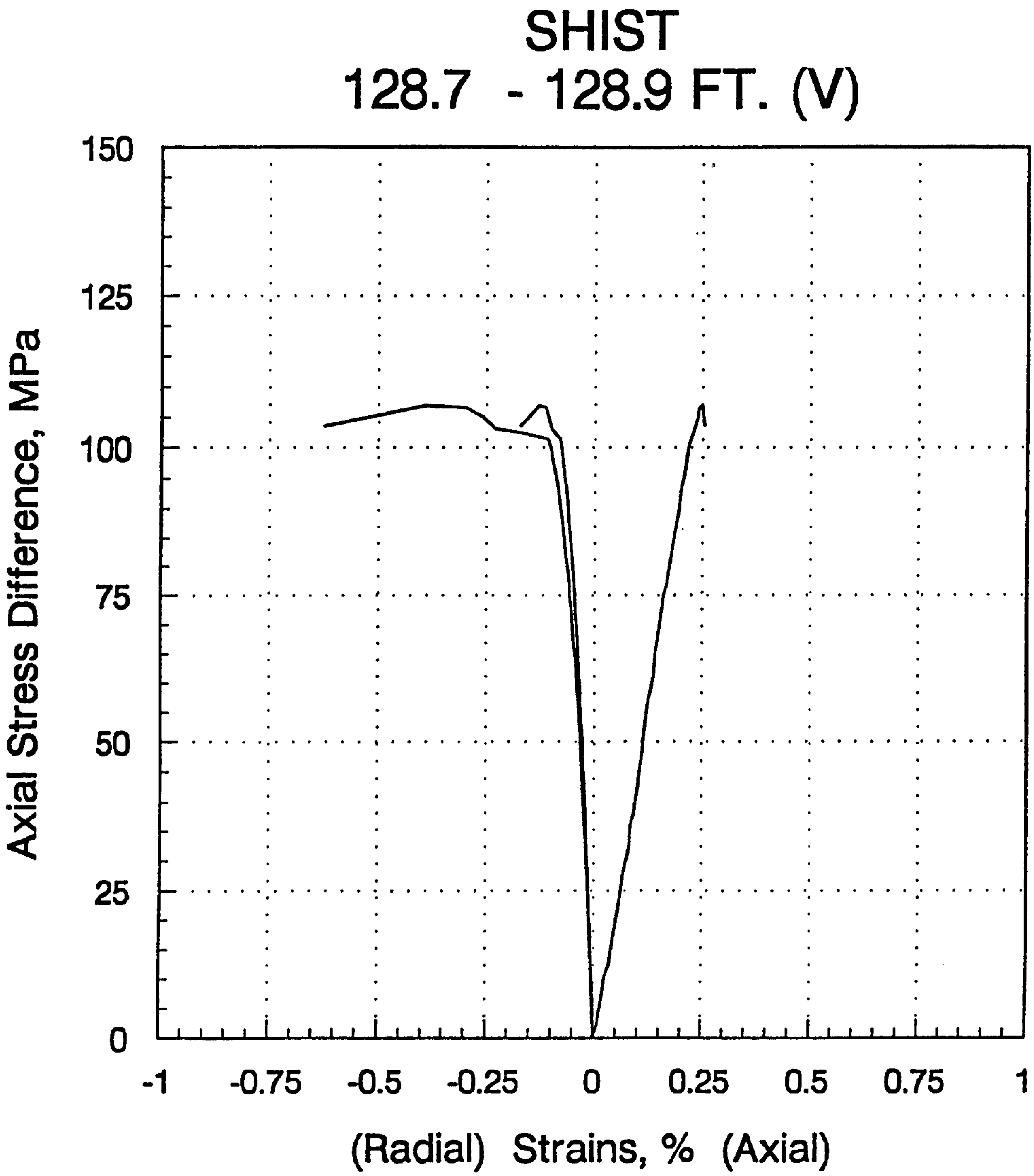

Figure A-10. Stress versus strain for sample 128.7 - 128.9 ft. (V).

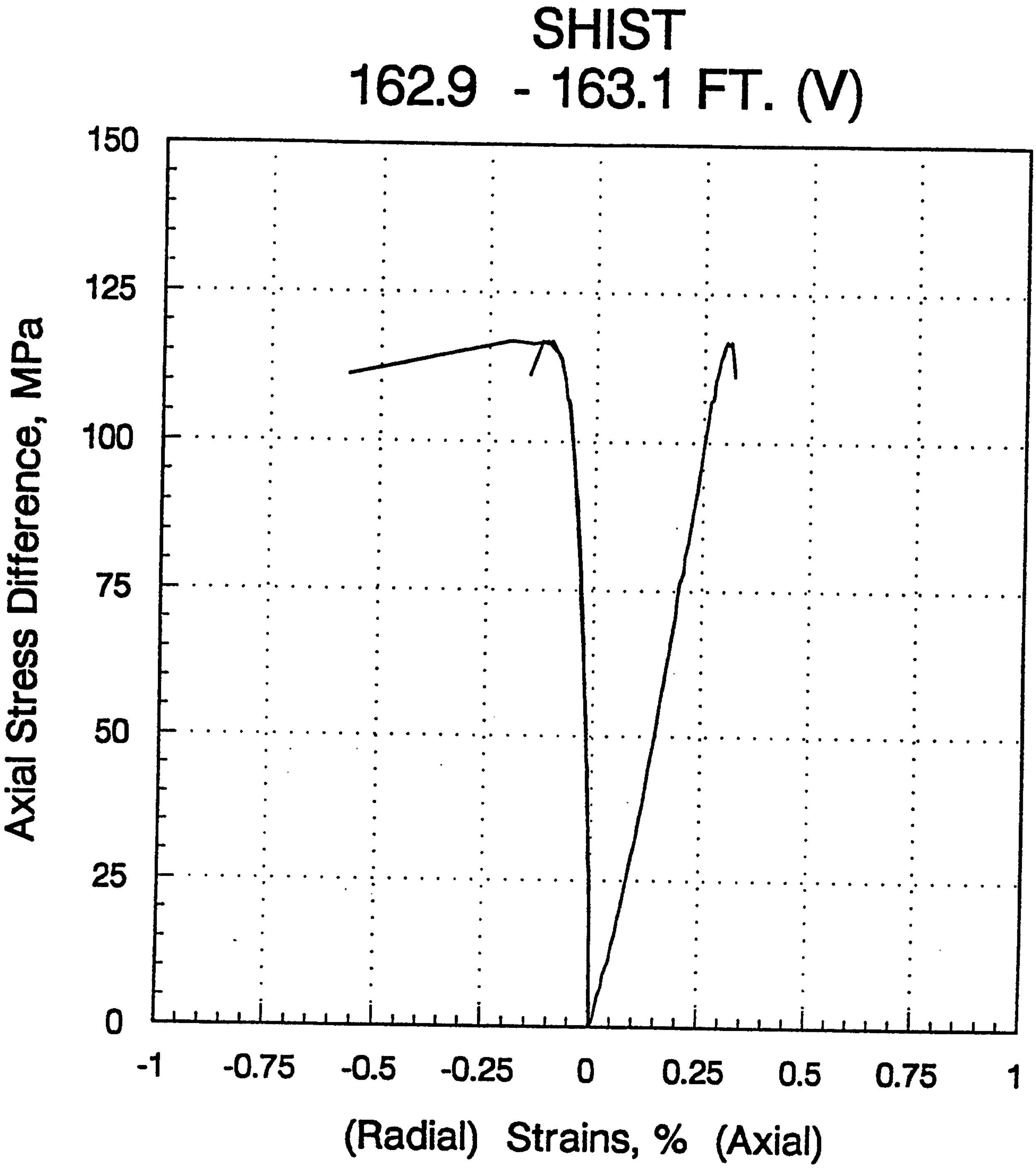

Figure A-11. Stress versus strain for sample 162.9 - 163.1 ft. (V).

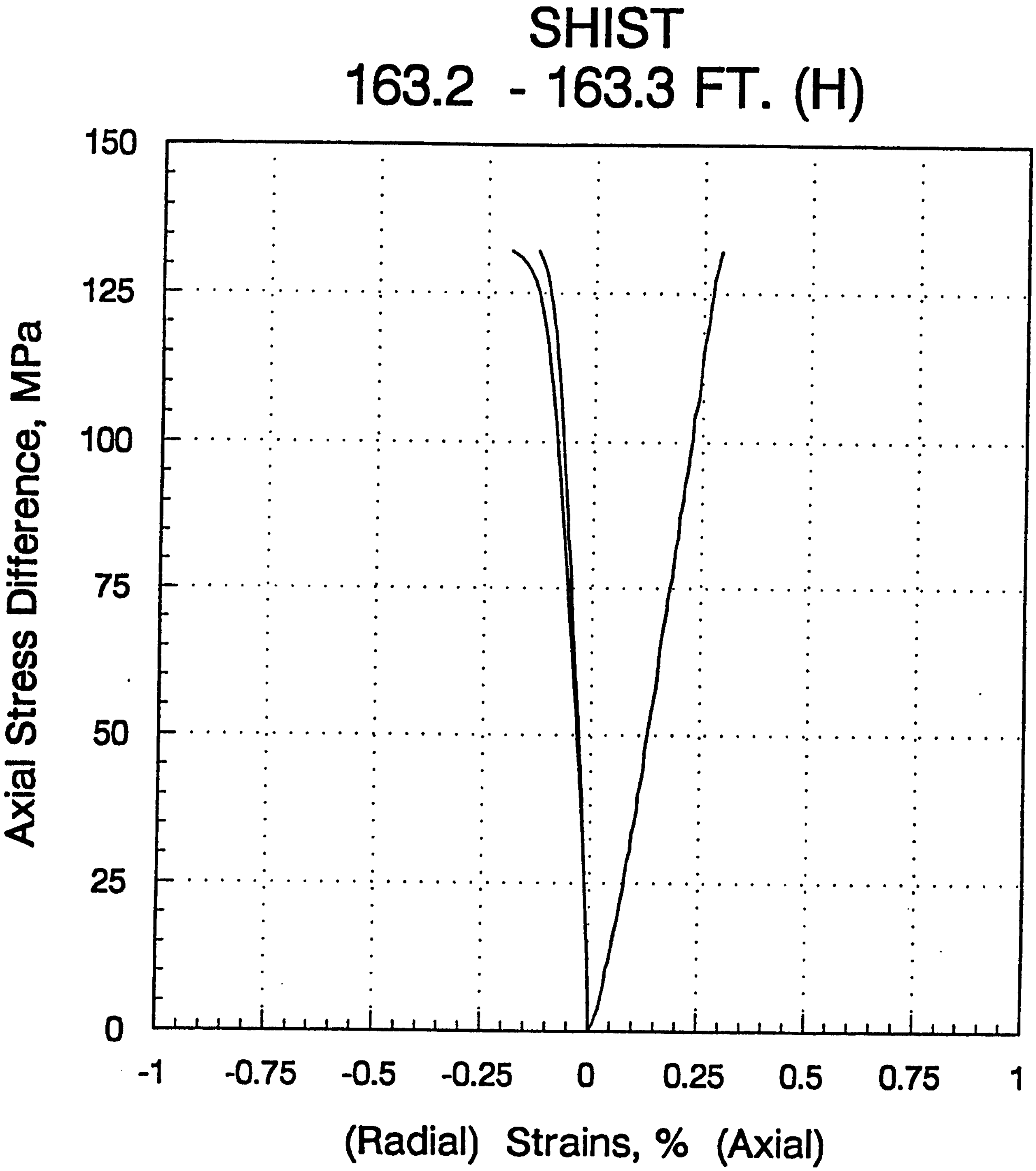

Figure A-12. Stress versus strain for sample 163.2 - 163.3 ft. (H).

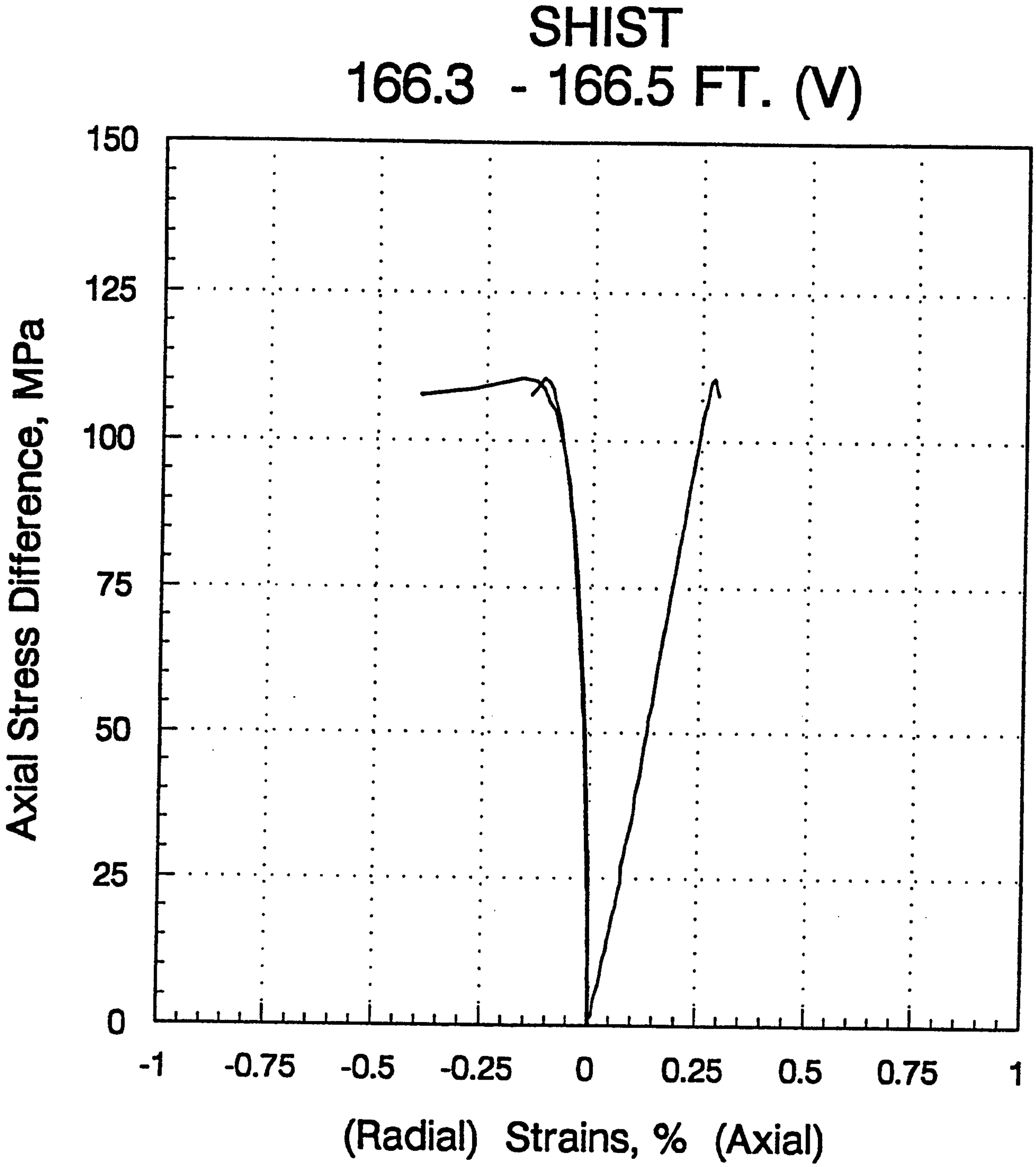

Figure A-13. Stress versus strain for sample 166.3 - 166.5 ft. (V).

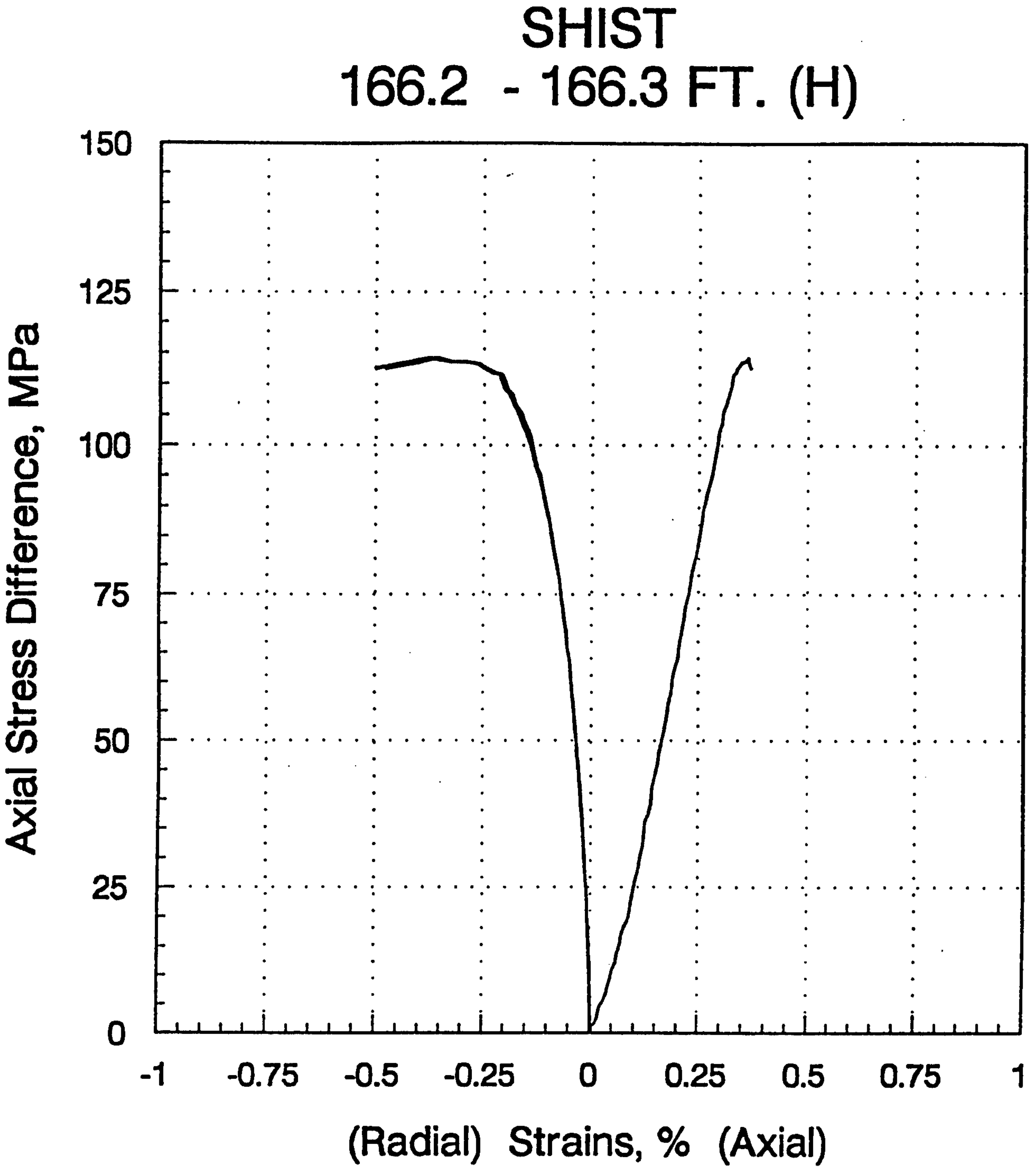

Figure A-14. Stress versus strain for sample 166.2 - 166.3 ft. (H).

APPENDIX B
MATERIAL PROPERTIES FOR THE SHIST SITE

B.1 PREPARATION.

Nominal 1 inch diameter plugs with lengths varying from 0.94 to 2 inches were cut from selected cores. Short lengths (lengths between 0.94 and 1.50 inches) were obtained for the perpendicular samples due to the size restrictions of the whole core (1.865 inches). One sample was exceptionally short with a length of 0.94 inches (depth 58.9 to 59.0 ft.) due to pre-existing fractures. A total of ten test plugs were cut, two from each depth interval (two parallel and two perpendicular with respect to the whole core axis). The test plugs were identified by their depth and orientation with respect to the whole core axis (|| or ⊥). Water was used as the circulating/cooling fluid during all cutting, coring, and grinding activities. In addition to the test plugs cut for material properties testing at TerraTek, gas gun samples were prepared from Core Hole #1 (depth interval 118.0 to 119.0 ft.) for dynamic testing at Sandia. A total of four visar samples were prepared and sent to Sandia on November 3, 1993. A list of the gas gun samples shipped is provided in Table B-1.

B.2 PROCEDURES.

Physical properties consisted of bulk density (dry), effective and true grain density, and effective and total porosity. Most of the core was received in an unpreserved dry state. Hence, moisture content and saturation was not determined on the unpreserved material. Following preparation, the test plugs were placed in an oven set at 105°C for a period of 24 hours to drive off any residual water imbibed in the samples during preparation. The dried samples were then weighed and the bulk volume measured employing the mercury immersion technique. The bulk density was calculated by dividing the mass of the test sample by its bulk volume. Effective grain density was determined using Boyle's Law helium porosimetry on the intact plug sample. Following the unconfined compression tests, each plug was pulverized to minus 100μm, and the true grain density measured using the water pycnometry method. From the bulk density and effective and true grain densities, the porosity (effective or total) was calculated using the relation:

$$\phi = 1 - \frac{\rho_d}{\rho_g} \tag{B.1}$$

where ϕ is the porosity, ρ_d is the dry bulk density, and ρ_g is the grain density.

Ultrasonic velocities (P- and S-waves) were measured on each plug at bench conditions prior to unconfined compression testing. Dynamic properties were calculated from the measured velocities and the test sample bulk density. Unconfined compression tests were conducted using an axial strain rate of $10^{-5}s^{-1}$ until catastrophic failure occurred. Both axial and radial deformation was measured during unconfined compressive loading. Static properties were calculated from the measured strains and axial stress. Ultrasonic velocity and unconfined compression testing was repeated on several samples to establish repeatability of the initial test results. The driving force behind the repeat testing was the anomalously low strength, moduli and ultrasonic velocities determined on this selection of core samples from the SHIST site (relative to the first set of samples tested previously).

B.3 RESULTS.

Tables B-2 through B-4 present the physical properties, ultrasonic velocities, and unconfined compressive strengths. Included in Table B-2 (physical properties) is the estimated occluded voids, which is the difference between the total and effective porosities. Stress-strain curves generated from the unconfined compression tests are included in Annex 2.

Consistent bulk, effective grain and true grain densities were measured for this material. Bulk densities ranged from 2.565 to 2.598 gm/cc and averaged 2.577 gm/cc (±0.012 gm/cc). Effective grain and true grain densities ranged from 2.619 to 2.629 gm/cc and 2.628 to 2.639 gm/cc, and averaged 2.625 gm/cc (±0.003 gm/cc) and 2.634 gm/cc (±0.004 gm/cc), respectively. The effective, total, and occluded porosities averaged 1.8% (±0.5), 2.2% (±0.4), and 0.3% (±0.1%), respectively. The effective and total porosity values are nearly twice those measured on the first set of material. This suggests that the second set of material may contain more fracture porosity due to their shallower depths.

Ultrasonic velocities were more variable as shown in Table B-3. P-wave and S-wave velocities ranged from 3.611 to 4.595 km/sec and 2.151 to 2.808 km/sec, respectively. As shown in Figure B-1, P-wave velocities fluctuate regardless of the orientation. Three of the five parallel oriented samples have faster velocities. Stronger anisotropy was noted for the first set of material where all of the P-wave velocities measured parallel to the axis of the whole core were consistently faster then P-wave velocities measured perpendicular to the core axis. Also, the average velocities (both P and S) determined on the second set of material are lower relative to the first set.

Compressive strengths were also variable with values ranging from 52.9 to 100.3 MPa. More fractures were observed in this set of material, which contributed to the overall low strengths. The average strength for the second set of SHIST samples tested was 73.4 MPa (±13.3 MPa). The average strength for the second set of material is more than 25% lower then the first set. As shown in Figure B-2, there is a weak correlation that the perpendicular plugs are slightly stronger then the parallel samples. However, due to the limited number of tests conducted, it is difficult to comment on any strength anisotropy relationships.

Table B-1. SHIST site gas gun samples shipped to Sandia on November 3, 1993.

Sample ID	Core Hole	Depth (ft)	Length (in)	Diameter (in)	Weight (gm)	Bulk Volume (cc)	Calipered Bulk Density (gm/cc)
I	#1	118.84-118.88	0.196	1.871	22.730	8.831	2.574
II	#1	118.88-118.92	0.196	1.870	22.696	8.821	2.573
III	#1	118.92-118.96	0.196	1.867	22.577	8.793	2.568
IV	#1	118.96-119.00	0.197	1.870	22.733	8.866	2.564

Table B-2. Summary of Physical Properties for SHIST Test Plugs.

Sample ID (ft)	Core Hole	Length (in)	Diameter (in)	Weight (gm)	Bulk Density (gm/cc)	Effective Grain Density (gm/cc)	Effective Porosity (%)	True Grain Density (gm/cc)	Total Porosity (%)	Occluded Porosity (%)
19.2 - 19.3 (⊥)	#1	1.501	0.996	48.929	2.565	2.625	2.3	2.639	2.8	0.5
19.3 - 19.5 (‖)	#1	1.999	0.996	65.451	2.565	2.623	2.2	2.631	2.5	0.3
46.5 - 46.6 (⊥)	#5	1.503	0.996	49.372	2.578	2.628	1.9	2.636	2.2	0.3
46.3 - 46.5 (‖)	#5	2.001	0.996	66.083	2.586	2.628	1.6	2.637	1.9	0.3
58.9 - 59.0 (⊥)	#3	0.940	0.996	30.351	2.568	2.627	2.2	2.628	2.3	0.1
59.0 - 59.2 (‖)	#3	1.999	0.996	65.572	2.568	2.629	2.3	2.634	2.5	0.2
75.4 - 75.5 (⊥)	#1	1.503	0.996	49.877	2.598	2.623	1.0	2.634	1.4	0.4
75.2 - 75.4 (‖)	#1	1.999	0.996	66.297	2.595	2.627	1.2	2.635	1.5	0.3
118.2 - 118.3 (⊥)	#1	1.411	0.996	46.395	2.576	2.622	1.8	2.639	2.4	0.6
118.0 - 118.2 (‖)	#1	2.001	0.996	65.778	2.575	2.619	1.7	2.630	2.1	0.4

⊥ designates perpendicular test plug - plug drilled perpendicular to the axis of the whole core.
|| designates parallel test plug - plug drilled parallel to the axis of the whole core.

B-3. Summary of Ultrasonic Velocities and Calculated Dynamic Properties for the SHIST Test Plugs.

Sample ID (ft)	Core Hole	Length (in)	Bulk Density (gm/cc)	P-Wave Velocity (km/sec)	S-Wave Velocity (km/sec)	Dynamic Properties			
						Poisson's Ratio	Young's Modulus (GPa)	Bulk Modulus (GPa)	Shear Modulus (GPa)
19.2 - 19.3 (⊥)	#1	1.501	2.565	4.165	2.384	0.26	36.6	25.4	14.5
19.3 - 19.5 (‖)	#1	1.999	2.565	3.611	2.151	0.23	29.1	17.9	11.8
46.5 - 46.6 (⊥)	#5	1.503	2.578	4.217	2.344	0.28	36.1	27.3	14.1
46.6 - 46.7 (⊥)	#5	1.524	*	4.274	2.708	0.17	-	-	-
46.3 - 46.5 (‖)	#5	2.001	2.586	4.595	2.808	0.20	49.0	27.2	20.4
46.7 - 46.9 (‖)	#5	2.052	*	4.490	2.537	0.27	-	-	-
58.9 - 59.0 (⊥)	#3	0.940	2.568	4.149	2.366	0.26	36.2	25.1	14.4
59.0 - 59.2 (‖)	#3	1.999	2.568	3.920	2.238	0.26	32.3	22.4	12.8
75.4 - 75.5 (⊥)	#1	1.503	2.598	4.460	2.512	0.27	41.5	30.1	16.4
74.9 - 75.0 (‖)	#1	1.512	*	4.571	2.803	0.20	-	-	-
75.2 - 75.4 (‖)	#1	1.999	2.595	4.549	2.760	0.21	47.8	27.4	19.7
75.0 - 75.2 (‖)	#1	2.022	*	4.258	2.776	0.13	-	-	-
118.2 - 118.3 (⊥)	#1	1.411	2.576	4.094	2.360	0.25	35.9	23.9	14.4
118.8 - 118.9 (⊥)	#1	1.524	*	4.204	2.547	0.21	-	-	-
118.0 - 118.2 (‖)	#1	2.001	2.575	4.397	2.633	0.22	43.5	25.9	17.8
118.6 - 118.8 (‖)	#1	1.971	*	4.330	2.490	0.25	-	-	-

* mass-density was not determined for this particular sample. Hence, moduli was not calculated.

⊥ designates perpendicular test plug - plug drilled perpendicular to the axis of the whole core.

‖ designates parallel test plug - plug drilled parallel to the axis of the whole core.

Table B-4. Summary of Static Mechanical Properties determined from Unconfined Compression Tests for the SHIST Test Plugs.

Sample ID (ft)	Core Hole	Compressive Strength (MPa)	Static Properties			
			Poisson's Ratio	Young's Modulus (GPa)	Bulk Modulus (GPa)	Shear Modulus (GPa)
19.2 - 19.3 (⊥)	#1	57.5	0.23	13.4	8.3	5.4
19.3 - 19.5 (∥)	#1	54.8	0.31	12.3	10.7	4.7
46.5 - 46.6 (⊥)	#5	82.7	0.19	15.5	8.4	6.5
46.6 - 46.7 (⊥)	#5	68.0	0.27	16.5	11.8	6.5
46.3 - 46.5 (∥)	#5	86.9	0.13	20.5	9.2	9.1
46.7 - 46.9 (∥)	#5	62.3	0.18	18.7	9.9	7.9
58.9 - 59.0 (⊥)*	#3	-	-	-	-	-
59.0 - 59.2 (∥)	#3	52.9	0.30	13.2	10.8	5.1
75.4 - 75.5 (⊥)	#1	100.3	0.13	17.6	7.9	7.8
74.9 - 75.0 (⊥)	#1	82.6	0.22	26.1	15.4	10.7
75.2 - 75.4 (∥)	#1	83.2	0.12	20.3	8.8	9.1
75.0 - 75.2 (∥)	#1	76.9	0.22	20.5	12.4	8.4
118.2 - 118.3 (⊥)	#1	80.6	0.19	16.7	9.0	7.0
118.8 - 118.9 (⊥)	#1	75.8	0.39	16.8	25.8	6.0
118.0 - 118.2 (∥)	#1	68.5	0.10	19.0	7.9	8.6
118.6 - 118.8 (∥)	#1	67.9	0.31	18.9	17.0	7.2

*Sample not tested - Not sufficient length (0.94 inches) for mechanical testing.
⊥ designates perpendicular test plug - plug drilled perpendicular to the axis of the whole core.
∥ designates parallel test plug - plug drilled parallel to the axis of the whole core.

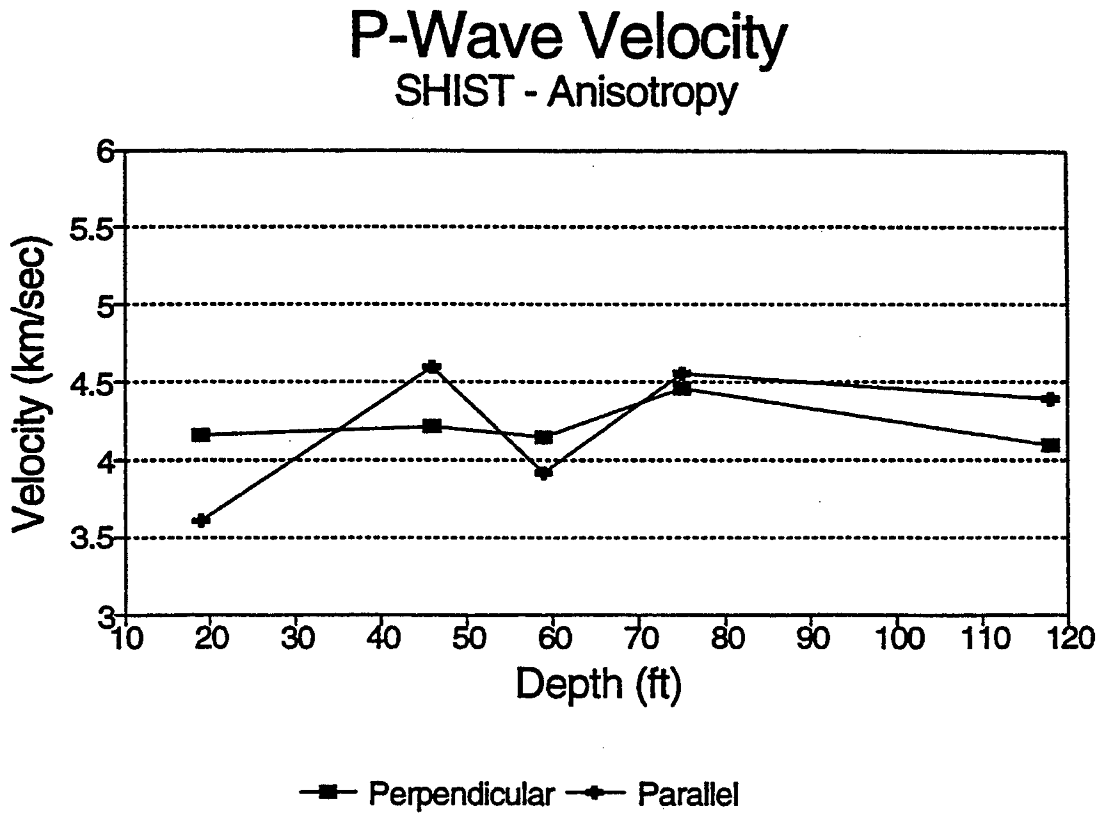

Figure B-1. P-wave velocity comparisons for selected samples from the SHIST site.

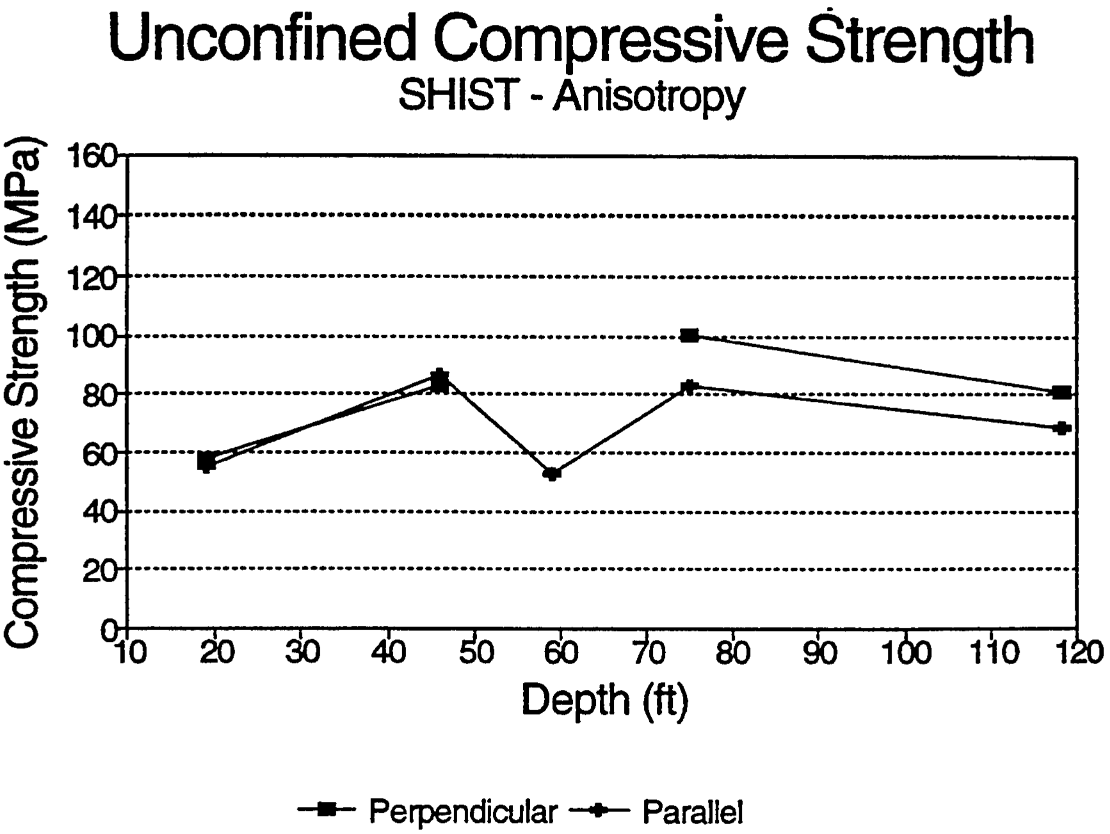

Figure B-2. Unconfined compressive strength comparisons for selected samples from the SHIST site.

Annex 2
Stress-Strain Plots - Unconfined Compression Tests

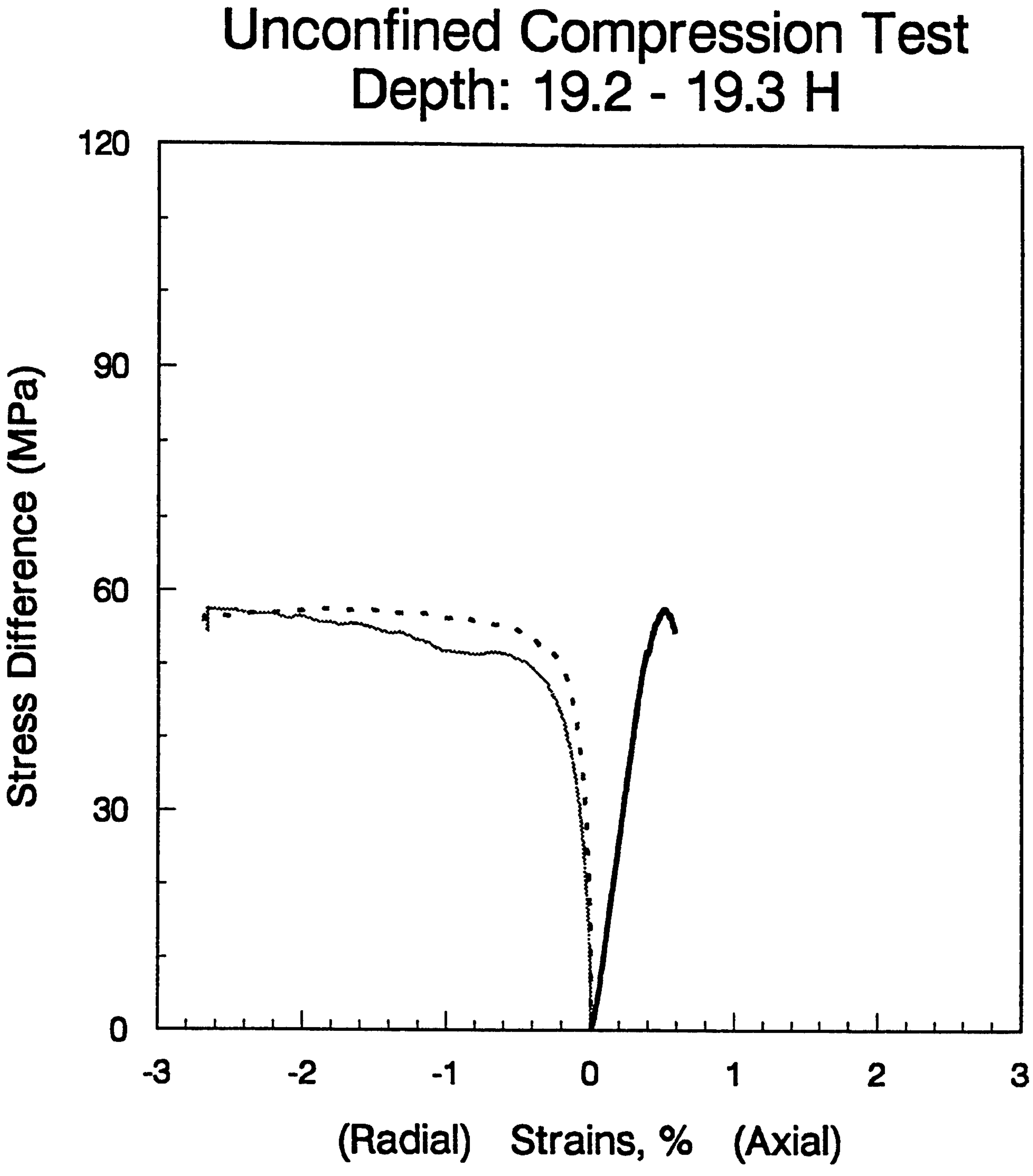

Figure B-3. Stress versus strain under unconfined compression conditions for sample 19.2 - 19.3 ft. (H).

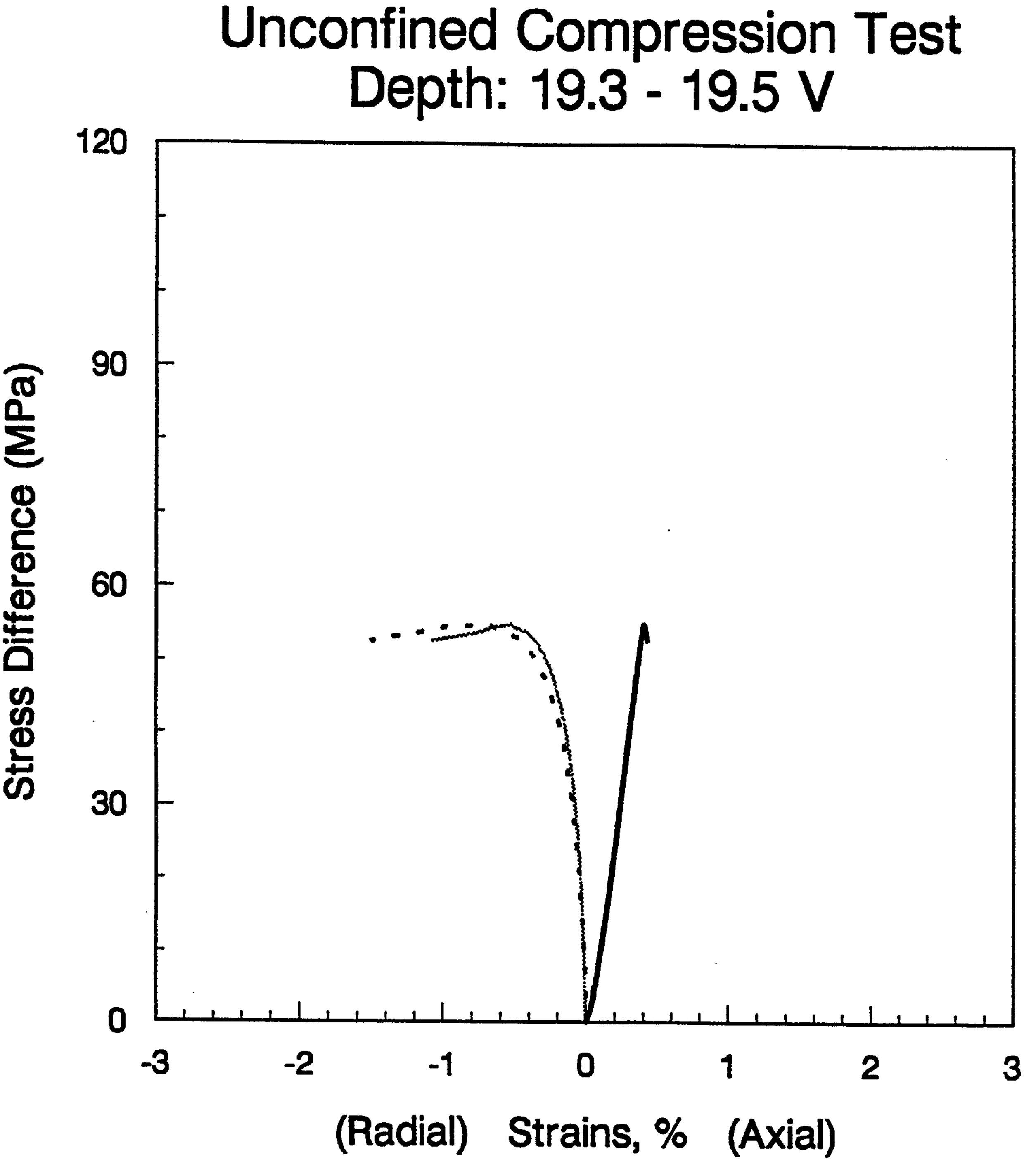

Figure B-4. Stress versus strain under unconfined compression conditions for sample 19.3 - 19.5 ft. (V).

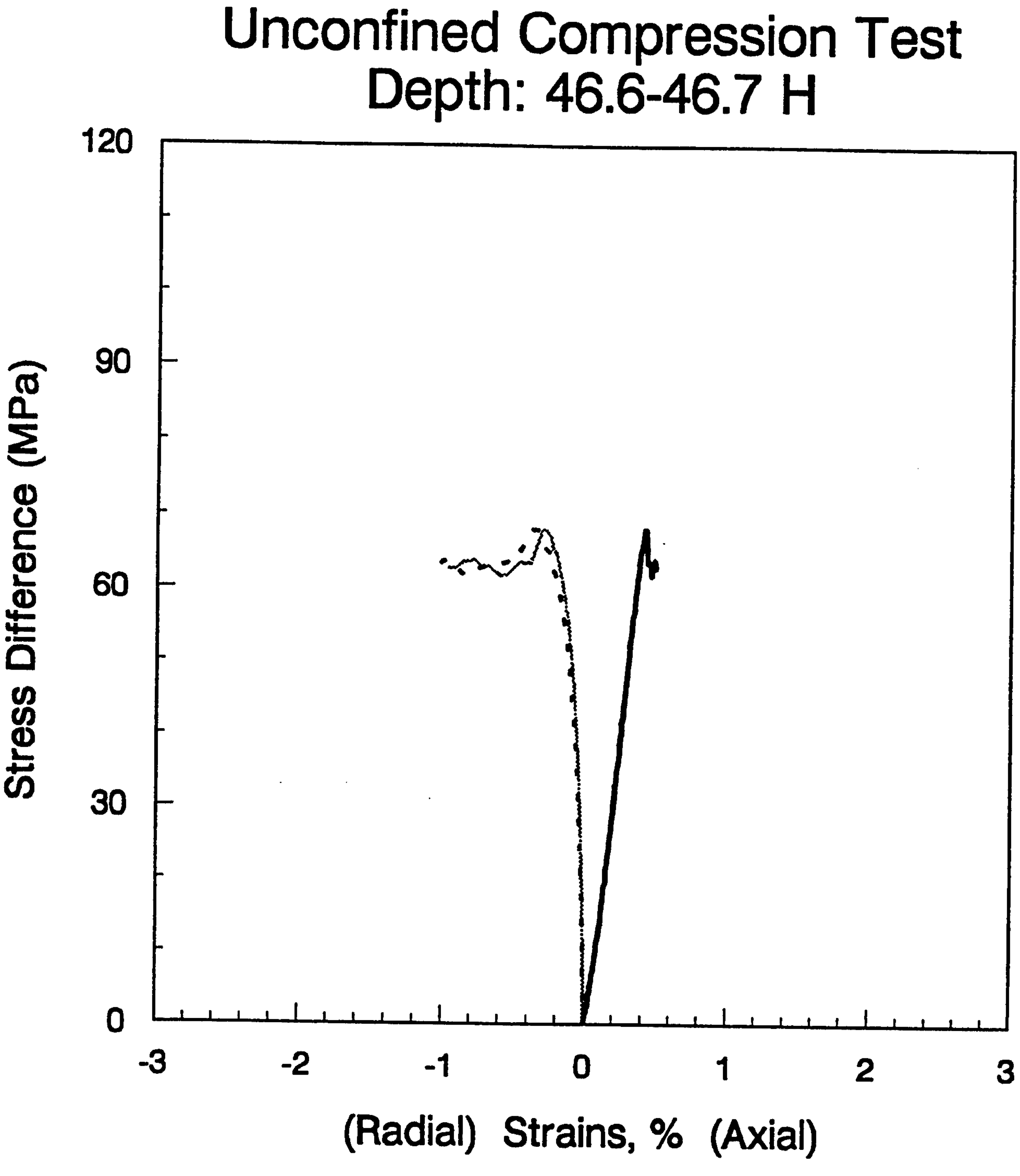

Figure B-5. Stress versus strain under unconfined compression conditions for sample 46.6 - 46.7 ft. (H).

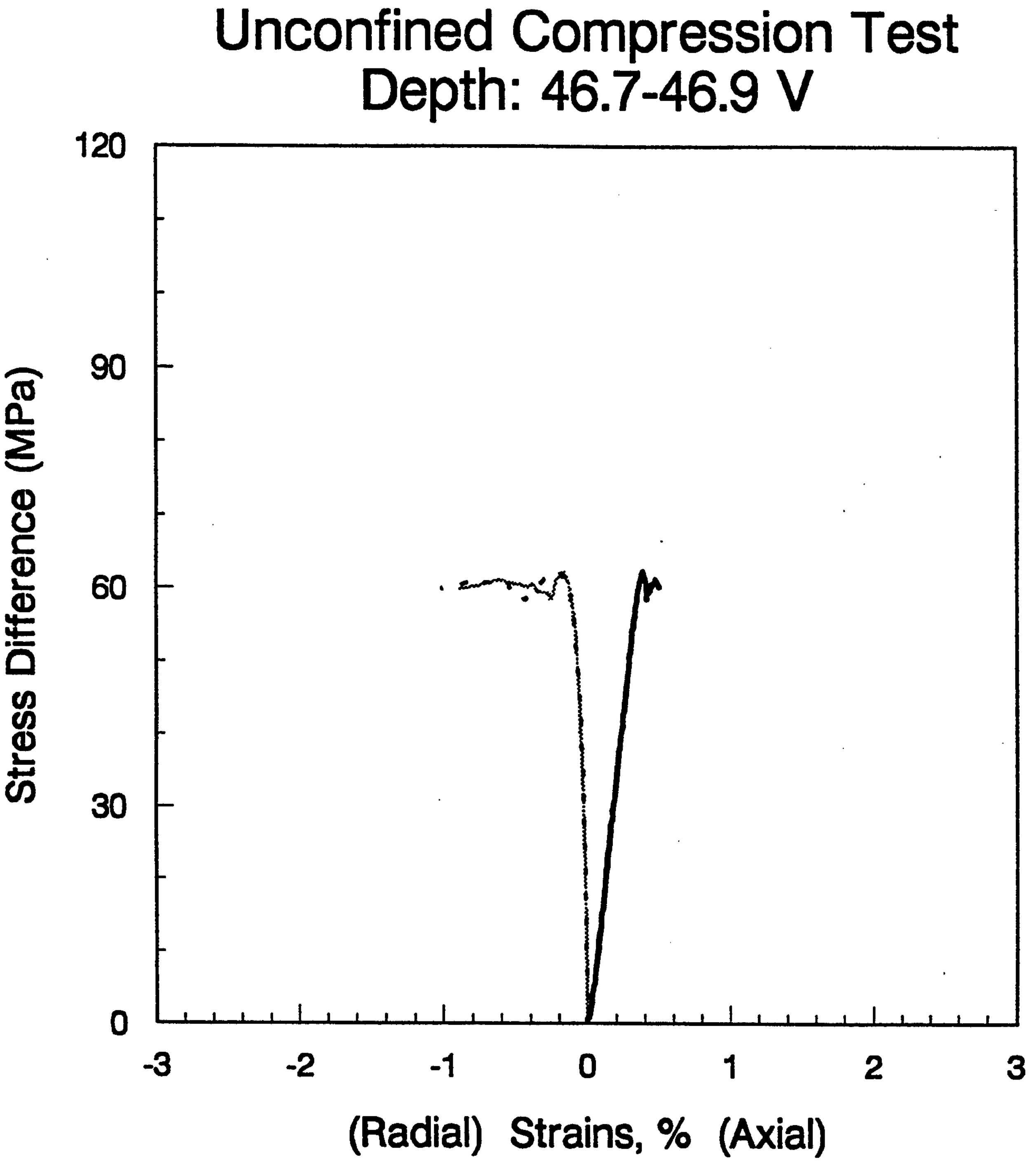

Figure B-6. Stress versus strain under unconfined compression conditions for sample 46.7 - 46.9 ft. (V).

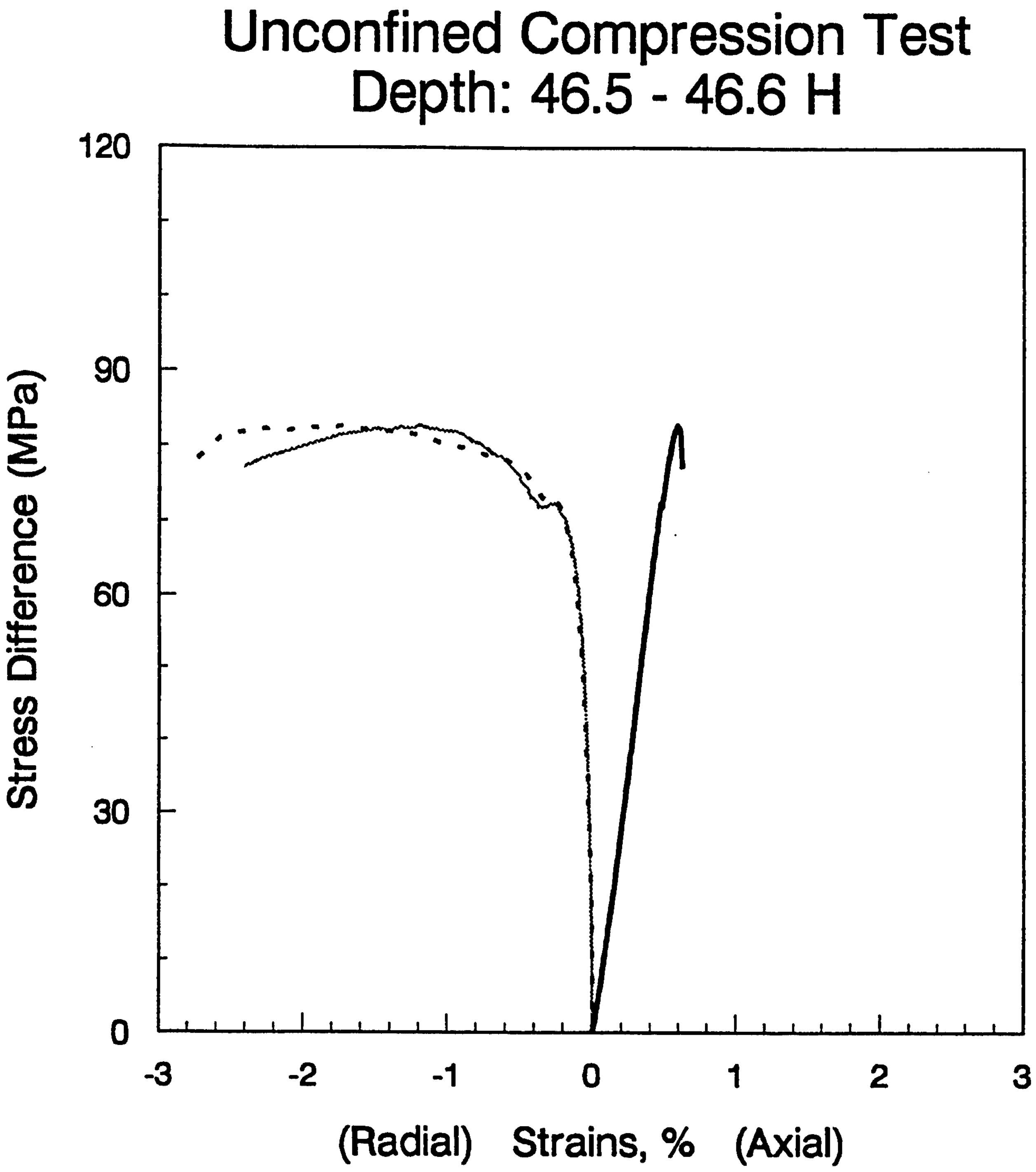

Figure B-7. Stress versus strain under unconfined compression conditions for sample 46.5 - 46.6 ft. (H).

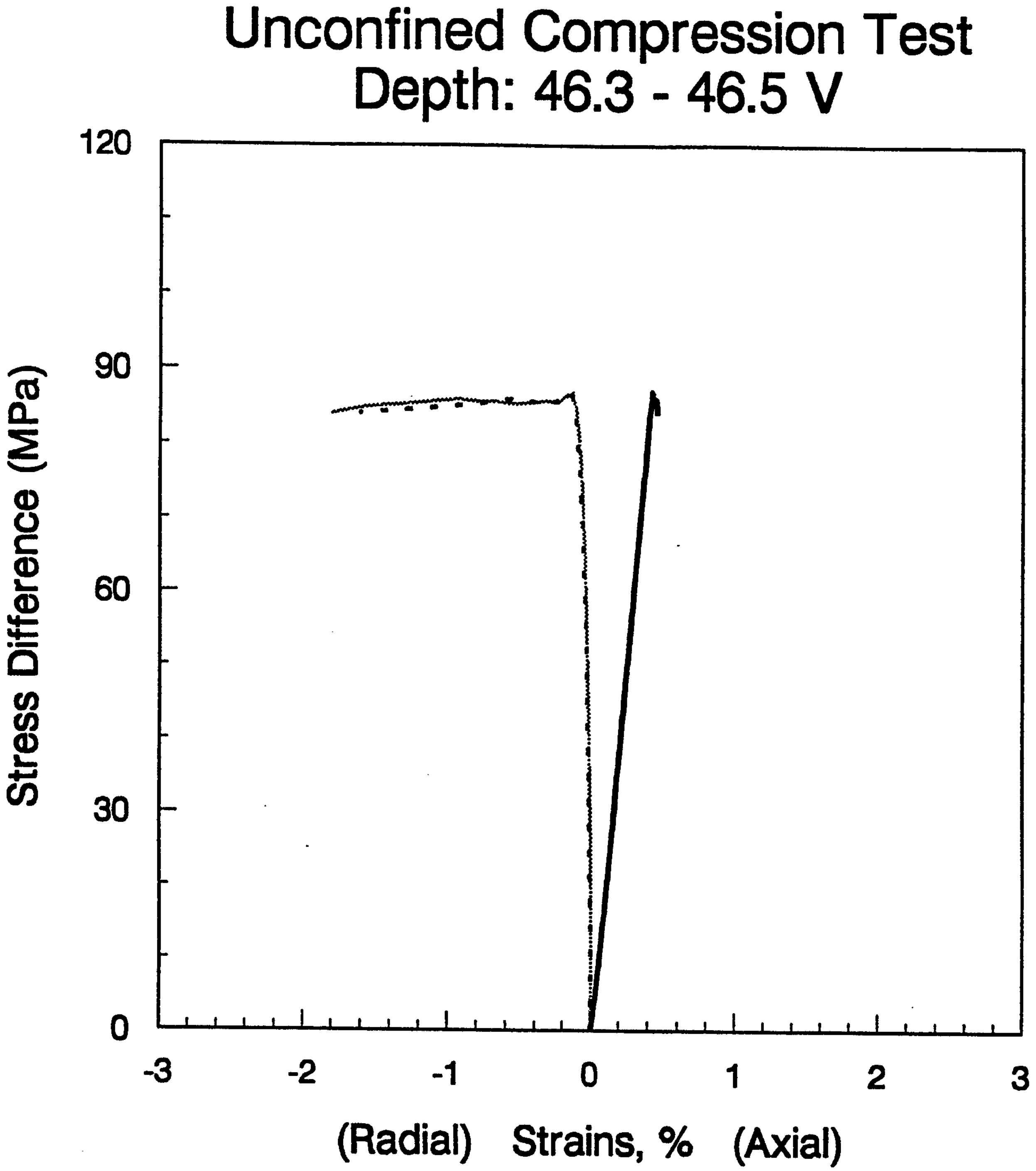

Figure B-8. Stress versus strain under unconfined compression conditions for sample 46.3 - 46.5 ft. (V).

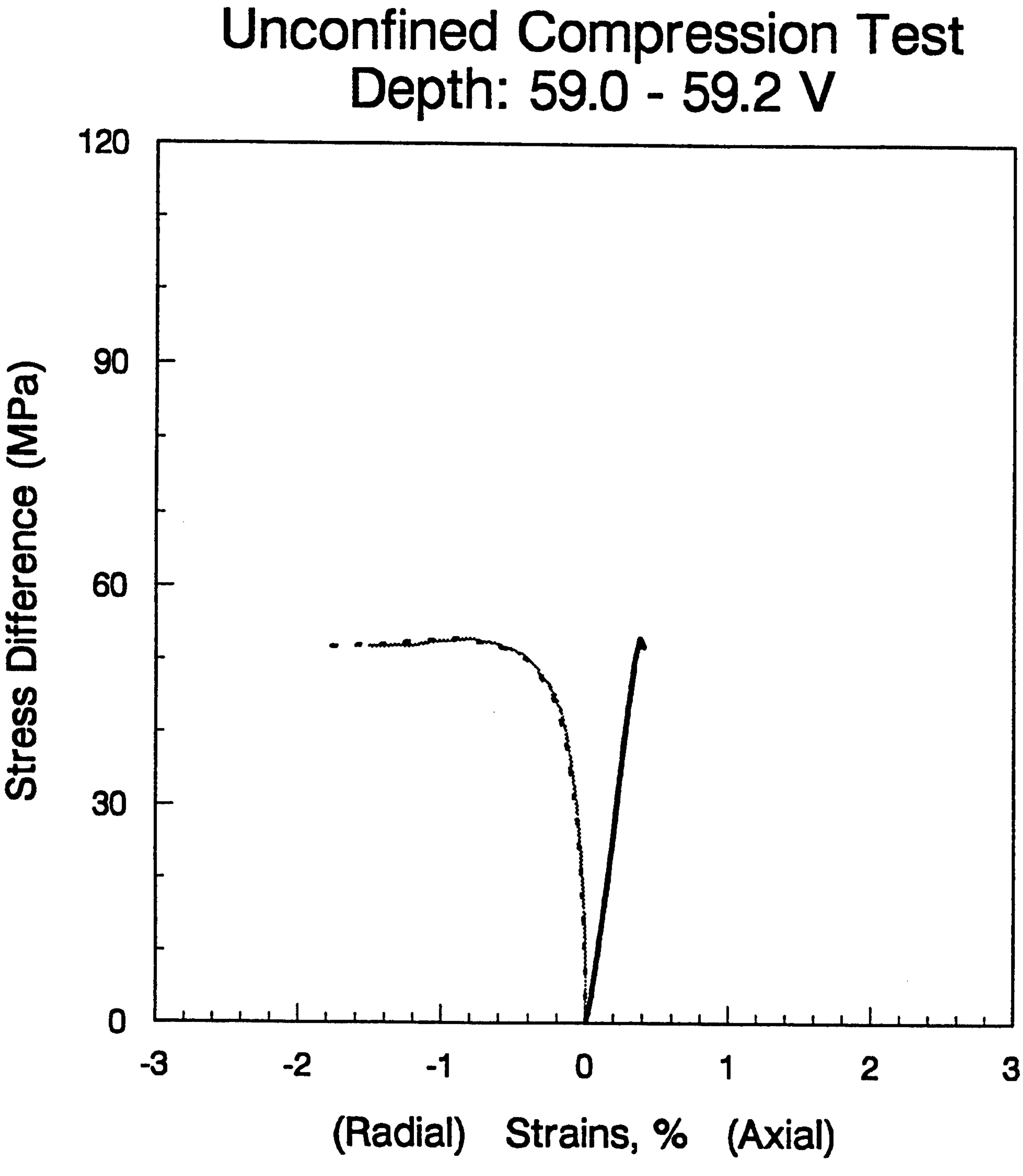

Figure B-9. Stress versus strain under unconfined compression conditions for sample 59.0 - 59.2 ft. (V).

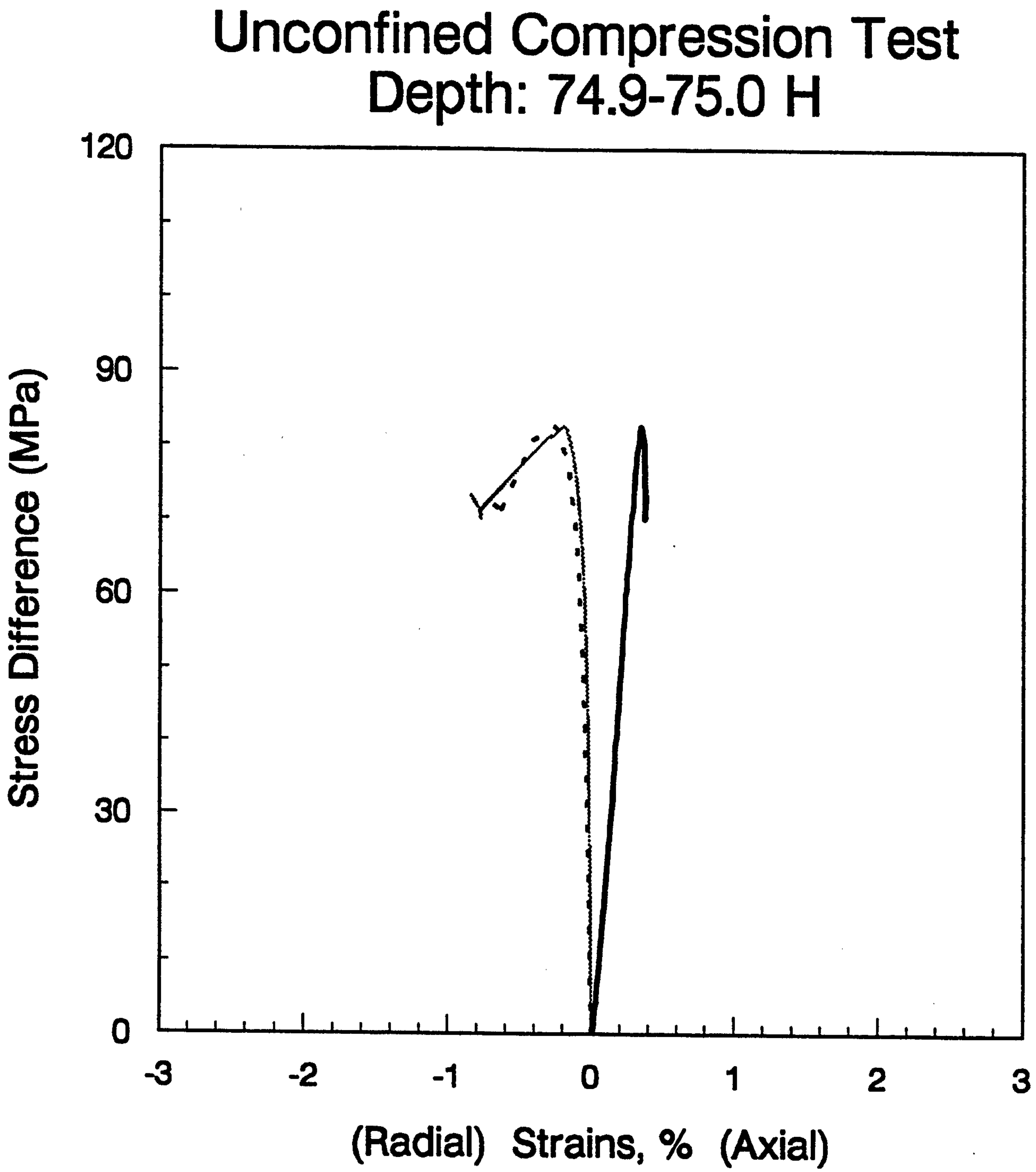

Figure B-10. Stress versus strain under unconfined compression conditions for sample 74.9 - 75.0 ft. (H).

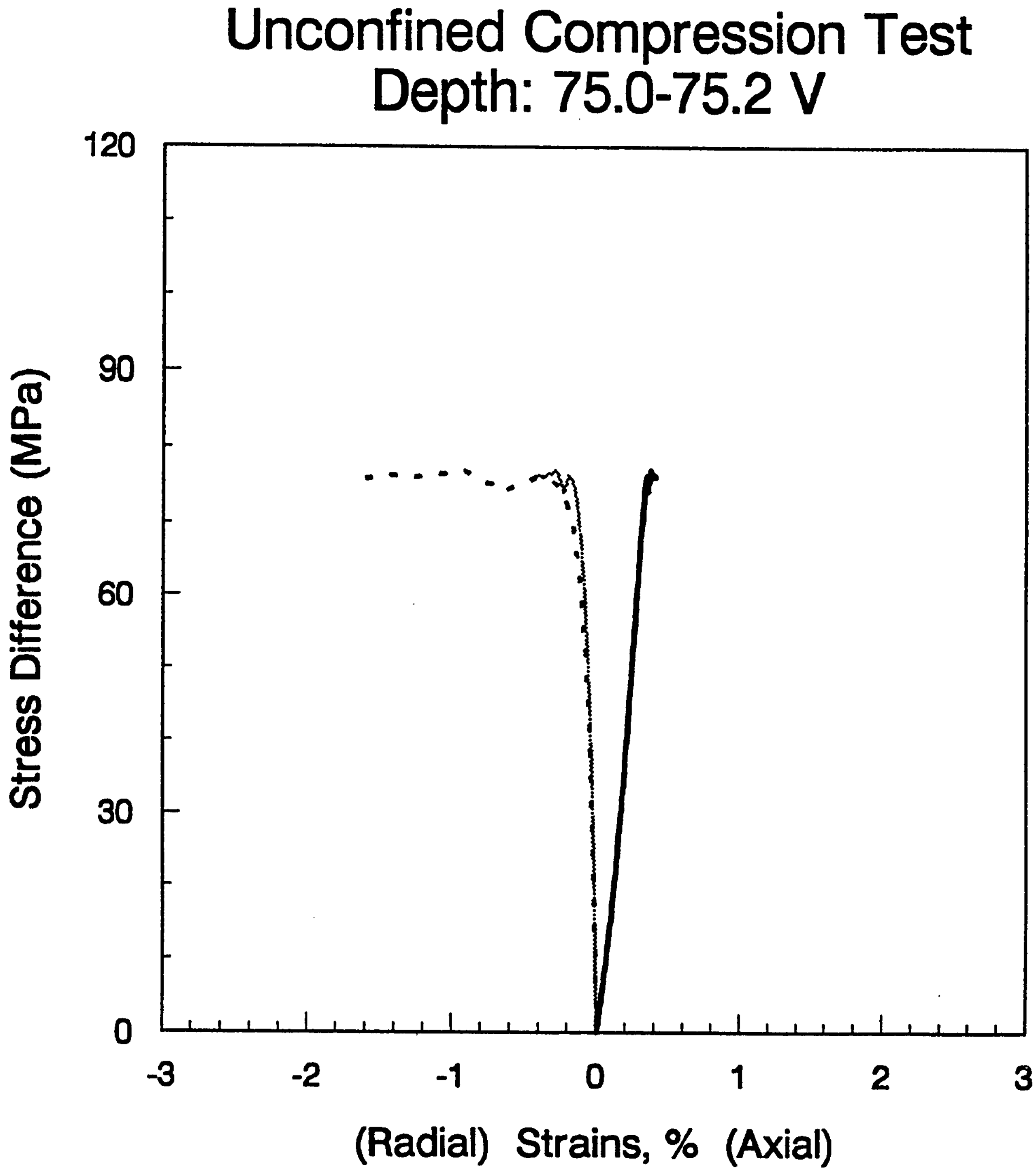

Figure B-11. Stress versus strain under unconfined compression conditions for sample 75.0 - 75.2 ft. (V).

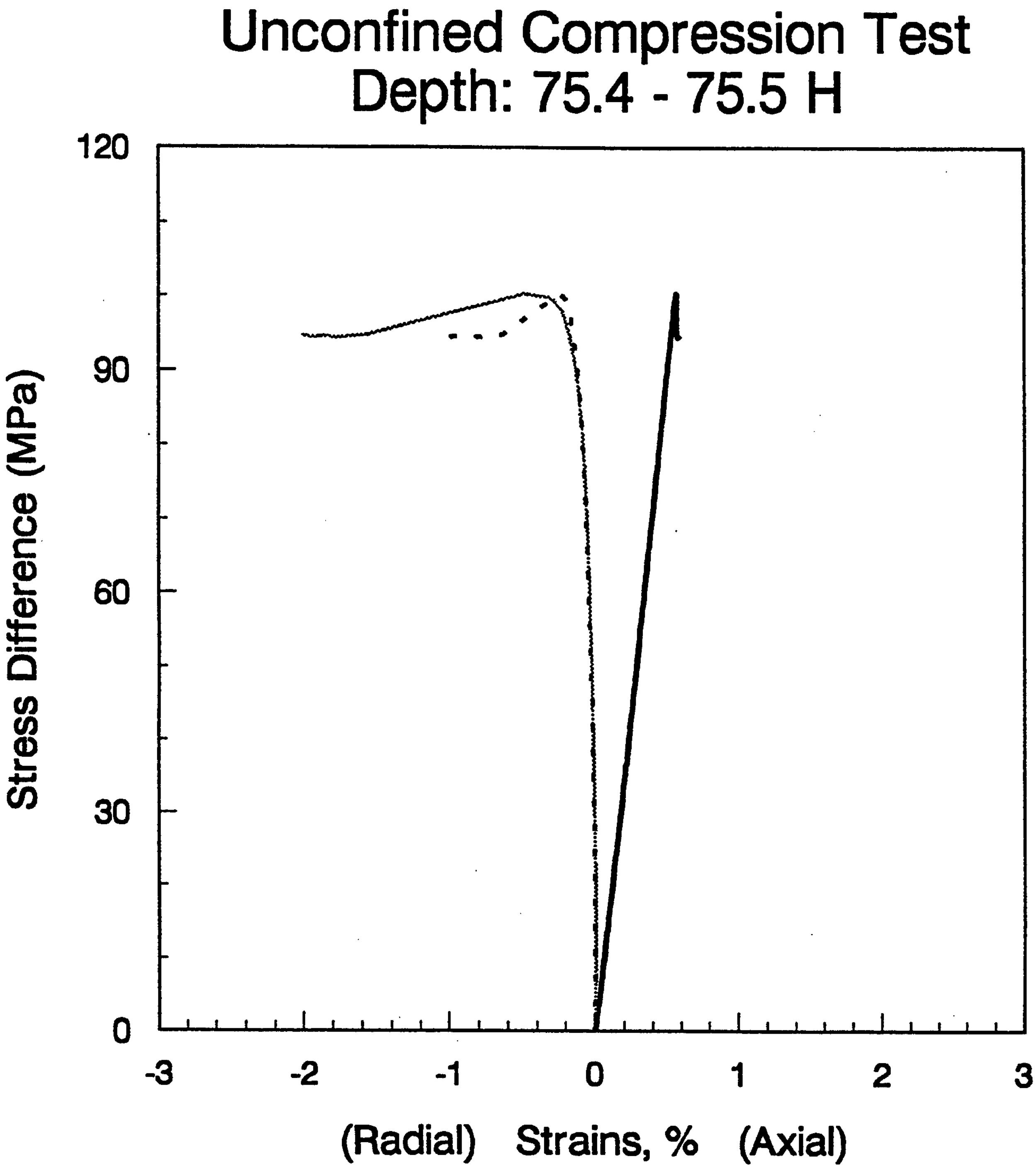

Figure B-12. Stress versus strain under unconfined compression conditions for sample 75.4 - 75.5 ft. (H).

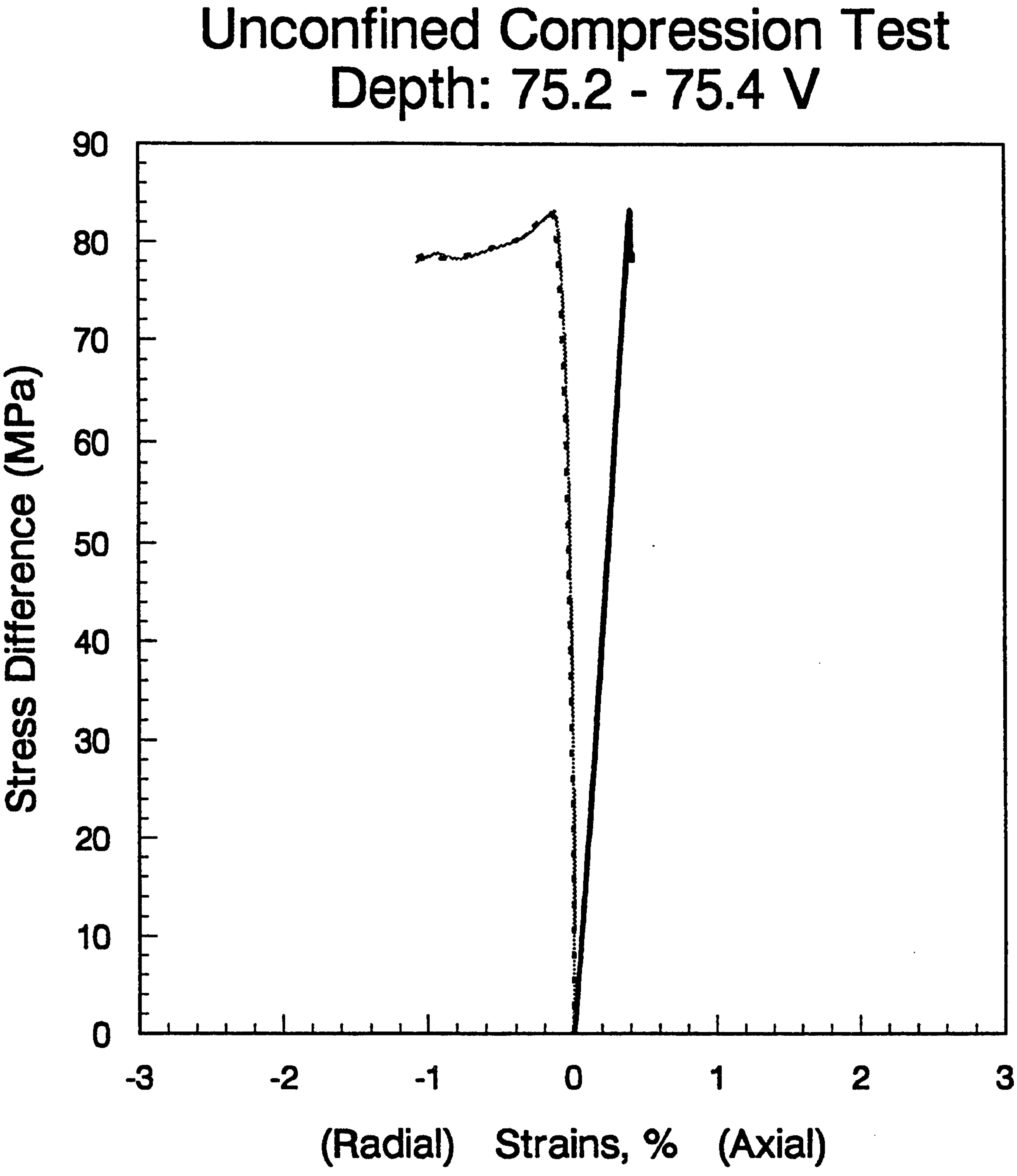

Figure B-13. Stress versus strain under unconfined compression conditions for sample 75.2 - 75.4 ft. (V).

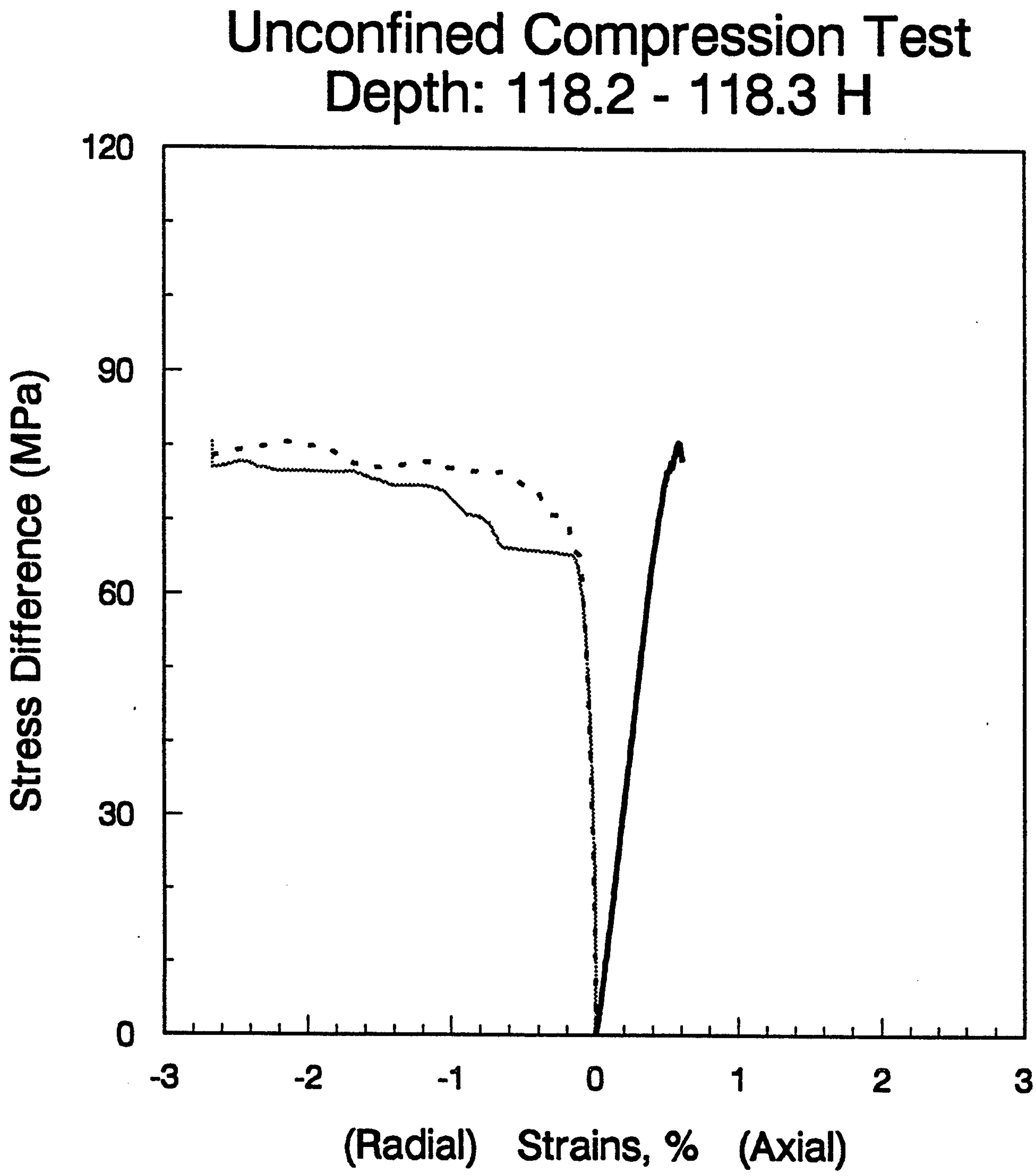

Figure B-14. Stress versus strain under unconfined compression conditions for sample 118.2 - 118.3 ft. (H).

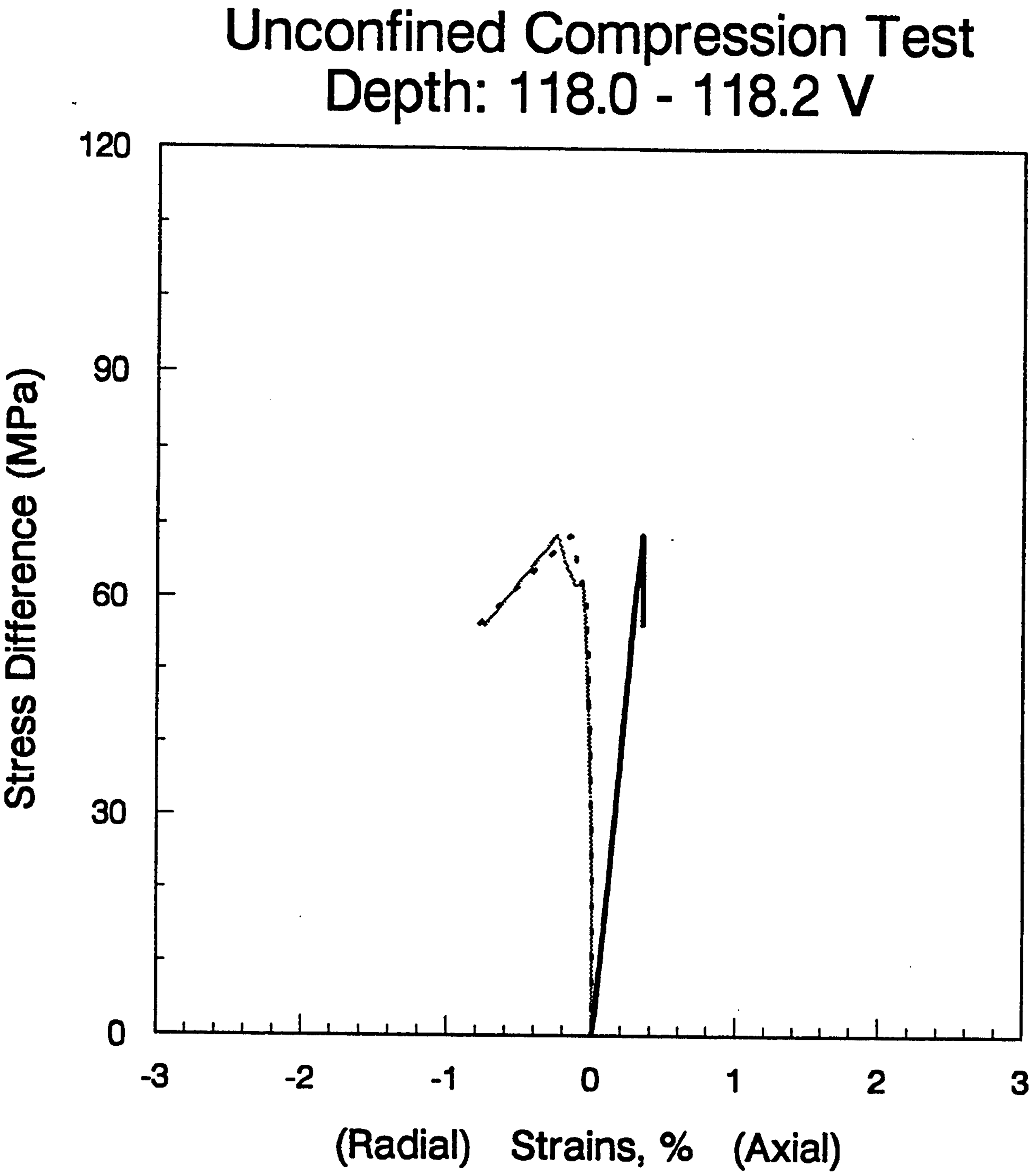

Figure B-15. Stress versus strain under unconfined compression conditions for sample 118.0 - 118.2 ft. (V).

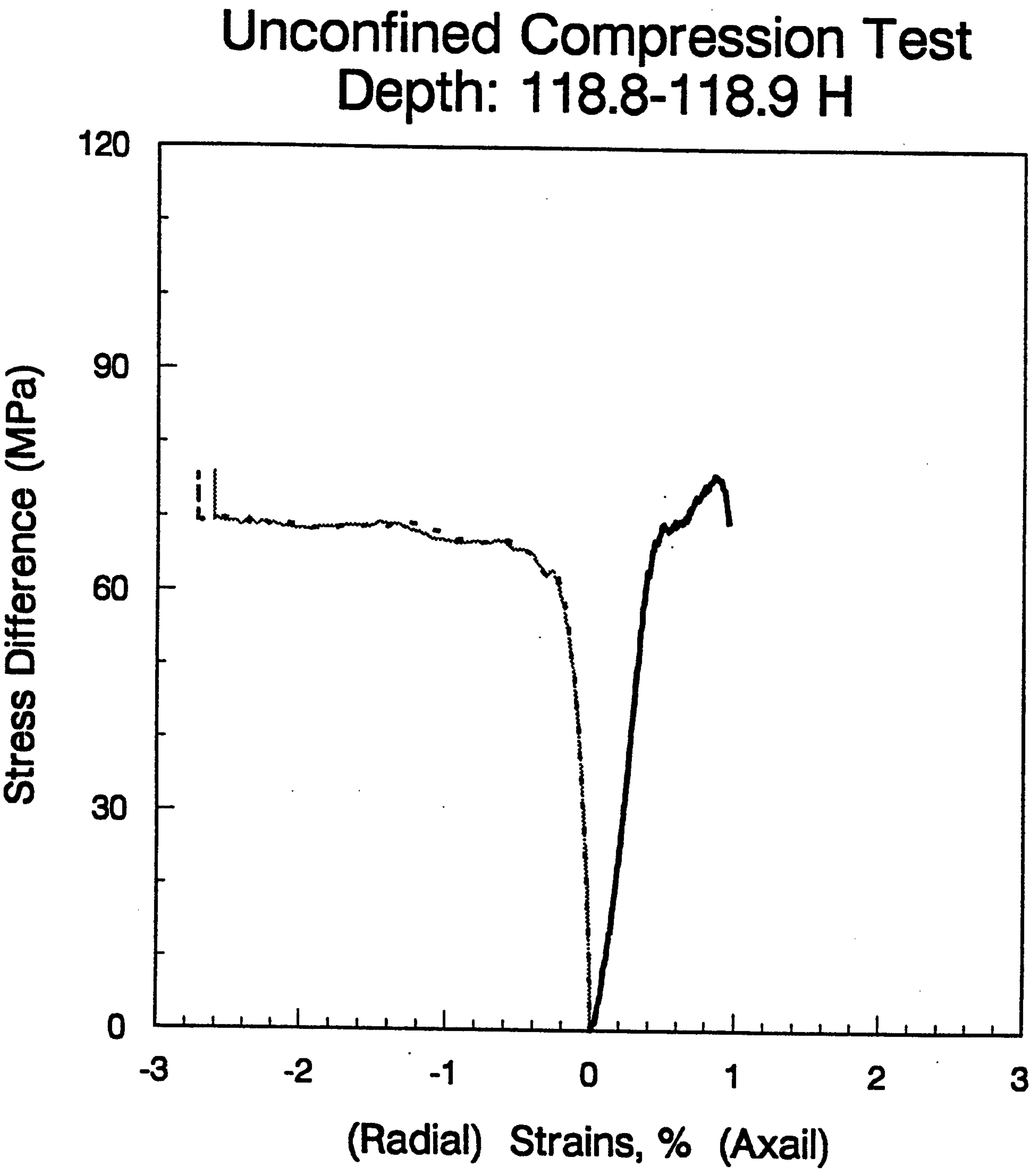

Figure B-16. Stress versus strain under unconfined compression conditions for sample 118.8 - 118.9 ft. (H).

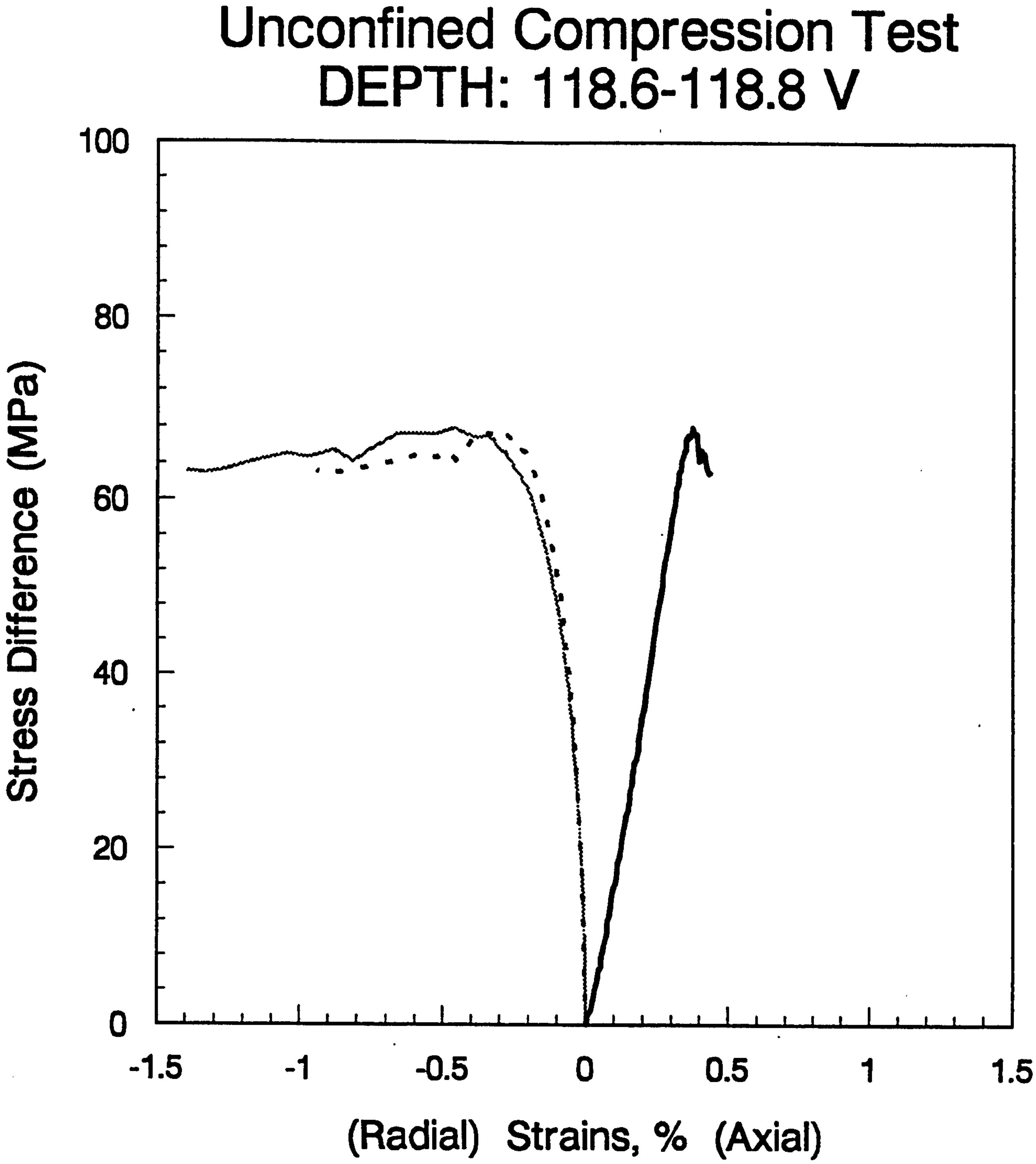

Figure B-17. Stress versus strain under unconfined compression conditions for sample 118.6 - 118.8 ft. (V).

APPENDIX C
CHARACTERIZATION OF GROUT FROM SHI-1 AND SHI-2

C.1 INTRODUCTION.

Laboratory tests were conducted on grout designated as SHI Mix #1 and SHI Mix #2. Two nominally 5 cm diameter by 30 cm long tubes were supplied by DNA for each grout mixture. The material was characterized by physical property measurements, ultrasonic velocity measurements, unconfined compression tests, and uniaxial strain tests. The majority of the characterization tests were performed on SHI Mix #2 as instructed by DNA personnel (A. Martinez, personal communication). Testing was performed on plug samples (25 mm by 50 mm) oriented both parallel and perpendicular to the core axis to determine any anisotropy in the mixture. A summary of the laboratory tests successfully completed on the grout is presented in Table C-1.

Table C-1. Summary of laboratory testing conducted on SHI #1 and SHI #2 grout.

Grout	Test Sample ID	Physical Properties	Ultrasonic Velocities	Unconfined Compression	Uniaxial Strain
SHI Mix #1 11-15-93	SHI-1-C ‖	–	✓	–	✓
	SHI-1-C ⊥	–	✓	–	–
SHI Mix #2 11-16-93	SHI-2-A ‖	✓	✓	✓	–
	SHI-2-A ⊥	✓	✓	✓	–
	SHI-2-B ‖	–	✓	✓	–
	SHI-2-B ⊥	–	✓	✓	–
	SHI-2-C ‖	–	✓	–	–
	SHI-2-C ⊥	–	✓	–	–
	SHI-2-D ‖	✓	✓	✓	–
	SHI-2-D ⊥	✓	✓	✓	–
	SHI-2-E ‖	–	✓	–	–
	SHI-2-E ⊥	–	✓	–	–
	SHI-2-F ‖	–	✓	–	✓
	SHI-2-F ⊥-	–	✓	–	✓

‖ - sample oriented parallel to the grout tube axis. ⊥ - sample oriented normal to the grout tube axis.

C.2 MATERIAL RECEIPT AND INSPECTION.

Four PVC tubes containing two grout mixtures were received at TerraTek on December 22, 1993. The two mixtures were designated as SHI Mix #1 (dated 11-15-93) and SHI Mix #2 (dated 11-16-93). The grout was sealed in the PVC tubes with wax and tape at the tube ends. Preservation upon receipt at TerraTek was considered poor for SHI Mix #1 since gaps between the tube and waxed-ends were visible. These flaws were not detected for the SHI Mix #2 grout. Hence, the preservation for SHI Mix #2 was considered good upon receipt. In either case, an additional coat of wax was immediately applied to all four tubes following the initial inspection. The grout tubes were stored in an environmental chamber (96% relative humidity and 60°F) prior to sample preparation.

C.3 PHYSICAL PROPERTY MEASUREMENTS.

Table C-2 summarizes the physical property measurements for the material dried at 60°C and 105°C prior to determining the dry bulk density and grain density. The 60°C drying temperature was used to reduce errors resulting from the loss of bound water occurring in the gypsum based grout. Some bound water may even be removed when using the 60°C drying temperature. Two grain density measurements were made for each physical properties sample. First, the effective grain density was determined for each plug sample (non-destructive technique). With plug specimens, the interconnected pores are flooded with gas and an effective grain density is determined (Boyle's Law gas pycnometry). The effective grain density and dry density are used to compute the effective porosity. Following the effective property measurements, ultrasonic velocities and compressive strength were determined for the dried samples. A second grain density measurement, known as the "true" grain density, was then determined for these samples following the mechanical tests using gas pycnometry (destructive technique used on pulverized samples). Using the true grain density and dry bulk density, the total or "matrix" porosity was calculated. The difference between the total and effective porosities is the amount of occluded voids (isolated pore space). Detailed physical property procedures are provided in Annex 3. As indicated in Table C-2, consistent values for as-received bulk density were measured ranging from 2.599 to 2.624 gm/cm^3. As expected, dry density values determined following 60°C drying are slightly higher than values determined from 105°C, with average values of 2.267 gm/cm^3 and 2.248 gm/cm^3, respectively.

Grain density shows little sensitivity to drying temperature between 60°C and 105°C. Effective and total grain densities average 3.283 gm/cm^3 and 3.364 gm/cm^3, for 60°C, and 3.282 gm/cm^3 and 3.365 gm/cm^3 for 105°C, respectively. The high grain density values reflect the fairly high concentration of ilmenite sand in these samples. (Ilmenite is an iron-titanium oxide mineral and has a density between 5.5 and 6 gm/cm^3.) Effective porosity ranged from 30.9 to 31.6%, and total porosity ranged from 32.5 to 33.5%.

Table C-2. Summary of Grout Physical Properties.

Sample ID	Density				Porosity	
	As-Received Bulk (gm/cc)	Dry Bulk (gm/cc)	Effective Grain (gm/cc)	True Grain (gm/cc)	Effective (%)	Total (%)
SH1-2-D ∥ Dried at 60°C	2.605	2.270	3.283	3.363	30.9	32.5
SH1-2-D ⊥ Dried at 60°C	2.599	2.264	3.282	3.364	31.0	32.7
SHI-2-A ∥ Dried at 105°C	2.624	2.256	3.288	3.365	31.4	33.0
SHI-2-A ⊥ Dried at 105°C	2.611	2.240	3.276	3.366	31.6	33.5

C.4 ULTRASONIC VELOCITY MEASUREMENTS.

Ultrasonic velocity measurements were performed at bench conditions on each of the plug specimens prior to static mechanical tests (tests conducted at ambient temperature and with a nominal axial stress of 1 MPa). Tests were performed on as-received specimens (preserved moisture content) and dried samples (samples dried at 60°C and 105°C). To measure the ultrasonic velocities (compressional (P) and shear (S) waves), two piezoelectric (1 MHz) crystals were placed in mechanical contact with the sample, one at each end. A high voltage pulse of short duration was then applied to one of the crystals, using a pulse generator. This pulse was received by the crystal at the opposite end of the specimen. Based on the time required for the pulse to travel through the length of the specimen, the P-wave and S-wave velocities were calculated. Detailed procedures are provided in Annex 3.

The ultrasonic velocities for the grout samples are presented in Table C-3. The dynamic Poisson's ratio and dynamic moduli (see Annex 3) are also included in Table C-3. The P-wave velocities for the preserved samples are consistent ranging from 2.86 to 3.18 km/sec, and averaging 3.10 km/sec (±0.12 km/sec). Slower velocities were measured for the SHI-1 grout. This may be attributed to the initial preserved condition (poorly preserved) of SHI-1, or the different pour date relative to SHI-2. The S-waves were similarly consistent ranging from 1.64 to 1.85 km/sec, with an average of 1.78 km/sec (±0.07 km/sec). The P-wave and S-wave velocities determined for the samples dried at 60°C were similar to the as-received samples; whereas, the velocities measured on the samples dried at 105°C were lower.

Dynamic Poisson's ratio and Young's modulus for the as-received samples ranged from 0.24 to 0.27 and 17.7 GPa to 22.4 GPa, respectively. Poisson's ratio and Young's modulus were more variable for the dried samples with values ranging from 0.14 to 0.20 and 12.6 GPa to 20.4 GPa, respectively.

C.5 STATIC MECHANICAL TEST RESULTS.

Both the SHI-1 and SHI-2 grout were subjected to uniaxial strain tests to determine stress-strain characteristics up to 400 MPa confining pressure. The uniaxial strain tests were performed using an axial strain rate of $5\times10^{-5}\text{sec}^{-1}$ to the 400 MPa lateral confining pressure boundary. Test procedures and definitions are provided in Annex 3. Both parallel and perpendicular specimens were tested under uniaxial strain conditions for grout SHI-2. Only a parallel grout specimen from SHI-1 was successfully tested (a jacket failure occurred for the perpendicular oriented sample during the uniaxial strain test). All uniaxial strain tests were conducted on preserved specimens (as-received moisture content). In addition to the uniaxial strain tests, the grout was further characterized by unconfined compression testing. The unconfined compression tests were performed on parallel and perpendicular oriented samples from SHI-2. No unconfined compression tests were performed on the SHI-1 material (per instruction from DNA, A. Martinez, personal communication). The unconfined tests were conducted on preserved (as-received moisture) and dried samples (samples dried at 60°C and 105°C) using an axial strain rate of 1×10^{-5} sec^{-1}. All of the mechanical tests were conducted on nominally 25 mm diameter by 38 to 50 mm long cylindrical samples (the shorter samples were the result of the core-size restriction and perpendicular orientation). Summary of the mechanical properties determined from the uniaxial strain tests are shown in Tables C-4 and C-5. Summary plots of the uniaxial strain tests are shown in Figures C-1 and C-2. The mechanical properties determined from the unconfined compression tests is provided in Table C-6. Individual graphical presentation of the tests are included in Annex 4 and Annex 5.

Table C-3. Dynamic Mechanical Properties determined from Ultrasonic Velocities.

Sample ID	Pre-Test Condition	Pre-Test Bulk Density (gm/cc)	P-Wave Velocity (km/sec)	S-Wave Velocity (km/sec)	Poisson's Ratio	Moduli		
						Young's (GPa)	Bulk (GPa)	Shear (GPa)
SHI-2-B ‖	As-Received	2.630	3.18	1.78	0.27	21.2	15.4	8.3
SHI-2-B ⊥	As-Received	2.619	3.17	1.83	0.25	21.9	14.6	8.8
SHI-2-C ‖	As-Received	2.608	3.13	1.79	0.26	21.0	14.6	8.3
SHI-2-C ⊥	As-Received	2.527	3.11	1.80	0.25	20.4	13.6	8.2
SHI-2-E ‖	As-Received	2.601	3.18	1.83	0.25	21.8	14.5	8.7
SHI-2-E ⊥	As-Received	2.564	3.14	1.78	0.26	20.5	14.2	8.1
SHI-2-F ‖	As-Received	2.628	3.15	1.81	0.26	21.6	15.0	8.6
SHI-2-F ⊥	As-Received	2.630	3.18	1.85	0.24	22.4	14.4	9.0
SHI-1-C ‖	As-Received	2.629	2.86	1.64	0.25	17.7	11.8	7.1
SHI-1-C ⊥	As-Received	2.629	2.90	1.68	0.25	18.5	12.3	7.4
SHI-2-D ‖	Dried 60°C	2.270	3.07	1.99	0.14	20.4	9.5	9.0
SHI-2-D ⊥	Dried 60°C	2.264	2.83	1.74	0.20	16.4	9.1	6.8
SHI-2-A ‖	Dried 105°C	2.256	2.57	1.67	0.14	14.3	6.6	6.3
SHI-2-A ⊥	Dried 105°C	2.240	2.48	1.54	0.19	12.6	6.8	5.3

C.5.1 Material Strain Characteristics.

A summary of the stress-strain curves are shown in Figure C-1. The maximum volumetric strain measured during the uniaxial strain tests was consistent for the SHI-2 material with values of 4.24% and 4.17%. The maximum volumetric strain measured for SHI-1 was considerably higher with a value of 9.22%. The measured permanent compaction (MPC) for the SHI-2 material averaged 1.41%, and the MPC for the SHI-1 grout was 6.35%. The difference in MPC and maximum volumetric strain between the SHI-1 and SHI-2 grout is attributed to the initial saturation. Due to the poor preserved condition of the SHI-1 grout, the saturation decreased (and consequently, the gas-filled porosity increased), resulting in a higher MPC. The initial slope (initial bulk modulus) was 42.8 x 10^2 MPa for both of the SHI-2 grout samples, and was 7.6 x 10^2 MPa for the SHI-1 sample. The low pressure bulk modulus for SHI-1 was 7.1 x 10^2 MPa, and 51.5 and 60.1 x 10^2 MPa for the SHI-2 samples. The loading and unloading bulk moduli vary randomly with values ranging from 110.6 to 117.4 x 10^2 MPa and 163.2 to 168.4 x 10^2 MPa, respectively.

Table C-4. Uniaxial strain mechanical property results for grout from SHI-1 and SHI-2.

Sample ID	Maximum Stress Difference (MPa)	Stress Difference Intercept (10^2 MPa)	Maximum Volumetric Strain (%)	Measured Permanent Compaction (%)	In-Situ Hysteresis (%)
SHI-1-C ‖	31.0	29.5	9.2	6.4	5.7
SHI-2-F ‖	27.9	26.0	4.2	1.4	1.3
SHI-2-F ⊥	28.2	25.9	4.2	1.4	1.3

C.5.2 Material Strength Characteristics.

Figure C-2 shows a summary of the material behavior in stress-stress space (axial stress difference versus confining pressure). The grout exhibit a maximum stress difference between 27.9 and 31.0 MPa during uniaxial strain loading. The consistent strengths correlate reasonably well with the consistent ultrasonic velocities. The grout from SHI-1 had a slightly higher strength (stress difference of 31.0 MPa), which may be attributed to the initial lower saturation.

C.5.3 Material Moduli.

Four other moduli were calculated: the loading and unloading apparent constrained moduli, from the axial stress versus axial strain plot, and the loading and unloading shear moduli, from the stress difference versus strain difference plot (see Annex 3). The loading apparent constrained moduli ranged from 115.3 to 124.4 x 10^2 MPa and the unloading apparent constrained moduli ranged from 194.6 to 227.0 x 10^2 MPa. The loading shear values were between 0.58 and 0.62 x 10^2 MPa and the unloading shear moduli ranged from 90.6 to 116.3 x 10^2 MPa.

Table C-5. Various uniaxial strain moduli for grout from SHI-1 and SHI-2.

Sample ID	Bulk Modulus (10^2 MPa)				Apparent Constrained Modulus (10^2 MPa)		Shear Modulus (10^2 MPa)	
	Initial	Low Pressure	Loading	Unloading	Loading	Unloading	Loading	Unloading
SHI-1-C ∥	7.6	7.1	110.6	164.6	115.3	194.6	0.58	115.1
SHI-2-F ∥	42.8	51.5	117.4	163.2	124.4	227.0	0.62	116.3
SHI-2-F ⊥	42.8	60.1	116.8	168.4	123.4	222.2	0.60	90.6

C.5.4 Unconfined Compression Tests.

The results of the unconfined compression tests are provided in Table C-6. The compressive strength, Poisson's ratio, and static moduli under unconfined conditions are included in Table C-6. Stress-Strain plots of the unconfined compression tests are provided in Annex 5.

As indicated in Table C-6, the strengths for the as-received samples is lower than the dried samples, with values of 21.0 and 24.1 MPa. The compressive strengths determined for the dried samples ranged from 37.8 to 45.2 MPa. The test samples dried at 105°C had slightly lower strengths than corresponding samples dried at 60°C. It may be possible that drying at 105°C damages the samples is some way (e.g., thermal cracking or desiccation fractures). However, since only two samples were tested following drying at 60°C and 105°C, there is not an appropriate statistical basis for trends (i.e., 60°C samples are stronger than samples dried at 105°C). Also, there does not appear to be an appreciable relationship between orientation and strength. The slightly higher strengths determined for most of the perpendicular-oriented samples may be attributed to their shorter lengths (nominally 38 mm - short length due to the whole core size restrictions). Due to endcap effects, a higher strength may be measured for a sample with a length/diameter ratio of less than 2:1 (this is the case for the perpendicular samples).

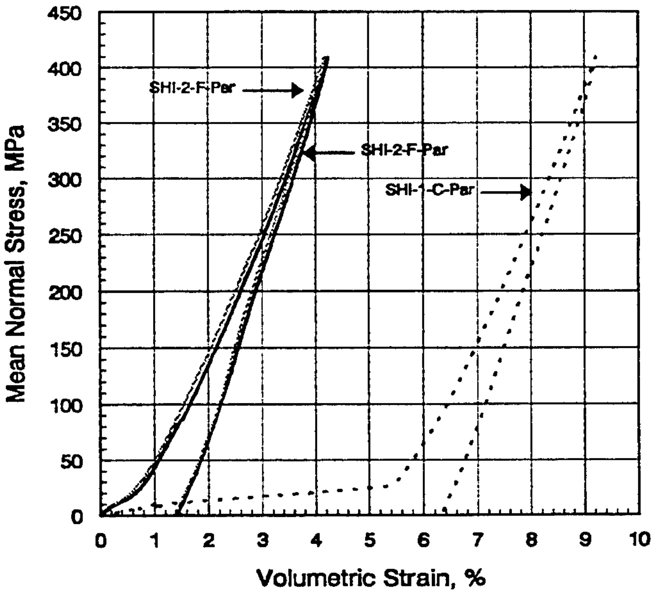

Figure C-1. Summary plot in pressure-volume space for the uniaxial strain tests performed on grout from SHI-1 and SHI-2.

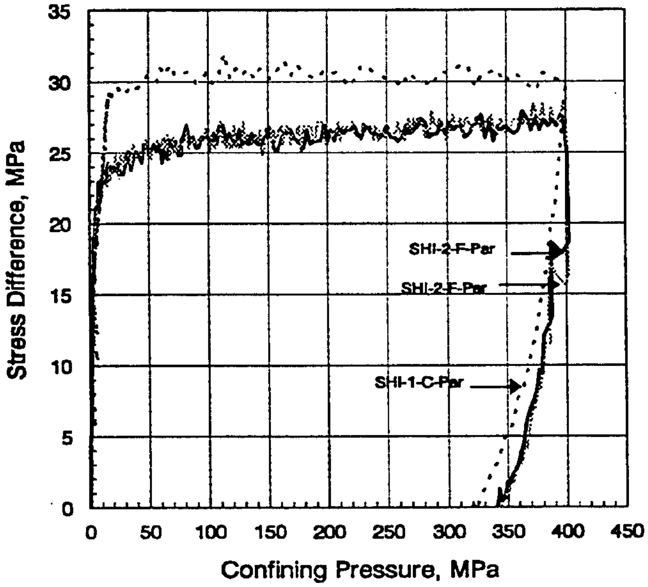

Figure C-2. Summary plot in axial stress difference-confining pressure space for the uniaxial strain tests performed on grout from SHI-1 and SHI-2.

Table C-6. Static Mechanical Properties determined from Unconfined Compression Tests.

Sample ID	Pre-Test Condition	Pre-Test Bulk Density (gm/cc)	Compressive Strength (MPa)	Poisson's Ratio	Moduli		
					Young's (GPa)	Bulk (GPa)	Shear (GPa)
SHI-2-B ∥	As-Received	2.630	21.0	0.17	8.89	4.55	3.79
SHI-2-B ⊥	As-Received	2.619	24.1	0.11	7.46	3.21	3.35
SHI-2-D ∥	Dried at 60°C	2.270	45.2	0.17	9.72	4.95	4.14
SHI-2-D ⊥	Dried at 60°C	2.264	44.4	0.19	11.31	6.06	4.76
SHI-2-A ∥	Dried at 105°C	2.256	37.8	0.18	7.22	3.75	3.07
SHI-2-A ⊥	Dried at 105°C	2.240	42.6	0.14	7.73	3.57	3.40

Annex 3
Experimental Procedures and Definitions

Experimental Procedures

Mechanical test samples are right circular cylinders with a length-to-diameter ratio of approximately 2:1. The sample diameter was as-received, unless there was a specific reason for coring to a smaller size. The specimens were cut with a diamond saw and end ground to 0.025 mm per mm length using water coolant. Care was taken during sample cutting and end grinding to ensure a minimum loss of moisture.

All mechanical tests were conducted using a servo-controlled triaxial testing apparatus to subject samples to desired stress states at controlled strain rates. The samples were isolated from the pressure-vessel confining fluid by an impermeable jacket, which was sealed at the sample ends against steel endcaps. Axial and lateral strains were measured using transducers which measured changes in the external sample dimensions. Stress difference was measured using a load cell within the vessel. Confining pressure was measured using a calibrated pressure transducer. All stress and strain data were recorded during the mechanical testing using a digital data acquisition system and analog X-Y recorders.

Uniaxial Strain Tests

The objective of the uniaxial strain test is to subject a sample to deviatoric loading and unloading while preventing any measurable radial deformation of the material. In order to accomplish this, both stress difference and confining pressure were simultaneously increased from the initial zero stress-state. The stress difference is applied at a strain rate of approximately 10^{-5} in/in/sec. The confining pressure is increased as needed to prevent radial deformation of the sample. After reaching the maximum confining pressure of 400 MPa, the stress difference and confining pressure are decreased simultaneously while maintaining zero radial strains. After reaching zero stress difference (i.e. a hydrostatic state of stress), the confining pressure is further reduced to zero. All uniaxial strain tests were conducted under undrained conditions, with “as-received” samples. Measurements made during the tests include axial and radial strain, stress difference and confining pressure.

Uniaxial Strain Definitions

The maximum volumetric strain is the maximum volumetric strain seen during a uniaxial strain test and generally occurs at the maximum mean normal stress level (about 400 MPa the P-V plot), shown as point D in Figure C-3.

The measured permanent compaction (MPC) is defined as the "permanent" volumetric strain that occurs after a load-unload cycle of a uniaxial strain test to a maximum lateral stress of 400 MPa. Point F corresponds to the MPC in Figure C-3.

The in-situ hysteresis is defined as the net volumetric strain between loading from, and unloading to, a mean stress level of 800 psi while following the uniaxial strain path.

Material Moduli Definitions

The stiffness of a material is defined by the bulk modulus in the region of interest. Because of the variation in stress-strain response of tuff, several different moduli were defined and calculated.

The initial bulk modulus is defined as the slope of the line on the P-V curve from point A to point B in Figure C-3.

The low pressure bulk modulus is the slope of the line which extends from the origin to a point on the loading portion of the curve, which is vertically above the measured permanent compaction, shown as line A-C in Figure C-3. Point F is the measured permanent compaction.

The loading bulk modulus is the slope of the line from the point on the loading portion of the curve, which is vertically above the measured permanent compaction point (point C), to the maximum mean normal stress. This corresponds to line C-D on Figure C-3.

The unloading bulk modulus is defined as the slope of the line from the maximum mean normal stress point, to the point at which the hydrostatic unloading begins, shown as line D-E on Figure C-3.

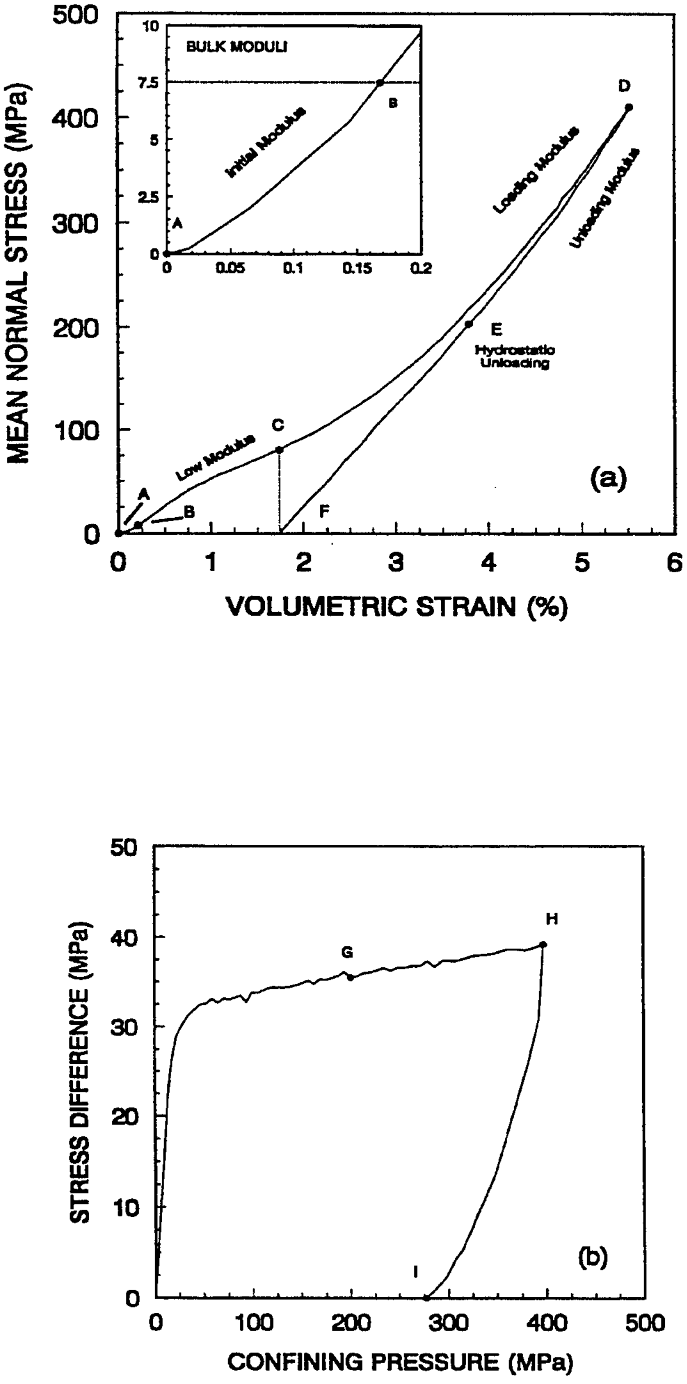

Figure C-3. Material properties and bulk moduli definitions.

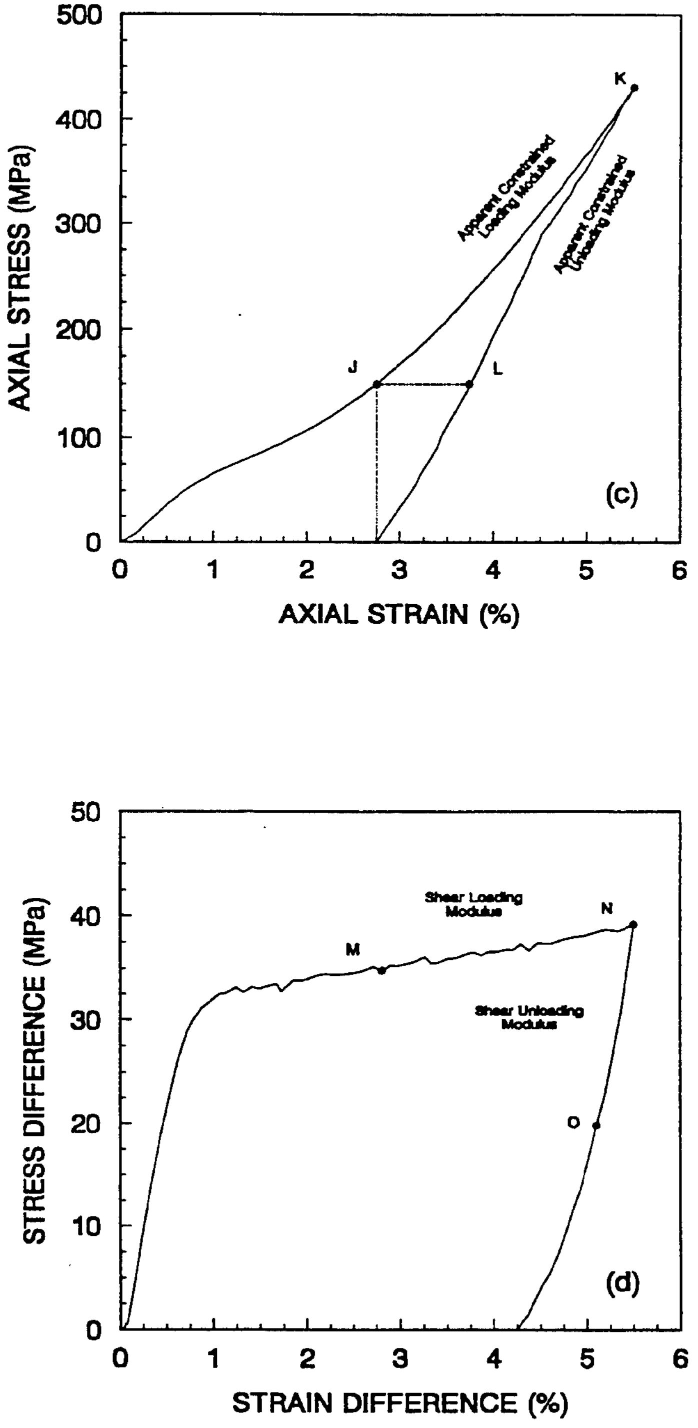

Figure C-4. Apparent constrained and shear moduli definitions.

The loading apparent constrained modulus is defined as the slope of the line from point J to point K in axial stress versus axial strain space, Figure C-4. J is a point on the loading curve which lies directly above where the axial stress equals zero on the unloading curve. K is the maximum axial stress.

The unloading apparent constrained modulus is defined as the slope of the line from the maximum axial stress, point K, to point L on the unloading curve.

The loading shear modulus is defined as the slope of the line from approximately 50% of the loading curve, in stress difference space, to the maximum stress difference, shown as line M-N in Figure C-4.

The unloading shear modulus is defined as the slope of the line from the maximum stress difference to approximately 50% of the unloading curve, shown as line N-O in Figure C-4.

Material Strength Definitions

The maximum stress difference is the maximum stress difference seen during an uniaxial strain test, and occurs at the peak lateral stress (400 MPa) for each test. It is denoted as point H in Figure C-3. The parameter is commonly referenced as the "strength" of the material.

The stress difference intercept was obtained by extrapolating a representative straight line to the ordinate through the stress difference versus confining pressure curve ranging from 200 to 400 MPa, where inelastic response dominates. Figure C-3 presents point G and H as the limits for straight line representation. The intercept on the ordinate is called the stress difference intercept.

Physical Property Measurement Procedures

Physical properties consisted of as-received weight in air, dry weight and effective and true grain volume for each test sample. Each set of physical property measurements was performed on a sample weighing between 50 and 70 gm cut immediately adjacent to the mechanical test sample. In many instances, physical properties were measured directly on the mechanical test samples. From these direct measurements, calculations were made to determine the as-received density, dry density, the effective porosity, and the total porosity (matrix porosity).

The bulk volume of regularly shaped specimens (usually right-circular cylinders) may be calculated from micrometer or caliper measurements. For cylindrical samples, an average of six diameter and four length readings, each accurate to 0.025 mm, are used for calculation of bulk volume. To measure the mass of the sample, a digital balance with a resolution of 0.001 gm was used.

Grain density was measured on test plugs and powders using the gas pycnometry technique. After the dry density measurement, the test plugs were inserted into a porosimeter, and the effective grain volume determined using Boyle's Law. Gas pycnometry is based on Boyle's Law, which holds that, at constant temperature, the volume of an ideal gas will vary inversely with the pressure:

$$\frac{P_1}{P_2} = \frac{V_2}{V_1} \tag{C.1}$$

where P_1 is the initial pressure in V_1, P_2 is the final pressure in V_2, V_1 is the initial volume and V_2 is the final volume.

The pressure in a reference vessel of known volume, V_1, is communicated with a vessel containing the sample. The porosimeter vessel is calibrated using a series of steel billets of known volume. V_1 is constant. By using different billets, V_2 increases by a known increment at each step of the calibration. As V_2 increases, the ratio P_1/P_2 also increases. From pressure-volume relationships with various billets of different, known volumes, linear regression is used to generate a relevant proportionality factor. This is used in subsequent calculations of grain volume:

$$V_g = \alpha\left(\frac{P_1}{P_2}\right) + b \tag{C.2}$$

where V_g is the grain volume, (α is a proportionality factor between grain volume and pressure ratio, and b is a constant (representing a zero offset due to "dead volume" in the porosimeter).

The grain density is calculated as follows:

$$\rho_g = \frac{W}{V_g} \tag{C.3}$$

where ρ_g is the grain density (gm/cm^3), W is the pre-test weight (gm), and V_g is the grain volume determined from the porosimeter (cm^3).

Gas pycnometry can be used to measure grain density on powdered (destructive) or plug (non-destructive) specimens, assuming all porosity is connected. With plug specimens, the interconnected pores are flooded with gas and an effective grain density is determined. The measurement is generally performed on an oven dried sample using a low to no sorptive gas (normally helium).

The dry density and the effective and true grain densities were used to calculate the effective porosity and total (matrix) porosity using the relation:

$$\text{Porosity} = 1 - \left(\frac{\rho_d}{\rho_g} \right) \tag{C.4}$$

where ρ_d is the dry density and ρ_g is either the effective or true grain density.

Utrasonic Velocity Measurements Procedures

Ultrasonic velocities were measured using the "Through-Transmission System" shown in block diagram form below. This is an adaptation of the technique introduced by Mattaboni and Schreiber[1] which is capable of measuring small elapsed times to a high degree of accuracy. Time measurements were obtained from the frequency synthesizer data (stability ± parts in 10^7/month, accuracy ± 0.001 percent).

The signal passing through the specimen was viewed on an oscilloscope and compared with the signal from the variable-frequency synthesizer (comparison wave). The latter was modified by

---

[1] Mattaboni, P., and Schreiber, E., "Methods of Pulse Transmission for Determining Sound Velocities," Journal of Geophysical Research, Vol 70, No. 20, pp. 5160-5163, 1967.

a pulse shaper to exactly match the wave which was passed through the specimen. Next, the pulse which excited the transmitting transducer was viewed, and its shape matched to that of the comparison wave. Once the pulse shapes were matched, they were made to coincide on the, oscilloscope to a high degree of precision. The transit time of the ultrasonic wave was obtained by dividing the length of the specimen by the transit time through the specimen. From the measured ultrasonic velocities and bulk density, the dynamic elastic properties of the samples were calculated. The formulae for calculating the dynamic properties from ultrasonic velocities are as follows[2]:

$$\nu_D = \frac{1}{2}\left(\frac{\left(\frac{V_p}{V_s}\right)^2 - 2}{\left(\frac{V_p}{V_s}\right)^2 - 1}\right) \tag{C.5}$$

$$E_D = V_s^2 \rho \left(\frac{3\left(\frac{V_p}{V_s}\right)^2 - 4}{\left(\frac{V_p}{V_s}\right)^2 - 1}\right) \tag{C.6}$$

$$K_D = \rho\left(V_p^2 - \frac{4}{3}V_s^2\right) \tag{C.7}$$

$$G_D = V_s^2 \rho \tag{C.8}$$

where V_p, V_s, E_D, ν_D, K_D, and G_D are the longitudinal wave velocity, shear wave velocity, dynamic Young's modulus, dynamic Poisson's ratio, dynamic Bulk modulus, and dynamic shear modulus, respectively.

---

[2] Jaeger, J.C., and Cook, N.G.W., *Fundamentals of Rock Mechanics*, Chapman and Hall, pp 183-187, 1979.

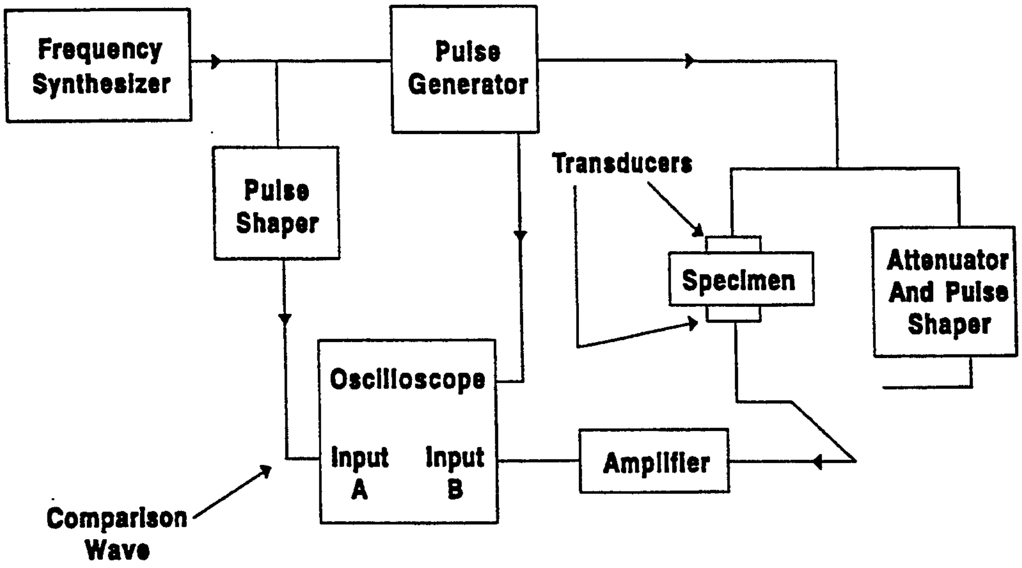

Figure C-5. Through transmission system for acoustic velocities.

Annex 4
Uniaxial Strain Plots

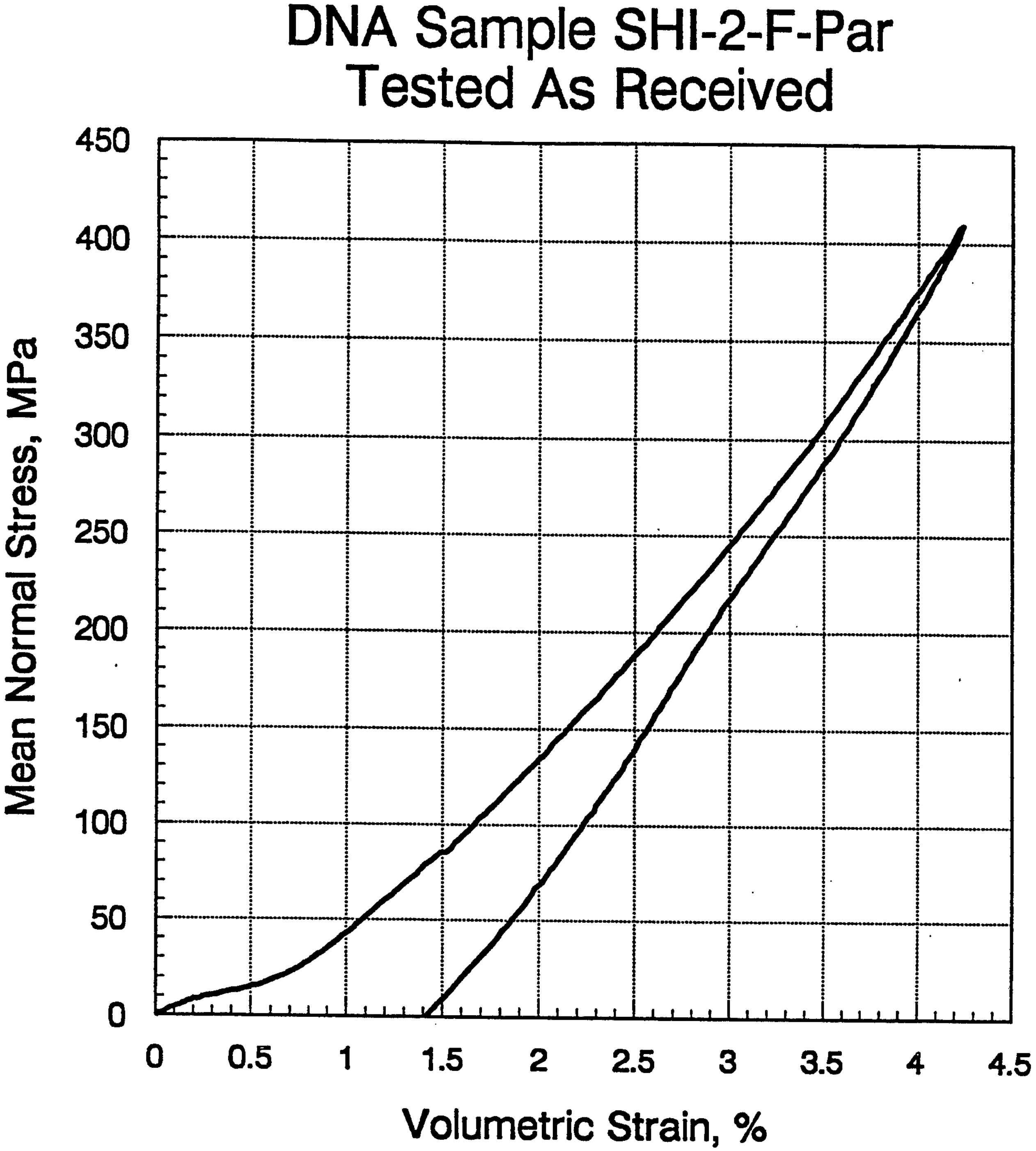

Figure C-6. Mean normal stress versus volumetric strain under uniaxial strain conditions for sample SHI-2-F-Par.

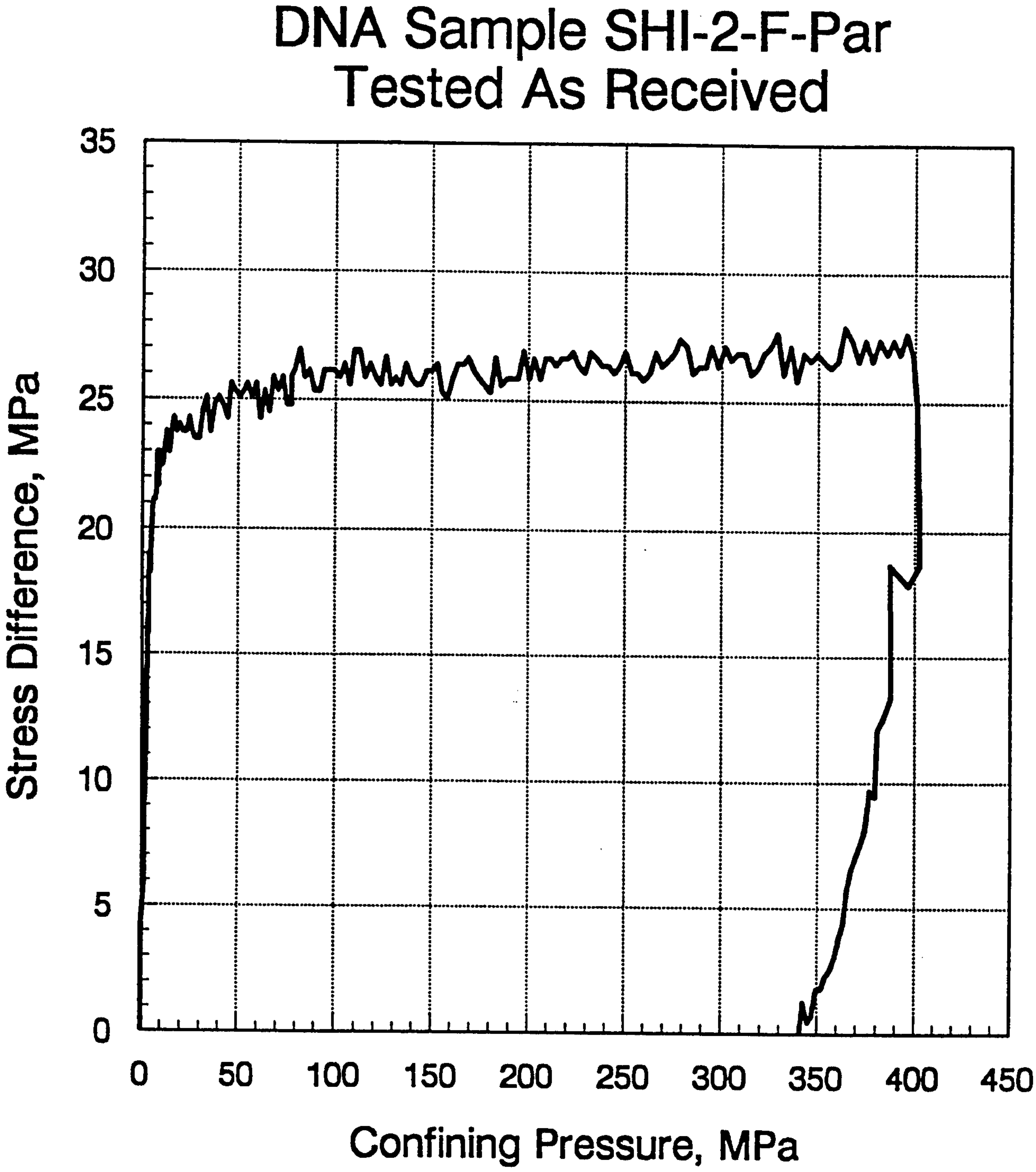

Figure C-7. Stress difference versus confining pressure under uniaxial strain conditions for sample SHI-2-F-Par.

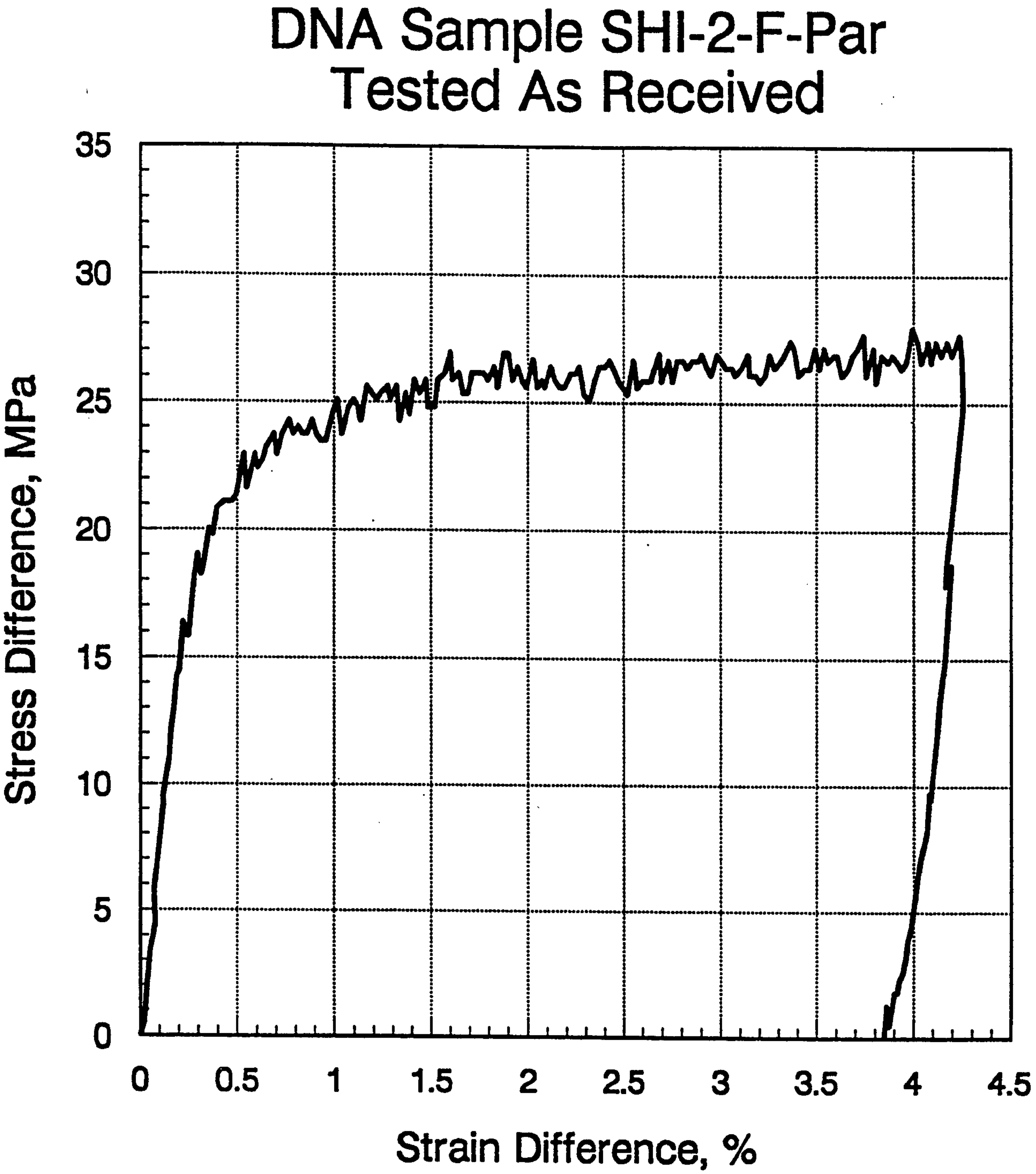

Figure C-8. Stress difference versus strain difference under uniaxial strain conditions for sample SHI-2-F-Par.

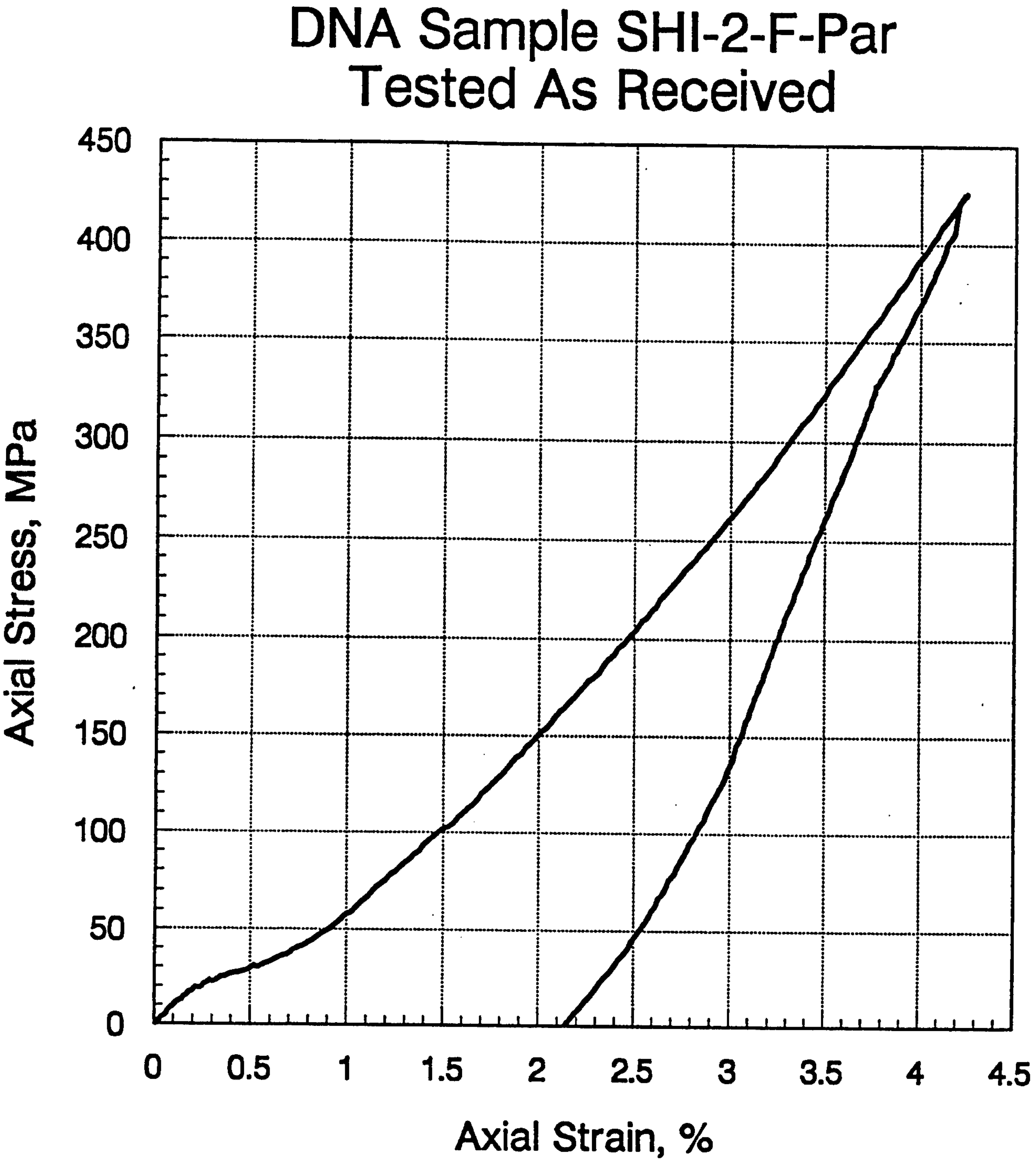

Figure C-9. Axial stress versus axial strain under uniaxial strain conditions for sample SHI-2-F-Par.

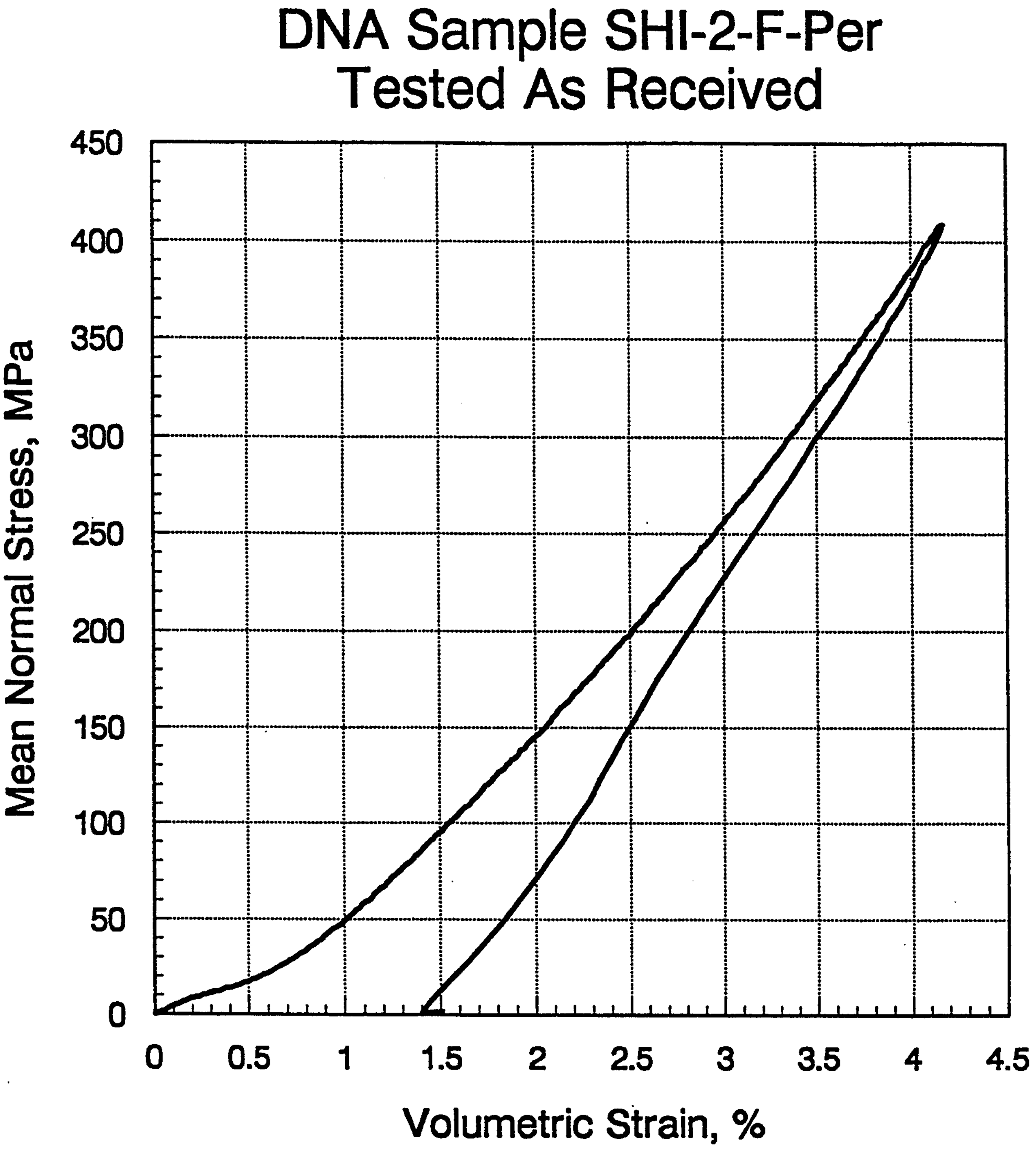

Figure C-10. Mean normal stress versus volumetric strain under uniaxial strain conditions for sample SHI-2-F-Per.

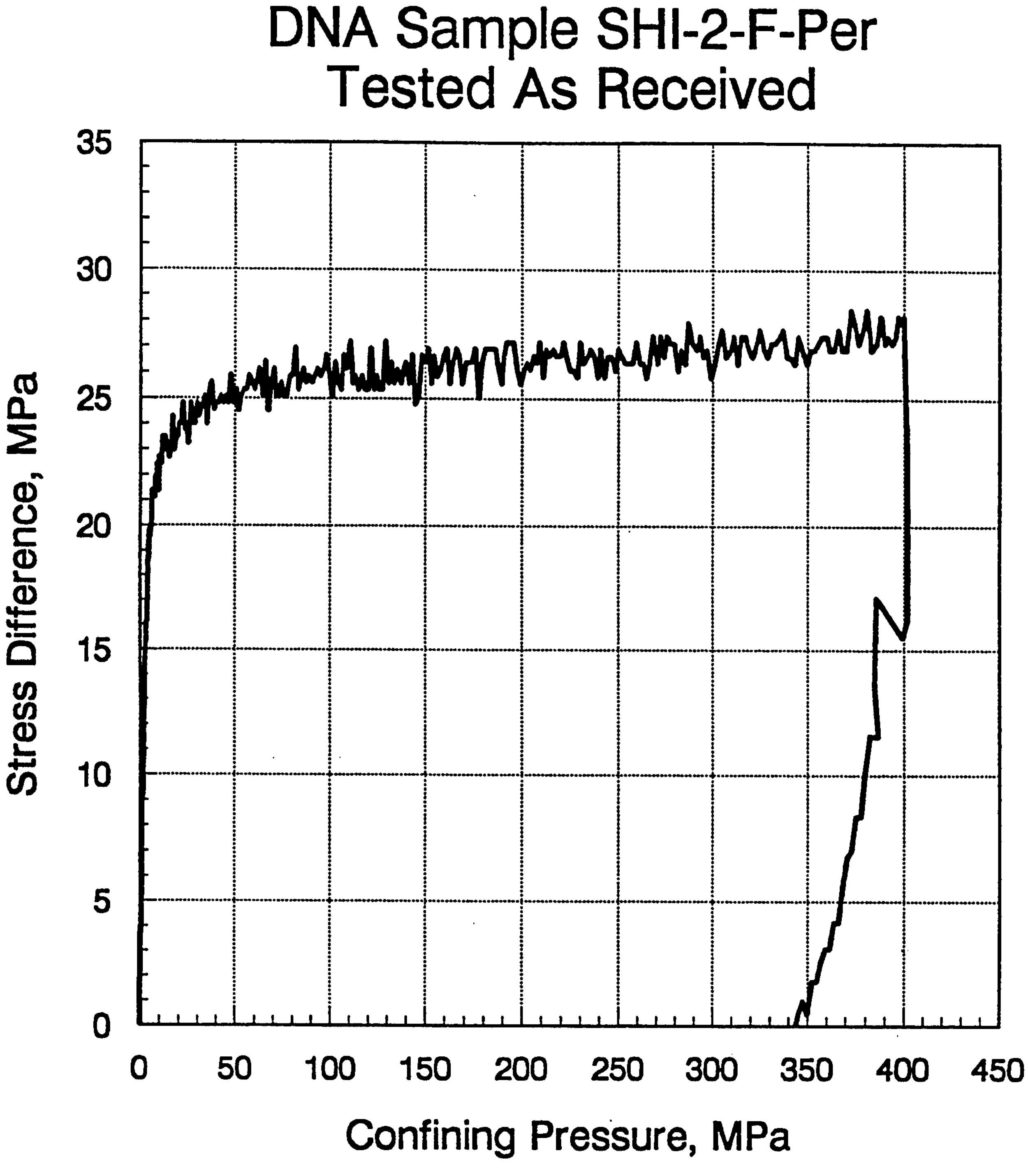

Figure C-11. Stress difference versus confining pressure under uniaxial strain conditions for sample SHI-2-F-Per.

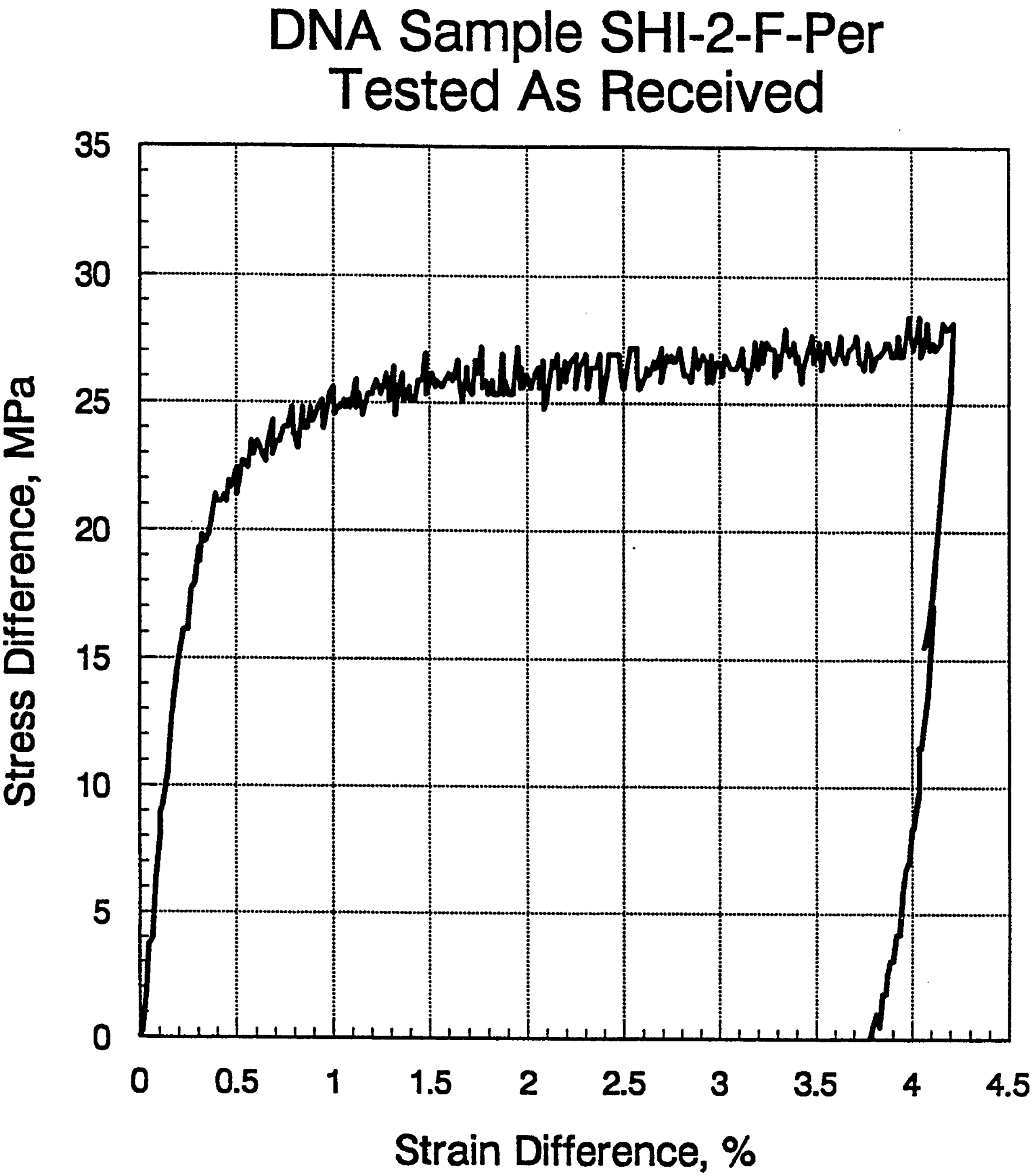

Figure C-12. Stress difference versus strain difference under uniaxial strain conditions for sample SHI-2-F-Per.

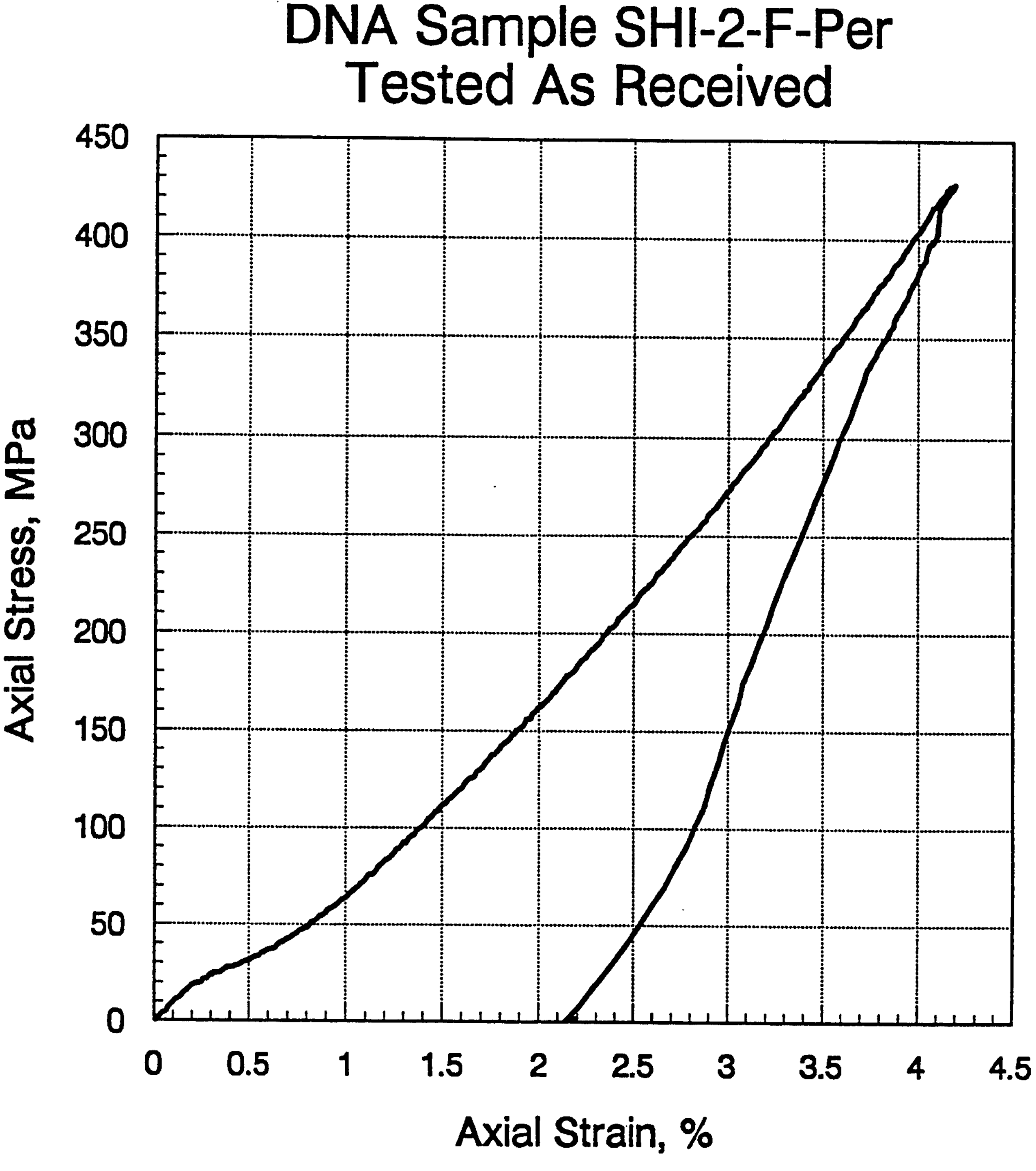

Figure C-13. Axial stress versus axial strain under uniaxial strain conditions for sample SHI-2-F-Per.

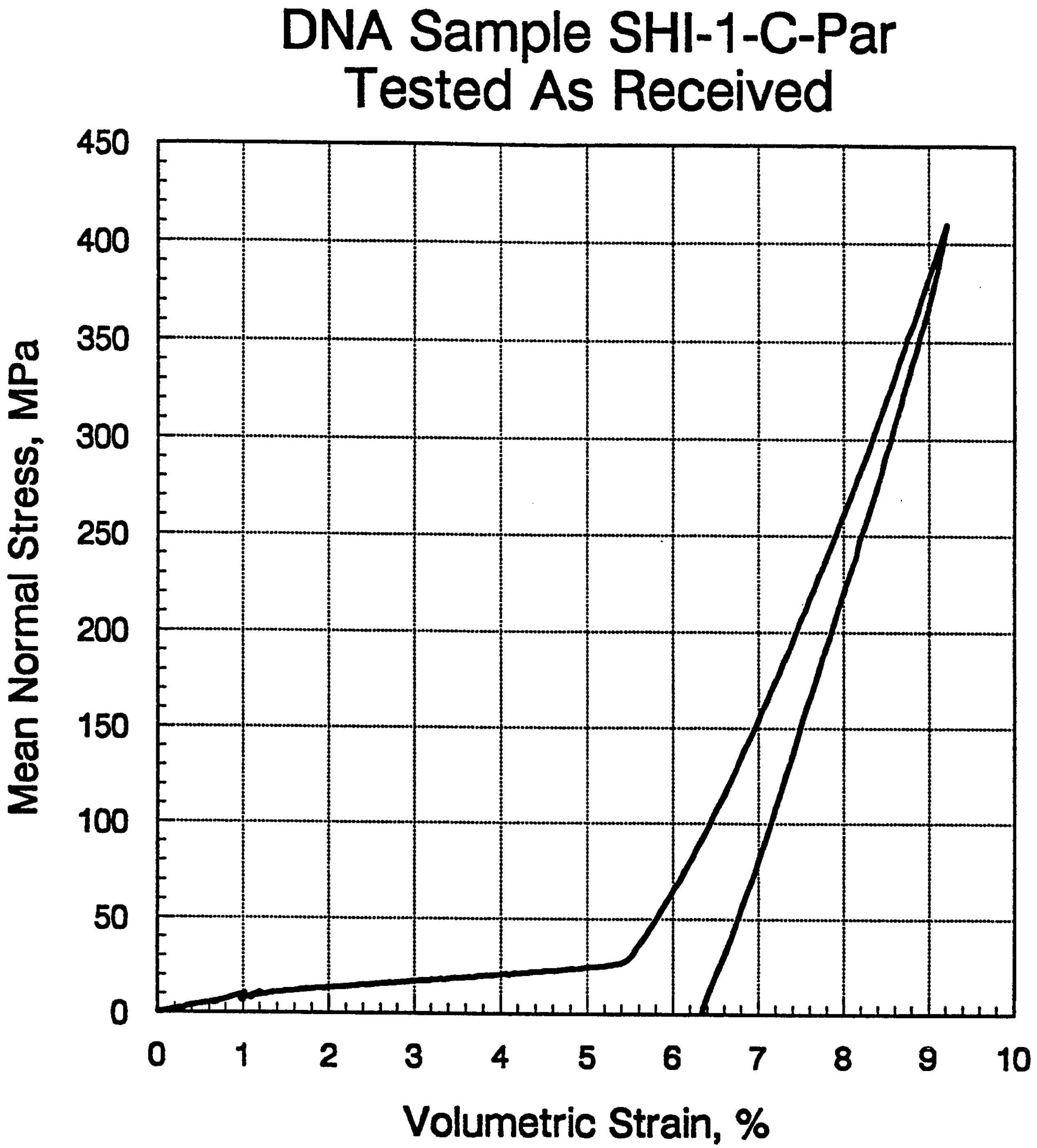

Figure C-14. Mean normal stress versus volumetric strain under uniaxial strain conditions for sample SHI-1-C-Par.

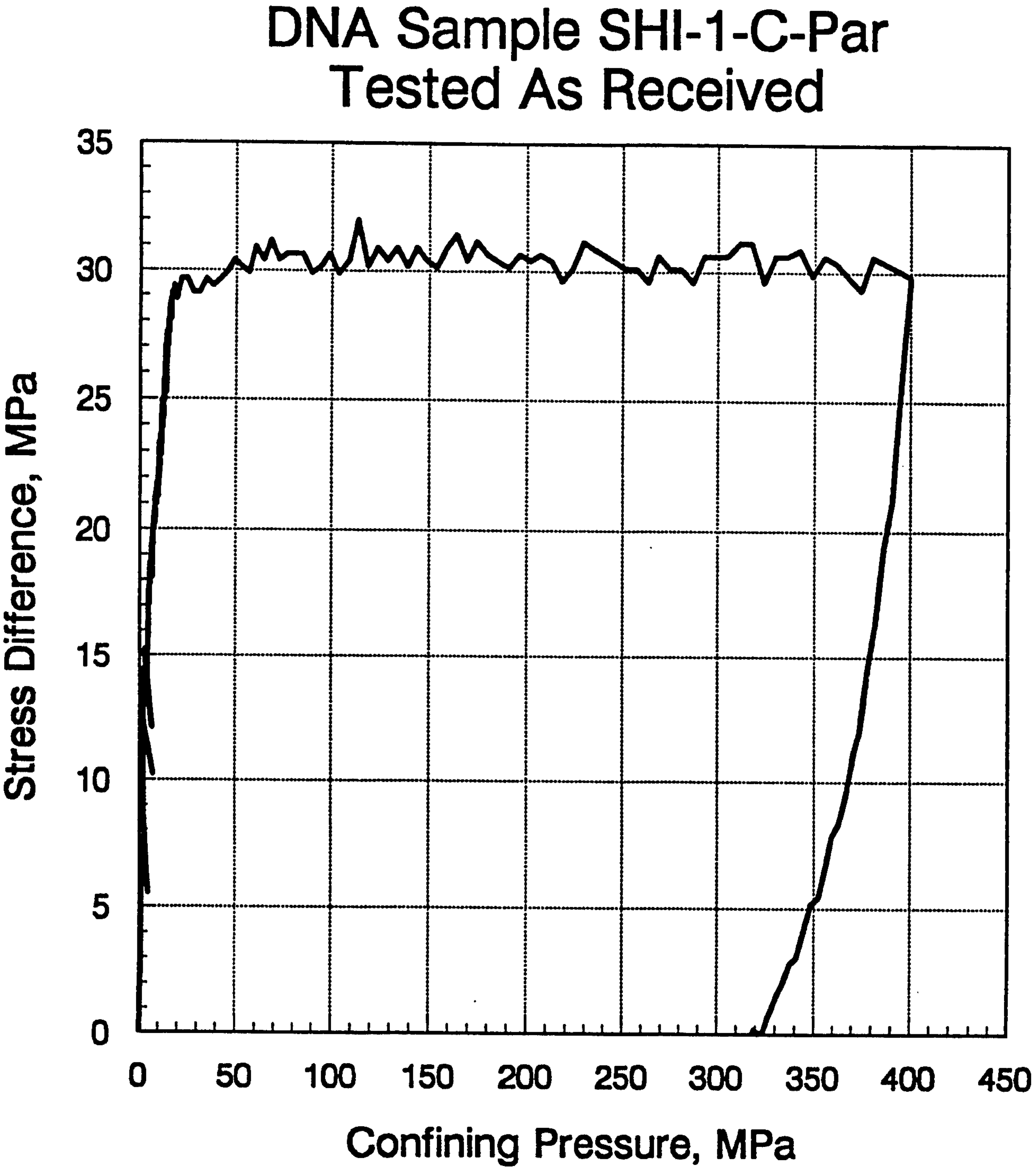

Figure C-15. Stress difference versus confining pressure under uniaxial strain conditions for sample SHI-1-C-Par.

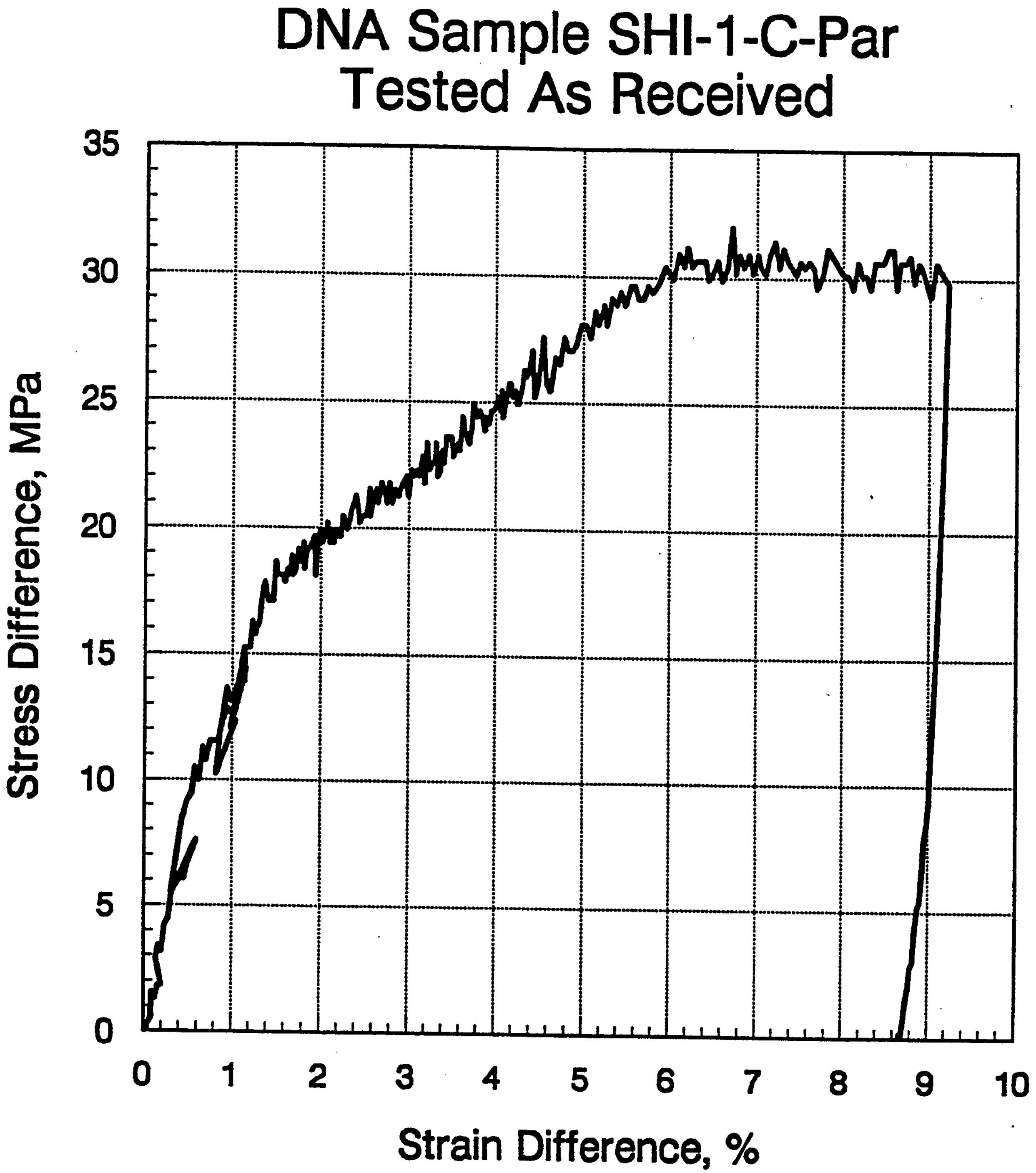

Figure C-16. Stress difference versus strain difference under uniaxial conditions for sample SHI-1-C-Par.

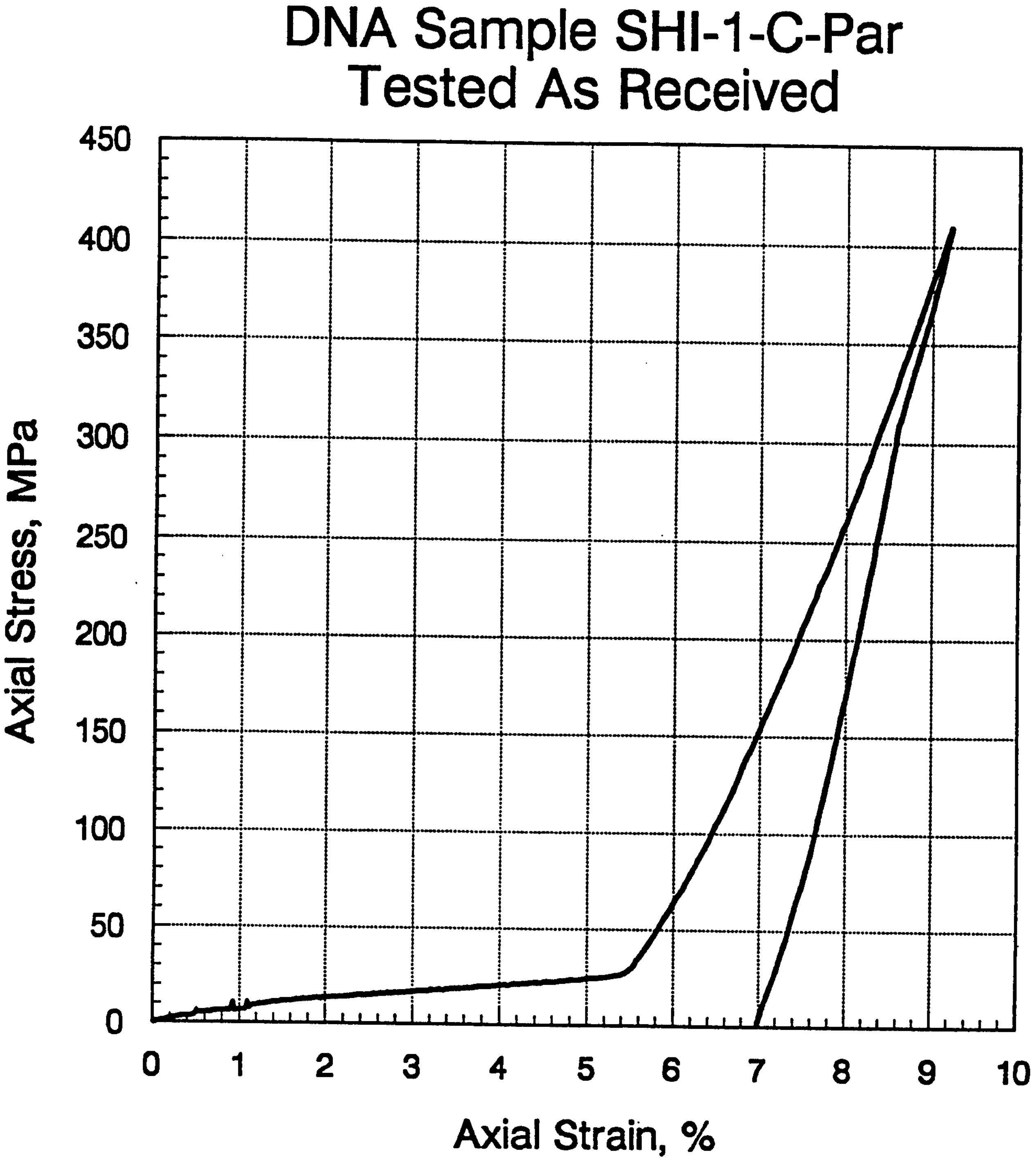

Figure C-17. Axial stress versus axial strain under uniaxial strain conditions for sample SHI-1-C-Par.

Annex 5
Unconfined Compression Stress-Strain Plots

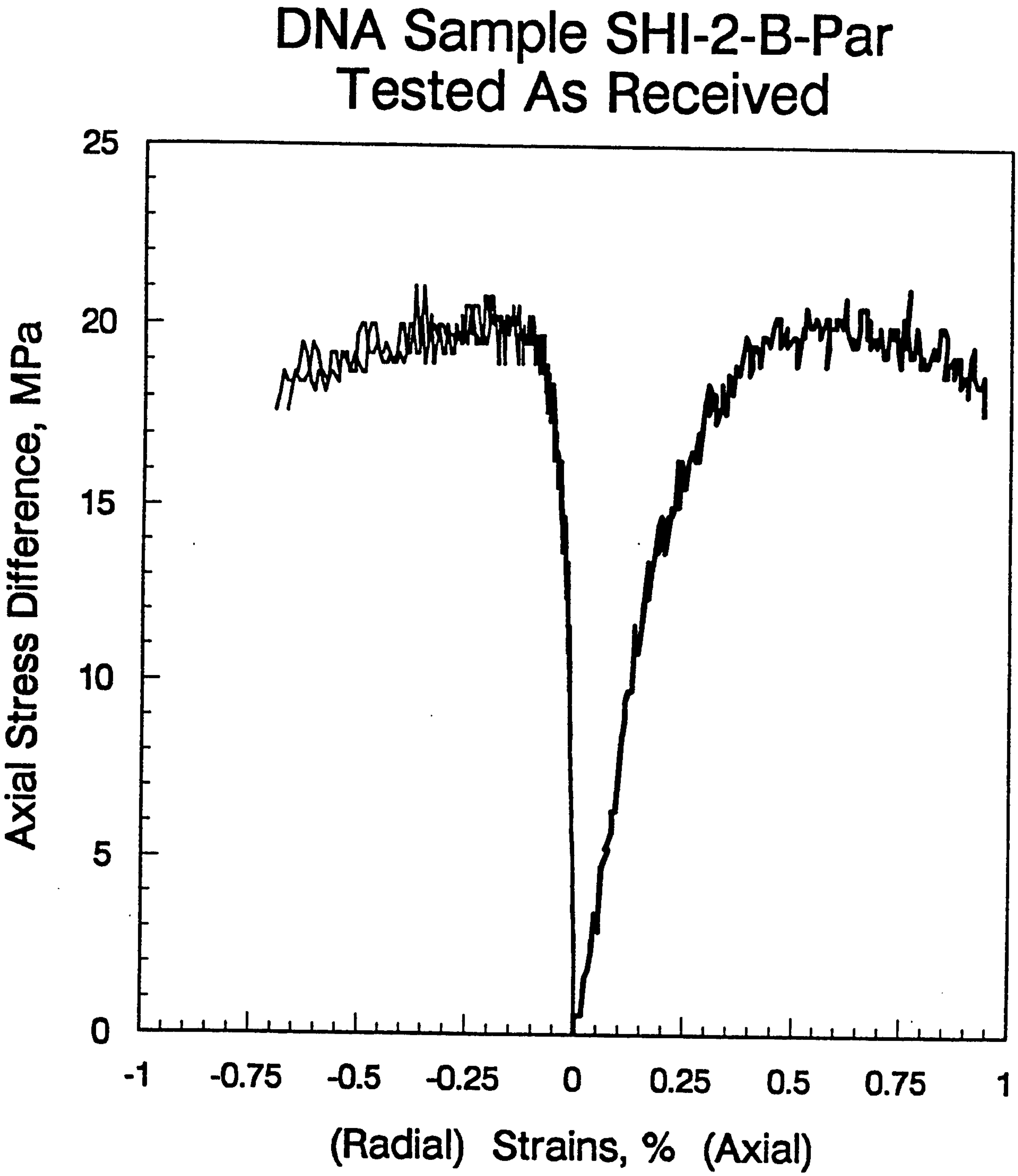

Figure C-18. Stress versus strain during unconfined compression for sample SHI-2-B-Par.

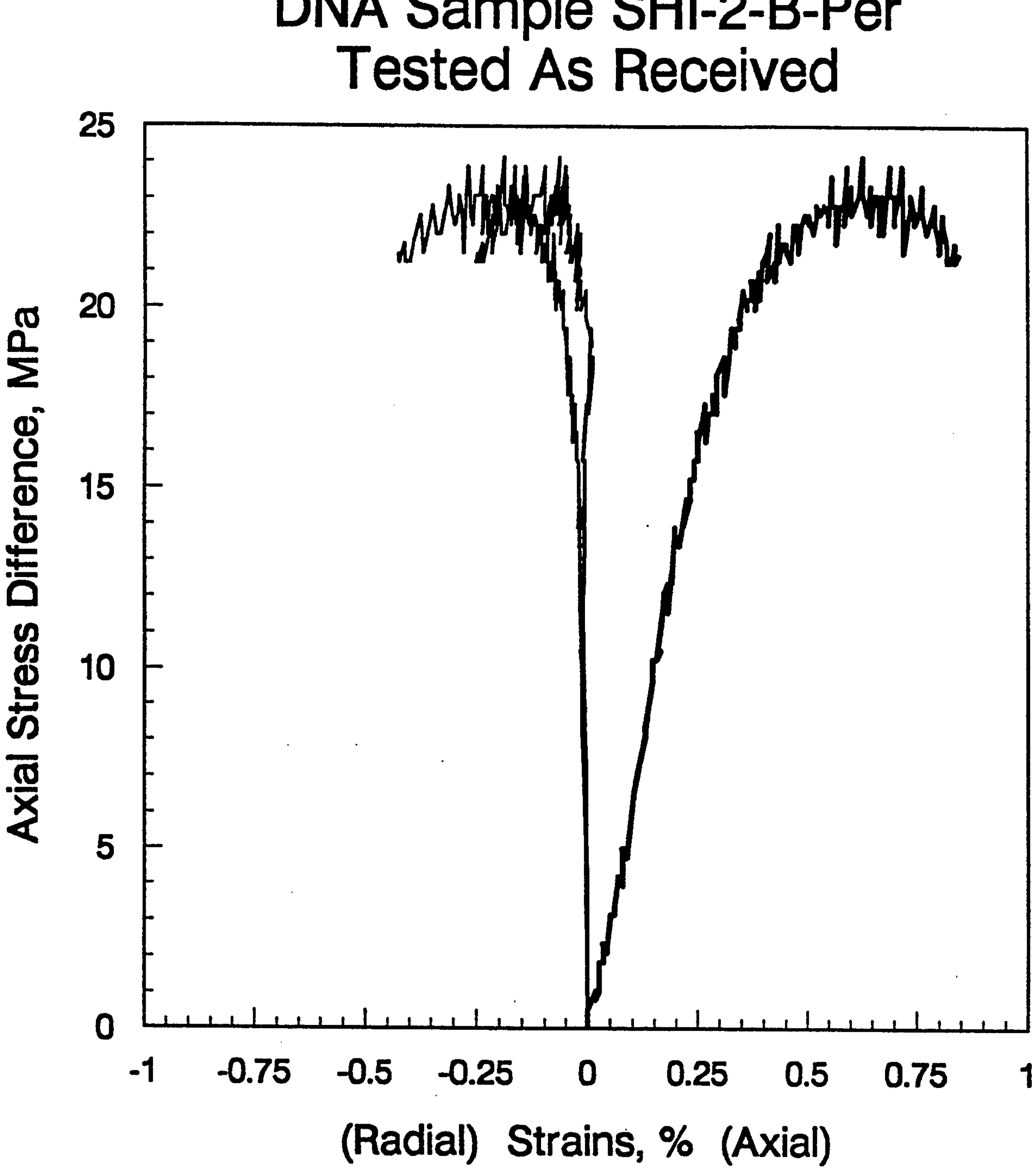

Figure C-19. Stress versus strain during unconfined compression for sample SHI-2-B-Per.

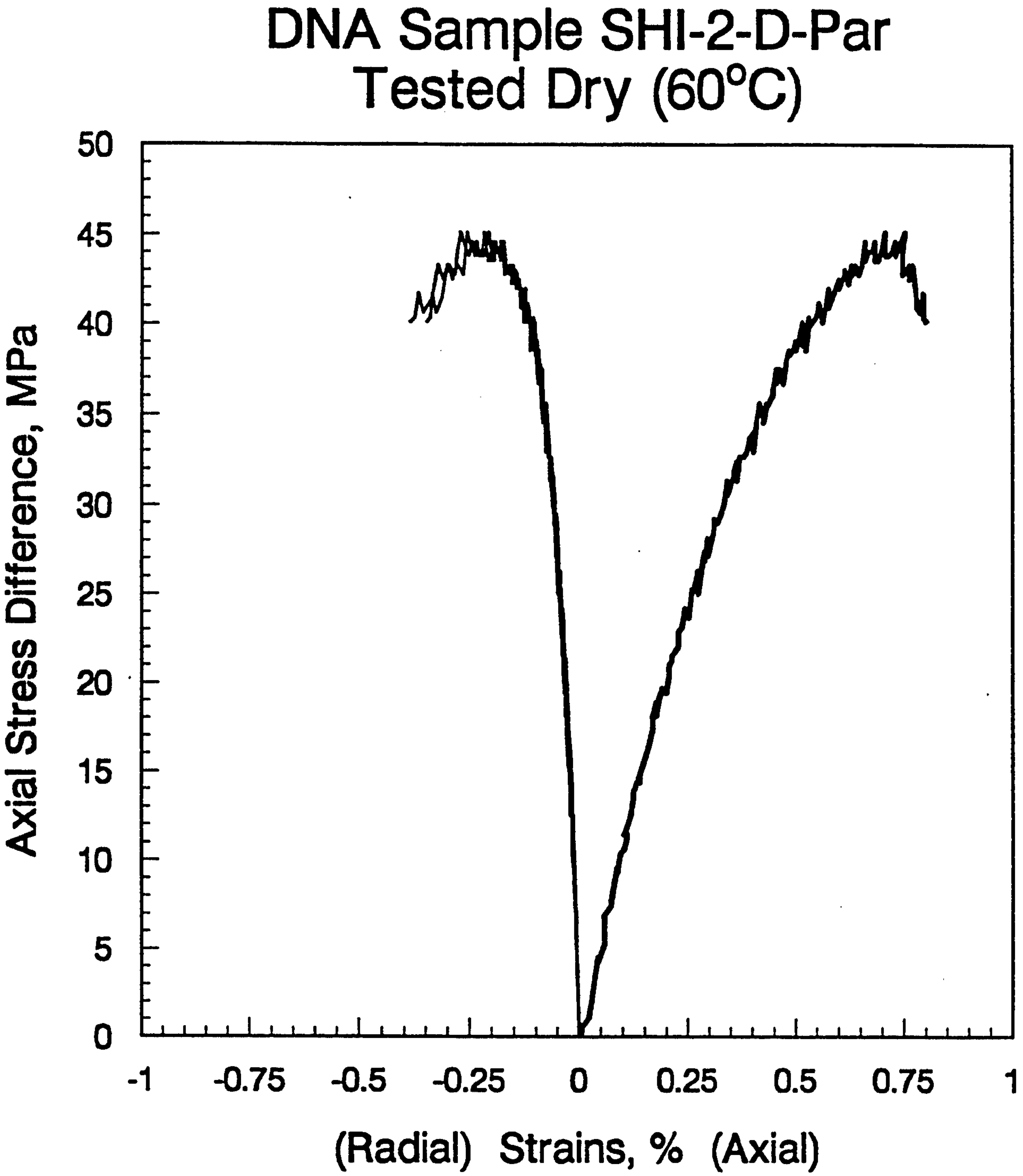

Figure C-20. Stress versus strain during unconfined compression for sample SHI-2-D-Par.

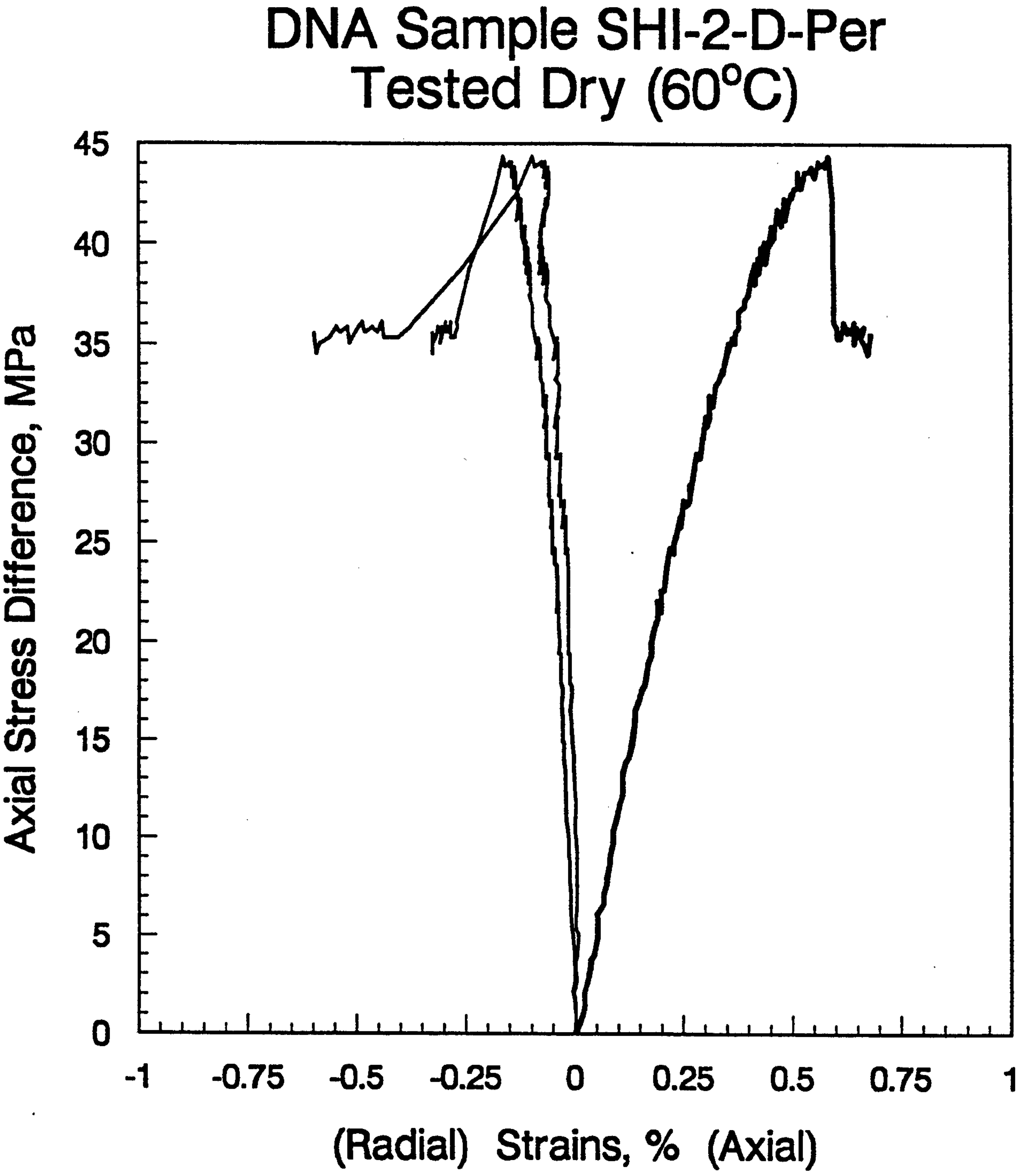

Figure C-21. Stress versus strain during unconfined compression for sample SHI-2-D-Per.

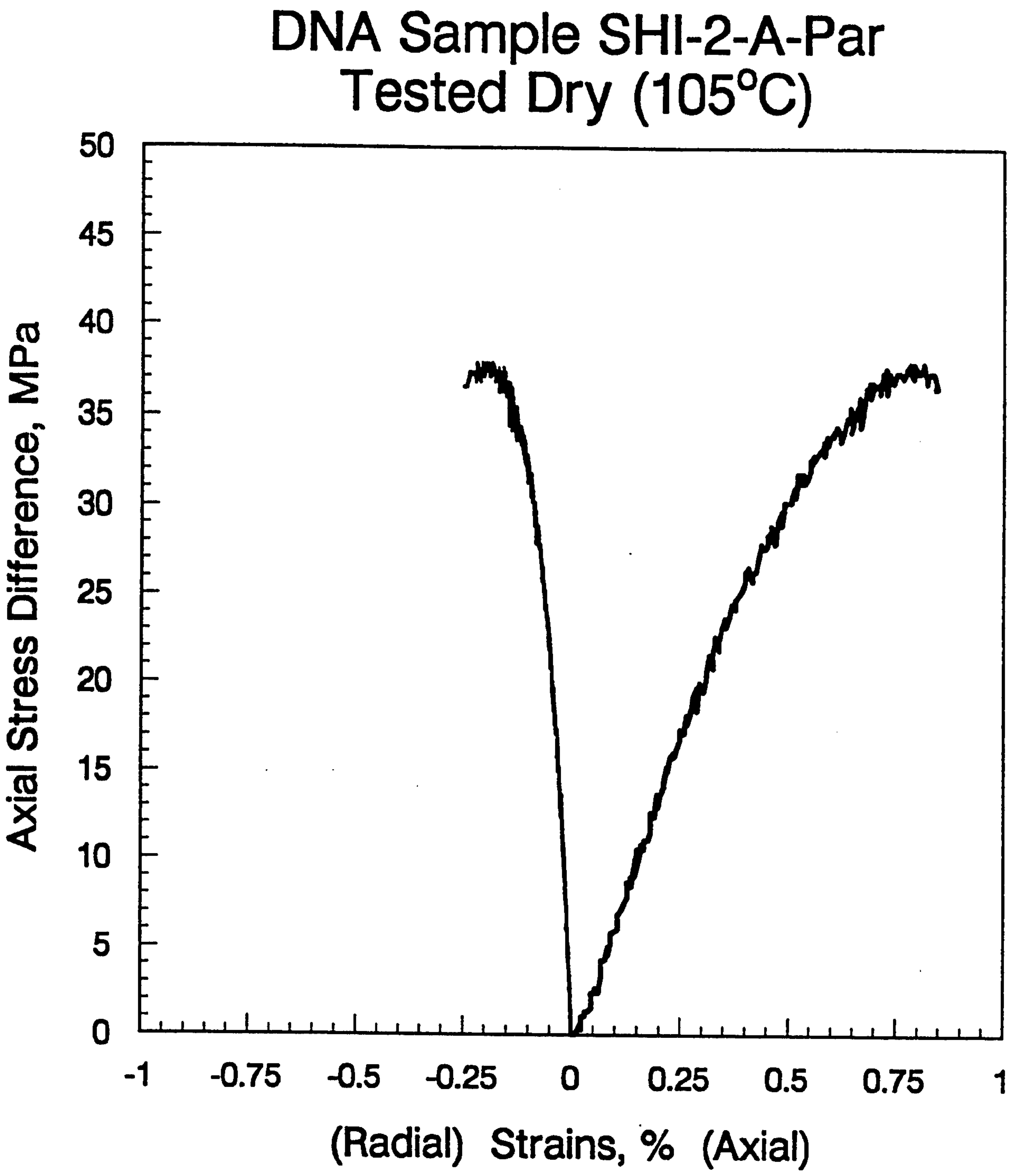

Figure C-22. Stress versus strain during unconfined compression for sample SHI-2-A-Par.

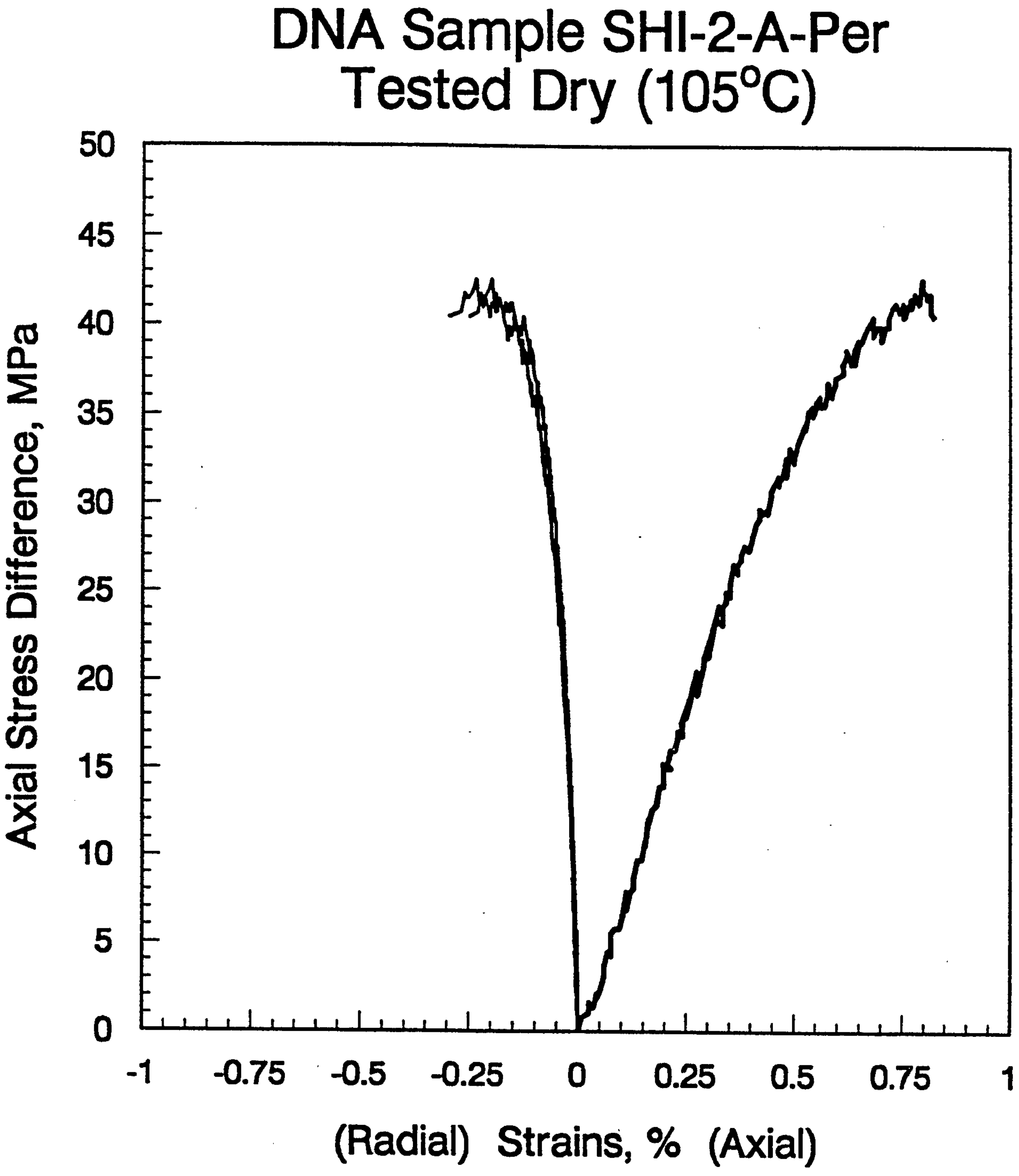

Figure C-23. Stress versus strain during unconfined compression for sample SHI-2-A-Per.

APPENDIX D
MATERIAL CHARACTERIZATION OF SAMPLES FROM THE LINCHBURG MINE

D.1 INTRODUCTION.

Laboratory tests were conducted on predominantly limestone core samples from the Linchburg mine. The core samples were retrieved from horizontal drill holes located in test chambers and drifts. Tests were conducted on thirteen core intervals to characterize the material. This included lithologic descriptions, physical property measurements, ultrasonic velocity measurements, uniaxial compression tests, and uniaxial strain tests. These tests were performed on plug specimens oriented both parallel and perpendicular with respect to the whole core axis. This was done to assess the degree of anisotropic behavior in strata in the test region. X-Ray Diffraction (XRD) analysis, to determine semi-quantitative mineralogy, was also performed on eight of the thirteen core samples. The laboratory test program, including the individual test sample location and orientation, is summarized in Table D-1.

Table D-1. Summary of laboratory test program conducted on the selected core samples from the Linchburg Mine.

Core ID	Test Chamber	Hole #	Test Plug ID[1]	Physical Properties	Ultrasonic Velocities	Unconfined Compression	Uniaxial Strain	XRD	Thin Section
1	4	2	1A-‖	✓	✓	✓		✓	✓
			1B-‖	✓	✓		✓		
			1C-⊥	✓	✓	✓			
2	4	2	2A-‖	✓	✓		✓		
			2B-‖	✓	✓	✓			
			2C-⊥	✓	✓	✓			
3	2	4	3A-‖	✓	✓	✓		✓	✓
			3B-‖	✓	✓		✓		
			3C-⊥	✓	✓	✓			
4	4	3	4A-‖	✓	✓	✓			
			4B-‖	✓	✓		✓	✓	✓
			4C-⊥	✓	✓	✓			

Table D-1. Summary of laboratory test program conducted on the selected core samples from the Linchburg Mine. (Continued)

Core ID	Test Chamber	Hole #	Test Plug ID[1]	Physical Properties	Ultrasonic Velocities	Unconfined Compression	Uniaxial Strain	XRD	Thin Section
5	7	3	5A-‖	✓	✓	✓		✓	✓
			5B-‖	✓	✓		✓		
			5C-⊥	✓	✓	✓			
6	2	3	6A-‖	✓	✓	✓			
			6B-‖	✓	✓		✓	✓	✓
			6C-⊥	✓	✓	✓			
7	2	1	7A-‖	✓	✓	✓			
			7B-‖	✓	✓		✓		
			7C-⊥	✓	✓	✓			
8	1	5	8A-‖	✓	✓	✓		✓	✓
9	3	5	9A-‖	✓	✓	✓		✓	✓
			9B-‖	✓	✓		✓		
			9C-⊥	✓	✓	✓			
10	3	4	10A-‖	✓	✓	✓			
			10B-‖	✓	✓		✓		
			10C-⊥	✓	✓	✓			
11	2	3	11A-‖	✓	✓				
			11B-‖	✓	✓				
			11C-⊥	✓	✓				
12	Left-Hand Drift	4	12A-‖	✓	✓	✓			
			12B-‖	✓	✓			✓	✓
			12C-⊥	✓	✓	✓			
13	Left-Hand Drift	1	13A-‖	✓	✓	✓			
			13B-‖	✓	✓		✓		
			13C-⊥	✓	✓	✓			

[1] ‖ and ⊥ designations indicate sample orientation with respect to the whole core axis (parallel and perpendicular orientation).

The majority of the test samples identified in Table D-1 are limestones and fractured cherts. In many instances, combinations of chert and carbonate in various proportions were observed in the test specimens. Core sample #5 was a laminated silty mudstone/shale containing no carbonates and was the only sample of this rock type tested. Annex 6 presents a brief lithologic description for all of the test plugs, including sample pre-test conditions (e.g., fractures, bedding, homogeneity). Excluding core sample #5, the mineralogy for all of the test samples was dominantly calcite and quartz. The samples are exceptionally dense with dry bulk densities averaging 2.69 gm/cm^3 (±0.04 gm/cm^3). As expected for dense carbonate rocks, effective porosities are low, averaging less than 0.5%. Compressional (P) wave velocities averaged 5.39 km/s (±0.31 km/s) and shear (S) wave velocities averaged approximately 3.18 km/s (±0.26 km/s). Unconfined compressive strengths varied from 53.6 to 195.5 MPa. Overall, significant mechanical and physical property differences were not determined between the two orientations, suggesting very limited anisotropy.

D.2 CORE RECEIPT AND PREPARATION.

One cardboard box containing thirteen core sections was delivered to TerraTek on May 9, 1994. Two of the thirteen core sections were broken in two pieces. The remaining core sections were intact with lengths ranging from 5 to 18 cm. All of the core was NX-size and was unpreserved. As outlined in Table D-1, three sets of test specimens (plugs) were used for characterization testing to examine any anisotropic behavior. Two sets were prepared parallel with respect to the core axis. These samples will be designated as "parallel" (orientation). The other set was prepared orthogonal to the first two sets (perpendicular to the core axis). These test plugs will be referred to as "perpendicular" (orientation). Due to the limited amount of core avaliable only one parallel sample was prepared from core sample #8.

Each test plug was cored from NX whole core using water as the circulating fluid. These test specimens had nominal diameters of 25 mm and lengths of 50 mm for the parallel oriented samples and 38 to 45 mm lengths for the perpendicular oriented samples. The shorter lengths for the perpendicular samples were due to the size restrictions of the NX core. The ends of each specimen were machined flat and parallel to ±0.025 mm.

The XRD/Lithology samples were selected on the basis of an obvious change in composition or texture. These samples (core numbers 1, 3, 4, 5, 6, 8, 9, and 12) were taken from the excess material surrounding the parallel test plug. One half of the excess material was used for determination of XRD semi-quantitative mineralogy and the other half was cut into a thin section for petrographic examination.

D.3 RESULTS.

D.3.1 XRD Mineralogy and Lithology.

The XRD mineralogy for the eight selected core samples is presented in Table D-2. The mineralogy in Table D-2 is semi-quantitative and is reported in weight percent. The mineralogy is profiled in Figure D-1 as a function of core sample number. Photomicrographs, illustrating the sample fabric and composition are presented in Annex 7. Specific test procedures used for determining XRD mineralogy are provided in Annex 8.

Table D-2. Summary of XRD mineralogy of selected samples from the Linchburg Mine.

Sample ID	Test Plug ID	Mineralogy, Approximate Weight %						
		Quartz	Calcite	Serpentine	Talc	Chlorite	Mica ±Illite[2]	Smectite
#1 Ch.4 Hole 2	1A-‖	1	99					
#3 Ch.2 Hole 4	3A-‖	20	79					1?
#4 Ch.4 Hole 3	4B-‖	2	98					
#5 Ch.7 Hole 3	5A-‖	22		53[1]	14	2?	9	
#6 Ch.2 Hole 3	6B-‖	1	99					
#8 Ch.1 Hole 5	8A-‖	75	25					
#9 Ch.3 Hole 5	9A-‖	20	80					
#12 L.H. Drift Hole 1	12B-‖	32	68					

[1] The serpentine group mineral is probably berthierine ($(Fe, Al)_3(Si, Al)_2O_5(OH)_4$).

[2] X-ray diffraction signature is similar for illite and micaeous minerals. Hence these mineral phases are not differentiated.

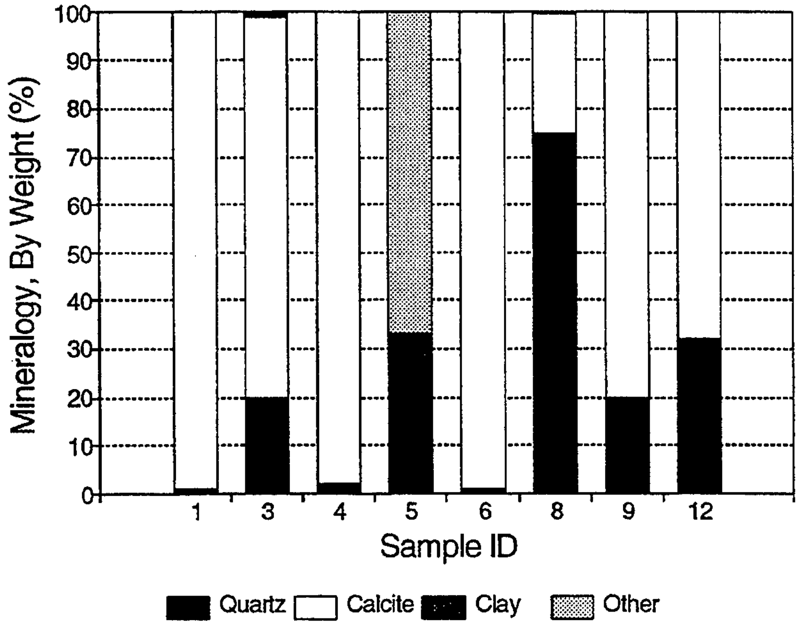

Figure D-1. XRD mineralogic profile for selected Linchburg Mine samples.

D.4 PHYSICAL PROPERTY RESULTS.

Dry bulk density, effective grain density, true grain density and the derived effective and total porosity for the thirteen core samples are presented in Tables D-3 and D-4. Also included in Tables D-3 and D-4 are the estimated occluded porosity, as determined from the difference between the total and effective porosity. The procedures used to measure physical properties are presented in Annex 8.

D.5 MECHANICAL PROPERTIES.

Tables D-5 through D-9 present the ultrasonic velocities, dynamic properties, compressive strengths and quasi-static properties determined from unconfined compression and uniaxial strain tests performed on parallel and perpendicular test specimens. Also included in Tables D-5 and D-6 is the pre-test bulk density. This was used with the ultrasonic velocities for determination of the dynamic mechanical properties. Table D-7 reports mechanical properties as well as the pre-test bulk density and the effective porosity determined for each test specimen prior to unconfined compression testing. Plots of stress difference versus axial and radial strain (if applicable) are included in Annex 9 for the parallel and perpendicular samples tested. Eleven parallel oriented samples were prepared for uniaxial strain testing. Uniaxial strain plots representing stress difference versus confining pressure, mean normal stress versus volumetric strain, axial stress versus axial strain, and stress difference versus strain difference are provided in Annex 10. Test procedures for the ultrasonic velocity measurements, unconfined compression tests, and uniaxial strain tests are provided in Annex 8.

Table D-3. Summary of physical properties of material from the Linchburg Mine.

Sample ID	Bulk Density (gm/cm^3)	Effective Grain Density (gm/cm^3)	True Grain Density (gm/cm^3)	Effective Porosity[1] (%)	Total Porosity (%)	Estimated Occluded Voids (%)
#1A ∥	2.695	2.695	2.700	0.01	0.19	0.18
#1B ∥	2.693	2.693	2.693	0.07	0.07	0
#1C ⊥	2.695	2.699	2.708	0.15	0.48	0.33
#2A ∥	2.679	2.702	2.702	0.85	0.85	0
#2B ∥	2.674	2.702	2.702	1.04	1.04	0
#2C ⊥	2.668	2.695	2.704	1.03	1.33	0.30
#3A ∥	2.645	2.663	2.663	0.66	0.66	0
#3B ∥	2.645	2.670	2.670	0.93	0.93	0
#3C ⊥	2.641	2.653	2.653	0.44	0.44	0
#4A ∥	2.686	2.707	2.707	0.78	0.78	0
#4B ∥	2.685	2.725	2.725	1.48	1.48	0
#4C ⊥	2.687	2.730	2.730	1.58	1.58	0
#5A ∥	2.831	2.835	2.867	0.15	1.26	1.11
#5B ∥	2.831	2.854	2.873	0.82	1.46	0.64
#5C ⊥	2.811	2.820	2.842	0.30	1.09	0.79
#6A ∥	2.691	2.693	2.693	0.08	0.08	0
#6B ∥	2.692	2.697	2.697	0.19	0.19	0
#6C ⊥	2.690	2.695	2.695	0.20	0.20	0

[1] Effective porosity calculated from the bulk volume and grain volume measurements.

Table D-3. Summary of physical properties of material from the Linchburg Mine. (Continued)

Sample ID	Bulk Density (gm/cm^3)	Effective Grain Density (gm/cm^3)	True Grain Density (gm/cm^3)	Effective Porosity[1] (%)	Total Porosity (%)	Estimated Occluded Voids (%)
#7A ‖	2.688	2.694	2.694	0.22	0.22	0
#7B ‖	2.686	2.695	2.695	0.33	0.33	0
#7C ⊥	2.684	2.694	2.700	0.36	0.59	0.23
#8A ‖	2.641	2.645	2.649	0.15	0.30	0.15
#9A ‖	2.686	2.699	2.699	0.49	0.49	0
#9B ‖	2.682	2.697	2.701	0.58	0.70	0.12
#9C ⊥	2.689	2.699	2.699	0.36	0.36	0
#10A ‖	2.699	2.703	2.703	0.14	0.14	0
#10B ‖	2.698	2.704	2.704	0.23	0.23	0
#10C ⊥	2.699	2.701	2.701	0.08	0.08	0
#11A ‖	2.648	2.651	2.651	0.09	0.09	0
#11B ‖	2.683	2.691	2.691	0.31	0.31	0
#11C ⊥	2.641	2.672	2.672	1.17	1.17	0
#12A ‖	2.690	2.695	2.695	0.22	0.22	0
#12B ‖	2.627	2.644	2.650	0.65	0.87	0.22
#12C ⊥	2.679	2.691	2.691	0.43	0.43	0
#13A ‖	2.695	2.695	2.699	0.02	0.15	0.13
#13B ‖	2.688	2.697	2.697	0.34	0.34	0
#13C ⊥	2.689	2.697	2.697	0.27	0.27	0

[1] Effective porosity calculated from the bulk volume and grain volume measurements.

Table D-4. Summary of ultrasonic velocities and dynamic mechanical properties.

Sample ID	Length (in)	Bulk Density (gm/cm^3)	P-Wave Velocity (km/s)	S-Wave Velocity (km/s)	Dynamic Poisson's Ratio	Dynamic Moduli		
						Young's (GPa)	Bulk (GPa)	Shear (GPa)
#1A ∥	1.936	2.695	5.31	3.14	0.23	65.4	40.4	26.6
#1B ∥	1.902	2.693	5.48	3.17	0.25	67.5	45.0	27.0
#1C ⊥	1.698	2.695	5.10	3.08	0.21	62.0	35.6	25.6
#2A ∥	1.424	2.679	5.35	2.92	0.29	58.8	46.7	22.8
#2B ∥	1.997	2.674	5.22	3.01	0.25	60.6	40.6	24.2
#2C ⊥	1.728	2.668	5.22	3.09	0.23	62.6	38.7	25.5
#3A ∥	1.887	2.645	5.70	3.58	0.17	79.6	40.2	34.0
#3B ∥	1.997	2.645	5.51	3.72	0.08	79.1	31.4	36.6
#3C ⊥	1.678	2.641	5.49	3.69	0.09	78.2	31.8	35.9
#4A ∥	1.997	2.686	5.31	2.99	0.27	60.9	44.1	24.0
#4B ∥	2.008	2.685	5.60	3.32	0.23	72.7	44.9	29.6
#4C ⊥	1.699	2.687	5.13	2.91	0.26	57.4	39.9	22.8
#5A ∥	1.792	2.831	4.86	3.13	0.15	63.5	30.2	27.6
#5B ∥	1.632	2.831	4.93	3.10	0.17	63.8	32.2	27.3
#5C ⊥	1.332	2.811	5.68	3.52	0.19	82.7	44.5	34.8
#6A ∥	2.006	2.691	5.27	3.07	0.24	63.0	40.4	25.4
#6B ∥	2.006	2.692	5.14	3.05	0.23	61.5	38.0	25.0
#6C ⊥	1.698	2.690	5.13	3.09	0.22	62.4	37.1	25.6

Table D-4. Summary of ultrasonic velocities and dynamic mechanical properties. (Continued)

Sample ID	Length (in)	Bulk Density (gm/cm^3)	P-Wave Velocity (km/s)	S-Wave Velocity (km/s)	Dynamic Poisson's Ratio	Dynamic Moduli		
						Young's (GPa)	Bulk (GPa)	Shear (GPa)
#7A ∥	1.996	2.688	5.25	2.74	0.31	53.0	46.5	20.2
#7B ∥	2.013	2.686	5.21	2.77	0.30	53.7	44.7	20.6
#7C ⊥	1.677	2.684	5.13	2.79	0.29	53.9	42.8	20.9
#8A ∥	1.978	2.721	5.64	3.78	0.09	84.9	34.5	38.9
#9A ∥	1.992	2.686	5.24	3.04	0.25	61.8	41.2	24.7
#9B ∥	2.013	2.682	5.11	2.95	0.25	58.3	38.9	23.3
#9C ⊥	1.698	2.689	5.22	3.01	0.25	60.9	40.6	24.4
#10A ∥	1.993	2.699	6.09	3.32	0.29	76.6	60.8	29.7
#10B ∥	2.013	2.698	6.04	3.31	0.29	75.9	60.3	29.4
#10C ⊥	1.677	2.699	5.87	3.34	0.26	75.9	52.7	30.1
#11A ∥	2.013	2.648	5.46	3.37	0.19	71.7	38.5	30.1
#11B ∥	1.993	2.683	5.03	2.83	0.27	54.5	39.5	21.5
#11C ⊥	1.678	2.641	5.35	3.33	0.18	69.3	36.1	29.4
#12A ∥	1.802	2.690	5.64	3.21	0.15	69.9	33.3	30.4
#12B ∥	1.056	2.627	5.15	3.53	0.06	69.2	26.2	32.6
#12C ⊥	1.698	2.679	5.94	3.23	0.29	72.1	57.2	27.9
#13A ∥	1.992	2.695	5.74	3.17	0.31	69.3	60.8	26.5
#13B ∥	2.013	2.688	5.71	3.19	0.27	69.6	50.4	27.4
#13C ⊥	1.677	2.689	5.13	3.24	0.17	65.9	33.3	28.2

Table D-5. Unconfined compressive strength and static moduli of samples from the Linchburg Mine.

Sample ID	Bulk Density (gm/cm^3)	Effective Porosity (%)	Compressive Strength (MPa)	Poisson's Ratio	Static Moduli		
					Young's (GPa)	Bulk (GPa)	Shear (GPa)
#1A ||	2.695	0.01	95.1	0.24	56.8	36.6	22.9
#1C ⊥	2.695	0.15	93.4	0.24	48.0	31.2	19.3
#2B ||	2.674	1.04	72.5	0.27	57.0	40.6	22.5
#2C ⊥	2.668	1.03	89.5	0.27	54.6	40.0	21.4
#3A ||	2.645	0.66	100.8	0.15	63.1	30.1	27.4
#3C ⊥	2.641	0.44	195.5	0.12	70.6	30.8	31.6
#4A ||	2.686	0.78	83.8	0.25	51.5	35.0	20.5
#4C ⊥	2.687	1.58	95.4	0.24	51.2	33.2	20.6
#5A ||	2.831	0.15	56.0	0.21	42.0	23.8	17.4
#5C ⊥	2.811	0.30	58.8	0.39	30.0	47.3	10.8
#6A ||	2.691	0.08	100.3	0.26	53.2	36.5	21.2
#6C ⊥	2.690	0.20	117.3	0.21	49.6	28.6	20.5
#7A ||	2.688	0.22	85.6	0.22	53.2	31.5	21.9
#7C ⊥	2.684	0.36	84.3	0.22	37.6	22.7	15.3
#8A ||	2.721	0.31	161.6	0.14	72.7	33.6	31.9
#9A ||	2.686	0.49	107.7	0.25	55.3	36.1	22.2
#9C ⊥	2.689	0.36	120.9	0.25	56.6	37.8	22.6
#10A ||	2.699	0.14	153.9	0.25	62.5	42.3	24.9
#10C ⊥	2.699	0.08	177.7	0.31	72.0	63.2	27.5
#11A ||	2.648	0.09	53.6	0.44	30.3	83.3	10.5
#11C ⊥	2.641	1.17	87.4	0.16	60.5	29.3	26.2
#12A ||	2.690	0.22	116.8	0.25	56.2	37.5	22.5
#12C ⊥	2.679	0.43	88.4	0.38	60.9	82.5	22.9
#13A ||	2.695	0.02	123.3	0.25	61.6	40.5	24.7
#13C ⊥	2.689	0.27	70.5	0.26	43.5	30.0	17.3

Table D-6. Summary of strength characteristics determined from uniaxial strain tests.

Sample ID	Maximum Axial Stress Difference (MPa)	Axial Stress Difference Intercept (MPa)	Maximum Volumetric Strain (%)	Measured Permanent Compaction (%)	Confining Pressure at zero Axial Stress Difference (MPa)
#1B ‖	228.6	192.5	1.2	<0.1	180
#2A ‖[1]	170.8	-	0.5	-	200
#3B ‖[1]	284.1	-	0.5	-	-
#4B ‖	204.3	179.7	1.0	0	210
#5B ‖	465.3	226.0	2.1	0.2	77
#6B ‖	251.6	212.8	1.2	<0.1	170
#7B ‖	232.5	197.2	1.4	0.1	273
#9B ‖	239.0	202.1	1.1	0	154
#10B ‖	291.4	249.8	1.0	0	127
#11B ‖[1]	212.5	~154.9	0.8	-	-
#13B ‖	256.3	218.7	1.3	0	173

[1] Sample failed (developed a catastrophic shear plane) during uniaxial strain loading. Hence, properties were determined (if possible) up to the peak axial stress difference.

Table D-7. Summary of moduli determined from uniaxial strain tests.

Sample ID	Loading Bulk Modulus (GPa)	Unloading Bulk Modulus (GPa)	Loading Apparent Constrained Modulus (GPa)	Unloading Apparent Constrained Modulus (GPa)	Loading Shear Modulus (GPa)	Unloading Shear Modulus (GPa)
#1B ||	43.4	50.3	56.1	72.4	6.0	41.3
#2A ||[1]	38.7	-	59.8	-	-	-
#3B ||[1]	28.5	-	62.6	-	-	-
#4B ||	51.0	57.1	67.2	81.1	9.0	53.6
#5B ||	29.0	36.3	46.3	61.4	19.6	45.6
#6B ||	44.8	53.6	58.1	78.7	9.5	48.2
#7B ||	39.6	42.9	49.6	70.3	5.5	57.3
#9B ||	47.5	56.3	59.4	80.1	9.1	45.6
#10B ||	55.0	60.1	71.0	88.2	12.4	51.5
#11B ||[1]	37.7	-	54.9	-	-	-
#13B ||	41.7	51.9	51.4	76.6	6.6	47.1

[1] Sample failed (developed a catastrophic shear plane) during uniaxial strain loading. Hence, properties were determined (if possible) up to the peak axial stress difference.

D.6 DISCUSSION.

D.6.1 Mineralogy and Lithology.

As is evident in Table D-2, the Linchburg Mine samples are composed predominantely of calcite and quartz. Core sample #5 is unique in that it contains no calcite and has high amounts of serpentine and talc. Excluding sample #5, the samples contain exclusively calcite and quartz in various proportions. Three distinct mineralogical groups are evident for the samples analyzed. Sample numbers 1, 4, and 6 contain over 90% calcite with minor amounts of quartz. Samples numbers 3, 9, and 12 contain between 68 and 80% calcite and moderate amounts of quartz (20 to 32%). Sample 8 is composed dominantly of quartz (75%) with moderate amounts of calcite (25%).

Several textural features are depicted from thin section photomicrographs (see Annex 7). In general, sample numbers 1, 4, and 6 are medium to coarse-grained crinoidal limestones (packstones/grainstones). Crinoidal fragments appear to dominate the carbonate grains; however, other fossil debris such as bryozoan, bivalve and coral fragments were observed. Calcitic overgrowth cements these grains and has filled essentially all available pore space. Samples 8 and 12 are fossilifereous chert and samples 3 and 9 are fossilifereous limestone with localized chert zones. For both of these groups, microcrystalline quartz has replaced calcitic fossils to some extent. Fractures are common in these samples (numbers 3, 8, 9, and 12) and are typically filled with calcite. Sample #5 exhibits distinct laminations with alternating thin beds (<1mm) of mudstone, siltstone, and very fine-grained sandstone. The limited porosity occurring in the silty/sandy mudstone is most likely associated with clays.

D.7 PHYSICAL PROPERTIES.

The bulk densities determined for the parallel samples on an average basis are fairly similar, with values ranging from 2.627 to 2.831 gm/cm^3 and average approximately 2.690 gm/cm^3 ±0.05 gm/cm^3. The bulk densities determined for the perpendicular samples ranged from 2.641 to 2.811 gm/cm^3 and average approximately 2.689 gm/cm^3 ±0.04 gm/cm^3. The highest bulk densities were determined for the laminated silty/sandy mudstone (core #5). These values reflect the high concentration of high density iron-magnesium minerals (serpentine, talc, and chlorite) occurring in core #5. The similar values and trends for both the parallel and perpendicular orientation are illustrated in Figure D-2. The material shows little anisoptropy as shown by the random variation between the two orientations. This is substantiated by the extremely small bulk density differences as indicated by the similar average values of 2.690 and 2.689 gm/cm^3 and the small standard deviation for both the parallel and perpendicular samples.

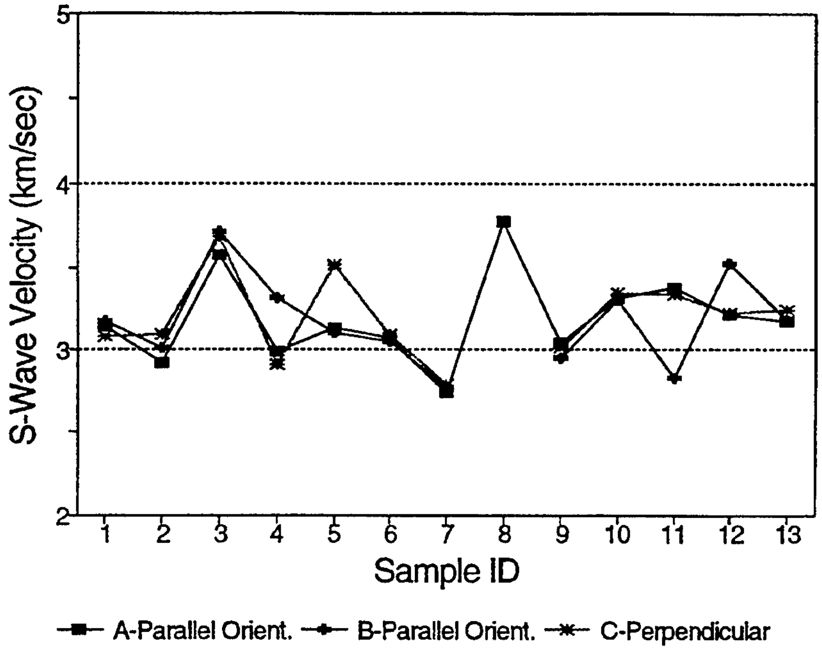

Figure D-2. Dry bulk density comparison of samples from the Linchburg mine.

Only minute differences (if any) occur between the effective and "true" grain densities determnined for both parallel and perpendicular samples. The average values are 2.702 and 2.704 gm/cm^3 for effective grain densities and 2.705 and 2.708 gm/cm^3 for true grain densities (standard deviations range from ±0.04 to ±0.05 gm/cm^3). The grain densities ranged from 2.644 to 2.873 gm/cm^3. Excluding core sample #5, the higher grain densities correlate well with a higher calcite content determined from XRD. Conversely, samples with a higher quartz content have lower grain densities. For example, core sample #8 had a quartz content of 75%, resulting in a relatively lower grain density (2.649 gm/cm^3). Slight differences in grain density may also be attributed to inhomogeneity (preferential sampling of sedimentary structure) caused by the sample orientation. The parallel samples can contain a number of laminations or "microstrata" (due to the orientation of the whole core with respect to the rock medium), which may be heterogeneous; whereas, the perpendicular samples are oriented along bedding and can contain a limited number of similar laminations or "microstrata". For example, if a core is interbedded with alternating calcite and quartz-rich layers, a perpendicular sample may be dominated by one or the other. In this scenario, the difference could be either 2.70 gm/cm^3 for calcite or 2.65 gm/cm^3 for quartz. A parallel sample will contain several layers depending on their thickness. As a result, the parallel sample will fall between 2.70 and 2.65 gm/cm^3. Hence, the slight differences between the two orientations may be attributed to localized mineralogical changes and not necessarily anisotropy.

As expected for dense carbonate rocks, porosity is very low. The parallel samples have effective porosities ranging from 0.01 to 1.48%, with an average value of 0.40%. The "total" porosity for the parallel samples is slightly higher with an average value of 0.54%. A somewhat higher porosity was determined for the perpendicular samples. The effective values range from 0.08 to 1.58% and average 0.51%. The total porosity averages approximately 0.67%. The occluded voids for both orientations range from 0 to 1.11% with an average of 0.11%.

Higher porosities were measured for core sample #5, regardless of sample orientation. Also, all of the total porosities were substantially higher than the effective porosities for core #5. This increase in porosity is reflected in the relatively higher occluded void content with values of 1.11%, 0.64%, and 0.79%. This sample was lithologically unique from the other samples due to the lack of carbonates and the occurrence of serpentine, talc and chlorite. As indicated in Figure D-3, reasonably consistent values of porosity were measured for the majority of the test samples.

D.8 ULTRASONIC VELOCITIES.

Ultrasonic velocities for both parallel and perpendicular specimens are illustrated in Figures D-4 and D-5. The P-wave and S-wave values are very consistent and there is typically little variation with orientation. The P-wave velocities measured on the parallel samples range from 4.86 to 6.09 km/s with an average of 5.40 km/s ±0.31 km/s. Similar P-wave velocities were

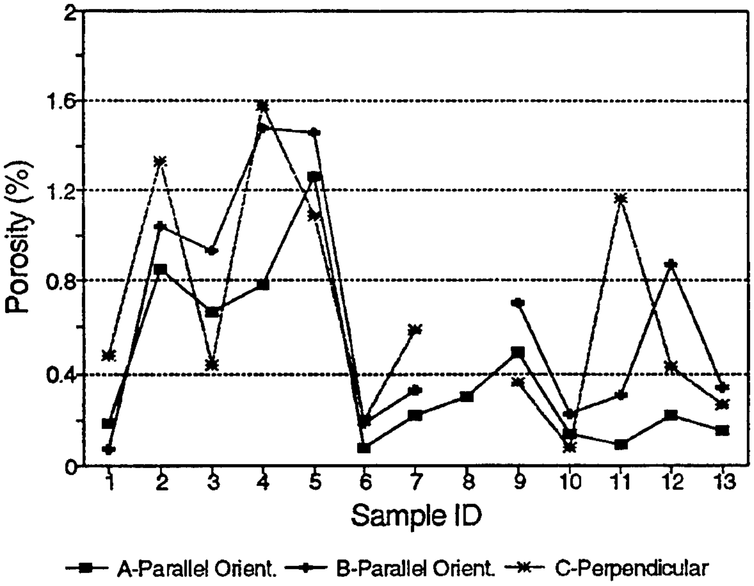

Figure D-3. Porosity comparison for samples from the Linchburg mine.

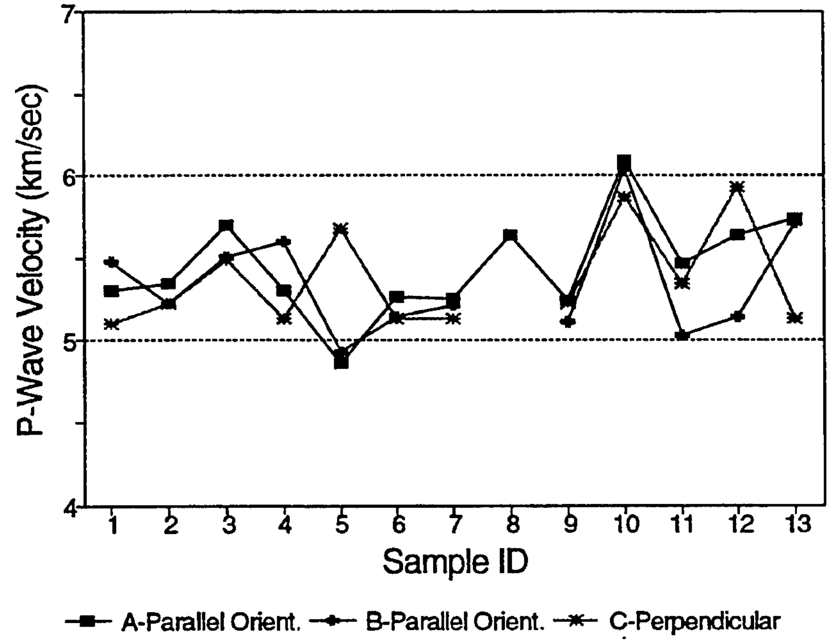

Figure D-4. P-wave velocities for material from the Linchburg mine.

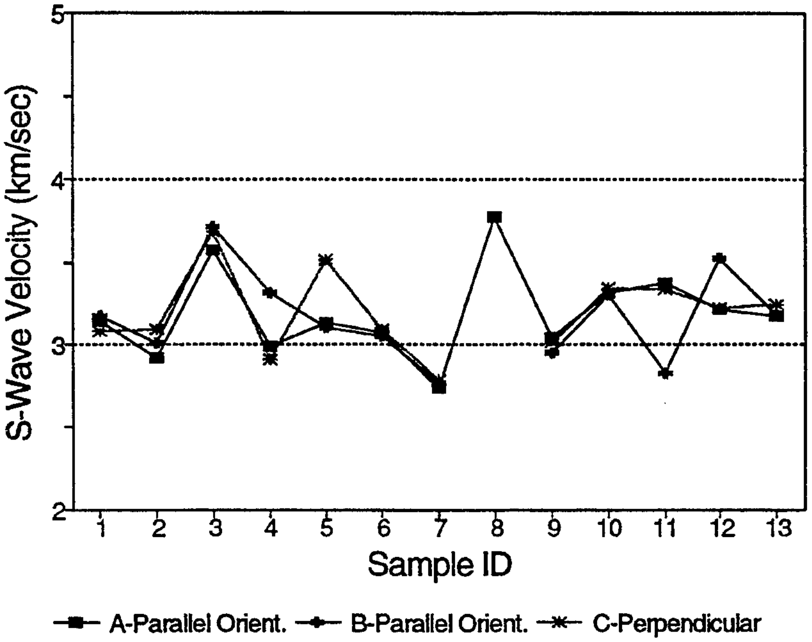

Figure D-5. S-wave velocities for material from the Linchburg mine.

determined for the perpendicular samples, which ranged from 5.10 to 5.94 km/s with an average of 5.37 km/s ±0.31 km/s. The parallel samples from core sample #5 had slightly lower velocities. The slightly lower values determined on the parallel samples from core #5 may be attributed to the direction of the wave front with respect to the orientation of the laminations. In this case, the compressional waves traveled normal to the laminations, resulting in a slower wave velocity. Furthermore, microfractures caused by laminae separations could also have led to a lower compressional wave velocity since these microfractures would be preferentially oriented perpendicular to the wave path. Conversely, the compressional wave travels along the laminations in the perpendicular samples. Hence, when laminations and bedding are present in the sample, a reduction in P-wave velocity is expected for orientations normal to the wave path. The silty/sandy mudstone (core #5) was the only sample exhibiting obvious laminations. The remaining test samples generally appeared massive, exhibiting healed joints and fractures at several orientations. As a result, the average P-wave velocities for the two orientations are exceptionally similar, with values of 5.40 and 5.37 km/s for the parallel and perpendicular samples, respectively.

Similar trends are shown for the S-wave velocities in Figure D-5. The S-wave velocity average is virtually the same for both orientations, with a value of 3.18 and 3.19 km/s ±0.26 km/s, respectively.

Average dynamic Young's modulus and Poisson's ratio are 66.6 GPa (±8.5) and 0.22 (±0.07), respectively, for the parallel samples. The dynamic Young's modulus and Poisson's ratio were essentially the same for the perpendicular samples, with average values of 66.9 GPa (±8.8) and 0.22 (±0.06), respectively. The dynamic bulk and shear moduli average 42.0 GPa and 27.4 GPa for the parallel samples and 40.9 GPa and 27.6 GPa for the perpendicular samples, respectively.

D.9 UNCONFINED COMPRESSION RESULTS.

Overall, the compressive strengths measured at ambient conditions varied from 53.6 to 161.6 MPa for the parallel samples and varied from 58.5 to 195.5 MPa for the perpendicular samples. Strengths determined for the silty/sandy mudstone (core #5) were low with values of 56.0 and 58.8 MPa. Other low strengths (e.g., 11A-||) were most likely attributed to pre-existing fractures. The variation in compressive strength is illustrated in Figure D-6. In many cases, as indicated in Table D-7 and Annex 6, strengths below 80 MPa were measured on samples exhibiting some sort of structural defect (pre-existing fractures, healed joints, heterogeneity, etc.).

Overall, the compressive strengths are fairly similar for both orientations, with average values of 100.8 MPa (±32.8 MPa) and 106.6 MPa (±41.2 MPa) for the parallel and perpendicular samples, respectively. There is a weak trend of slightly higher compressive strengths for the perpendicular samples (for eight of twelve test samples). It should be noted that if structural flaws (healed joints etc.) were avoided during preparation the strengths would be considerably higher for many samples. The averages reported were determined from samples that were randomly prepared (i.e. healed joints were not avoided). Hence, it is anticipated that the averages are probably representative of the strata in the vicinity of the test chambers.

Poisson's ratio determined for the parallel samples averaged 0.24 ±0.07, ranging from 0.14 to 0.44. Similar values for Poisson's ratio were determined for the perpendicular samples which range from 0.12 to 0.38 (average of 0.25 ±0.08).

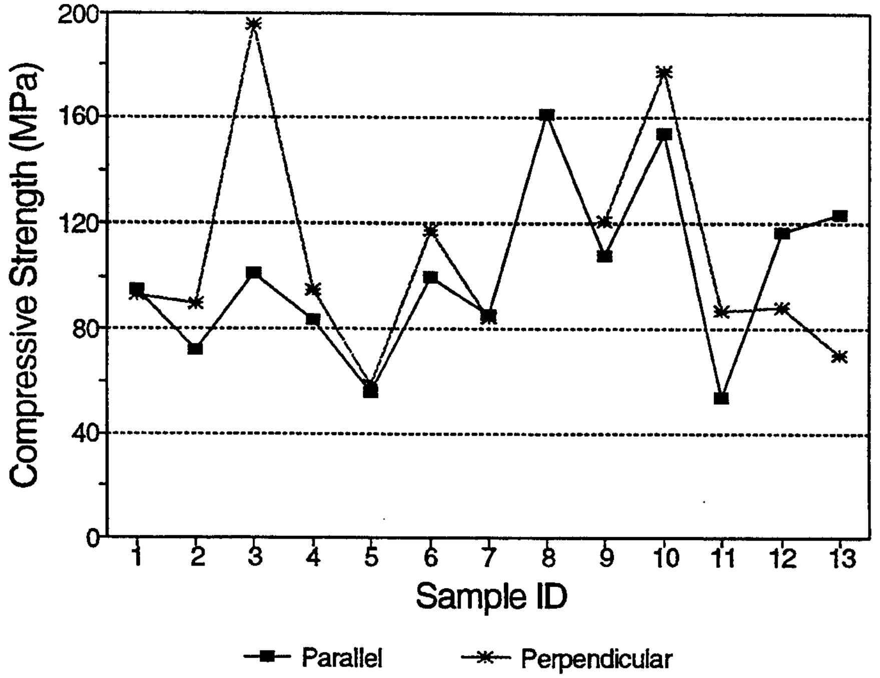

Figure D-6. Unconfined compressive strengths for material from the Linchburg mine.

For the most part, consistent values of Young's modulus were determined for both test sample orientations. Young's modulus for the parallel samples ranges from 30.3 to 72.7 GPa and averages 55.0 GPa (±10.3 GPa). Young's modulus for the perpendicular samples ranges from 30.0 to 70.6 GPa and averages 52.9 GPa (±12.4 GPa). Differences in Young's modulus between the two orientations are attributed to fractures, with one exception. The silty/sandy mudstone (core #5) had significant differences in moduli for the two orientations. For this particular rock these differences in moduli are, attributed to the orientation of the laminations. The axial load was applied normal to the laminations for the parallel sample. Hence, in this instance, it is easy to visualize more strain due to compacting laminations. Since more strain occurs due to the probable compaction of the laminations, a lower Young's modulus is calculated.

The static bulk and shear moduli showed less variation between orientations, with the parallel samples averaging 39.0 and 22.3 GPa, and the perpendicular samples averaging 39.7 and 21.3 GPa, respectively.

Significant and important differences are seen between the static and dynamic mechanical properties. The dynamic values are predominantly higher then their static counterparts. The dynamic Young's moduli average approximately 1.2 to 1.3 times higher than the static values for the parallel and perpendicular sample sets, respectively.

The differences observed in dynamic versus static properties may be attributed to the degree of elastic versus non-recoverable response of the material tested. The dynamic moduli primarily sense an elastic response to extremely low stresses and strains. The static moduli are based on a more elastic/permanent deformation response to higher stresses and strains. Dynamic moduli over a continuous vertical profile, can theoretically be determined from sonic logging. The ideal scenario is a cross-correlation between static and dynamic laboratory values and logging values. This would allow routine logging procedures to be used (i.e. density and velocity logs), with correlation of the logging values as required.

D.10 UNIAXIAL STRAIN RESULTS.

As indicated in Table D-7, eleven uniaxial strain tests were performed on parallel oriented test samples. Test sample 12B was too short for testing and core sample #8 was of insufficient size for more than one test sample. Three of the eleven samples failed during uniaxial strain loading. Test samples 2A, 3B, and 11B were all heterogeneous, exhibiting multiple, pre-existing fractures. These pre-existing sample conditions contributed to sample failure during uniaxial strain loading.

The maximum axial stress difference reached during uniaxial strain loading ranged from 170.8 to 465.3 MPa. Permanent compaction following uniaxial strain and hydrostatic unloading ranged from 0 to 0.2%. Higher values of permanent computation correlates with higher values of axial stress difference. The maximum volumetric strain measured ranged from 0.5 to 2.1% (maximum volumetric strain typically occurs at the maximum mean normal stress during uniaxial strain loading).

Bulk, apparent constrained, and shear moduli were determined from both the loading and unloading stress-strain curves. For dense material, such as the material from the Linchburg mine, the loading bulk modulus was determined from between zero and the peak mean normal stress (mean normal stress versus volumetric strain). The unloading bulk modulus was determined from the peak mean normal stress to a mean normal stress level where hydrostatic unloading began. The loading and unloading apparent constrained modulus were calculated from the axial stress versus axial strain curves. For both the loading and unloading segments, the slope of the line occurring between approximately 100 MPa and the peak axial stress was used. The loading and unloading shear modulus was determined from the axial stress difference versus the strain difference curves. The loading shear modulus was determined between approximately 50% and the peak axial stress difference, and the unloading shear modulus was calculated between the peak axial stress difference and approximately 50% of the unloading curve.

The loading and unloading bulk moduli ranged from 28.5 to 55.0 GPa and 36.3 to 60.1 GPa, respectively. The loading apparent constrained modulus ranged from 46.3 to 71.0 GPa and the unloading apparent constrained modulus ranged from 61.4 to 88.2 GPa. The loading and unloading shear moduli ranged from 5.5 to 19.6 GPa and 41.3 to 57.3 GPa, respectively.

Annex 6
Test Sample Identification and Initial Condition

Table D-8. Test Sample Identification and Initial Condition.

Core # ID	Test Plug ID	Comments/Initial Condition
#1 Ch. 4 Hole 2	1A-||	Dense limestone - minor fractures (healed with probable calcite), fairly homogeneous, coarse grained.
	1B-||	Dense limestone - minor fractures (healed with probable calcite), fairly homogeneous, coarse grained.
	1C-⊥	Dense limestone - heterogeneous, 1/3 sample is fine-grained and 2/3 coarse. Healed fracture along contact between fine and coarse grained material.
#2 Ch. 4 Hole 2	2A-||	Dense limestone - multiple fractures at various angles (partially healed), fairly homogeneous, coarse grained.
	2B-||	Dense limestone - multiple fractures at various angles (partially healed), fairly homogeneous, coarse grained.
	2C-⊥	Dense limestone - fractures oriented sub-parallel to plug axis (partially healed), heterogeneous, coarse grained with chert nodules.
#3 Ch. 2 Hole 4	3A-||	Partially silicified limestone - multiple fractures (healed with calcite?) at various angles, medium to coarse grained, heterogeneous.
	3B-||	Partially silicified limestone - multiple fractures (healed with calcite?) at various angles, heterogeneous, fine to coarse grained.
	3C-⊥	Partially silicified limestone - multiple fractures (healed with calcite?) at various angles, heterogeneous, fine to coarse grained.
#4 Ch. 4 Hole 3	4A-||	Dense limestone - minor healed fractures at various angles, homogeneous, coarse grained.
	4B-||	Dense limestone - minor healed fractures at various angles, homogeneous, coarse grained.
	4C-⊥	Dense limestone - fractures sub-parallel to plug axis (healed with calcite?), homogeneous, coarse grained.
#5 Ch. 7 Hole 3	5A-||	Interbedded mudstone - layers of silt, mud, and sand oriented sub-perpendicular to plug axis, heterogeneous, millimeter clasts abundant.
	5B-||	Interbedded mudstone - layers of silt, mud, and sand oriented sub-perpendicular to plug axis, heterogeneous, clasts.
	5C-⊥	Interbedded mudstone - layers of silt and mud and sand oriented sub-parallel to plug axis, heterogeneous, minor fractures, clasts.

Table D-8. Test Sample Identification and Initial Condition. (Continued)

Core # ID	Test Plug ID	Comments/Initial Condition
#6 Ch. 2 Hole 3	6A-∥	Dense limestone - minor fractures (healed with probable calcite) sub-parallel to plug axis, homogeneous, medium grained.
	6B-∥	Dense limestone - minor fractures (healed with probable calcite) sub-parallel to plug axis, homogeneous, medium grained.
	6C-⊥	Dense limestone - minor fractures (healed with probable calcite) at various angles to plug axis, homogeneous, medium grained.
#7 Ch. 2 Hole 1	7A-∥	Dense limestone - minor fractures at various angles (healed with calcite?), homogeneous, coarse grained.
	7B-∥	Dense limestone - fractures at various angles (healed with calcite?), heterogeneous, fine to coarse grained.
	7C-⊥	Dense limestone - fractures oriented sub-perpendicular to plug axis (healed with calcite?), heterogeneous, fine to coarse grained.
#8 Ch. 1 Hole 5	8A-∥	Silicified limestone - fractures at various angles (healed with calcite?), fairly homogeneous, fine to medium grained.
#9 Ch. 3 Hole 5	9A-∥	Dense limestone - minor fractures at various angles, fairly homogeneous, medium to coarse grained.
	9B-∥	Dense limestone - fractures at various angles (healed with calcite?), heterogeneous, fine to medium grained with chert nodules.
	9C-⊥	Dense limestone - minor fractures at various angles, homogeneous, fine to medium grained.
#10 Ch. 3 Hole 4	10A-∥	Dense limestone - minor fractures at various angles, fairly homogeneous with predominantly fine grained material, coarser material consisting of lithic clasts and chert lenses observed.
	10B-∥	Dense limestone - large fracture at 30° to plug axis (calcite healed), fairly homogeneous with predominantly fine grained material, coarser material (lithic clasts and chert) observed.
	10C-⊥	Dense limestone - minor fractures sub-perpendicular to plug axis, fairly homogeneous, dominantely fine grained with minor amounts of coarse material.

Table D-8. Test Sample Identification and Initial Condition. (Continued)

Core # ID	Test Plug ID	Comments/Initial Condition
#11 Ch. 2 Hole 3	11A-||	Partially silicified dense limestone - fractures at various angles (partially healed with probable calcite), heterogeneous with fine and coarse grained material.
	11B-||	Silicified dense limestone - fractures at various angles (healed with probable calcite), heterogeneous with two distinct layers sub-parallel to plug axis. One layer is silicified and the other is calcareous.
	11C-⊥	Chert - fractures at various angles (partially healed with calcite?), heterogeneous with coarse carbonate clasts and chert nodules.
#12 L.H. Drift Hole 4	12A-||	Dense limestone with chert - fractures at various angles (healed with calcite?), heterogeneous with medium grained carbonates and substantial chert clasts.
	12B-||	Dense limestone with chert - fractures at various angles (healed with calcite?), heterogeneous, fine to medium grained carbonates and substantial chert clasts (short sample <25mm in length).
	12C-⊥	Dense limestone - fractures at various angles (healed with calcite?), heterogeneous, predominantly fine to medium grained carbonates with minor amounts of chert clasts.
#13 L.H. Drift Hole 1	13A-||	Dense limestone - minor fractures at various angles, fairly homogeneous, medium grained with minor amounts of chert clasts.
	13B-||	Dense limestone - fractures at various angles (healed with calcite?), fairly homogeneous, medium grained.
	13C-⊥	Dense limestone - fractures sub-perpendicular to plug axis, fairly homogeneous, medium grained.

Annex 7
Thin Section Micrographs and Descriptions

PLATE 1 (Page D-28)
Sample No. 1

A. Low-magnification overview of medium-to-coarsely crystalline crinoidal limestone. Large, unicrystalline crinoid fragments constitute the most abundant grain type, though less common bryozoan, bivalve, and coral fragments are also present. Grains are well cemented by calcitic, syntaxial overgrowth cement, leaving essentially no interparticle porosity. Crinoid fragments in the lower portion of view exhibit minor replacement by chert (light-brown patches). Plane-polarized light. (20X)

B. Higher-magnification view of crinoid (and a few bryozoan) fragments and syntaxial overgrowth cement. Original allochems are characterized by a "dirtier" appearance in comparison to "clean", inclusion-free overgrowths. Note that interparticle pores are thoroughly occluded by cement. Linear feature in the right portion of view is a thin, calcite-filled fracture. Plane-polarized light. (40X)

Sample No. 3

C. General overview of fractured chert illustrating how microcrystalline quartz has replaced what was once fossiliferous limestone (note possible fenestellid bryozoan in the center of view). Cross-cutting fractures are commonly filled with calcite (pink-stained) and finely crystalline, greenish clays. Larger fractures, not shown here, may contain cherty gouge fragments, in addition to cements. Disseminated calcite in the matrix could represent unreplaced original calcite or calcite that has replaced chert during and/or after fracturing. Lack of visible blue epoxy in this view indicates the tight, nonporous nature of the sample fabric. Plane-polarized light. (20X)

D. Higher-magnification view showing how quartz occurs as microcrystalline (cherty) replacement, pore- and fracture-filling megaquartz, and minor pore-filling chalcedony. Also shown are calcite-filled fractures and unreplaced biotic fragments. Original biotic fragments and other allochems include crinoid debris, bryozoans, bivalve fragments, and possible nonskeletal grains; in most cases, however, they are difficult to identify because of poor preservation of internal structure. Crossed nicols. (40X)

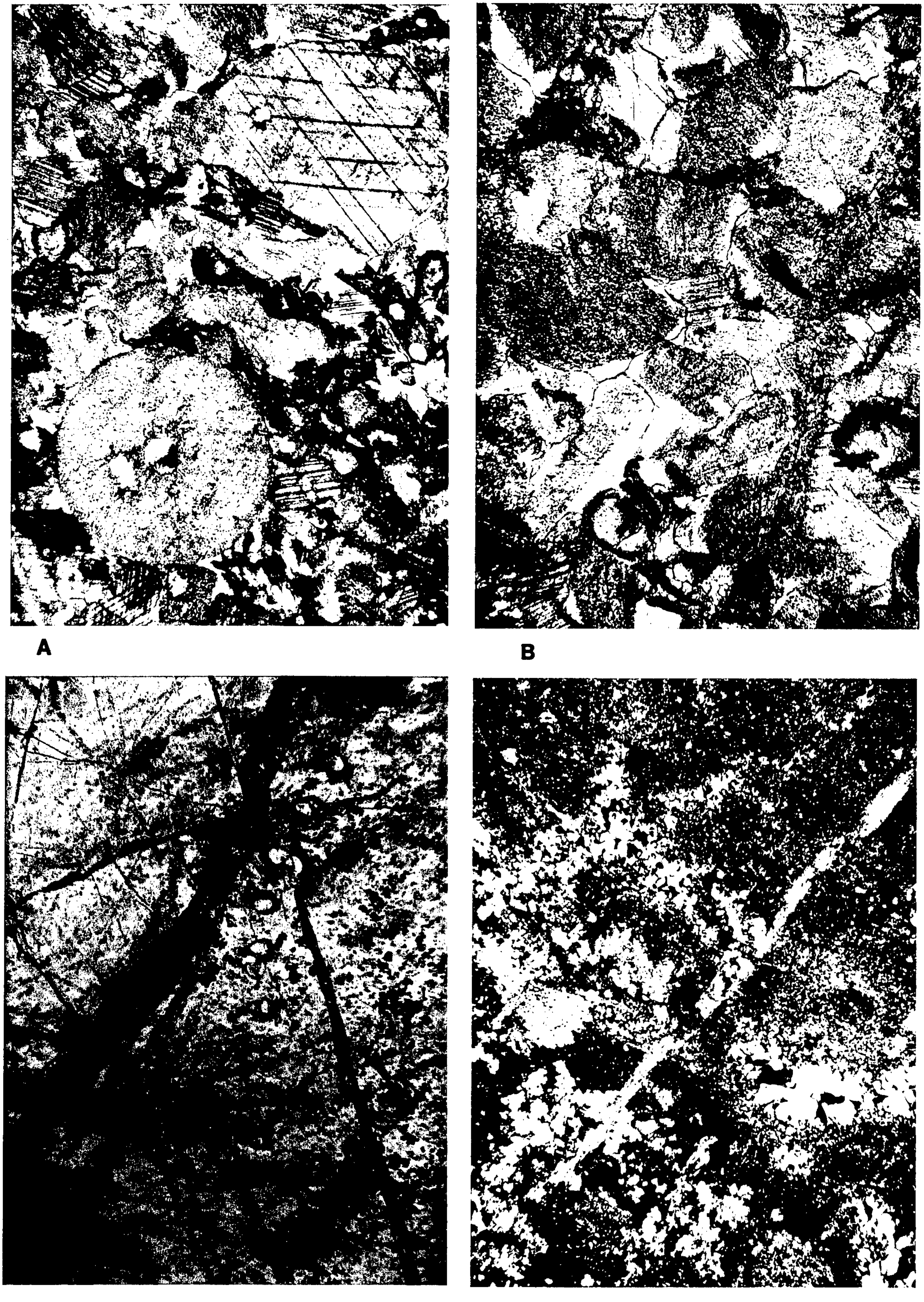
A
B
C
D

PLATE 2 (Page D-30)
Sample No. 4

A. General overview of coarsely crystalline, crinoidal limestone. Though crinoids are most pervasive, other grain types include bryozoan and bivalve fragments, and rare Foraminifera. Intense physical and chemical compaction has produced interpenetrative and sutured grains contacts and numerous microstylolites. The primary stylolite in the center of view has juxtaposed areas of differing grain size (lower portion of view is notably finer-grained). White, rounded patches are sites of replacement by chalcedony. Plane-polarized light. (40X)

B. Detailed view highlighting a crinoid fragment that has been partially replaced by microcrystalline quartz. Compaction of grains was less intense in this portion of the sample because grains are only somewhat flattened and syntaxial overgrowths are intact. Porosity in this sample is limited to thin, partially open microfractures. Crossed nicols. (40X)

Sample No. 5

C. Low-magnification overview of wavy-to-irregularly laminated, silty/sandy mudstone. Lamination is defined by alternation of thin beds of mudstone, siltstone, and very fine-grained sandstone. Wavy, convoluted texture and lenticular beds are most likely the result of both bioturbation and soft-sediment deformation. Porosity is restricted to microporosity associated with clay matrix and narrow dehydration fractures. Plane-polarized light. (20X)

D. Higher-magnification view of texture illustrating matrix-supported fabric and grain types. Grains are angular and poorly sorted, and are commonly composed of mono- and polycrystalline quartz, chert, possible glauconite (light-brown grains), shaly rip-up clasts, and accessory pyrite, zircon, and tourmaline. Larger, irregularly shaped grains are biotic fragments partially replaced by chert, illite/mica, and/or pyrite. Clay-rich matrix is most likely composed of mixed-layer illite-smectite. Plane-polarized light. (40X)

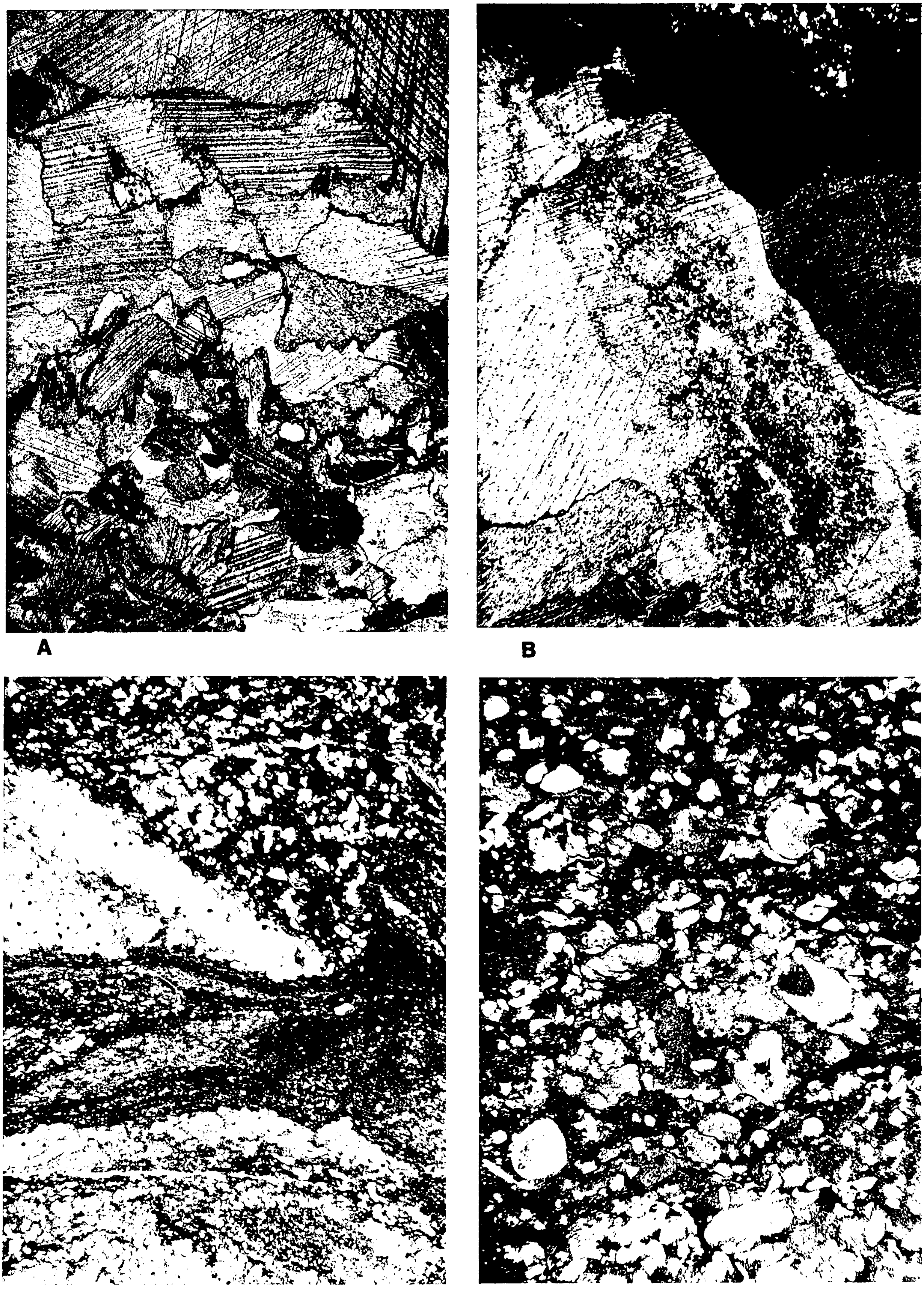
A
B
C
D

PLATE 3 (Page D-32)
Sample No. 6

A. Low-magnification overview of medium-to-coarsely crystalline limestone containing abundant crinoid debris and other fossil fragments. Interpenetrative-to-sutured grain contacts, stylolites, and microstylolites record intense grain compaction. Most interparticle calcite cement has been dissolved during chemical compaction and stylolitization. Note the lack of visible porosity in the sample fabric. Plane-polarized light. (20X)

B. Detailed view of unstained portion of the sample highlighting compaction features. Microstylolites are characterized by high amplitudes and thin residue seams, whereas better developed stylolites exhibit low amplitudes and thick residue seams. Flattened and irregular grain shapes also indicate intense compaction. Single-unit crystals are most likely echinoderms, and foliated or layered fragments are derived from bivalves. Plane-polarized light. (40X)

Sample No. 8

C. General overview of fossiliferous chert containing relict bryozoan fragments. Texture in this sample is similar to that in sample 3, where microcrystalline and chalcedonic quartz have thoroughly replaced bioclastic limestone. Numerous filled and partially filled natural fractures, three of which are shown here, also characterize this sample. Common fracture fillings include calcite, quartz, and clay. Isolated fracture porosity is the only porosity type visible in this view and throughout the sample. Plane-polarized light. (20X)

D. Higher-magnification view of pervasive chert replacement. Though most original skeletal fragments have been replaced, some remain calcitic, such as the large echinoderm fragment exhibiting high relief. The distribution of fibrous chalcedony indicates that it is most likely filling or replacing original intergranular pores. Note partially clay-filled fracture cross-cutting fabric in the center of view. Crossed nicols. (40X)

A

B

C

D

PLATE 4 (Page D-34)
Sample No. 9

A. Low-magnification overview of coarsely crystalline, fossiliferous limestone. General texture is similar to that in other limestone samples in this study, but contains more bryozoan debris in addition to crinoids, bivalves, ostracodes, ooids, and intraclasts. Sparry calcite occurs as an interparticle, syntaxial overgrowth cement and eliminates essentially all interparticle pore space. Compaction features are not nearly so well developed in this sample, and replacement by chert is very minor in extent. Plane-polarized light. (20X)

B. Detailed view of a coated intraclast containing biotic fragments and syntaxial overgrowth cement. Outside of intraclast, grains include crinoids, bryozoans, and bivalves well cemented by “cleaner” calcite spar. The lack of blue epoxy indicates the paucity of visible porosity in this sample. Plane-polarized light. (40X)

Sample No. 12

C. General overview of highly fractured chert exhibiting much of its original limestone texture. Darker patches represent replaced “ghosts” of original fossil fragments, such as crinoids and bryozoans. Parts of this sample have remained calcitic and unreplaced by quartz. Nature and orientation of cross-cutting microfractures indicate that several generations of fractures are present. Larger fracture in the center of view contains angular, cherty gouge material cemented by calcite. Narrower fractures exhibit some open porosity (blue). Plane-polarized light. (20X)

D. High-magnification view of fracture-filling material. Platy-to-fibrous green mineral is interpreted as clay; its fairly high birefringence and greenish-brown color suggest that it is an Fe/Mg-rich muscovite (phengite). Clay most likely precipitated after calcite. Note nearby microfracture and dissolution porosity. Plane-polarized light. (100X)

A

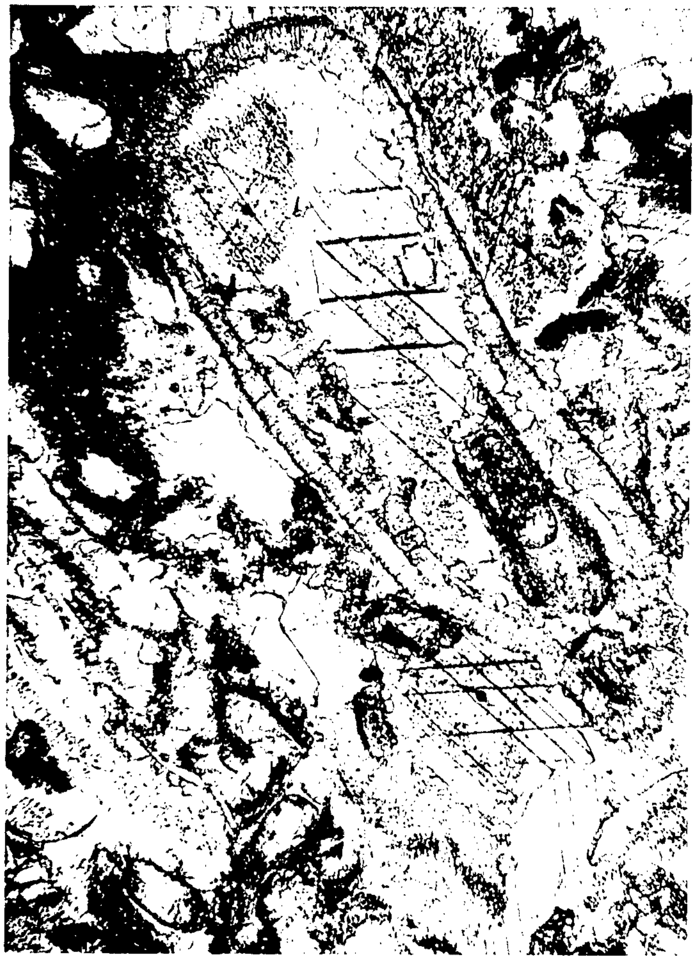

B

C

D

Annex 8
Test Procedures

XRD AND LITHOLOGIC EXAMINATION.

X-Ray Diffraction (XRD) was performed to quantify the mineralogy of eight of 13 core sections. The analysis was performed on representative one-gram splits of the bulk samples. XRD samples were ground in acetone in an agate mortar to <325 mesh (<45 microns). The powder was X-rayed at $2°2\theta$ per minute from 10 to $65°2\theta$, and $1°2\theta$ per minute from 2 to $10°2\theta$, using a Phillips XRG-3100 diffractometer. Duplicate samples were X-rayed to verify the existence of minerals detected in the original samples. Approximate weight percentages of individual minerals were determined by comparing diagnostic peak intensities with those generated by standard pure phases, mixed in various known proportions.

Lithologic examination, using hand samples and thin sections, was performed to distinguish textural and compositional variations in the eight samples. The thin sections were stained for calcite identification and were injected with blue epoxy for pore space detection. Photomicrographs were taken to illustrate sample fabric, including porosity, fossil content and mineralogy. These descriptions were conducted to compliment the measurements of mechanical properties as determined from the ultrasonic velocity present uniaxial compression and uniaxial strain testing. Hence, detailed descriptions characterizing specific fossils and depositional environments, were not performed.

PHYSICAL PROPERTY MEASUREMENTS.

As part of the initial material characterization, the effective grain density, dry bulk density and effective porosity were determined. Non-destructive physical property measurements were performed on each test specimen (parallel and perpendicular orientation).

Prior to any testing, each test specimen was oven dried at 105°C for a period of 24 hours. Bulk volume was determined using the mercury immersion technique. The bulk density was determined simply by dividing the mass of the test specimen by its bulk volume.

The effective grain volume was determined on each test specimen using the gas pycnometry technique. Gas pycnometry is based on Boyle's Law, which holds that, for a gas at constant temperature, the volume of the gas will vary inversely with the pressure:

$$\frac{P_1}{P_2} = \frac{V_2}{V_1} \qquad \text{(D.1)}$$

where:

P_1 is the initial pressure in V_1,
P_2 is the final pressure in V_2,
V_1 is the initial volume, and
V_2 is the final volume.

A calibration curve is constructed by measuring the volume of known, standard billets. The known volumes are, plotted against the ratio P_l/P_2 and a linear equation is fitted to the data. The recorded pressure ratio with a sample in the porosimeter is then used to determine the effective grain volume (V_g) from the calibration curve. The grain density is calculated as follows:

$$\rho_g = \frac{W}{V_g} \qquad \text{(D.2)}$$

where:

ρ_g is the grain density,
W is the pre-test weight, and
V_g is the grain volume determined from the porosimeter.

A fabricated gas expansion porosimeter is used at TerraTek, helium gas is used. The grain densities determined with gas pycnometry for intact plug specimens are effective grain densities, not total, as the gases only penetrate interconnected porosity. Hence, porosity derived from the effective grain density is an indication of interconnected porosity, not the true total porosity. In order to measure the specimen's total porosity, a supplementary destructive grain density technique is required.

Grain density was measured again on post-test specimens, also using gas pycnometry. Following the mechanical testing, each test specimen was reduced to a powder capable of passing through a 325 mesh sieve (<45 microns). A dried powdered sample (dried at 105°C for 16 to 24 hours), weighing between 25 and 35 grams (W_d), is placed into a cup which is inserted into the porosimeter vessel. The volume of the powder is determined as intact plug specimen. This yields true grain density.

Both the effective and the total porosity are calculated using the following relation:

$$\phi = 1 - \left(\frac{\rho_d}{\rho_g} \right) \tag{D.3}$$

where:

ϕ is the porosity (either effective or total),
ρ_d is the dry bulk density, and
ρ_g is the grain density (effective or true).

ULTRASONIC VELOCITY MEASUREMENTS.

Compressional (P) and shear (S) wave velocities were measured on all of the test specimens (parallel and perpendicular orientation) at bench conditions; specifically at a nominal axial stress of approximately 1 MPa. To measure the P and S-wave velocities, two piezoelectric (1 MHz) crystals were placed in mechanical contact with the sample, one at each end. A high voltage pulse of short duration was then applied to one of the crystals, using a pulse generator. This pulse was received by the crystal at the opposite end of the specimen. Based on the time required for the pulse to travel through the length of the specimen, the P and S-wave velocities were calculated. The formulae for calculating the dynamic properties are as follows[1]:

---

[1] Jaegar, J.C. and Cook, N.G.W., *Fundamentals of Rock Mechanics,* Chapman and Hall, pp. 183-187, 1979.

$$E_D = C_s^2 \rho \left[\frac{3\left(\frac{C_p}{C_s}\right)^2 - 4}{\left(\frac{C_p}{C_s}\right)^2 - 1} \right] \tag{D.4}$$

$$\nu_D = \frac{1}{2} \left[\frac{\left(\frac{C_p}{C_s}\right)^2 - 2}{\left(\frac{C_p}{C_s}\right)^2 - 1} \right] \tag{D.5}$$

$$K_D = \rho \left(C_p^2 - \frac{4}{3} C_s^2 \right) \tag{D.6}$$

$$G_D = C_s^2 (\rho) \tag{D.7}$$

where:

E_D	is Young's modulus,
ν_D	is Poisson's ratio,
K_D	is Bulk modulus,
G_D	is Shear modulus,
ρ	is Bulk density,
C_P	is Compressional velocity, and
C_s	is Shear velocity.

UNIAXIAL COMPRESSION TESTS.

After the physical and ultrasonic velocity measurements were performed, one of the parallel samples and the perpendicular sample were mechanically tested to determine unconfined compressive strength. In addition, elastic moduli were calculated from the measured deformation resulting from the applied axial stress. The Linchburg mine material is dominated by competent dense limestone. For several samples, it was anticipated that brittle castastrophic failure would ensue on reaching the maximum compressive strength of the material under unconfined conditions (zero confining pressure). Hence, for some samples, two loading cycles were performed to protect the transducers that measure axial and radial deformation. During the first cycle, axial and radial deformation were recorded up to an axial stress of 100 MPa on the first cycle. Prior to the second cycle, the axial stress was reduced to zero and the radial transducers (cantilevers) were removed. The sample was then loaded to failure. In most cases, the test sample unexpectedly failed prior to 100 MPa. Hence, stress-strain data exists to failure for these samples. Axial stress for both loading cycles was increased using a servo-controlled axial strain rate of 1 x 10^{-5}/s. Axial strain, radial strain and axial stress were recorded continuously (where applicable) through both loading cycles, using a digital data acquisition system.

UNIAXIAL STRAIN TESTS.

Uniaxial Strain: An axial compressive stress was applied such that a constant axial strain rate was maintained while the confining pressure was varied to maintain zero radial strain. The load piston was reversed when the confining pressure reached a prescribed value and the sample was unloaded to a hydrostatic stress state while maintaining the zero radial strain condition. The hydrostatic stress was typically unloaded to zero pressure at a nominal rate of 1.4 MPa/s. The loading and unloading constrained modulus, bulk modulus, and shear modulus, and the permanent compaction were typically determined.

Specific parameters were calculated from the uniaxial strain tests. For completeness, some of the more common terms are defined as follows.

> **Maximum volumetric strain.** The maximum volumetric strain occurring during a uniaxial strain test usually occurs at the maximum mean normal stress level (confining pressure of about 400 MPa). Under uniaxial strain conditions, the volumetric strain is represented by the axial deformation since radial strain is prevented.
>
> **Measured permanent compaction (MPC).** This is the "permanent" volumetric strain existing after a load-unload cycle following a uniaxial strain test, to a maximum lateral stress of 400 MPa. This is the non-recoverable deformation following a uniaxial strain test and is directly related to the volume of air-filled voids (void collapse due to shear enhanced compaction) occurring in the sample prior to testing.

Loading bulk modulus. This is the slope of the line on the mean normal stress versus volumetric strain curve from a point on the curve which is vertically above the measured permanent compaction and extending to the maximum mean normal stress. This region of the loading curve is primarily influenced by the intrinsic properties of the solid material (most of the air-filled voids are presumably crushed).

Unloading bulk modulus. This is the slope of the line on the mean normal stress versus volumetric strain curve extending from the maximum mean normal stress to a point at which hydrostatic unloading begins (axial stress difference of zero).

Loading apparent constrained modulus. This is the slope of the line on the axial stress versus axial strain curve extending from a point on the loading curve that occurs vertically above where the axial stress equals zero on the unloading curve to the maximum axial stress.

Unloading apparent constrained modulus. This is the slope of the line on the axial stress versus axial strain curve extending from the maximum axial stress to a point on the unloading curve where hydrostatic unloading begins.

Loading shear modulus. This is the slope of the line on the axial stress difference versus strain difference curve extending from approximately 50% of the measured strain during loading to the maximum stress difference.

Unloading shear modulus. This is the slope of the line on the axial stress difference versus strain difference curve extending from the maximum stress difference to a point in the curve at approximately 50% at the stress difference during unloading curve.

Maximum axial stress difference. This is the maximum stress difference usually occurring at the peak lateral stress (400 MPa) during a uniaxial strain test.

Annex 9
Stress-Strain Plots
Unconfined Compression Tests

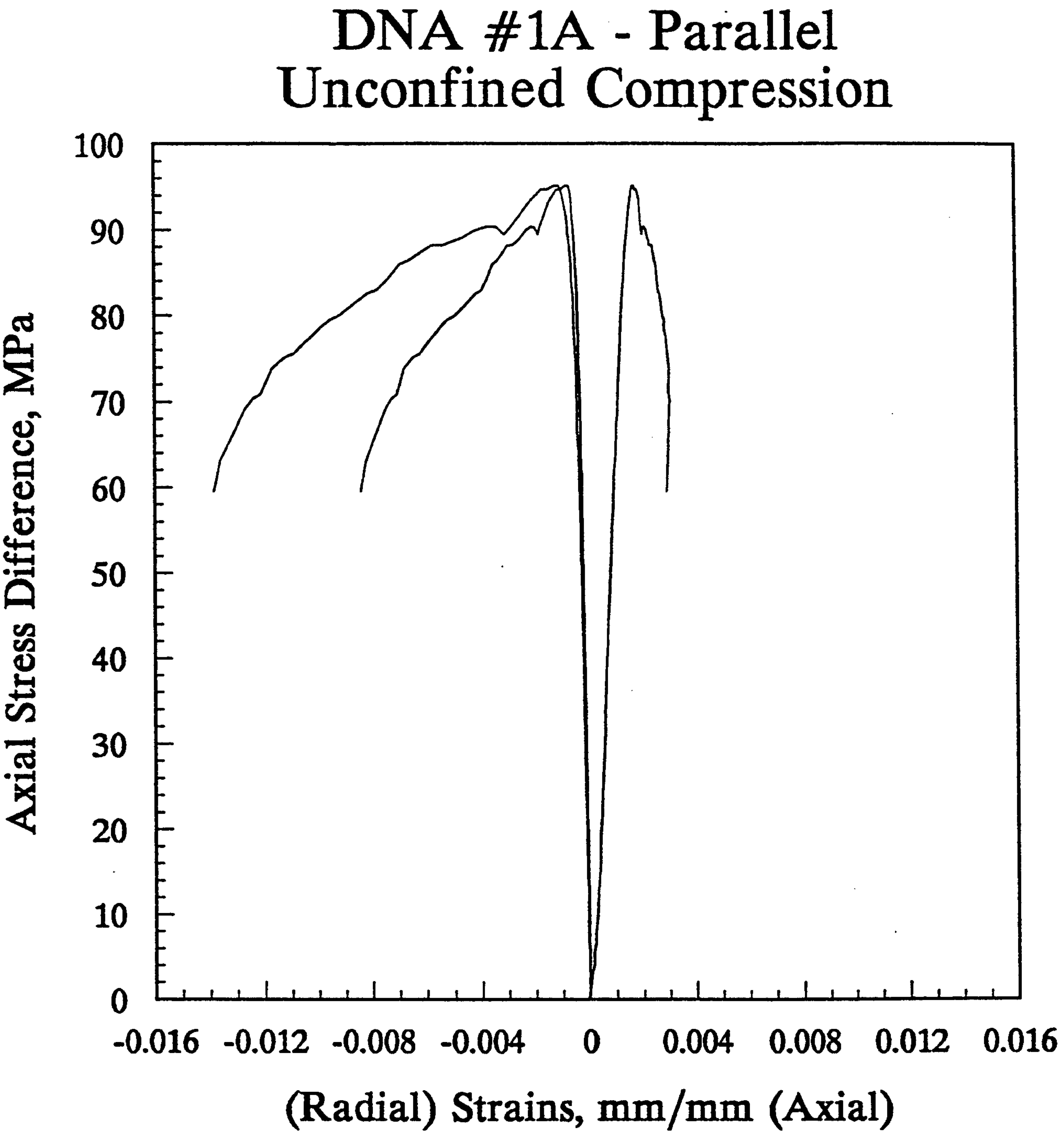

Figure D-7. Stress versus strain during unconfined compression for sample #1A - Parallel.

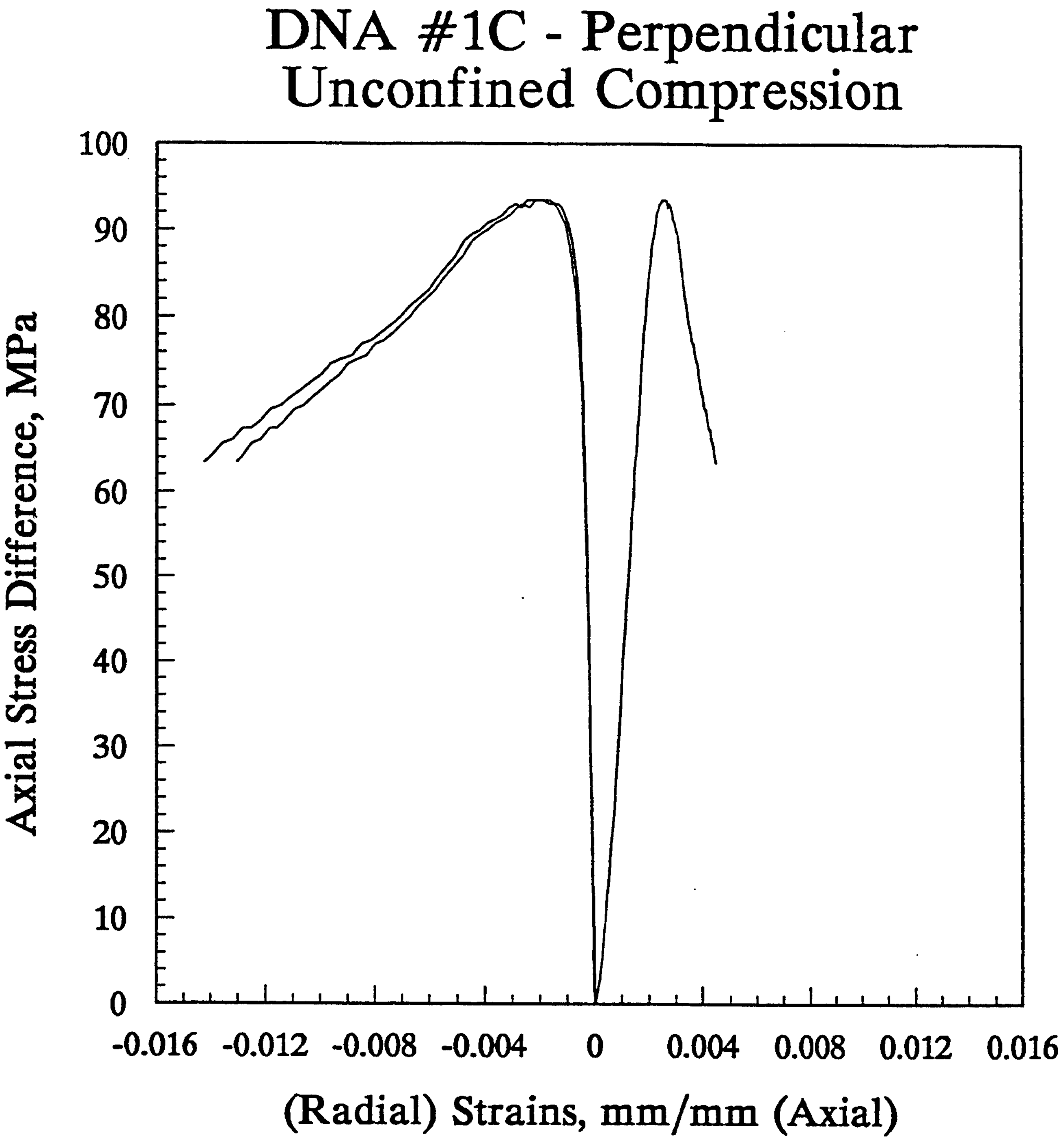

Figure D-8. Stress versus strain during unconfined compression for sample #1C - Perpendicular.

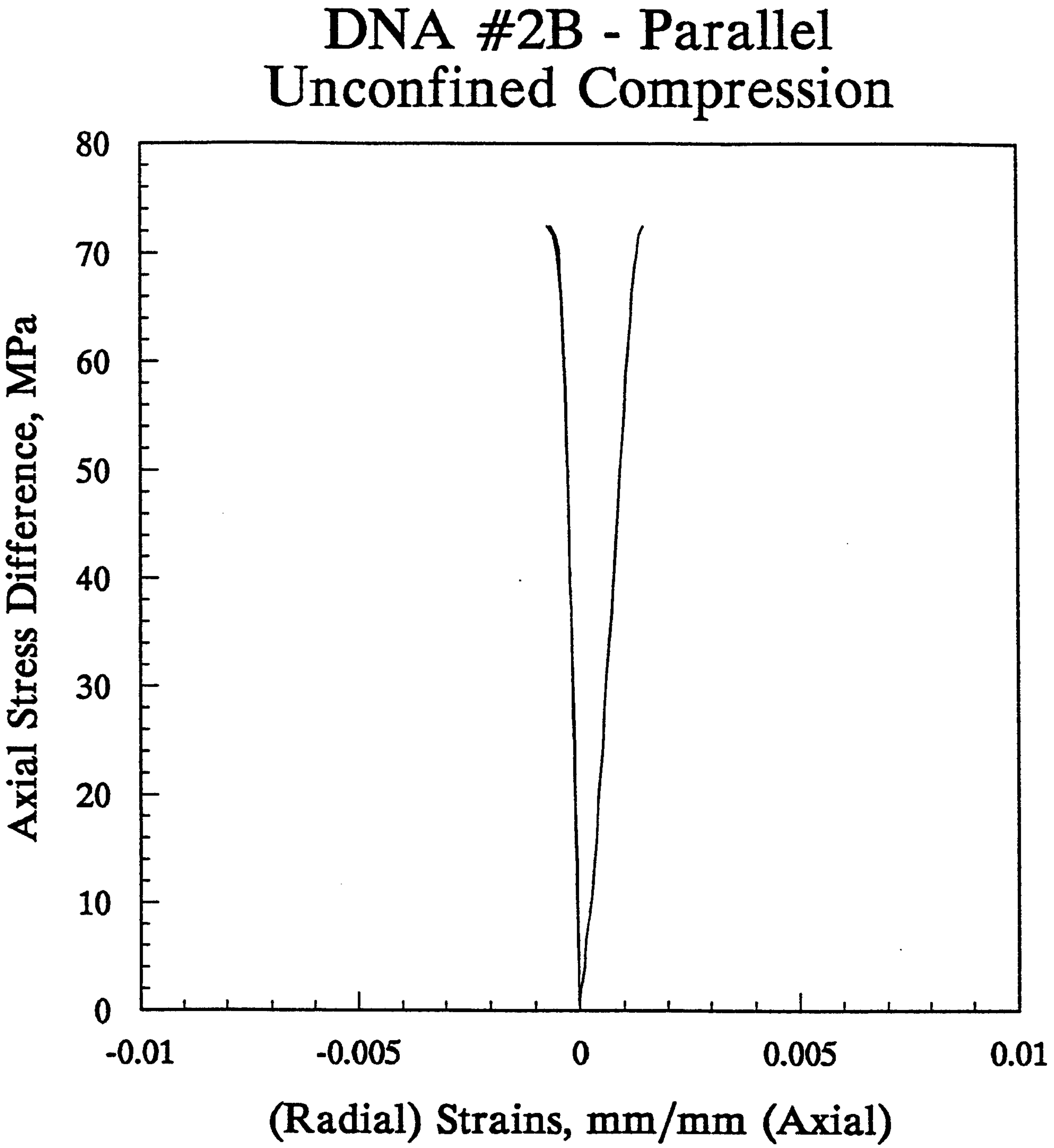

Figure D-9. Stress versus strain during unconfined compression for sample #2B - Parallel.

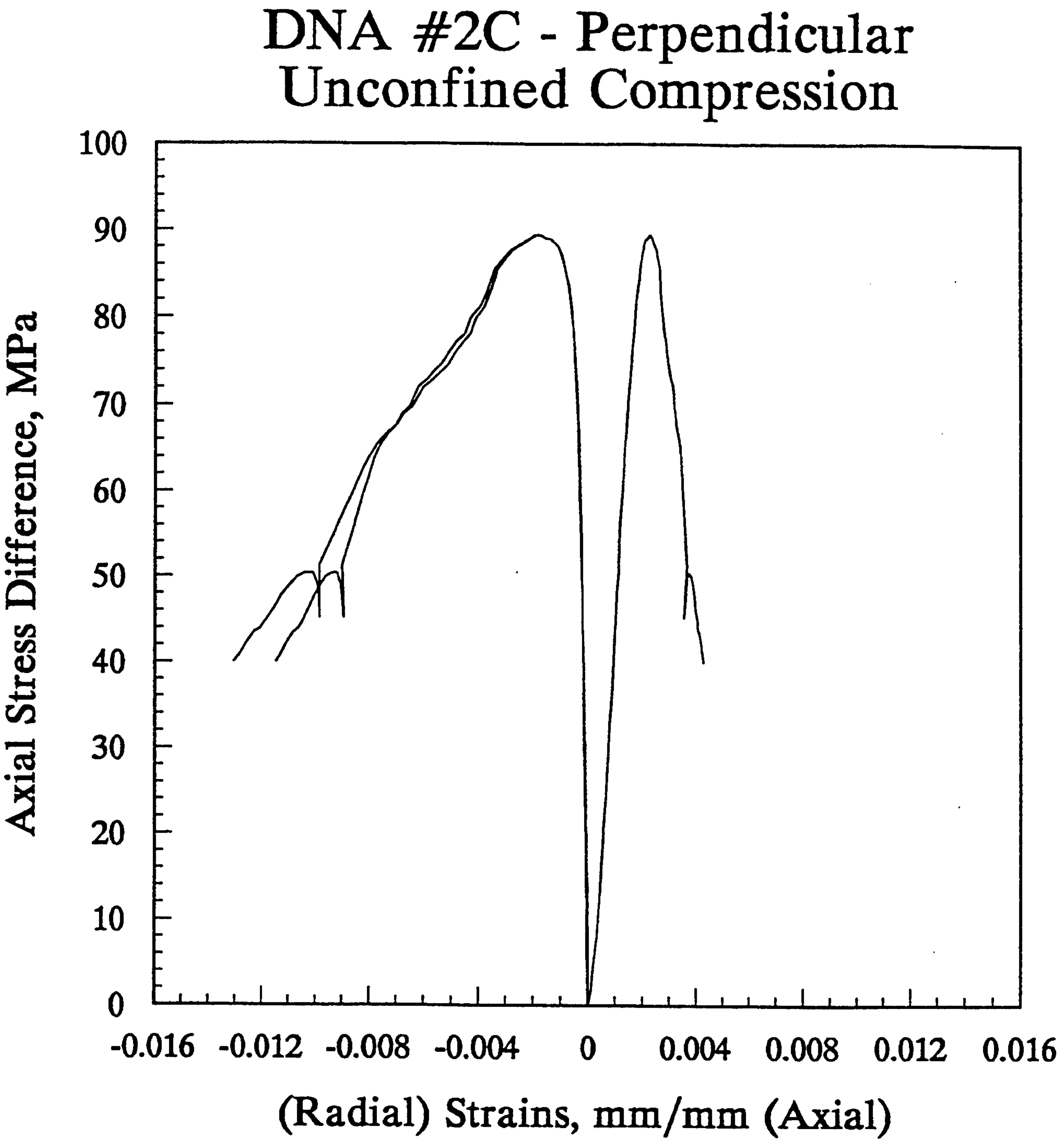

Figure D-10. Stress versus strain during unconfined compression for sample #2C - Perpendicular.

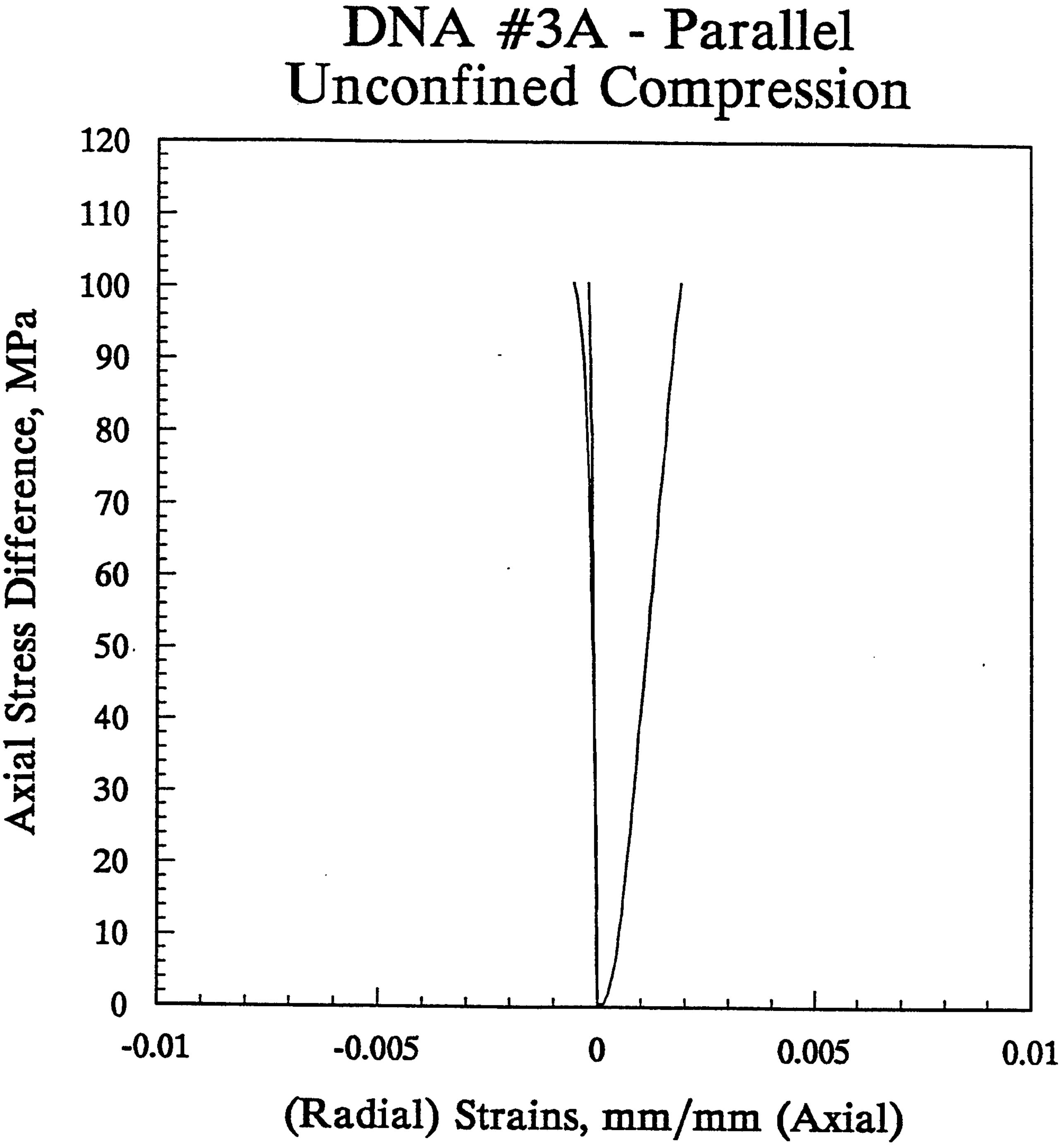

Figure D-11. Stress versus strain during unconfined compression for sample #3A - Parallel.

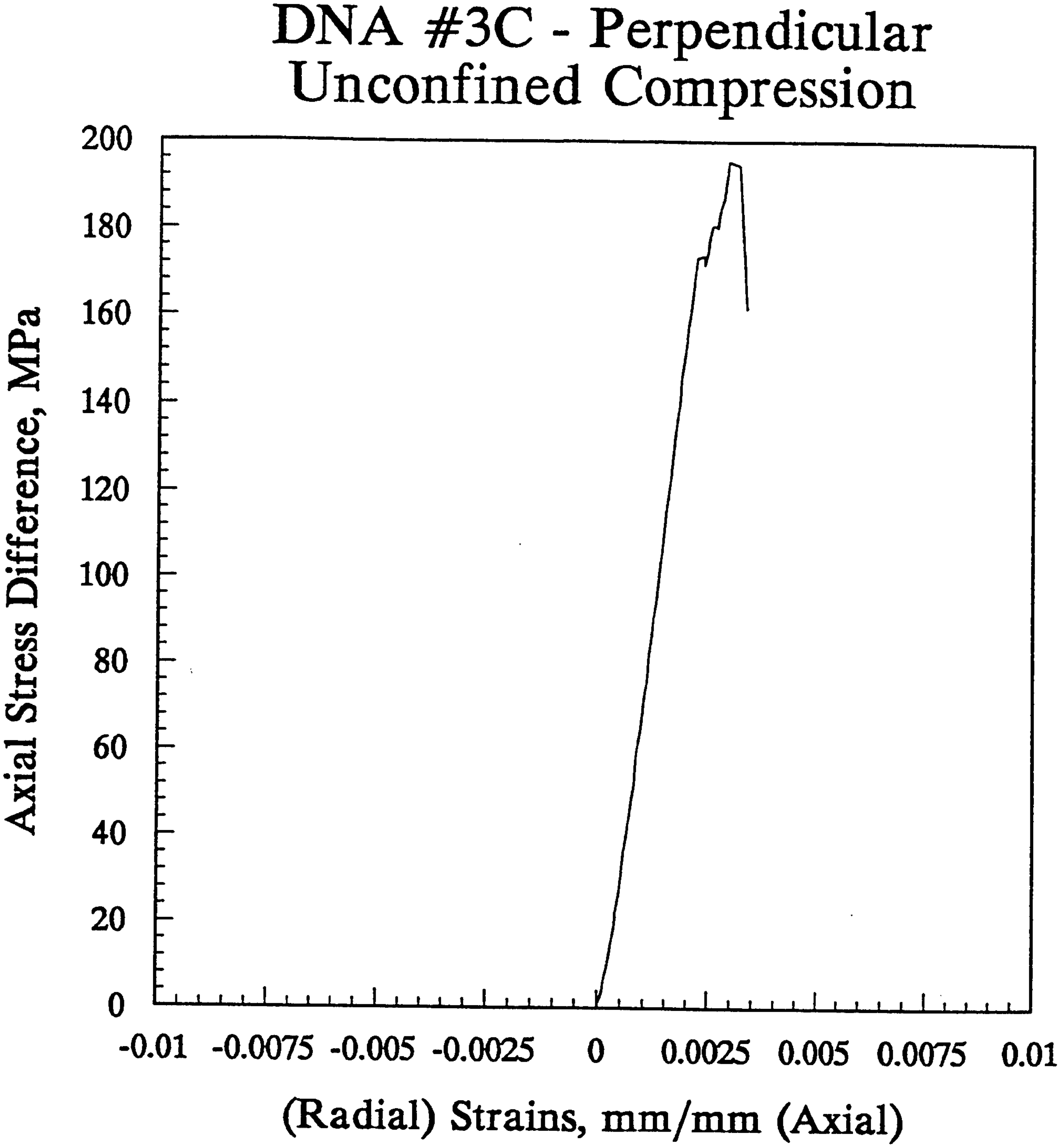

Figure D-12. Stress versus strain during unconfined compression for sample #3C - Perpendicular.

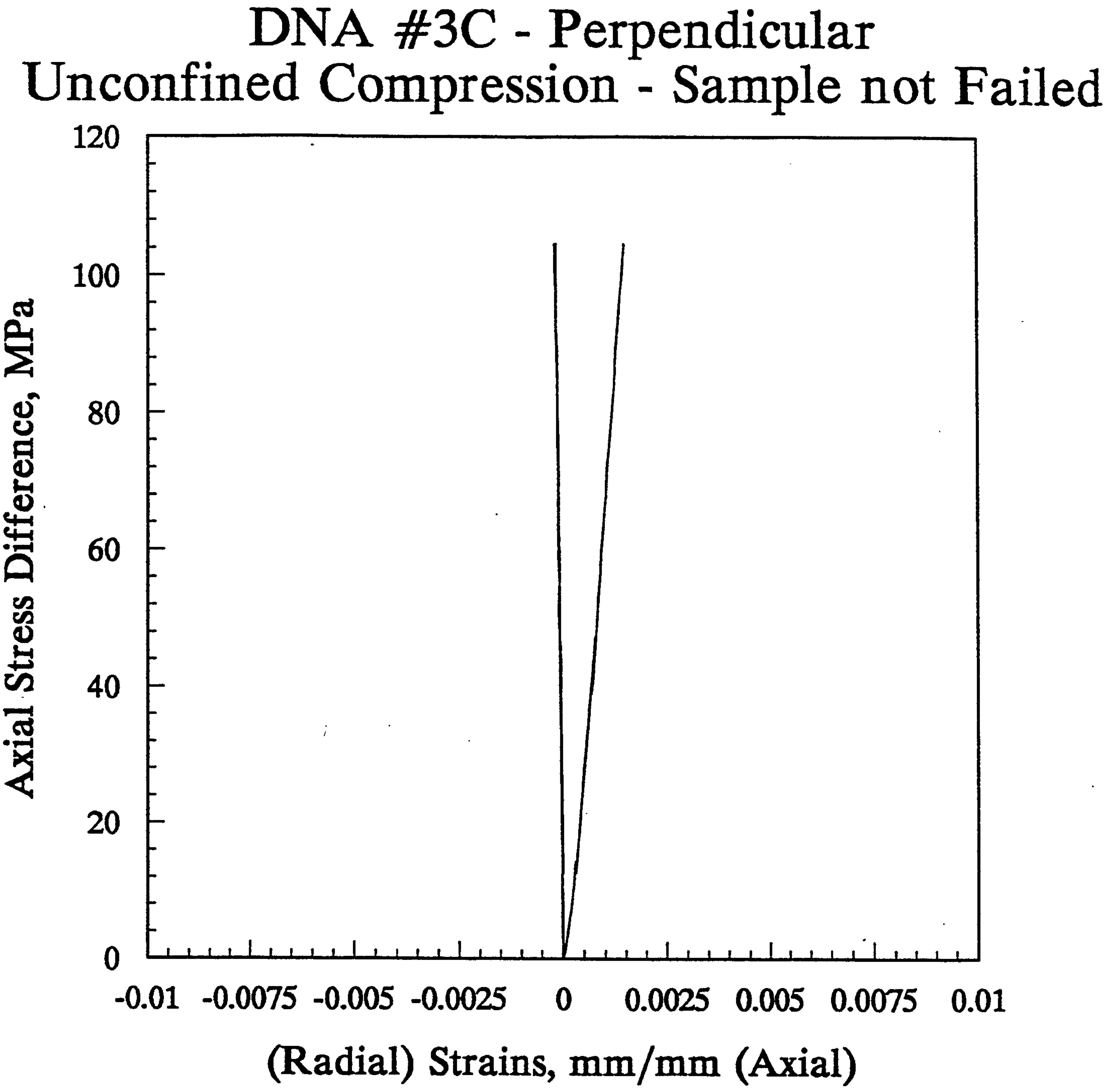

Figure D-13. Stress versus strain during unconfined compression for sample #3C - Perpendicular.

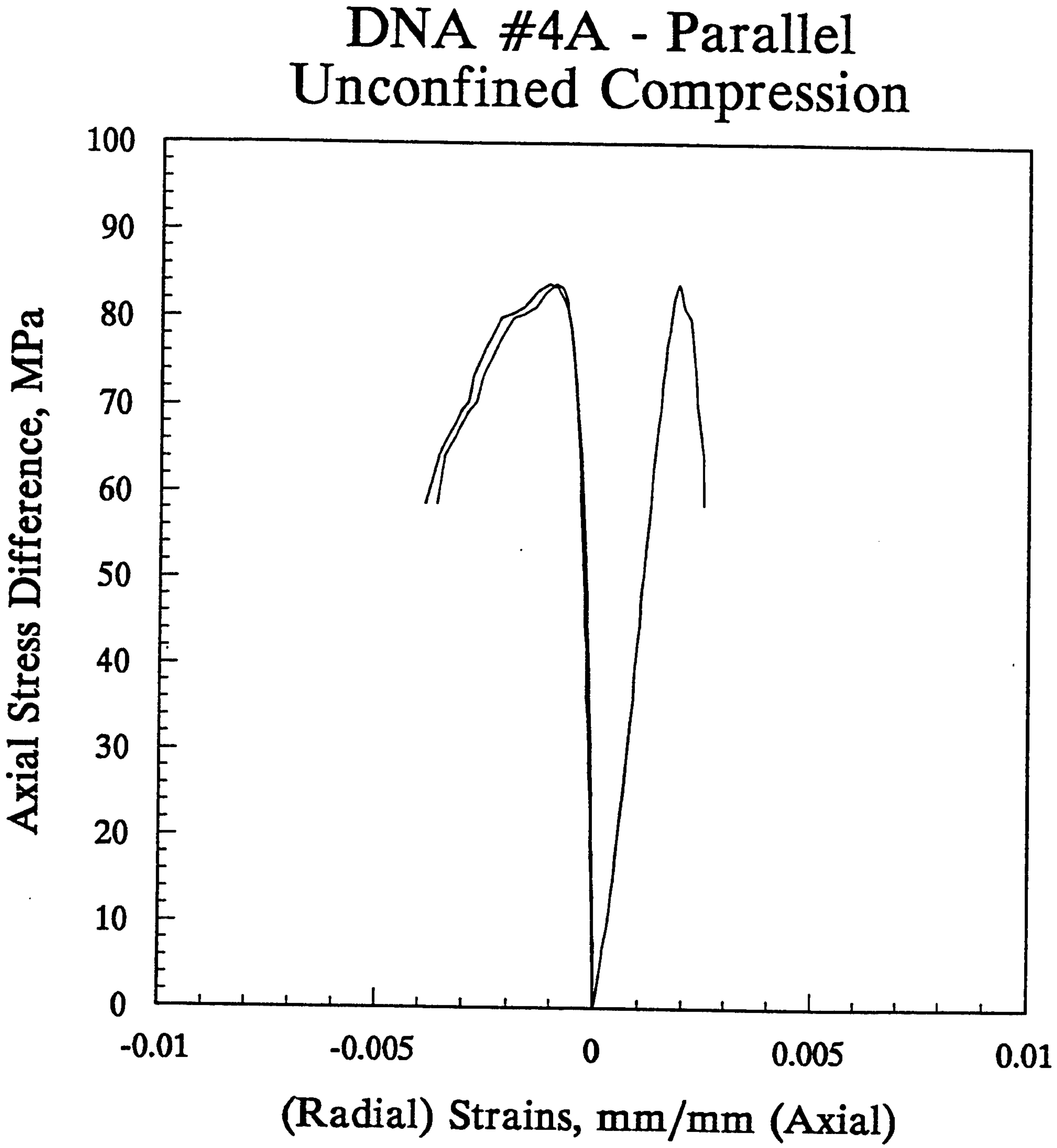

Figure D-14. Stress versus strain during unconfined compression for sample #4A - Parallel.

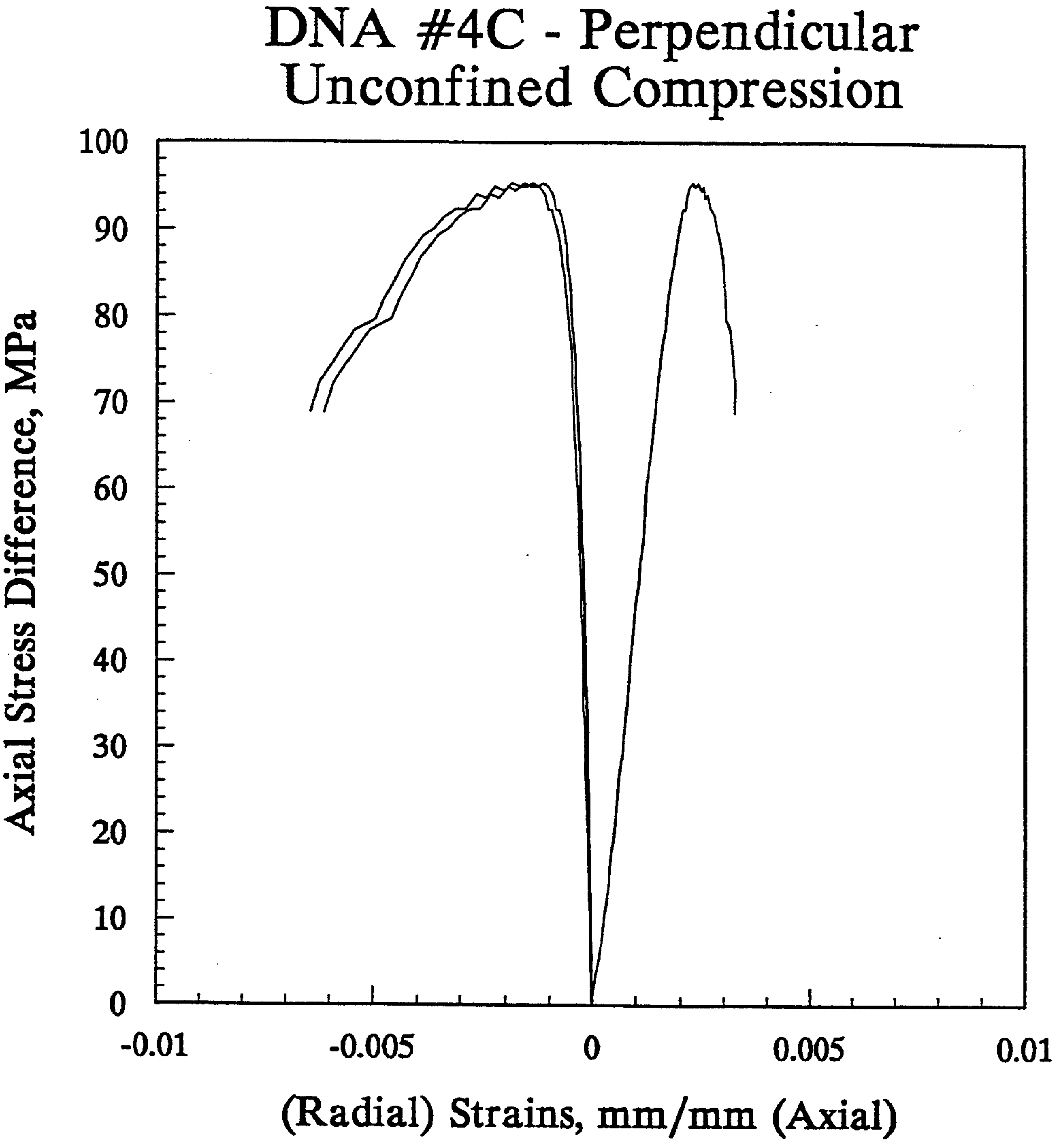

Figure D-15. Stress versus strain during unconfined compression for sample #4C - Perpendicular.

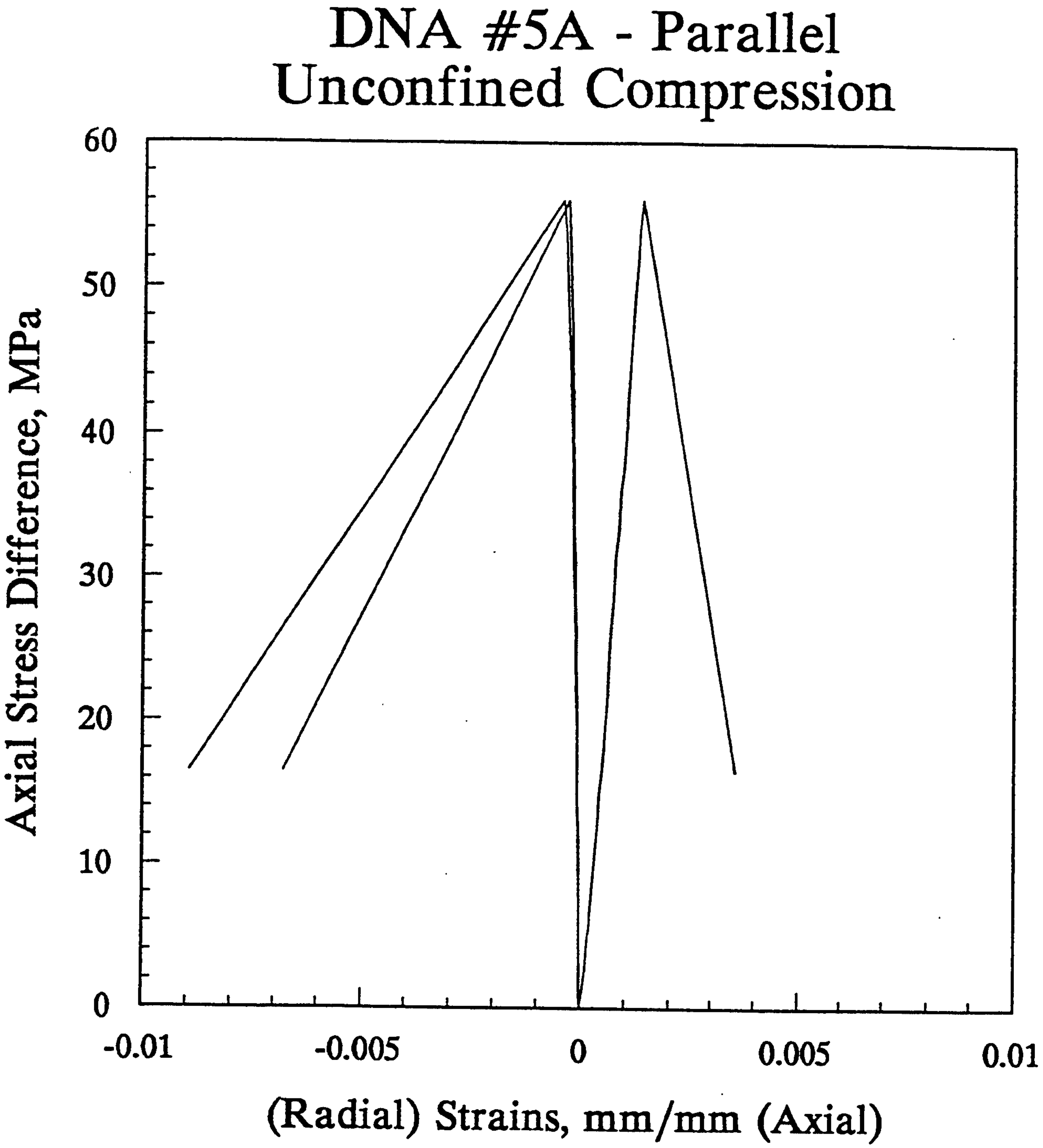

Figure D-16. Stress versus strain during unconfined compression for sample #5A - Parallel.

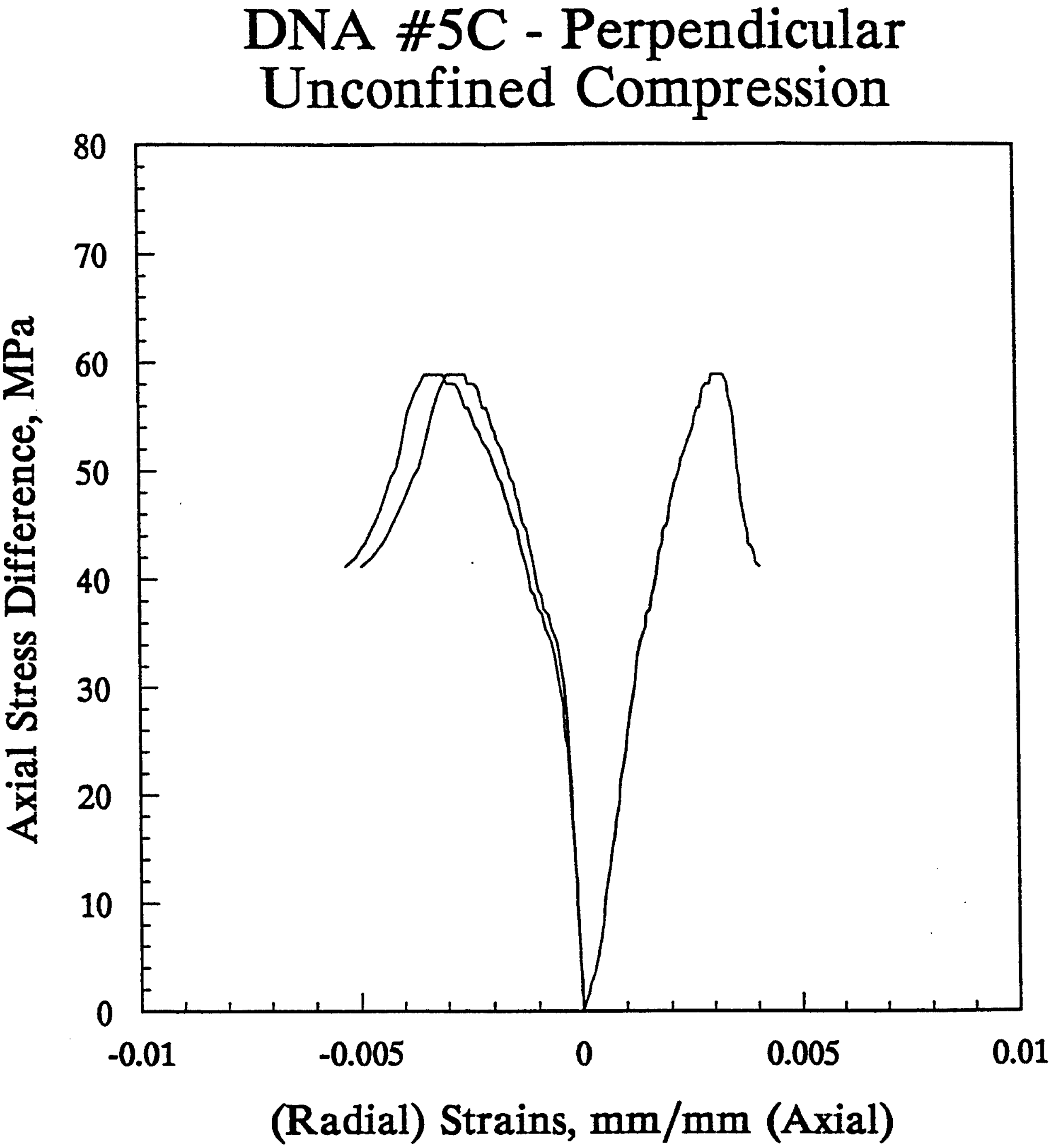

Figure D-17. Stress versus strain during unconfined compression for sample #5C - Perpendicular.

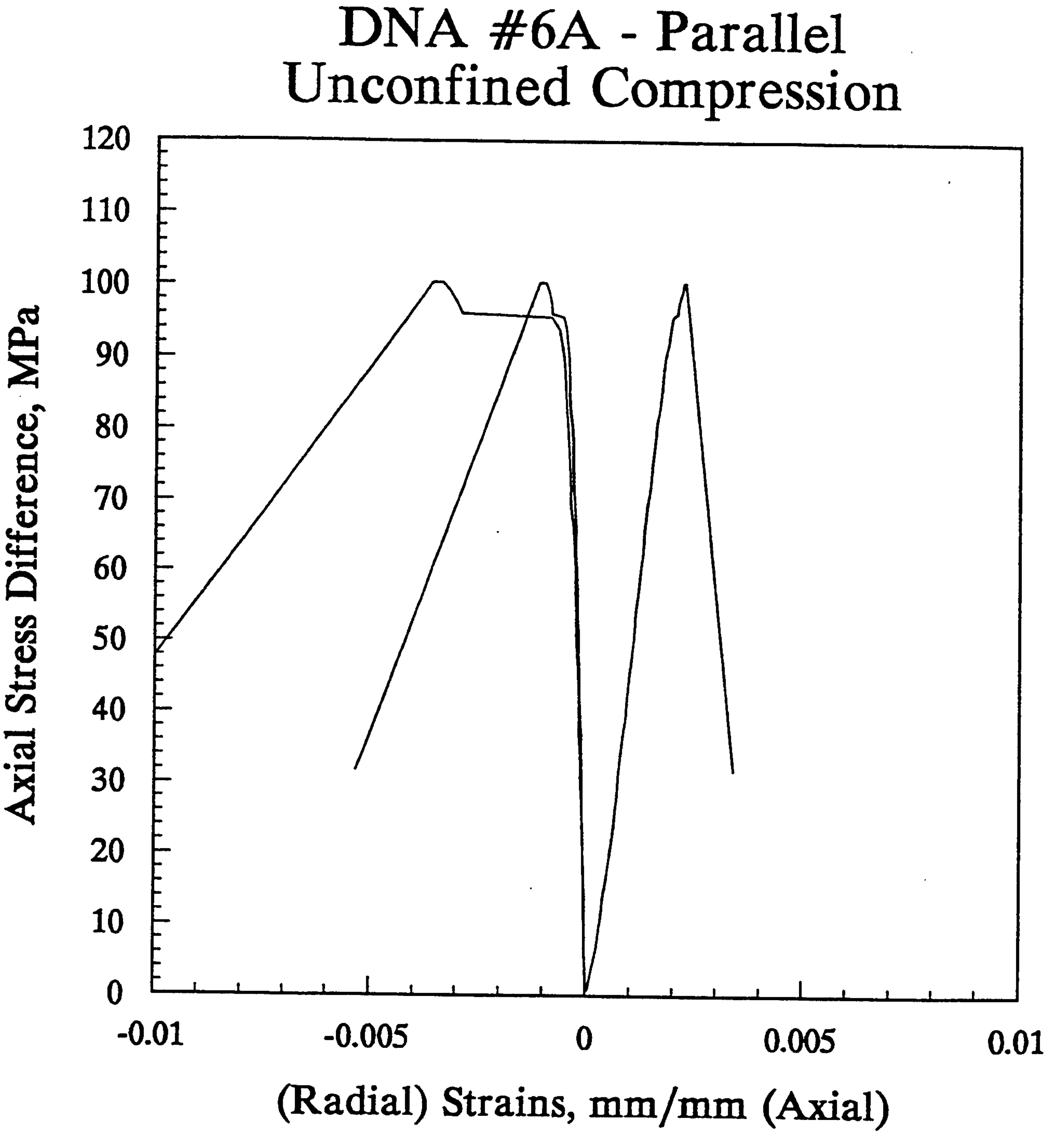

Figure D-18. Stress versus strain during unconfined compression for sample #6A - Parallel.

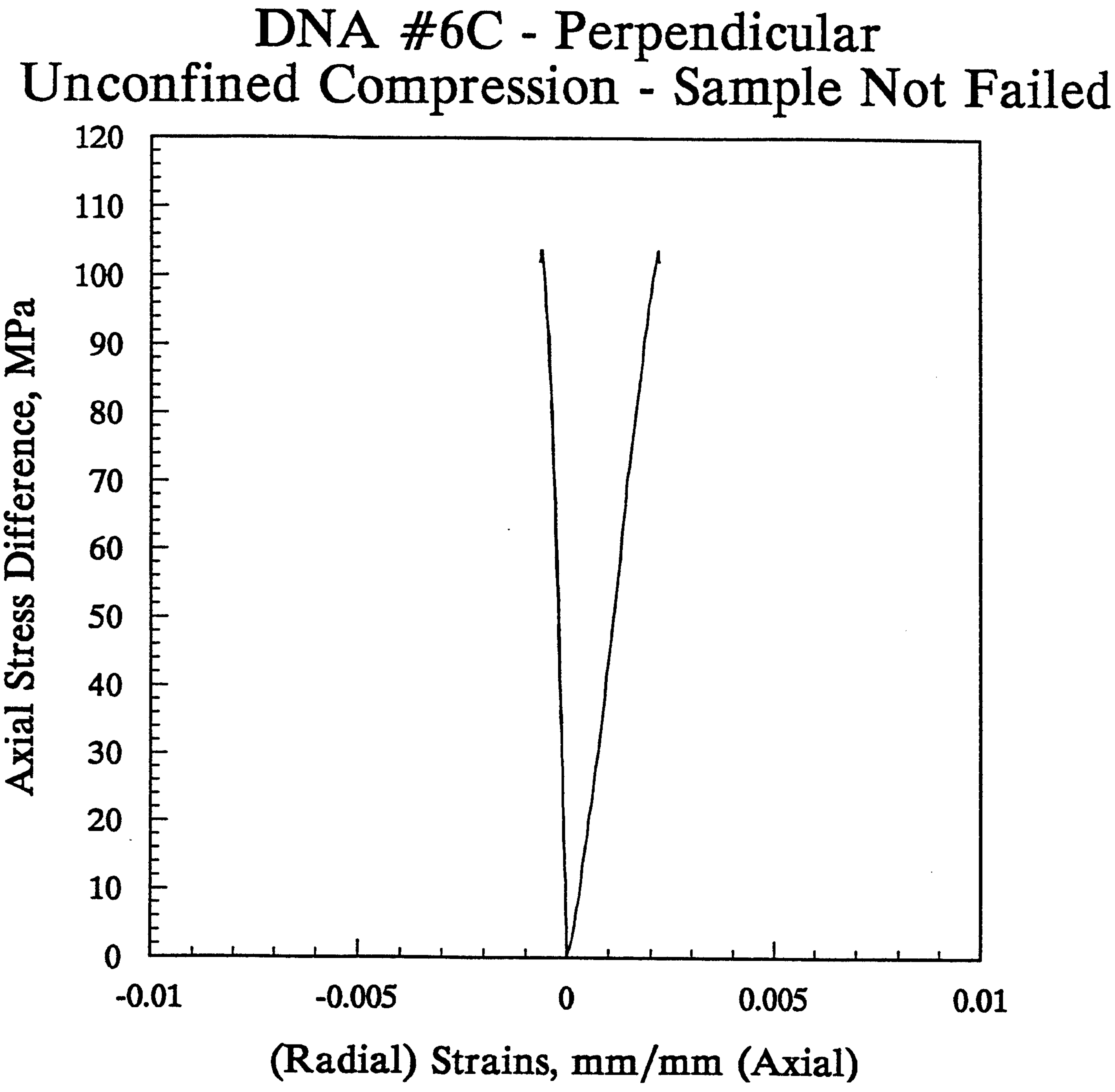

Figure D-19. Stress versus strain during unconfined compression for sample #6A - Perpendicular.

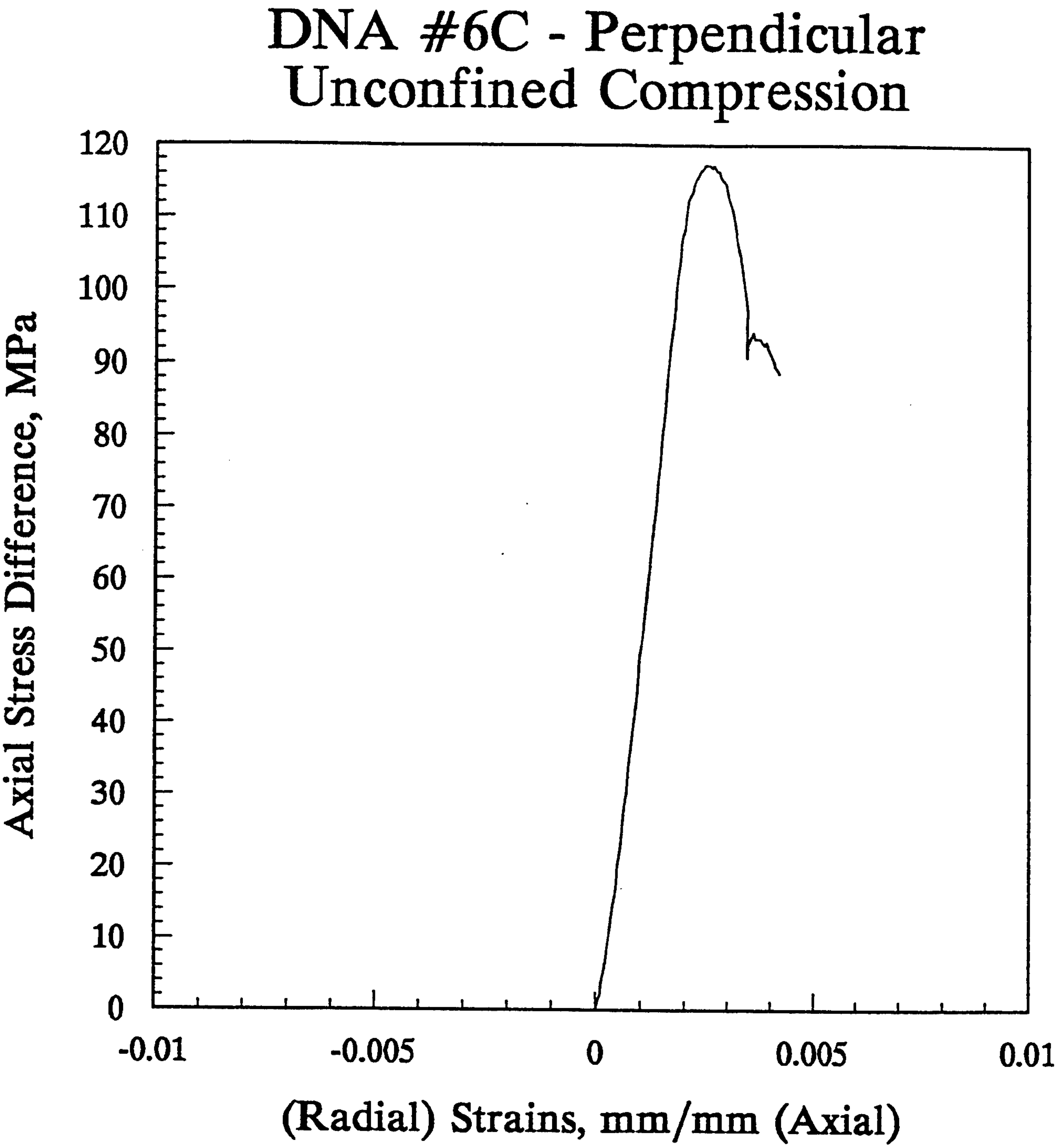

Figure D-20. Stress versus strain during unconfined compression for sample #6C - Perpendicular.

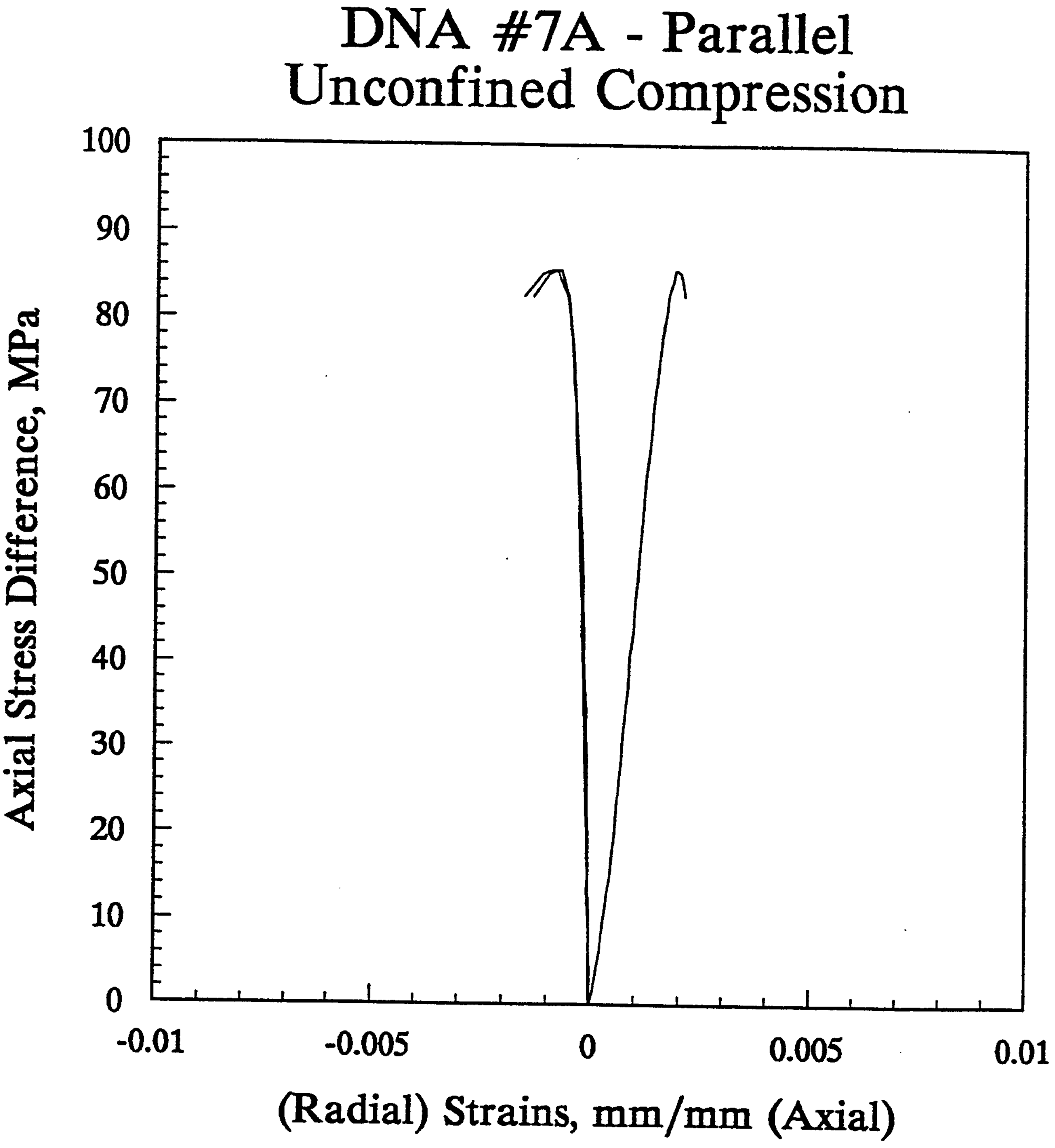

Figure D-21. Stress versus strain during unconfined compression for sample #7A - Parallel.

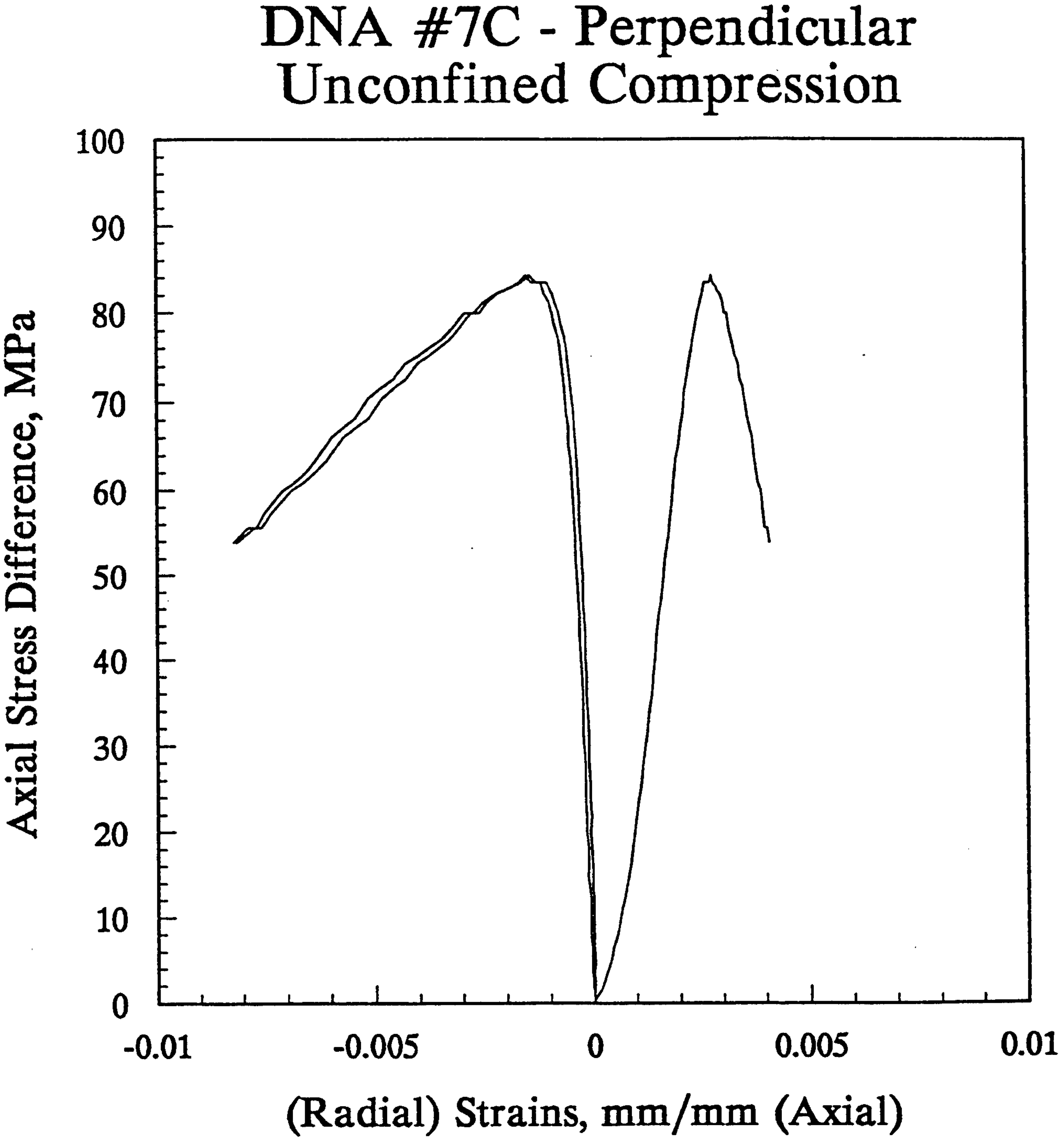

Figure D-22. Stress versus strain during unconfined compression for sample #7C - Perpendicular.

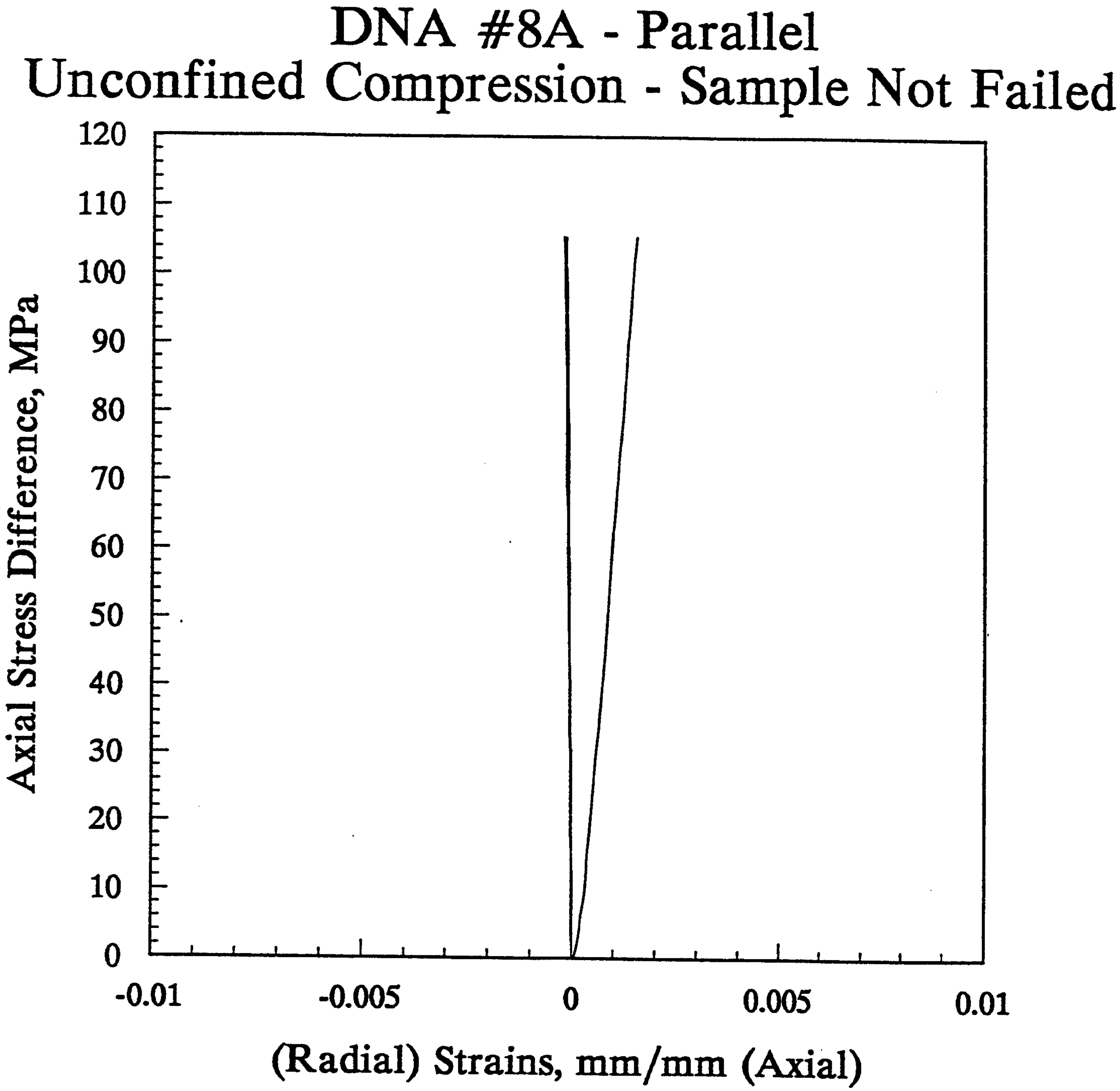

Figure D-23. Stress versus strain during unconfined compression for sample #8A - Parallel.

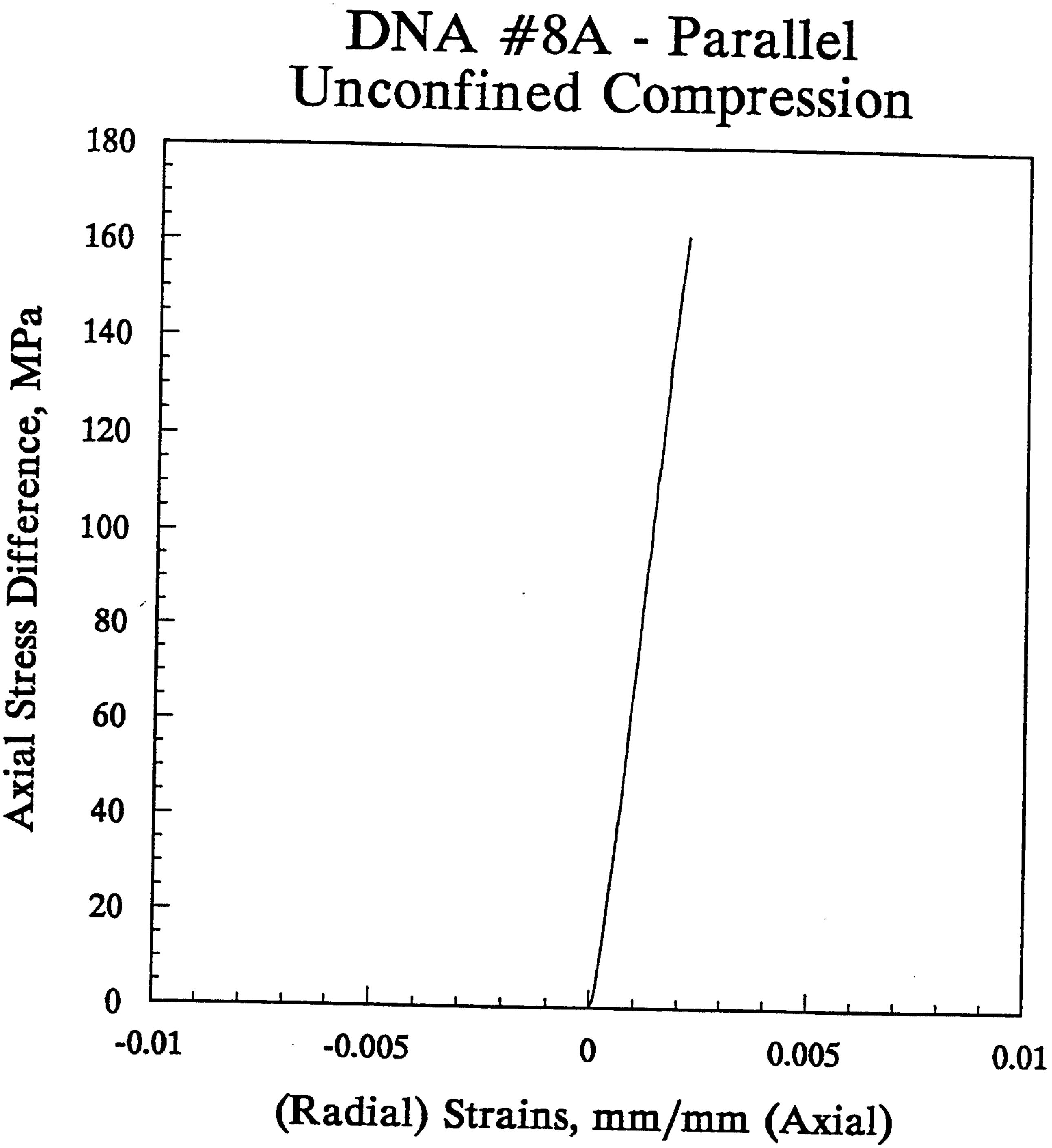

Figure D-24. Stress versus strain during unconfined compression for sample #8A - Parallel.

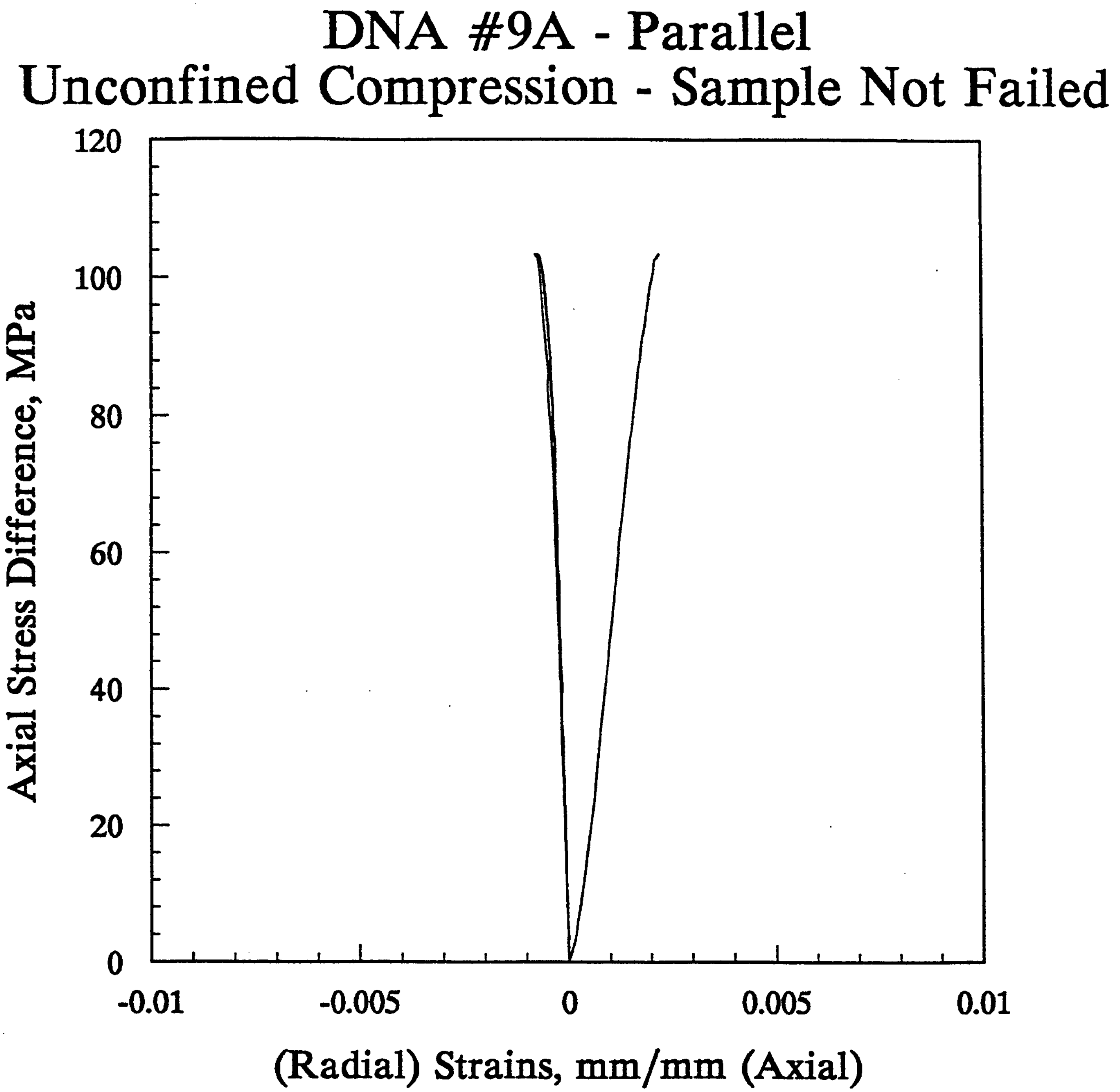

DNA #9A - Parallel
Unconfined Compression - Sample Not Failed

Figure D-25. Stress versus strain during unconfined compression for sample #9A - Parallel.

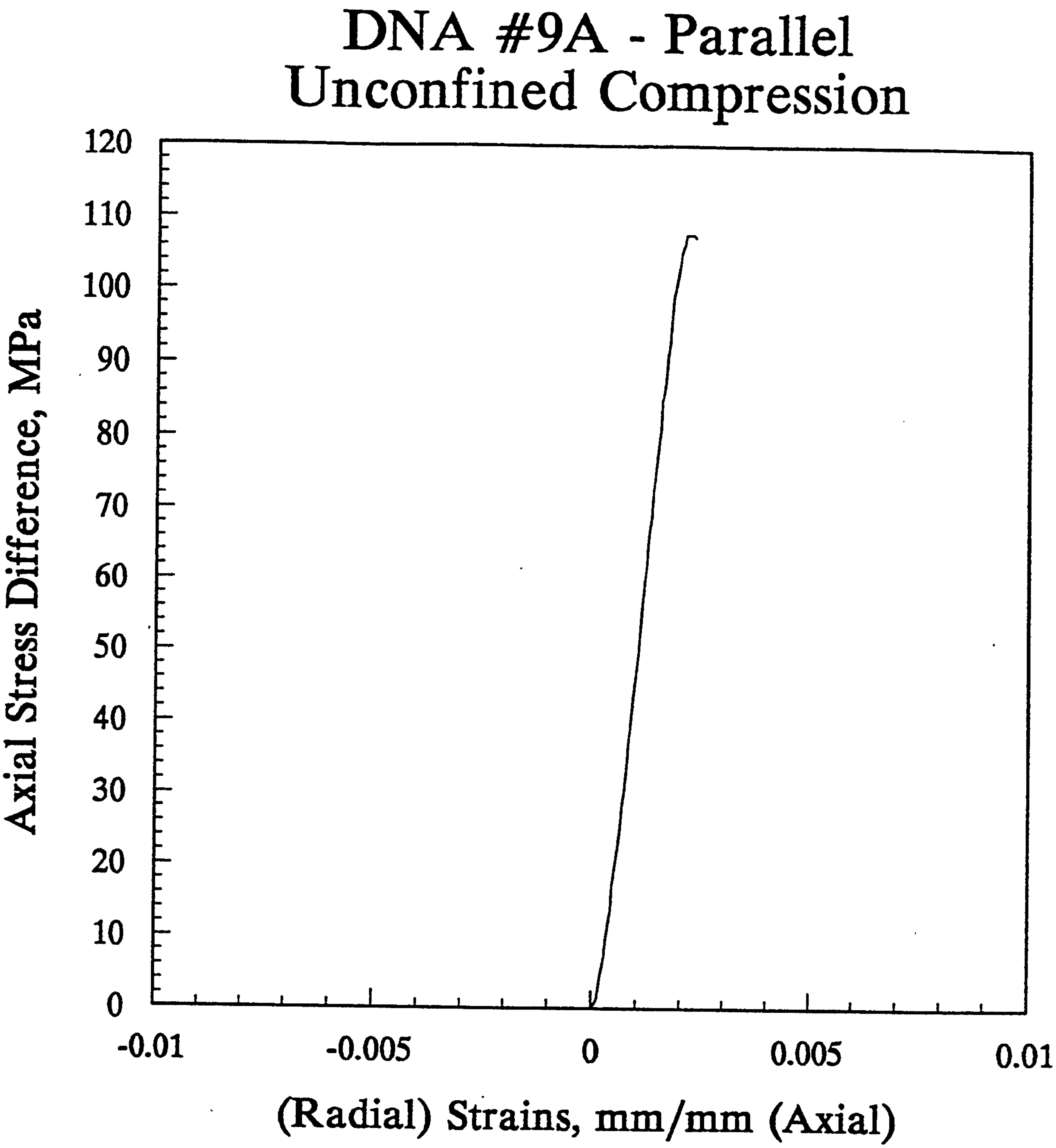

Figure D-26. Stress versus strain during unconfined compression for sample #9A - Parallel.

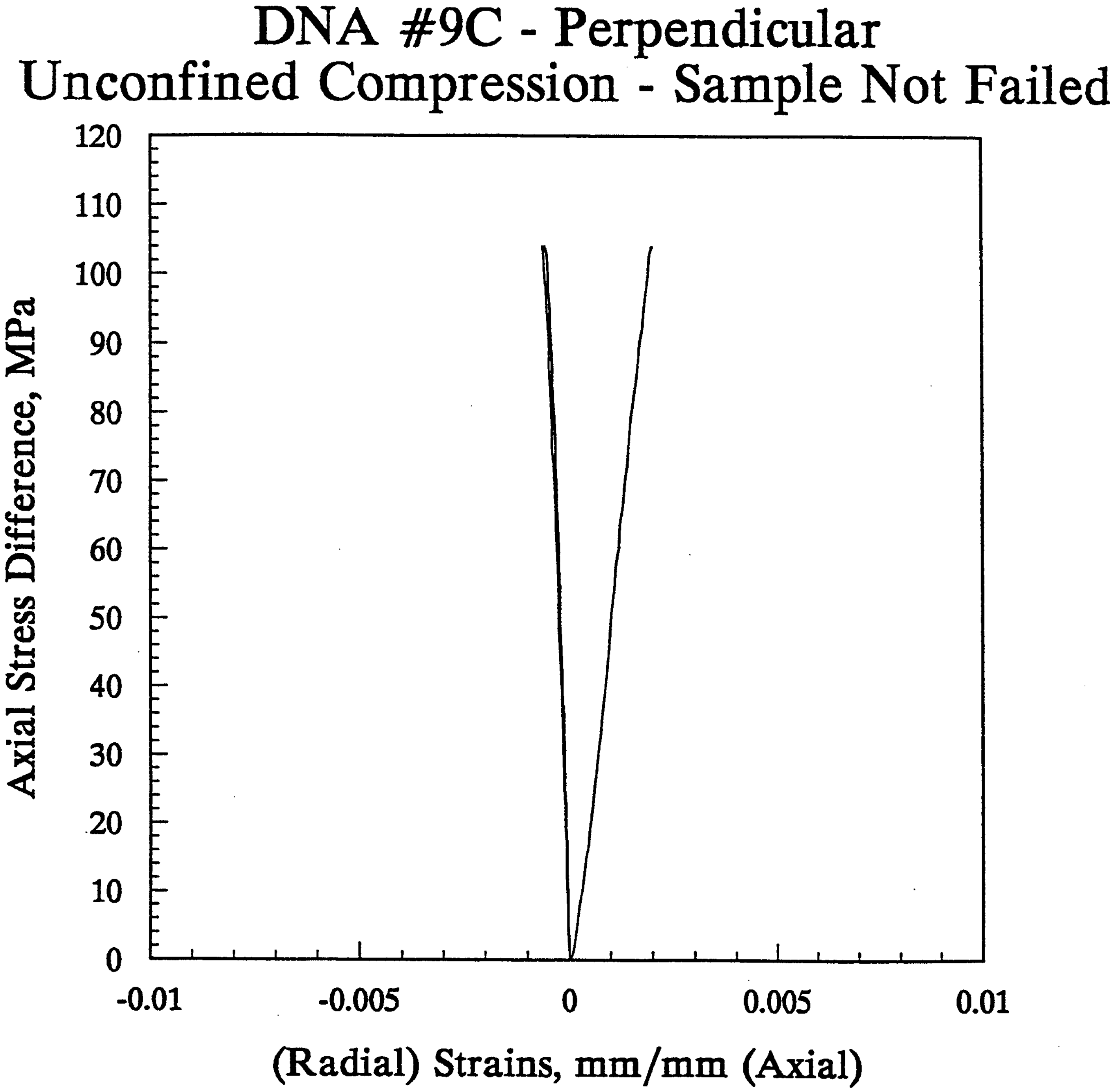

Figure D-27. Stress versus strain during unconfined compression for sample #9C - Perpendicular.

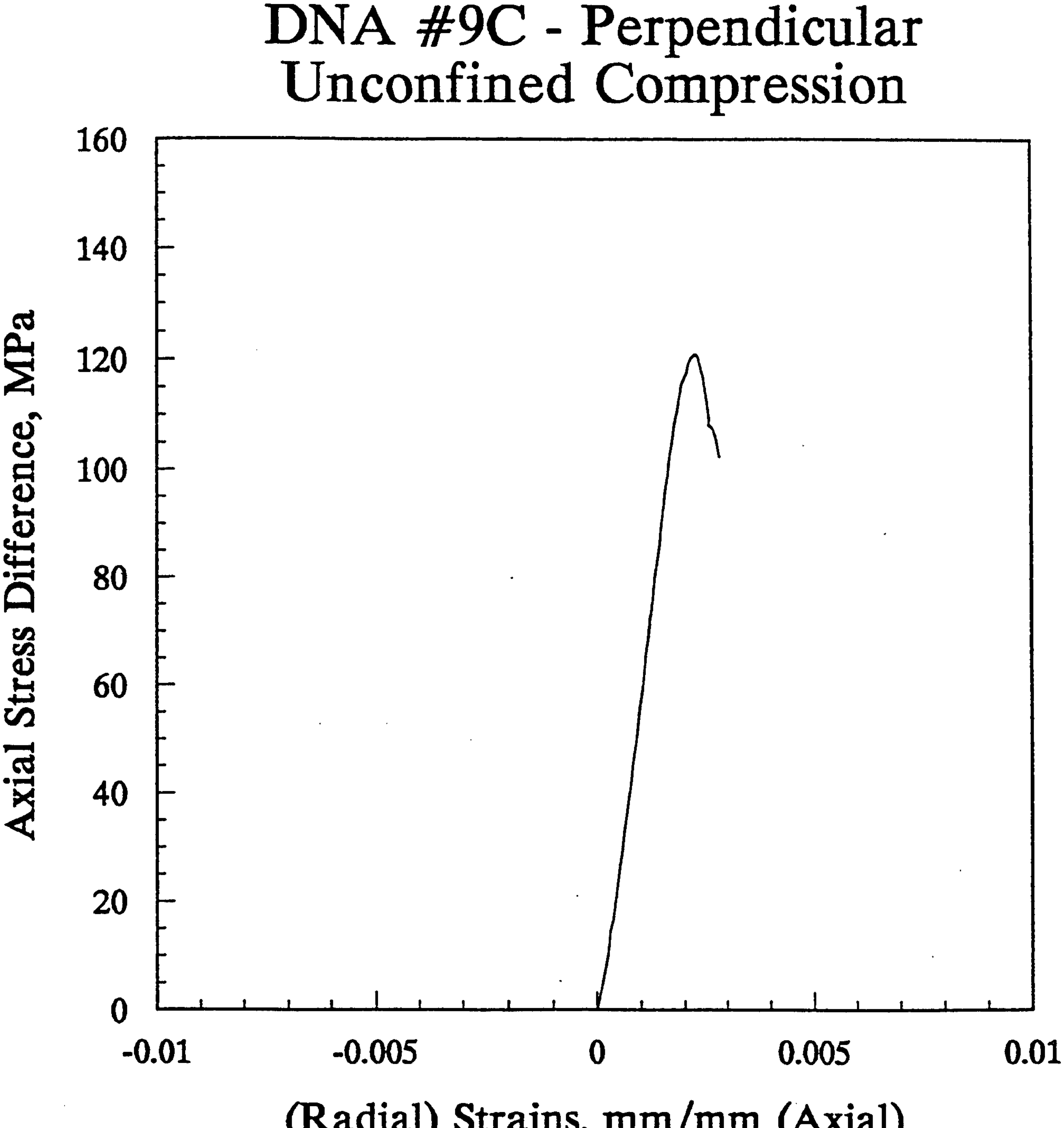

Figure D-28. Stress versus strain during unconfined compression for sample #9C - Perpendicular.

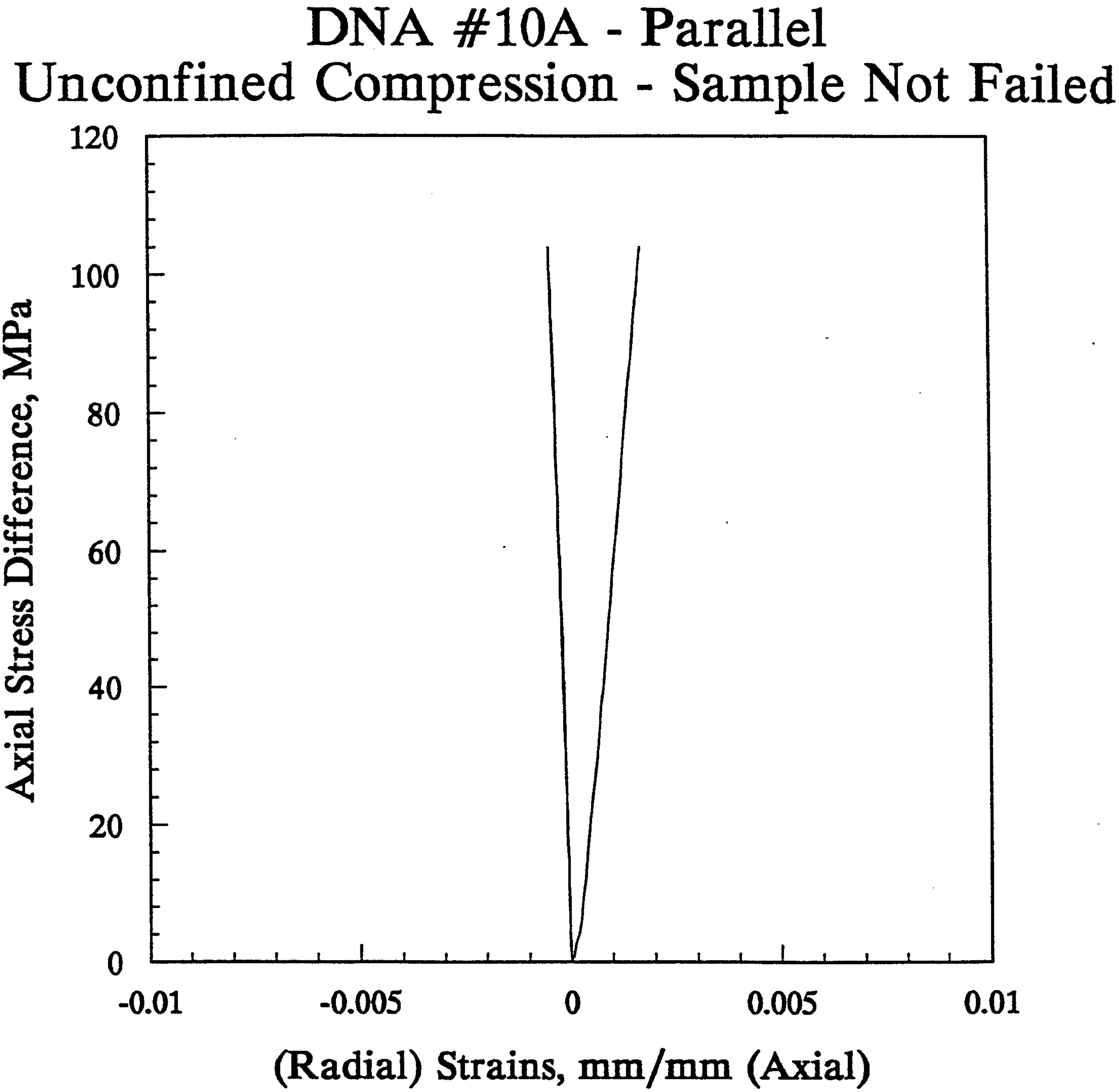

Figure D-29. Stress versus strain during unconfined compression for sample #10A - Parallel.

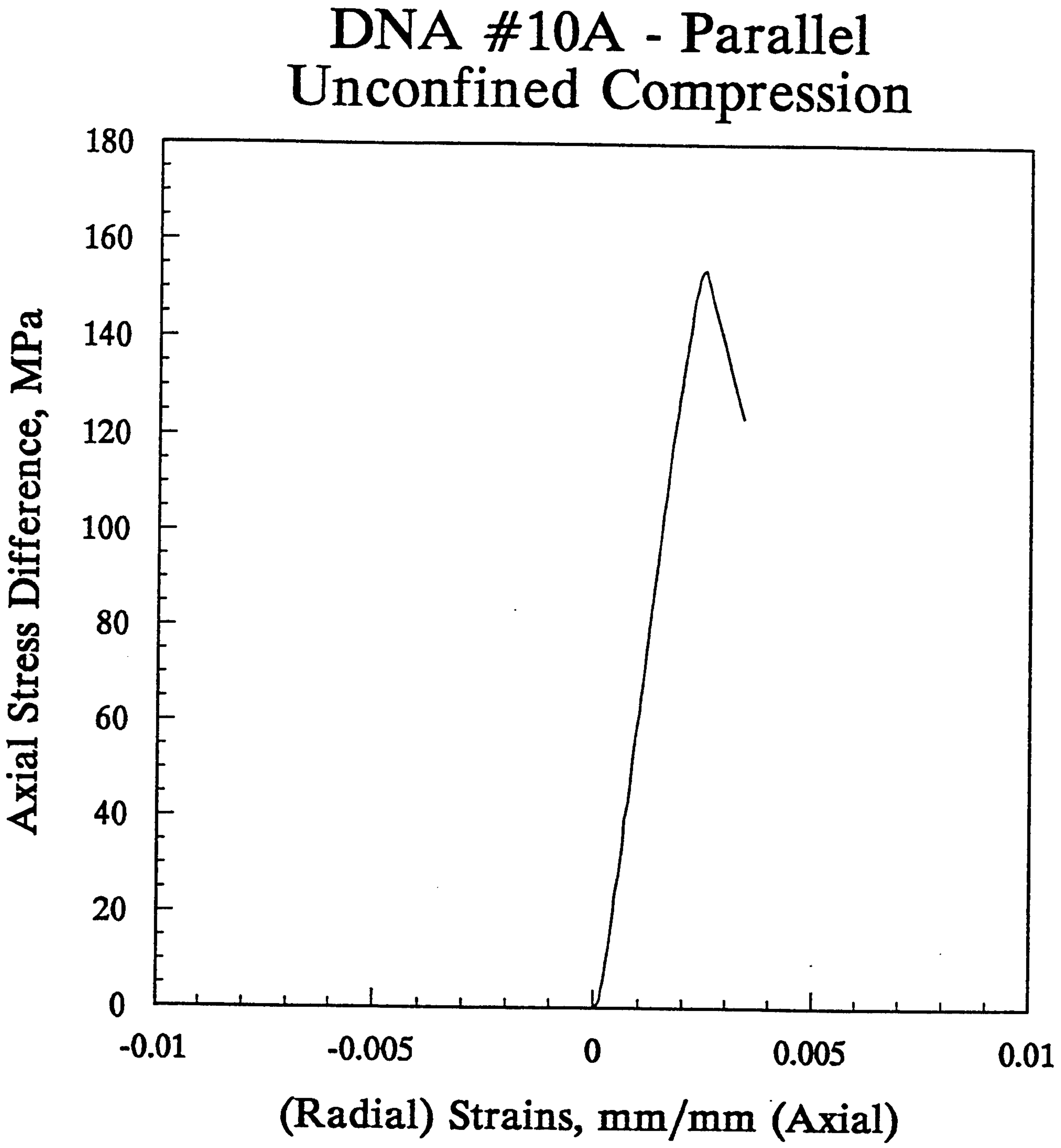

Figure D-30. Stress versus strain during unconfined compression for sample #10A - Parallel.

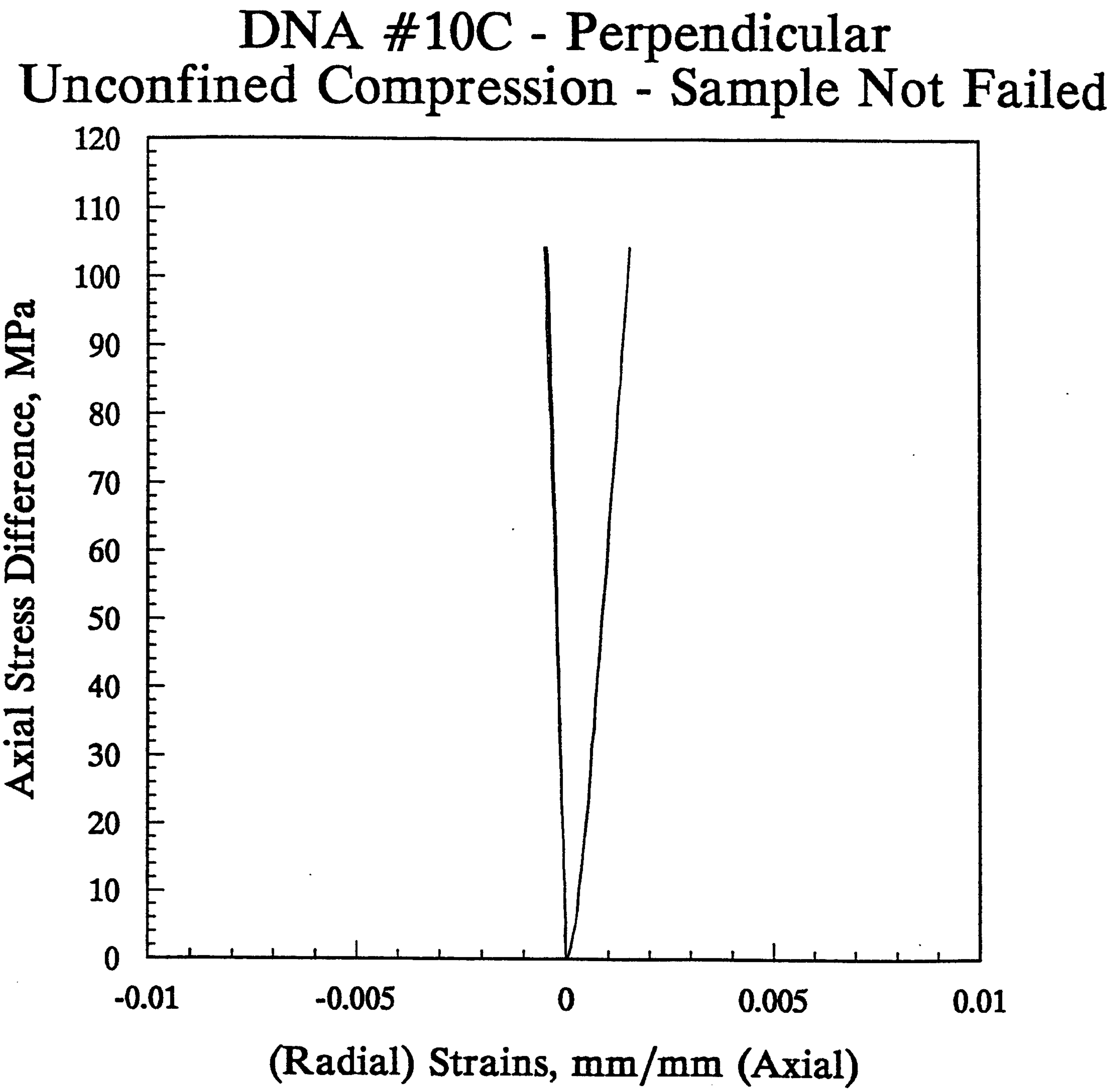

Figure D-31. Stress versus strain during unconfined compression for sample #10C - Perpendicular.

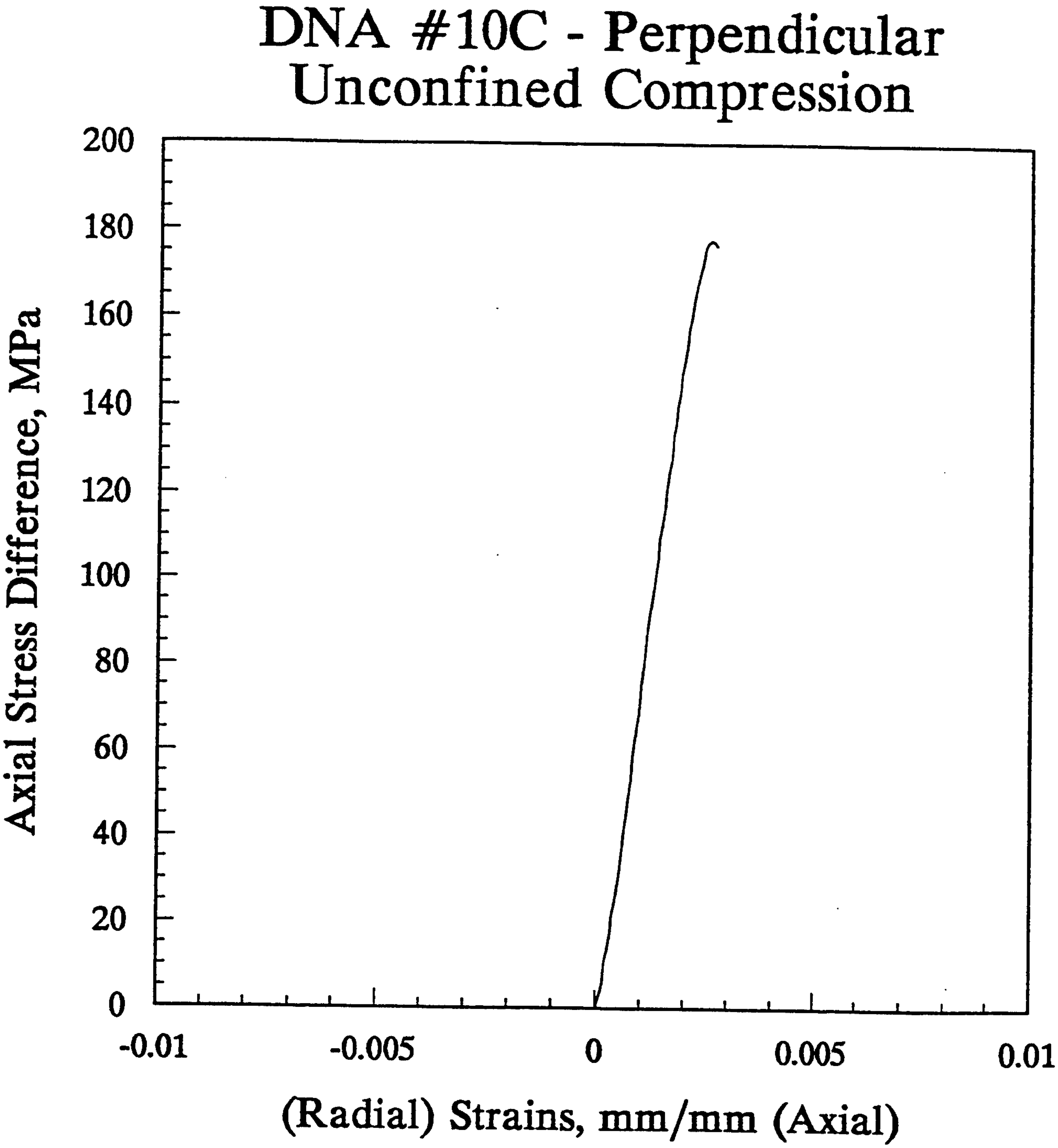

Figure D-32. Stress versus strain during unconfined compression for sample #10C - Perpendicular.

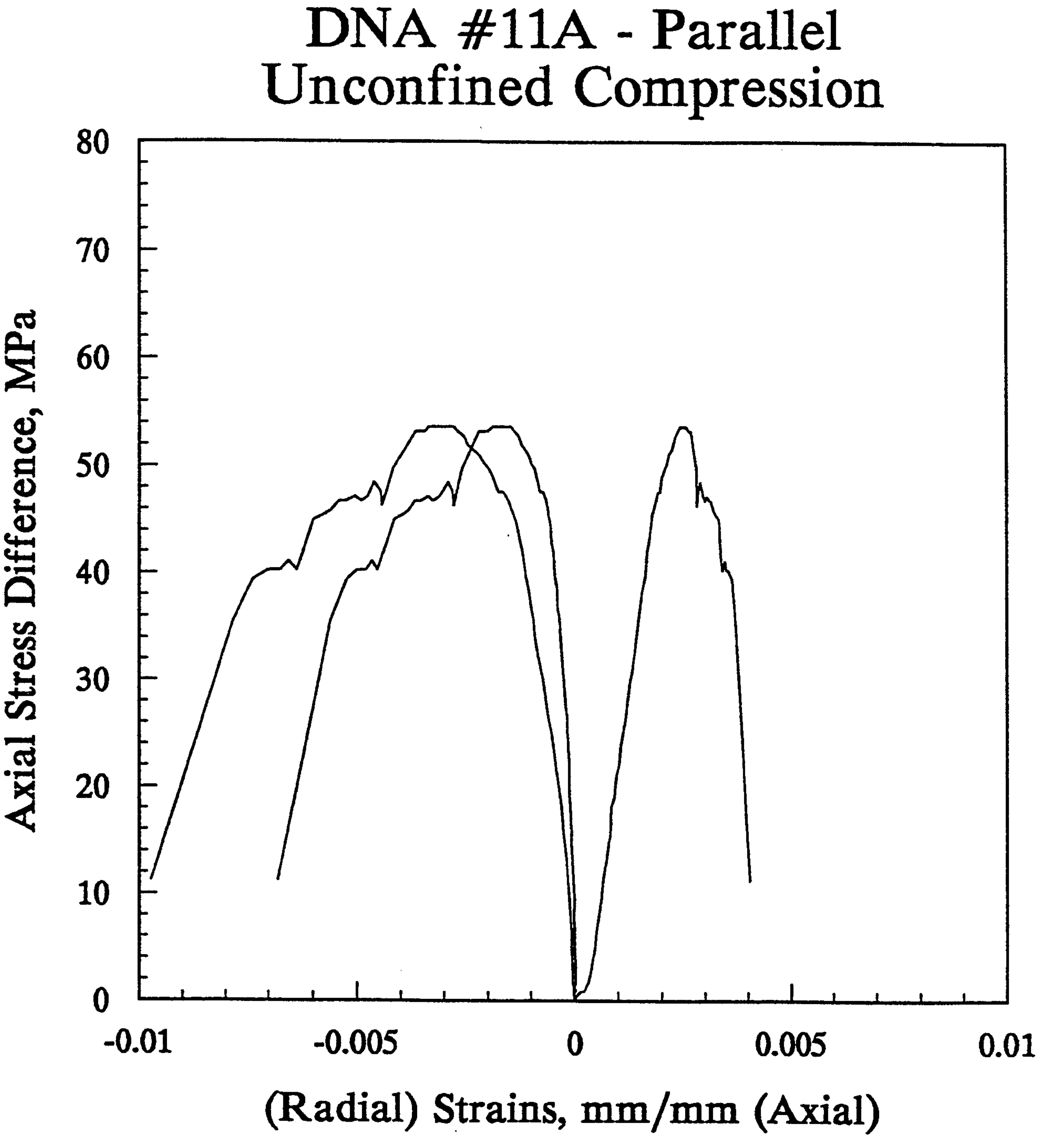

Figure D-33. Stress versus strain during unconfined compression for sample #11A - Parallel.

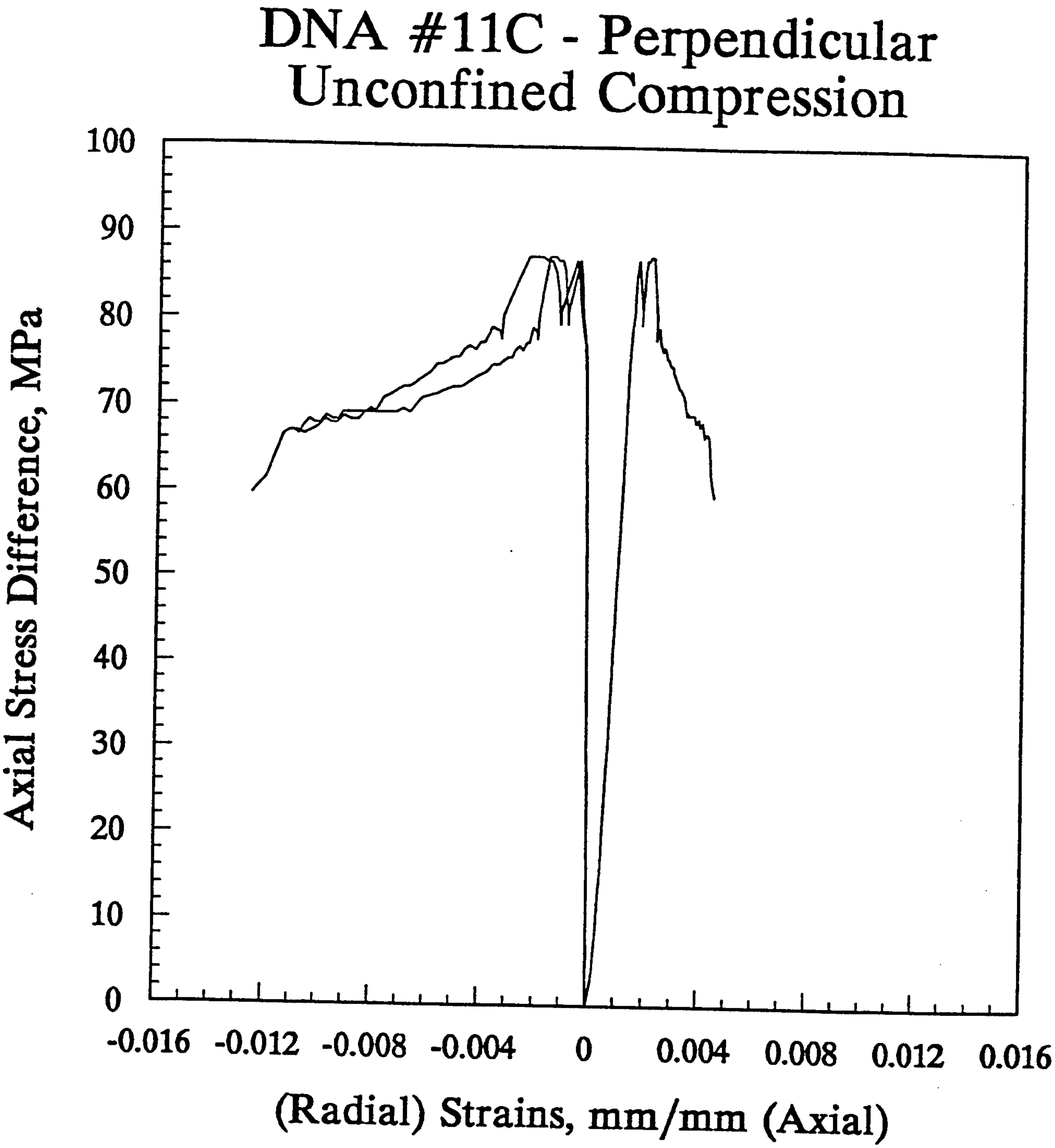

Figure D-34. Stress versus strain during unconfined compression for sample #11C - Perpendicular.

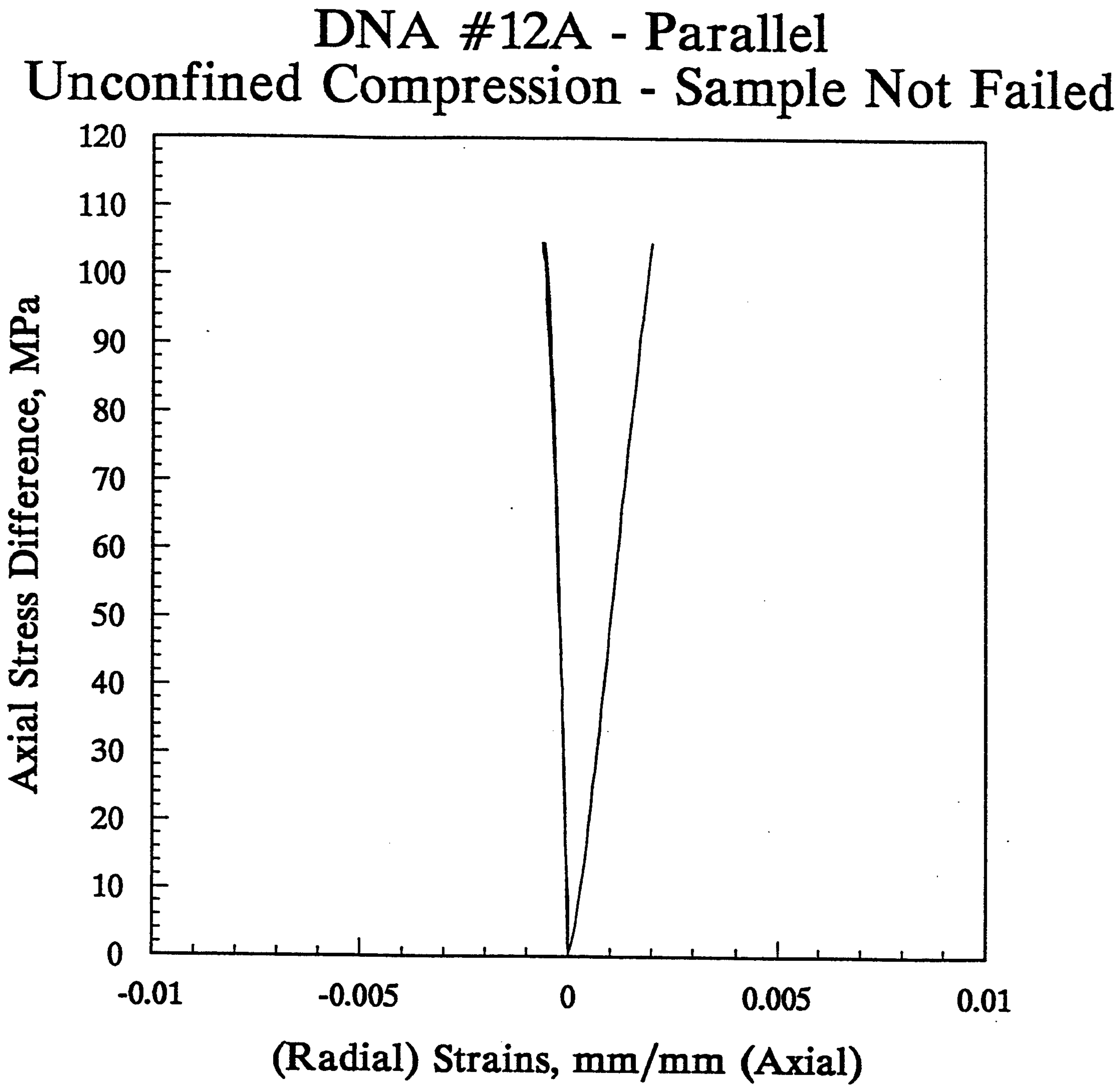

Figure D-35. Stress versus strain during unconfined compression for sample #12A - Parallel.

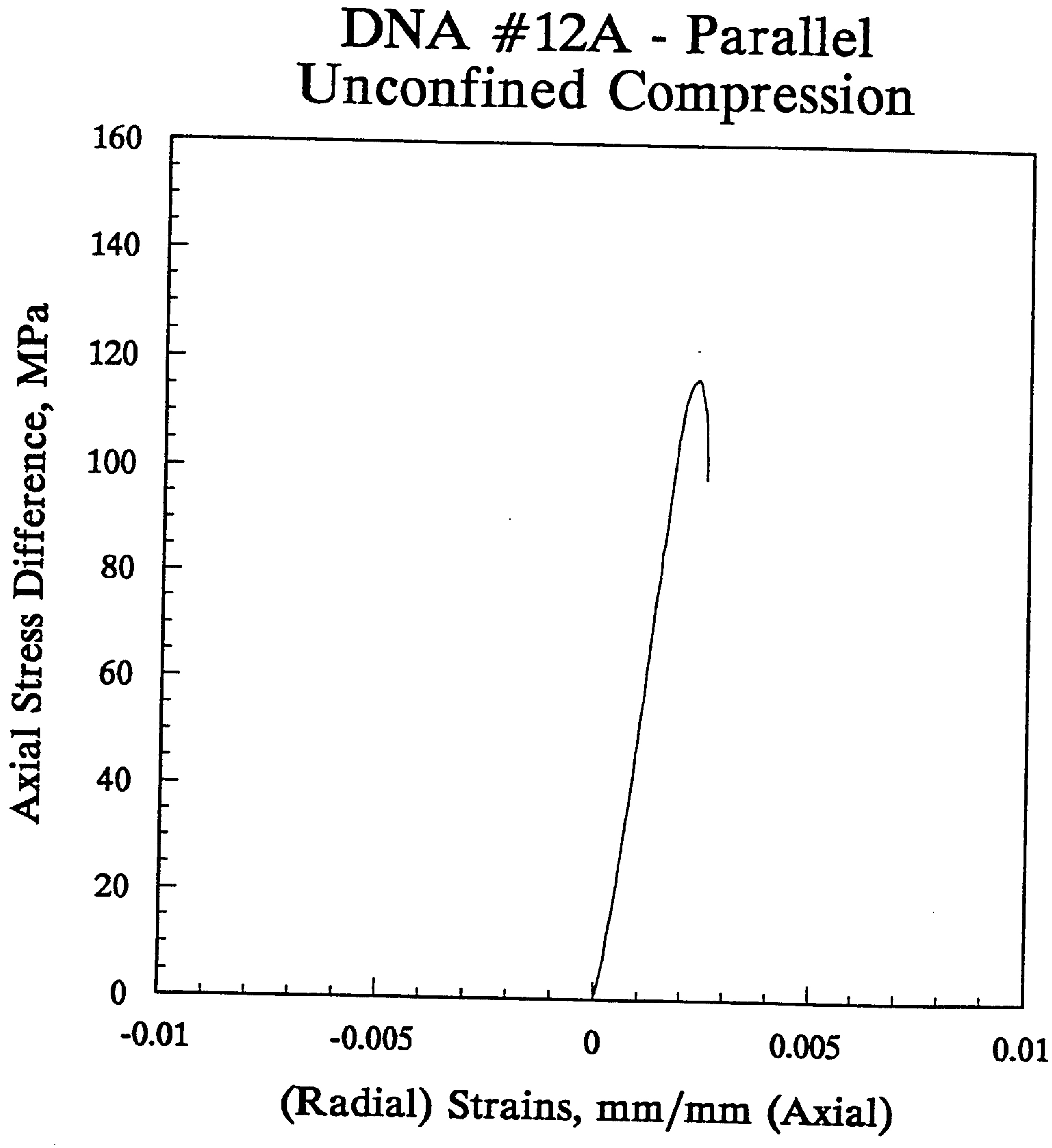

Figure D-36. Stress versus strain during unconfined compression for sample #12A - Parallel.

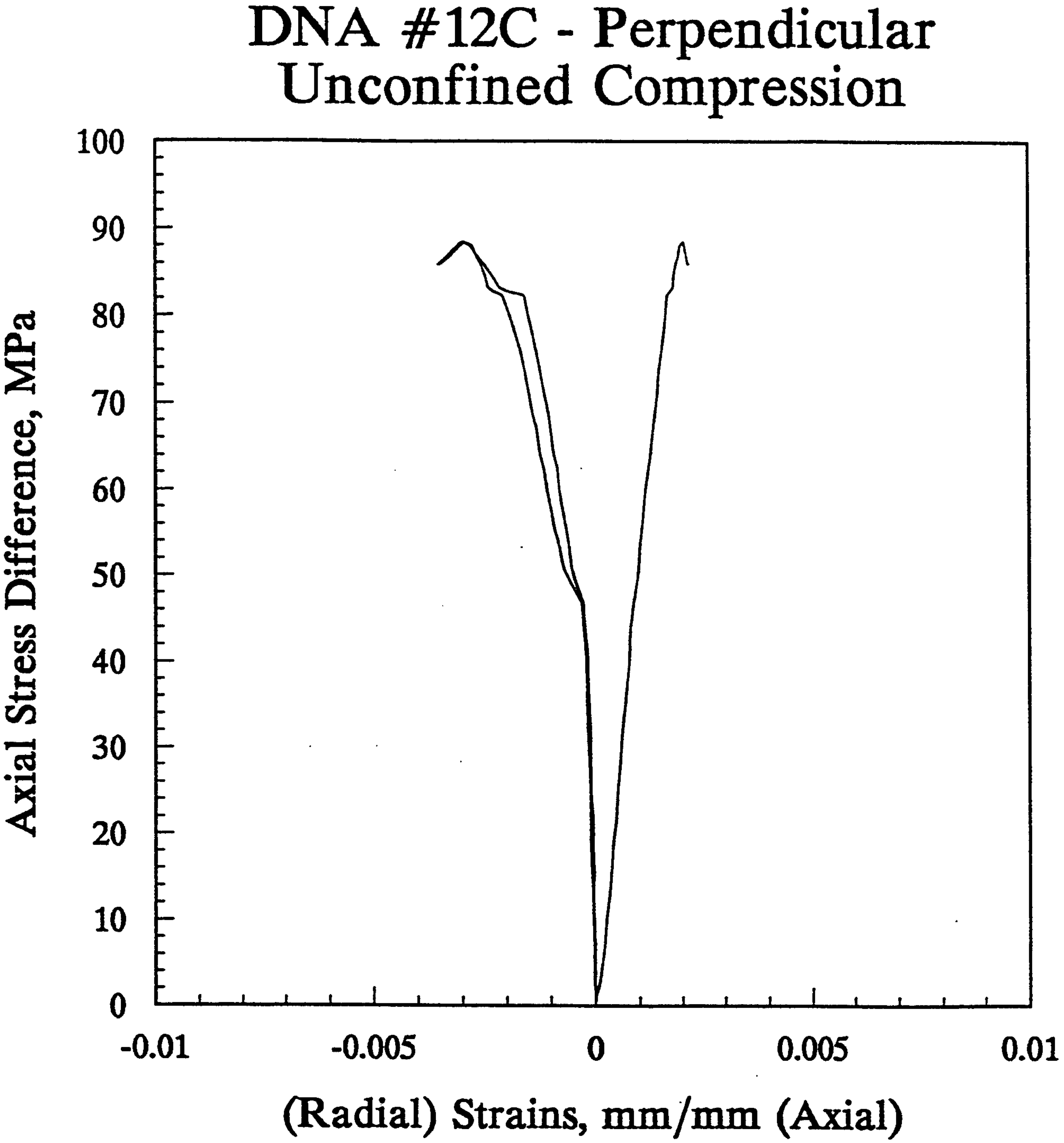

Figure D-37. Stress versus strain during unconfined compression for sample #12C - Perpendicular.

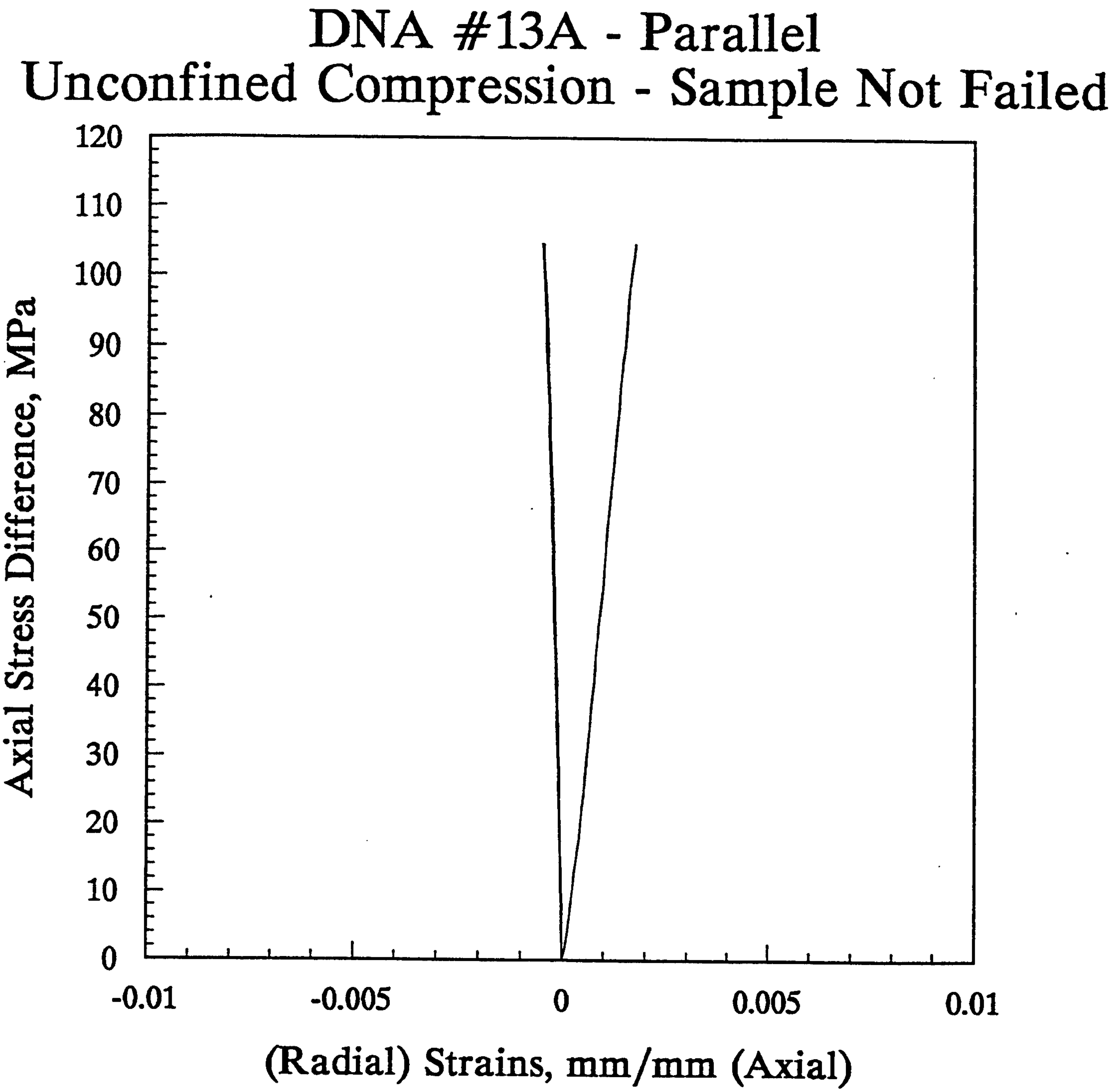

Figure D-38. Stress versus strain during unconfined compression for sample #13A - Parallel.

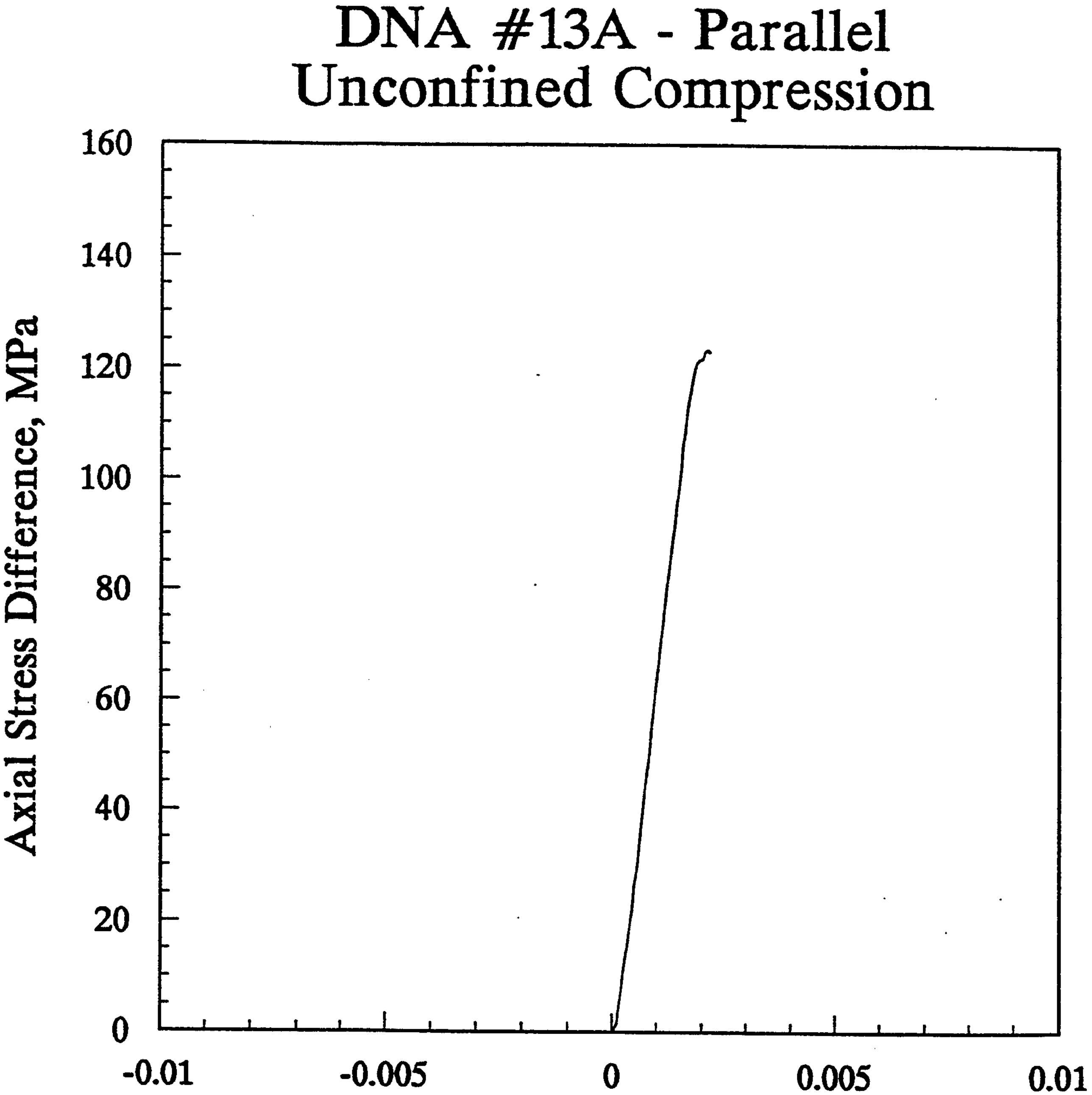

Figure D-39. Stress versus strain during unconfined compression for sample #13A - Parallel.

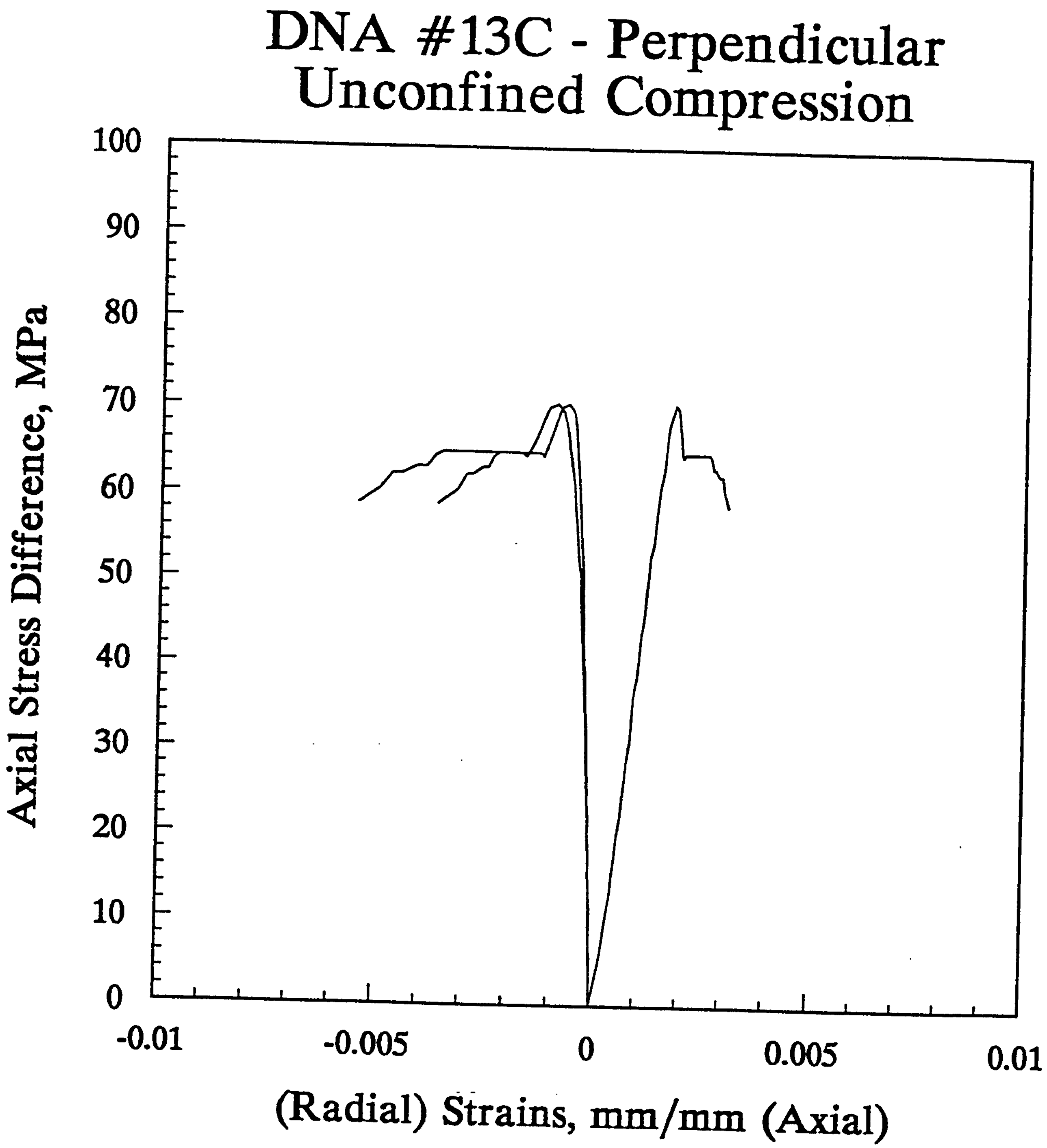

Figure D-40. Stress versus strain during unconfined compression for sample #13C - Perpendicular.

Annex 10
Uniaxial Strain Graphical Presentations

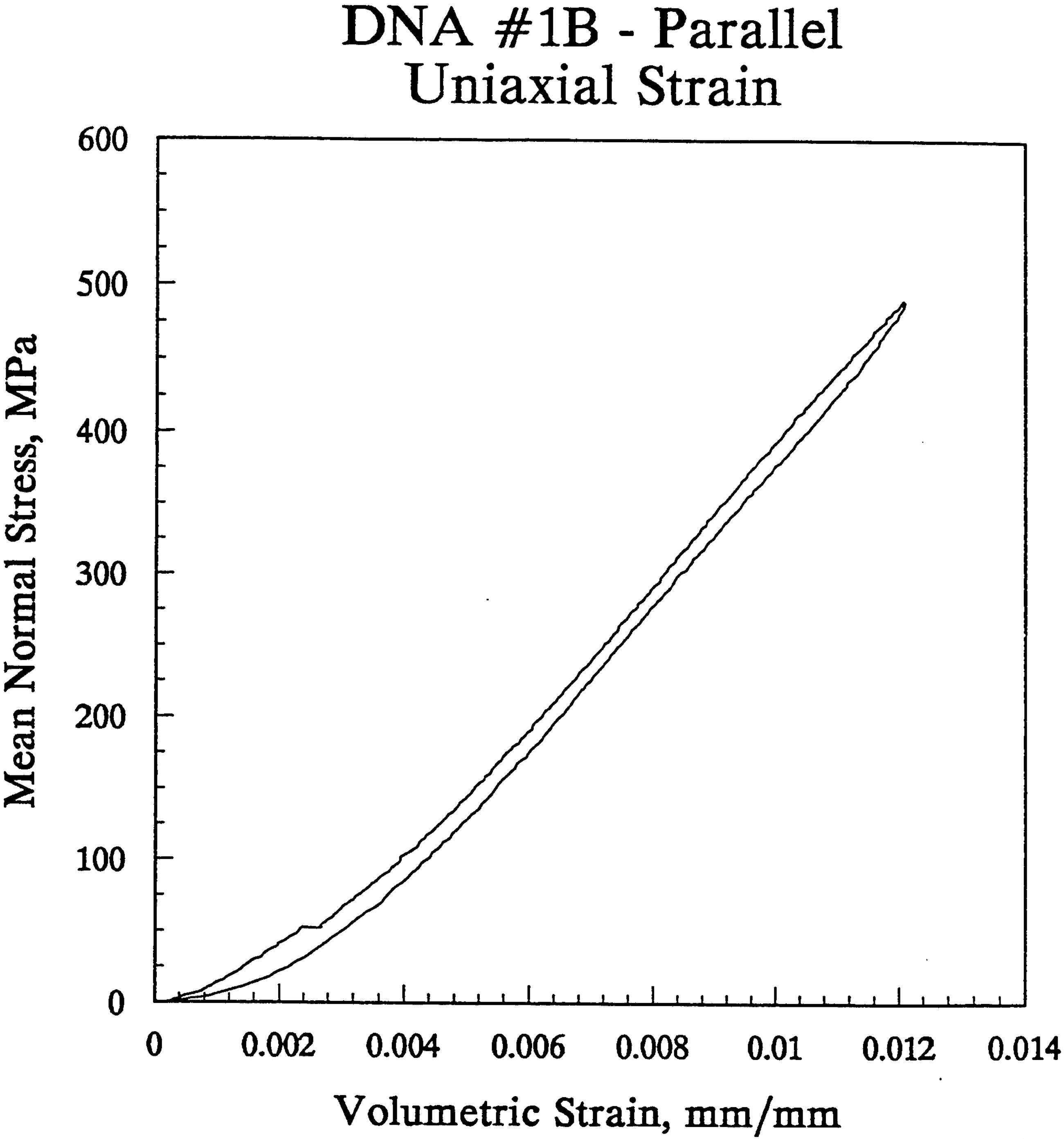

Figure D-41. Mean normal stress versus volumetric strain under uniaxial strain conditions for sample #1B - Parallel.

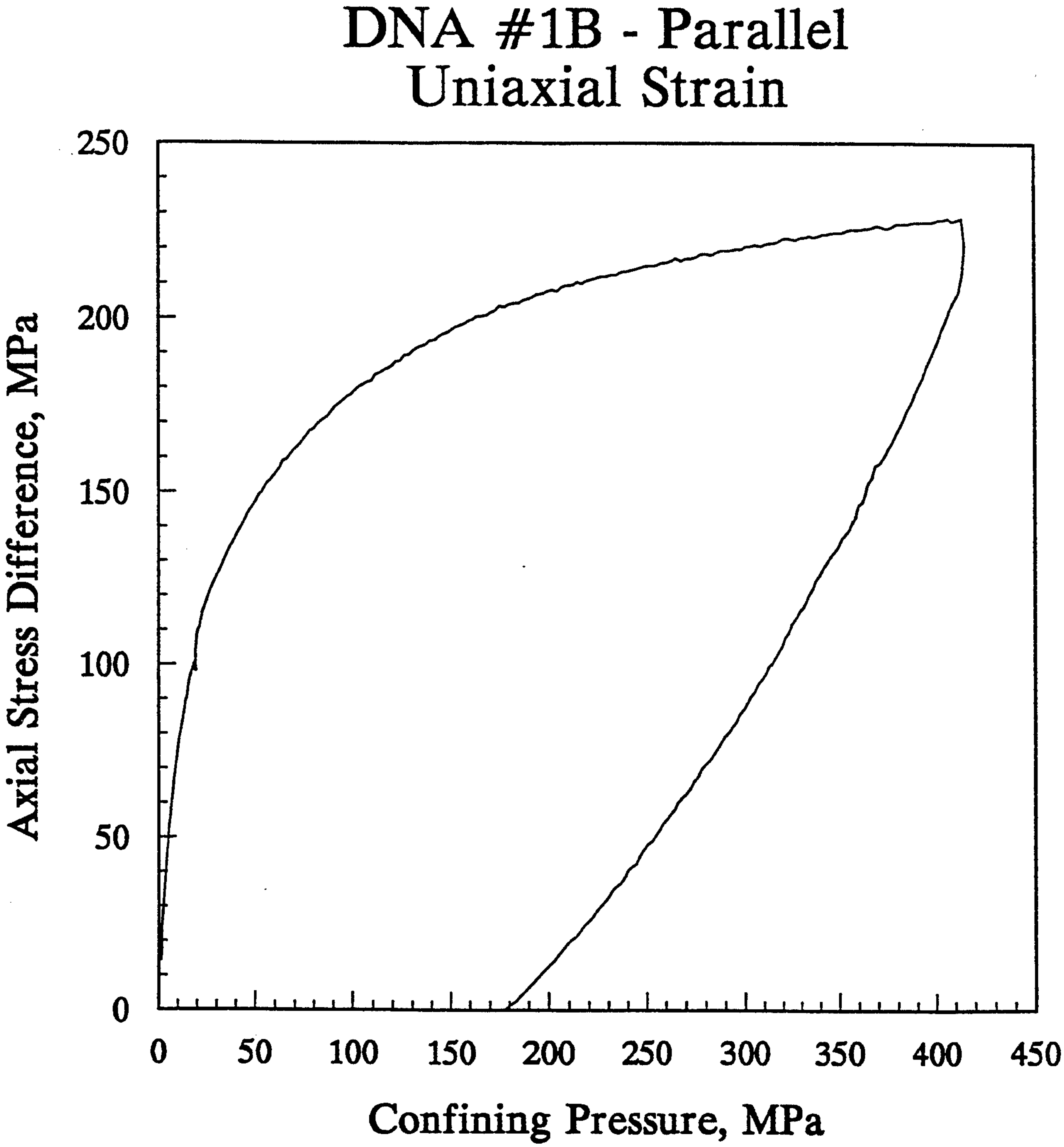

Figure D-42. Axial stress difference versus confining pressure under uniaxial strain conditions for sample #1B - Parallel.

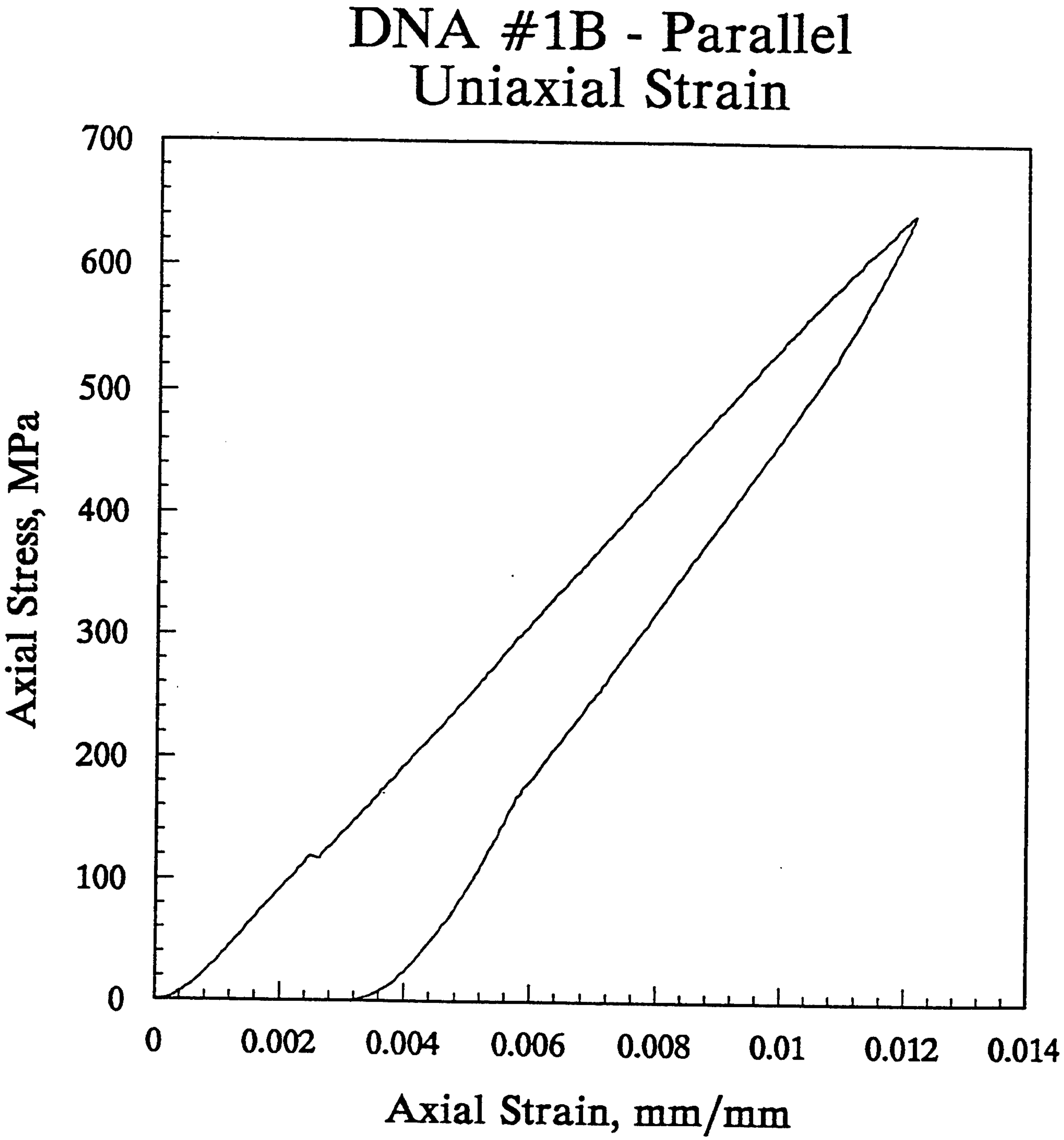

Figure D-43. Axial stress versus axial strain under uniaxial strain conditions for sample #1B - Parallel.

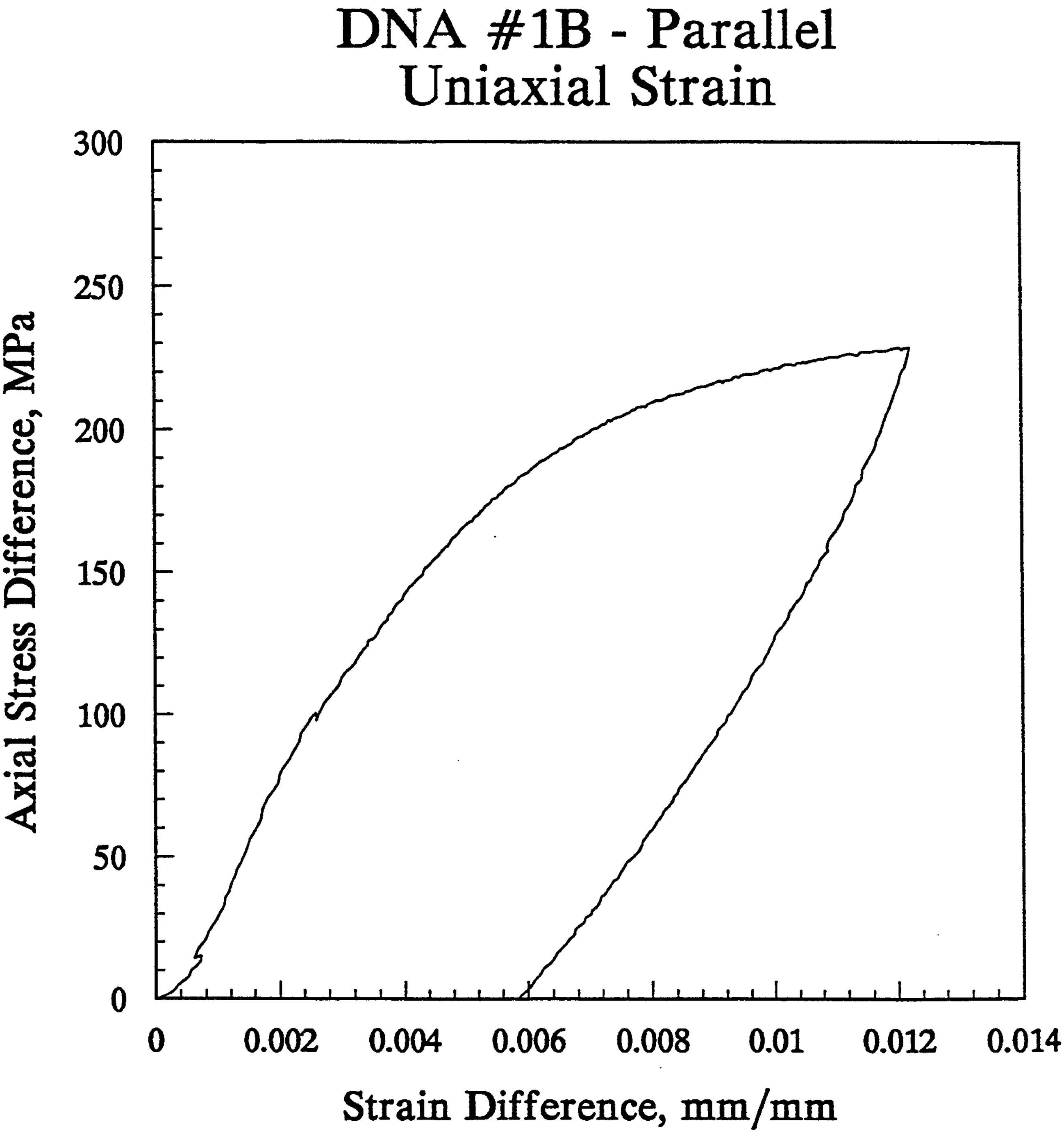

Figure D-44. Axial stress difference versus strain difference under uniaxial strain conditions for sample #1B - Parallel.

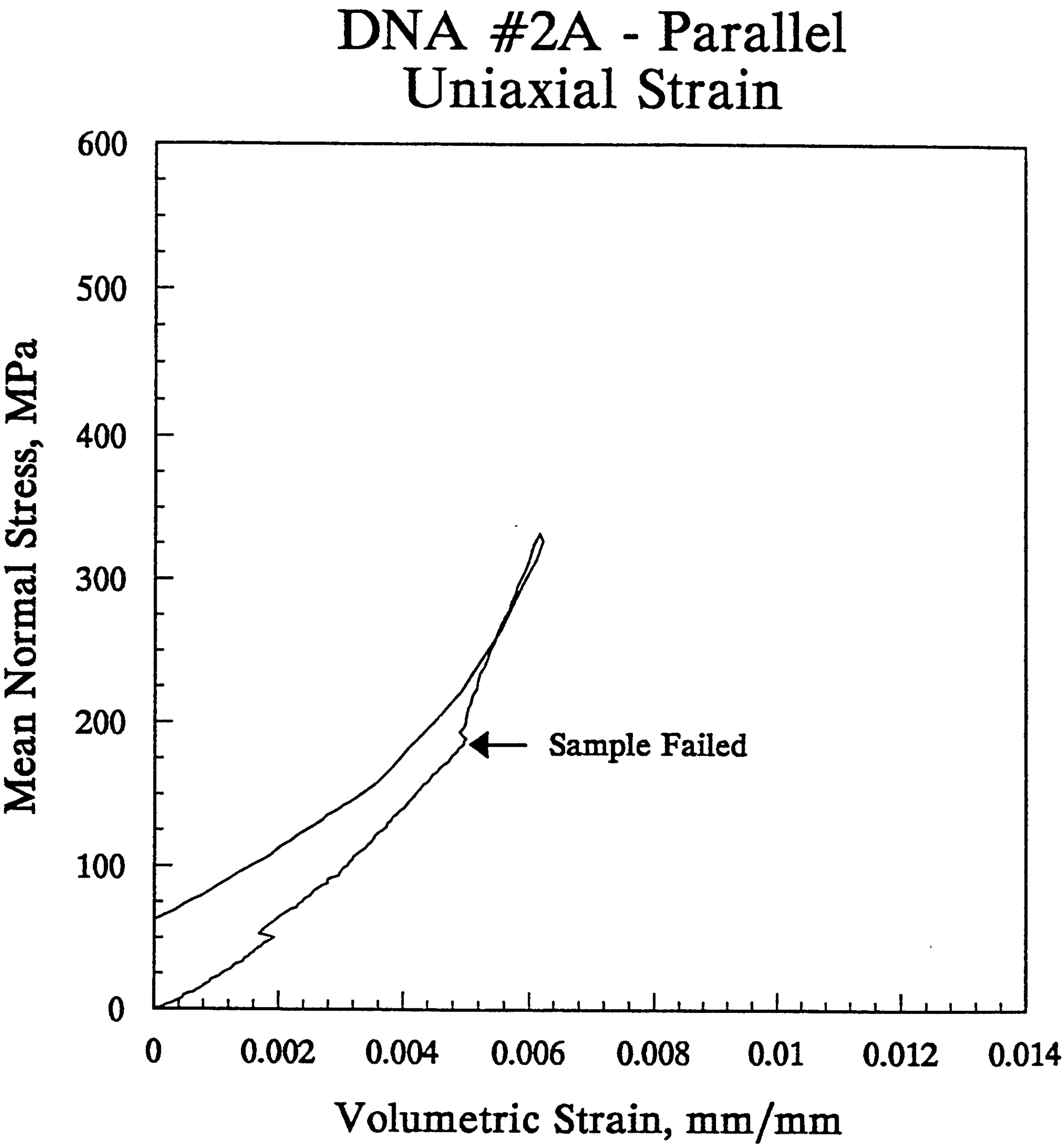

Figure D-45. Mean normal stress versus volumetric strain under uniaxial conditions for sample #2A - Parallel.

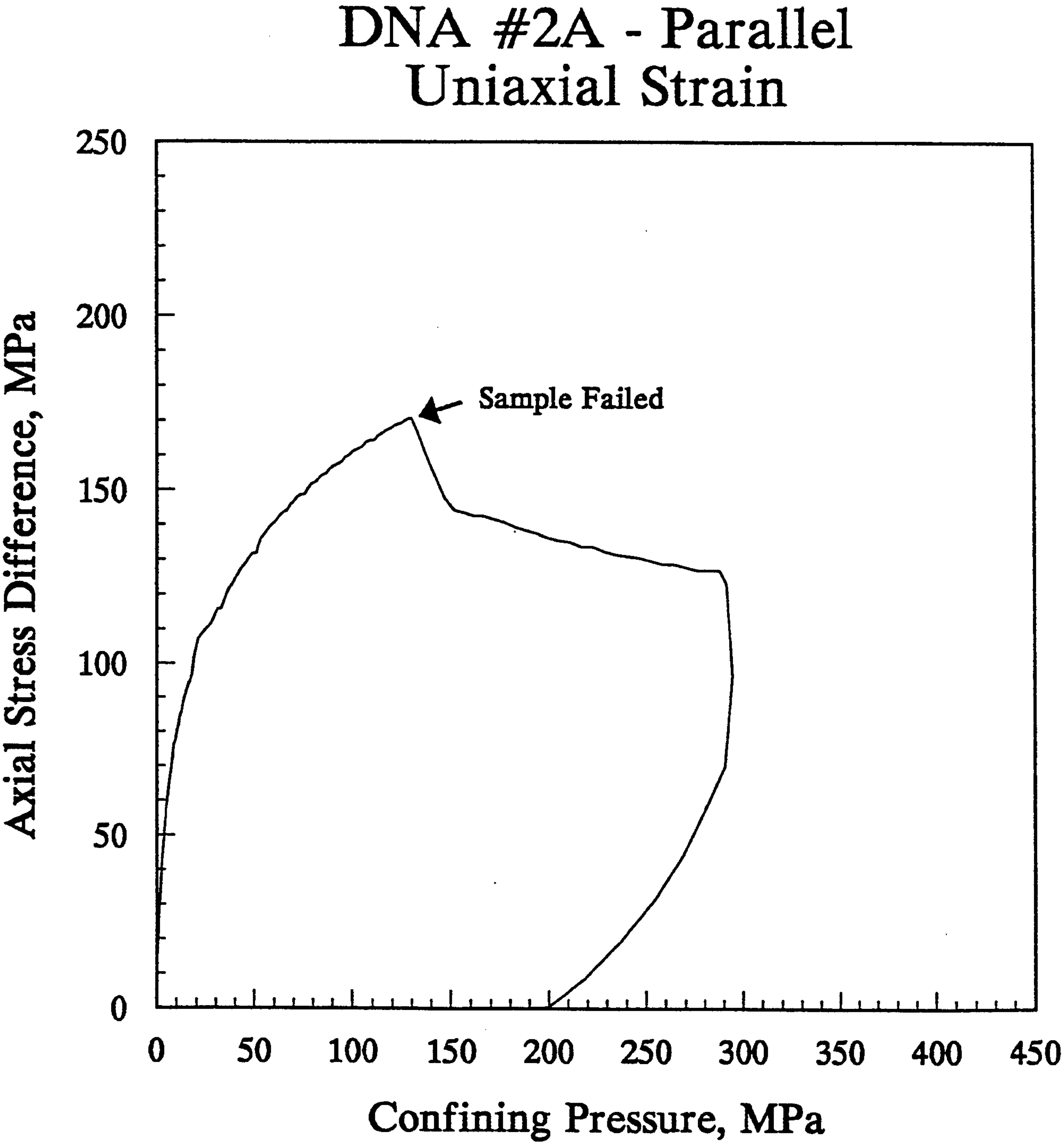

Figure D-46. Axial stress difference versus confining pressure under uniaxial strain conditions for sample #2A - Parallel.

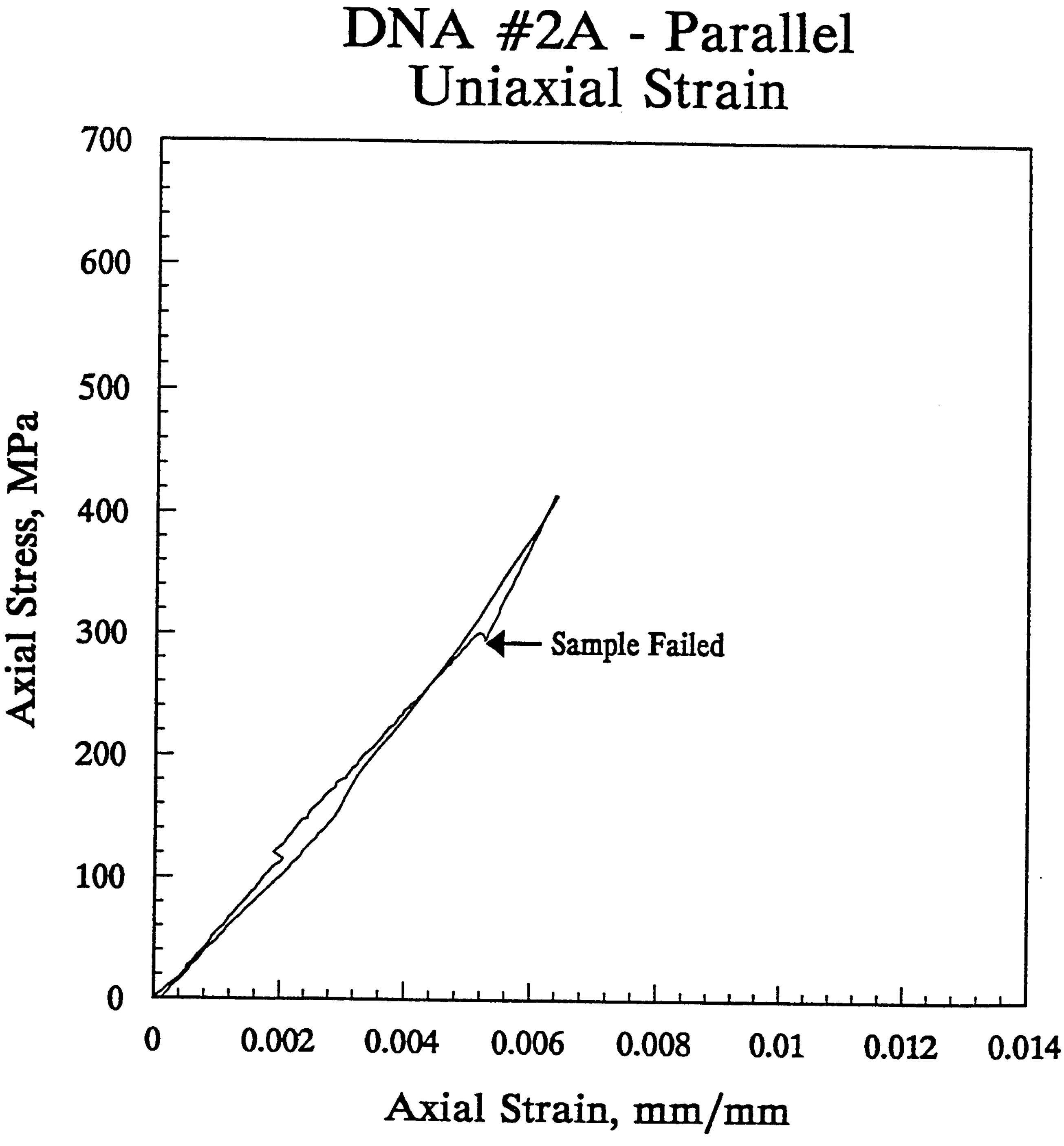

Figure D-47. Axial stress versus axial strain under uniaxial strain conditions for sample #2A - Parallel.

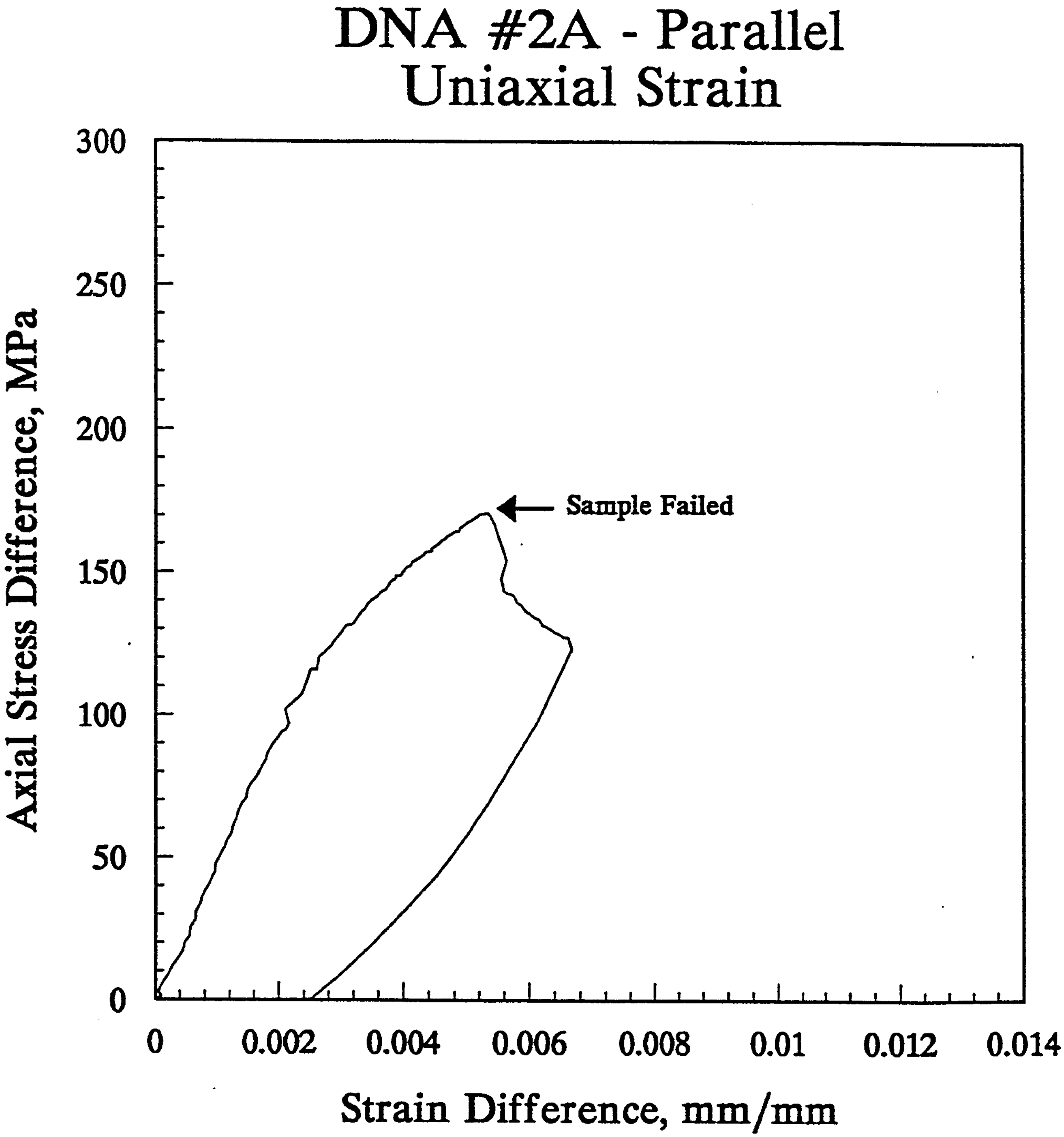

Figure D-48. Axial stress difference versus strain difference under uniaxial strain conditions for sample #2A - Parallel.

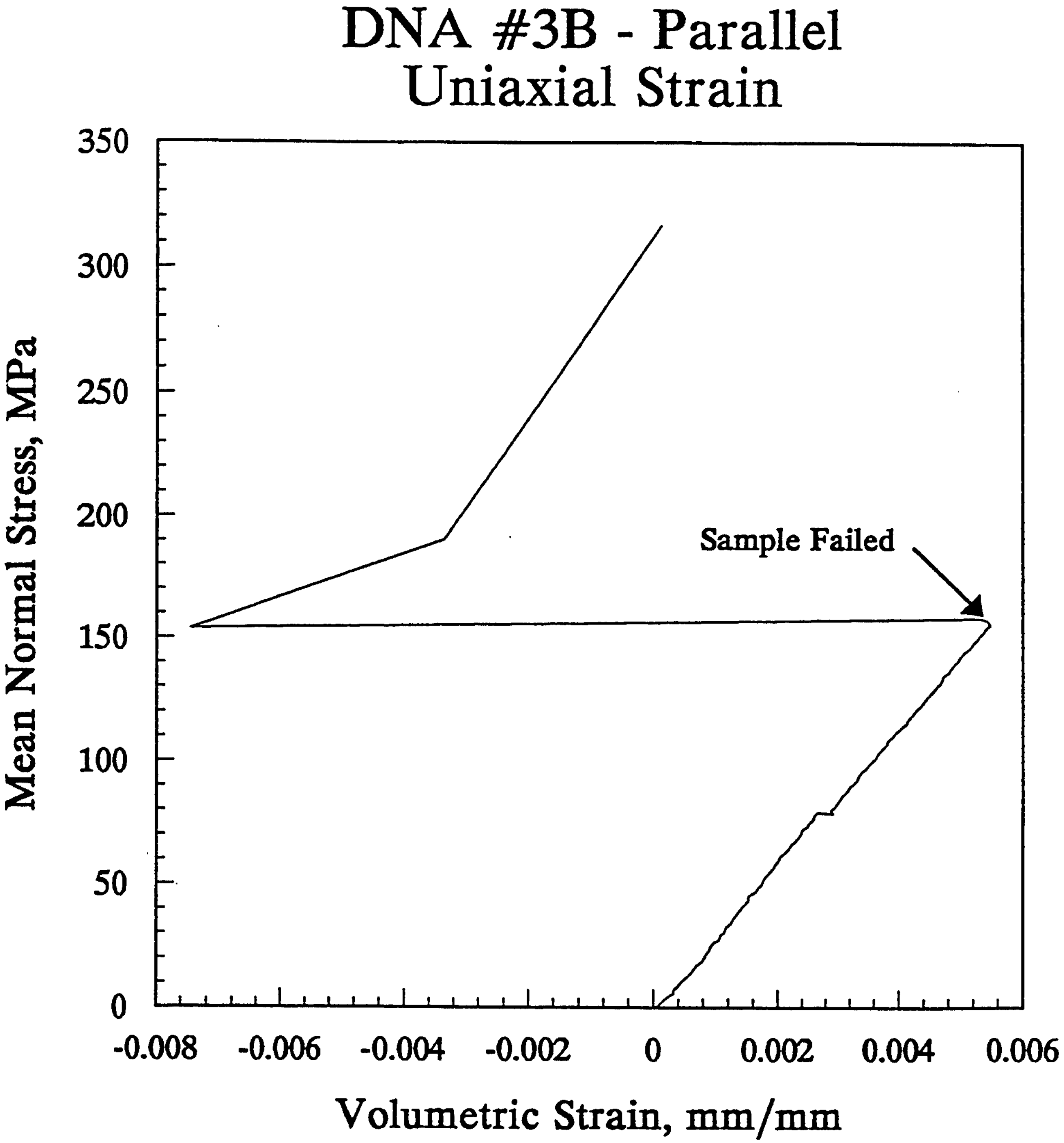

Figure D-49. Mean normal stress versus volumetric strain under uniaxial strain conditions for sample #3B - Parallel.

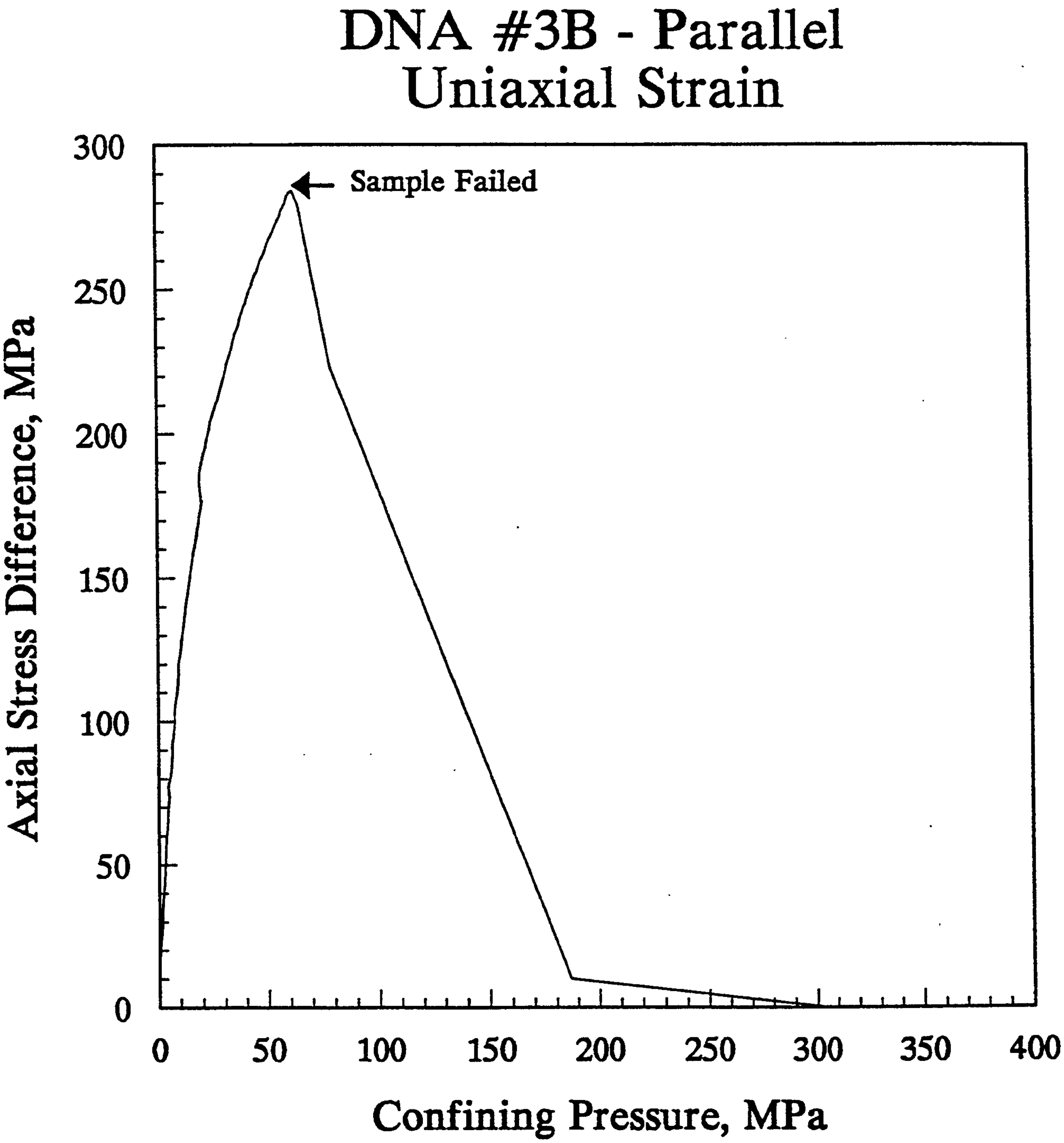

Figure D-50. Axial stress difference versus confining pressure under uniaxial strain conditions for sample #3B - Parallel.

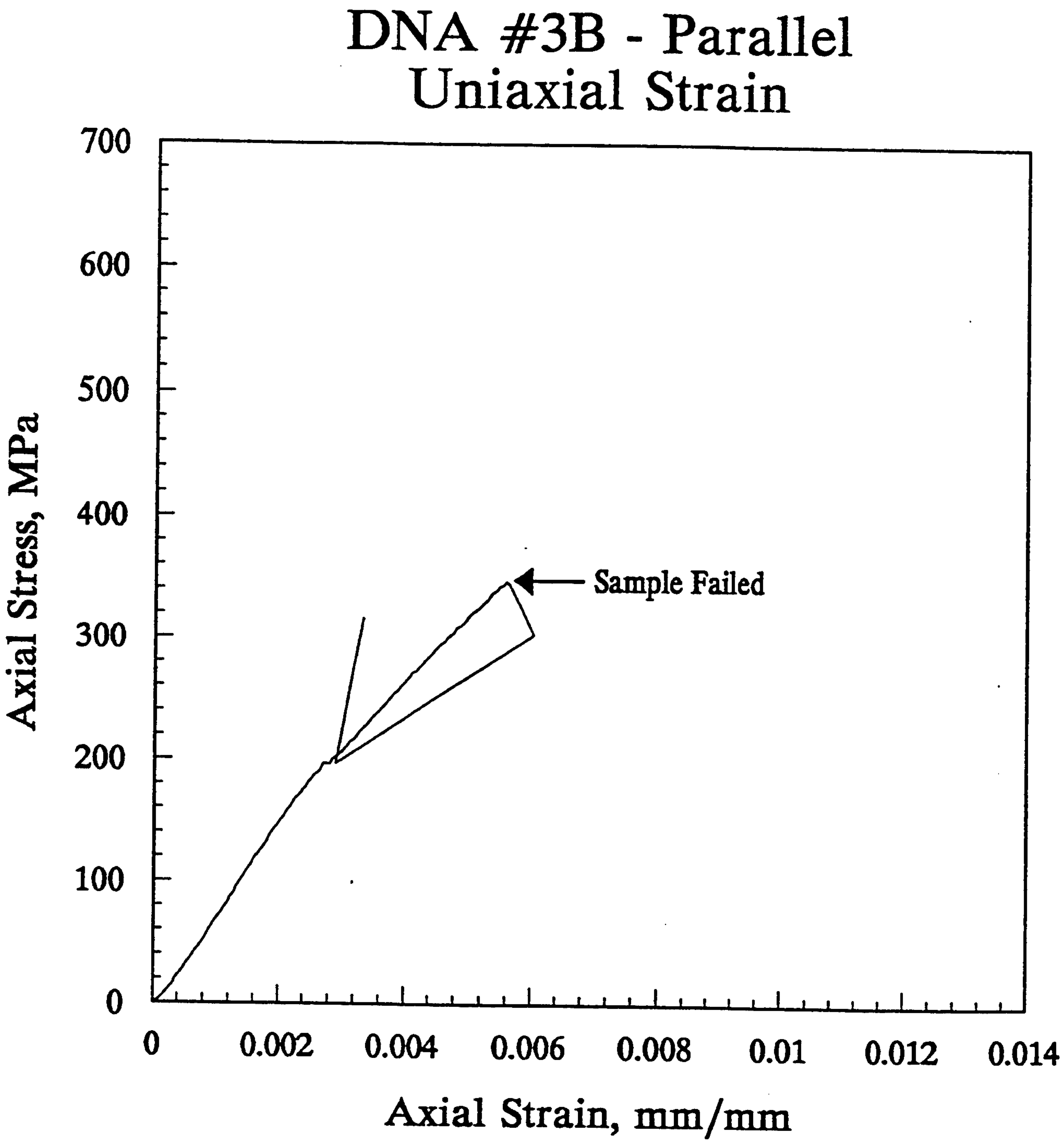

Figure D-51. Axial stress versus axial strain under uniaxial strain conditions for sample #3B - Parallel.

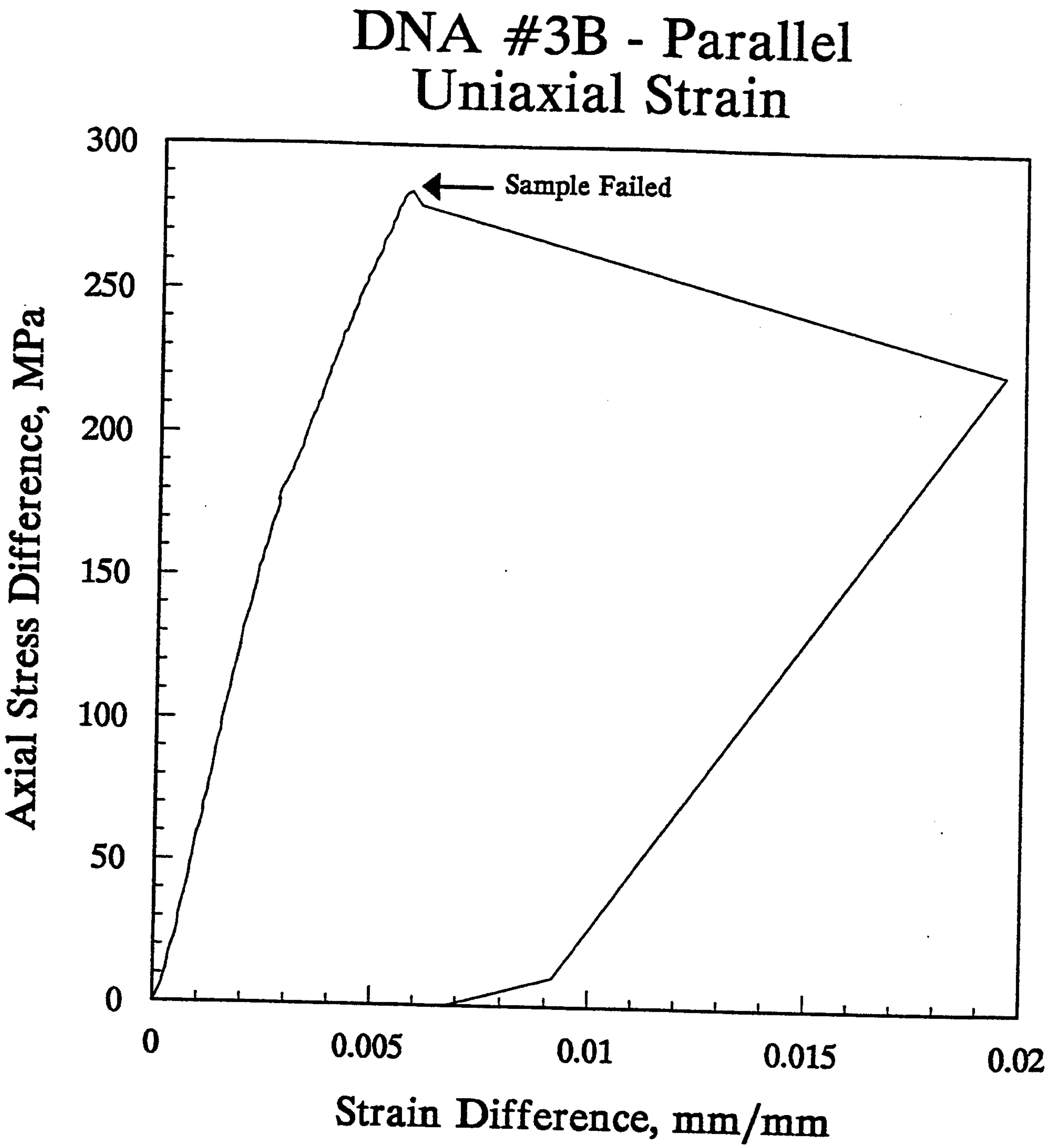

Figure D-52. Axial stress difference versus strain difference under uniaxial strain conditions for sample #3B - Parallel.

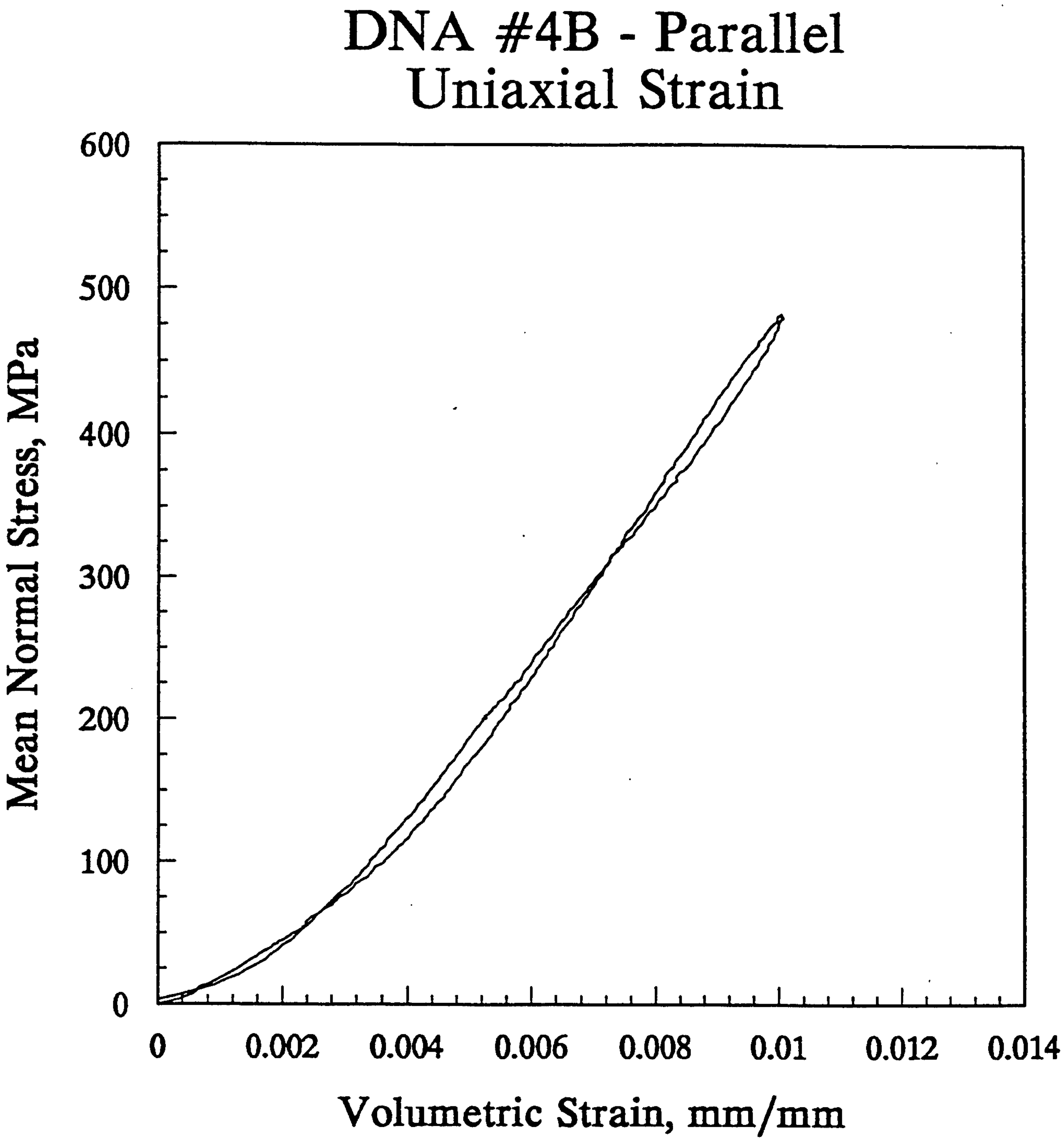

Figure D-53. Mean normal stress versus volumetric strain under uniaxial strain conditions for sample #4B - Parallel.

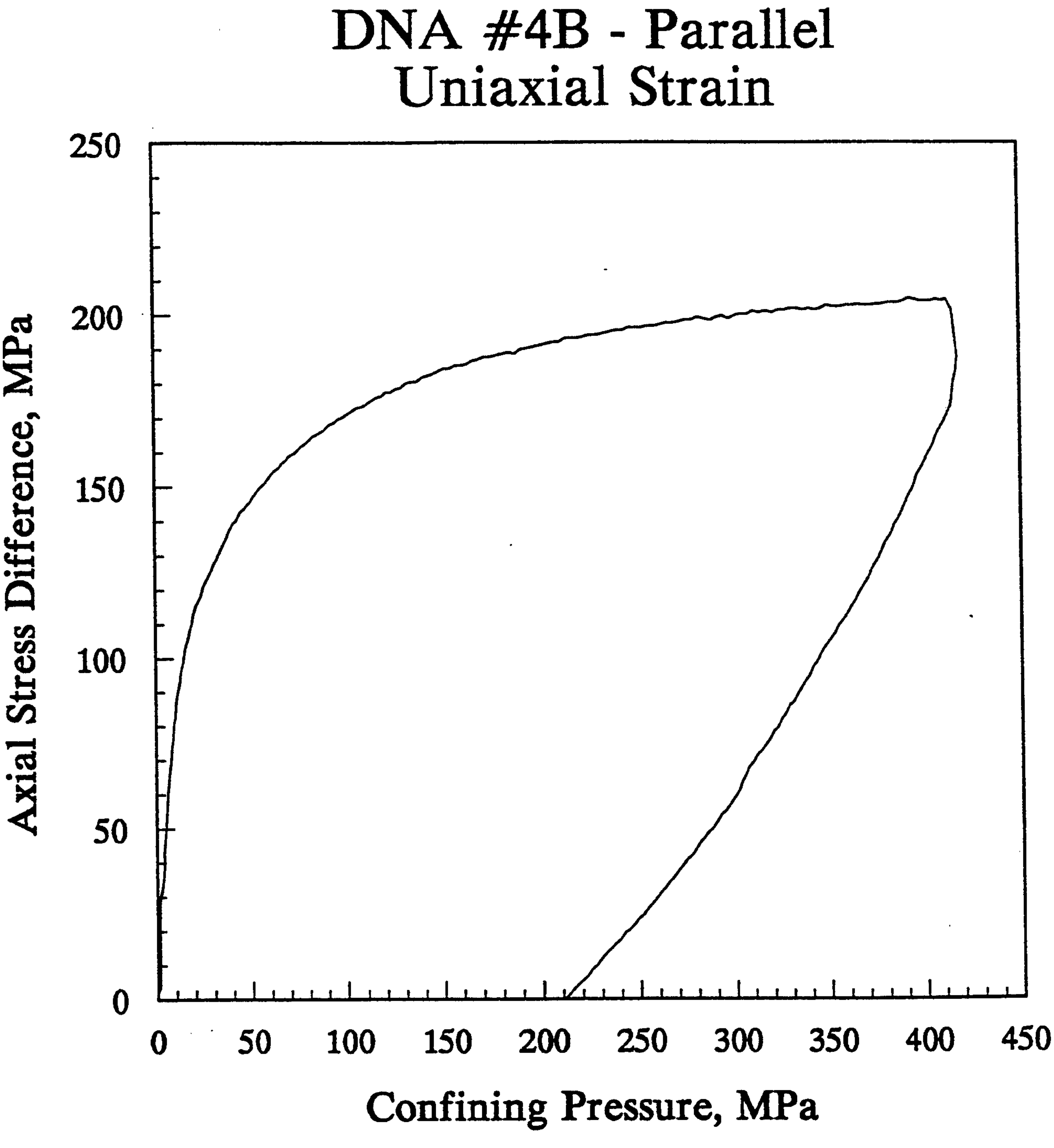

Figure D-54. Axial stress difference versus confining pressure under uniaxial stress conditions for sample #4B - Parallel.

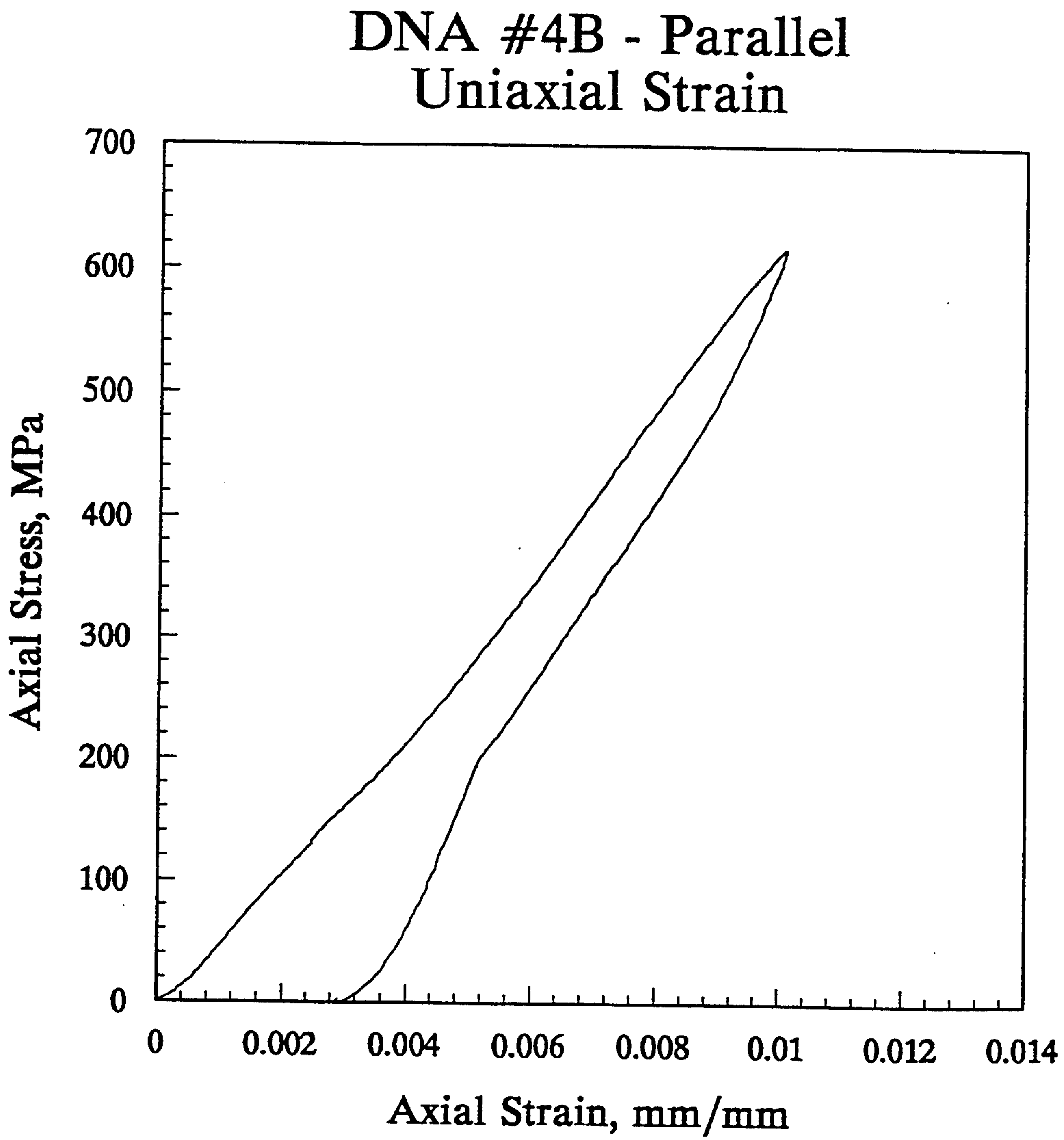

Figure D-55. Axial stress versus axial strain under uniaxial strain conditions for sample #4B - Parallel.

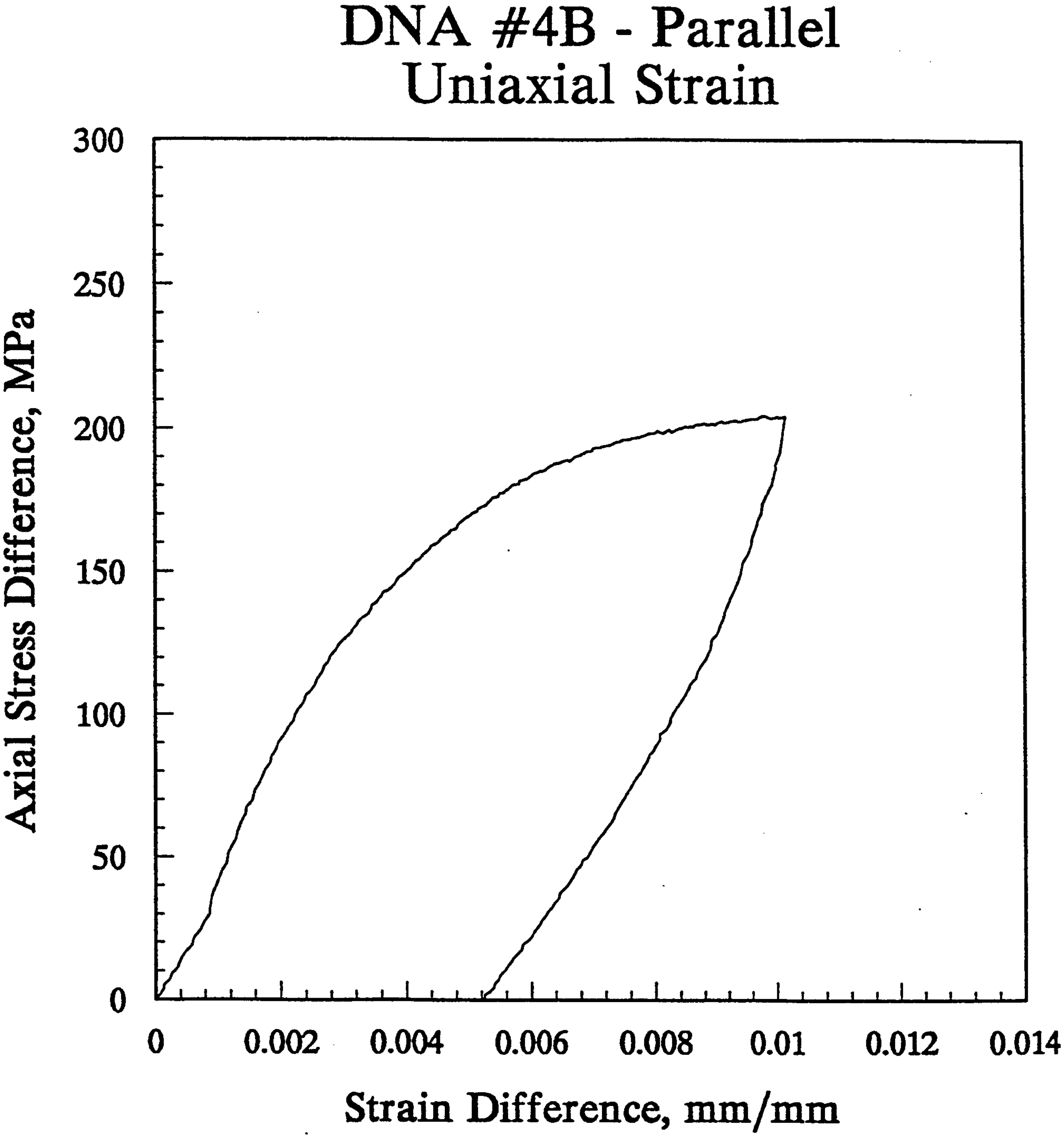

Figure D-56. Axial stress difference versus strain difference under uniaxial strain conditions for sample #4B - Parallel.

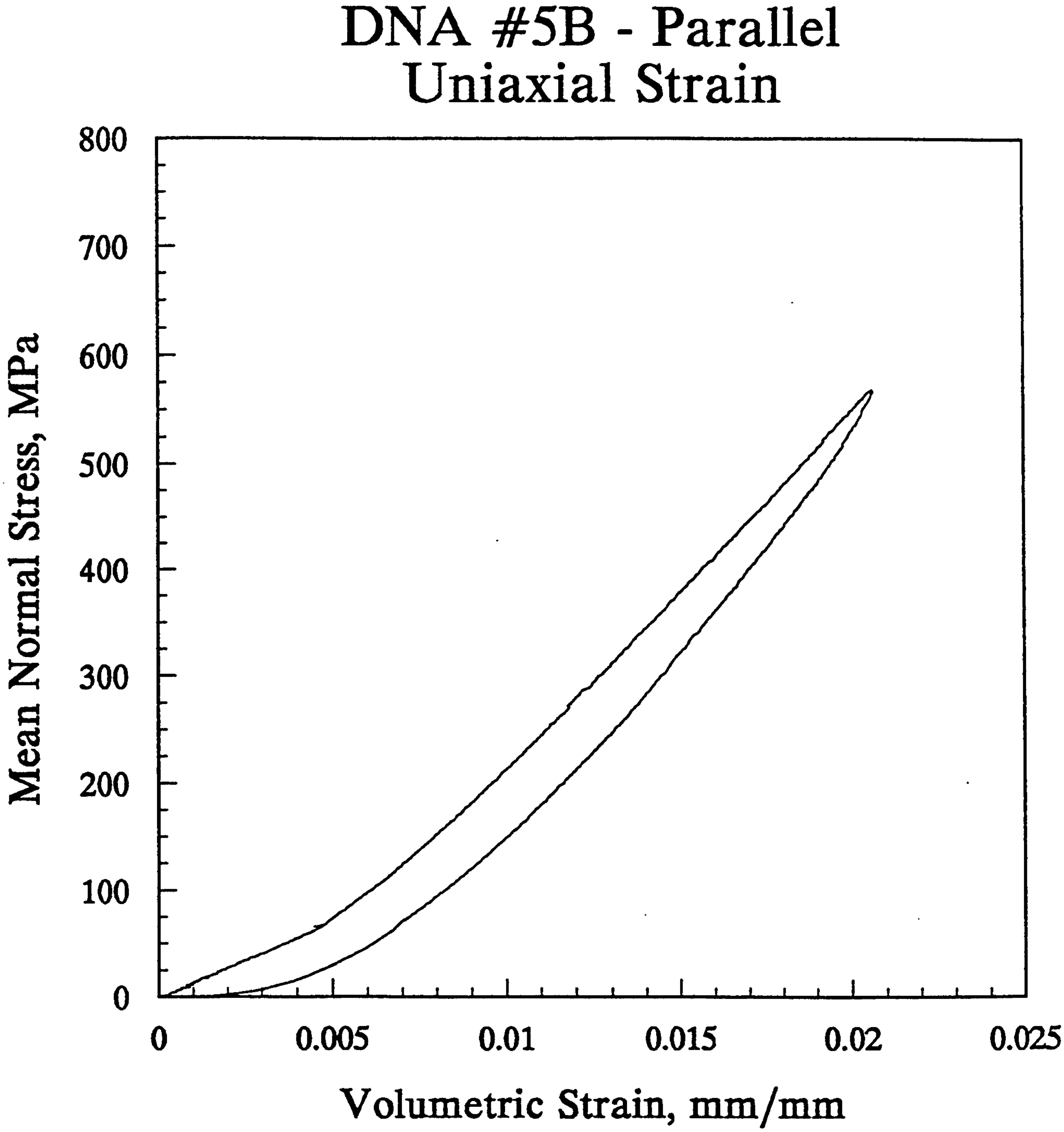

Figure D-57. Mean normal stress versus volumetric strain under uniaxial strain conditions for sample #5B - Parallel.

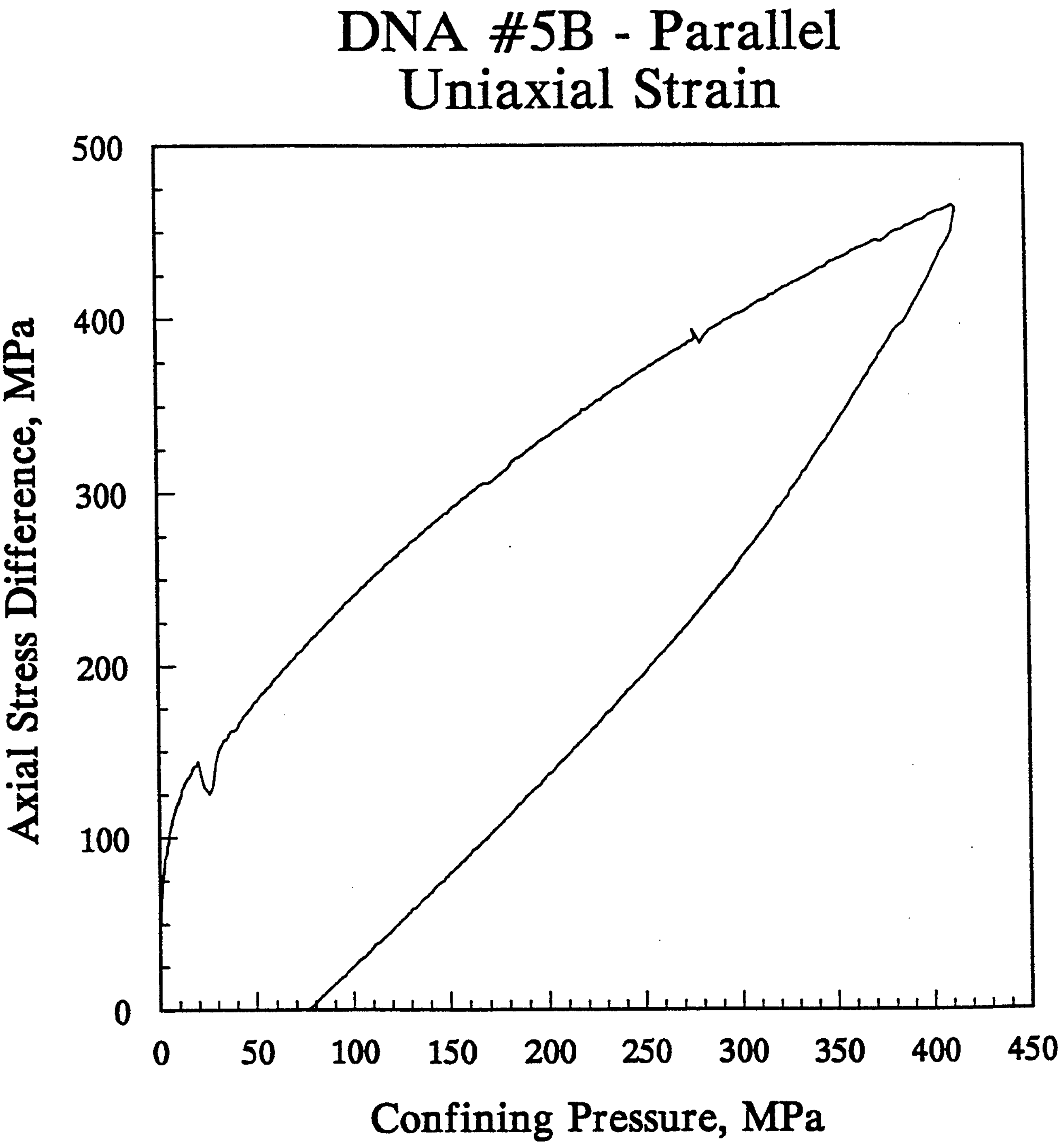

Figure D-58. Axial stress difference versus confining pressure under uniaxial strain conditions for sample #5B - Parallel.

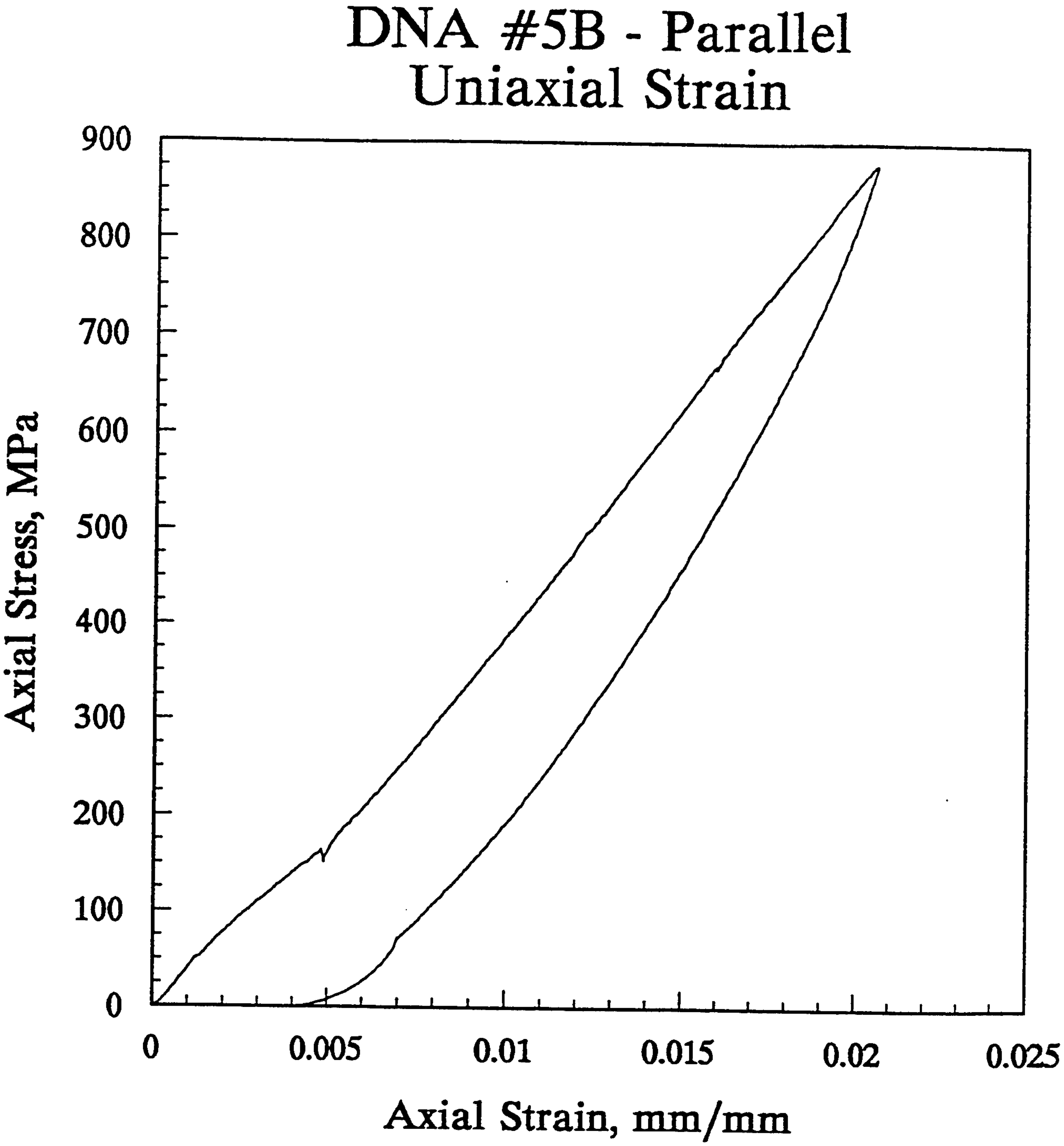

Figure D-59. Axial stress versus axial strain under uniaxial strain conditions for sample #5B - Parallel.

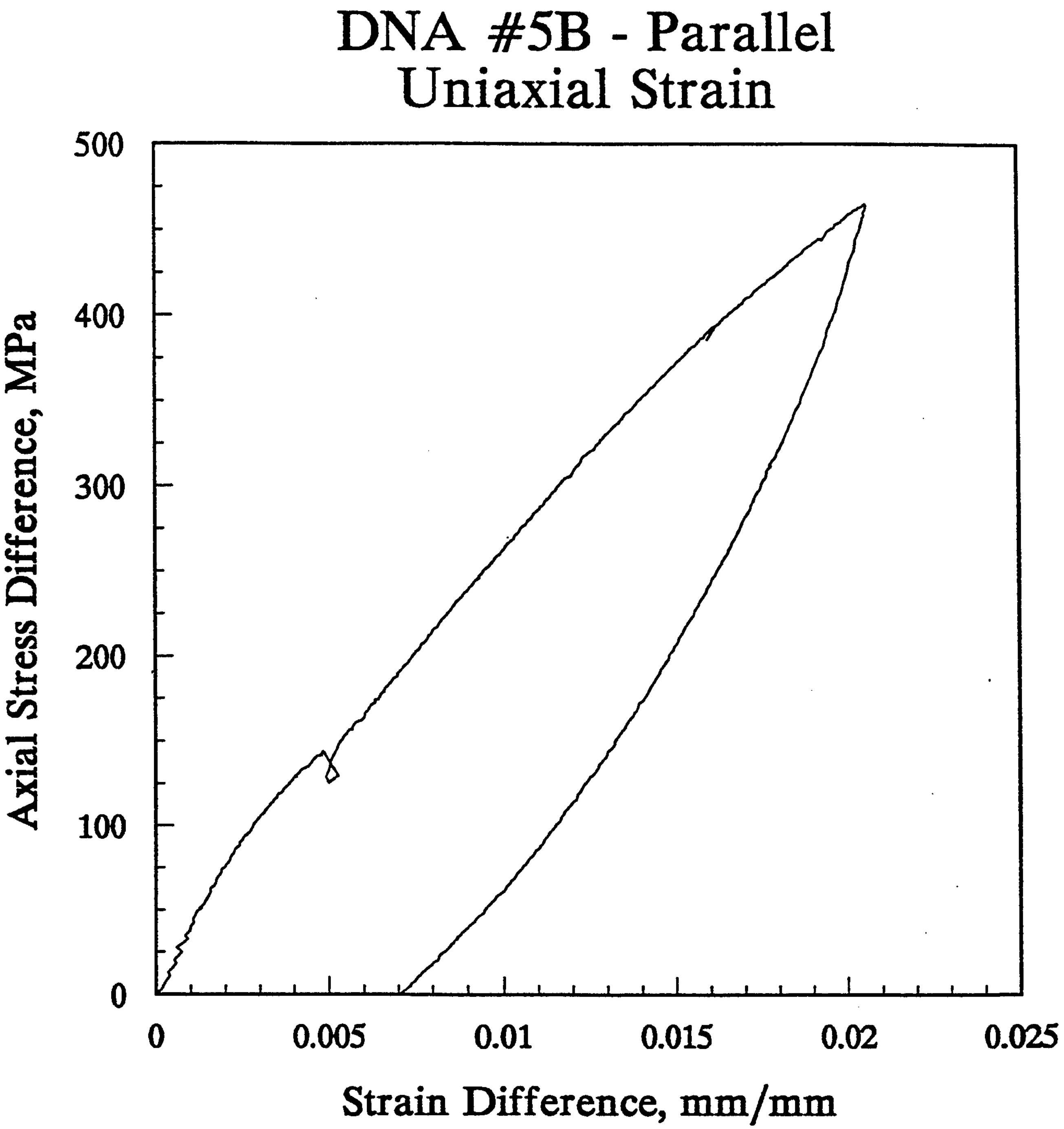

Figure D-60. Axial stress difference versus strain difference under uniaxial strain conditions for sample #5B - Parallel.

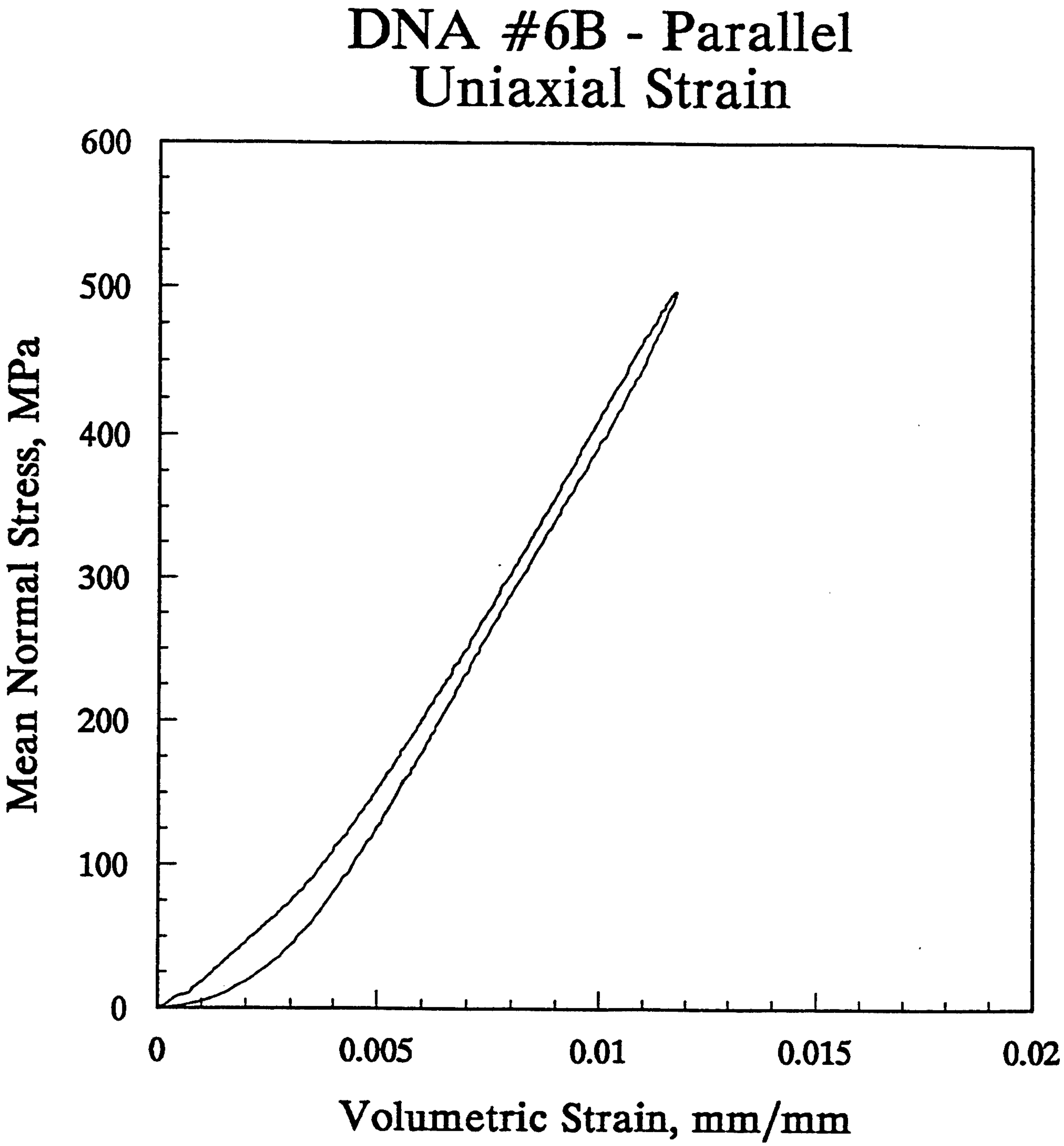

Figure D-61. Mean normal stress versus volumetric strain under uniaxial strain conditions for sample #6B - Parallel.

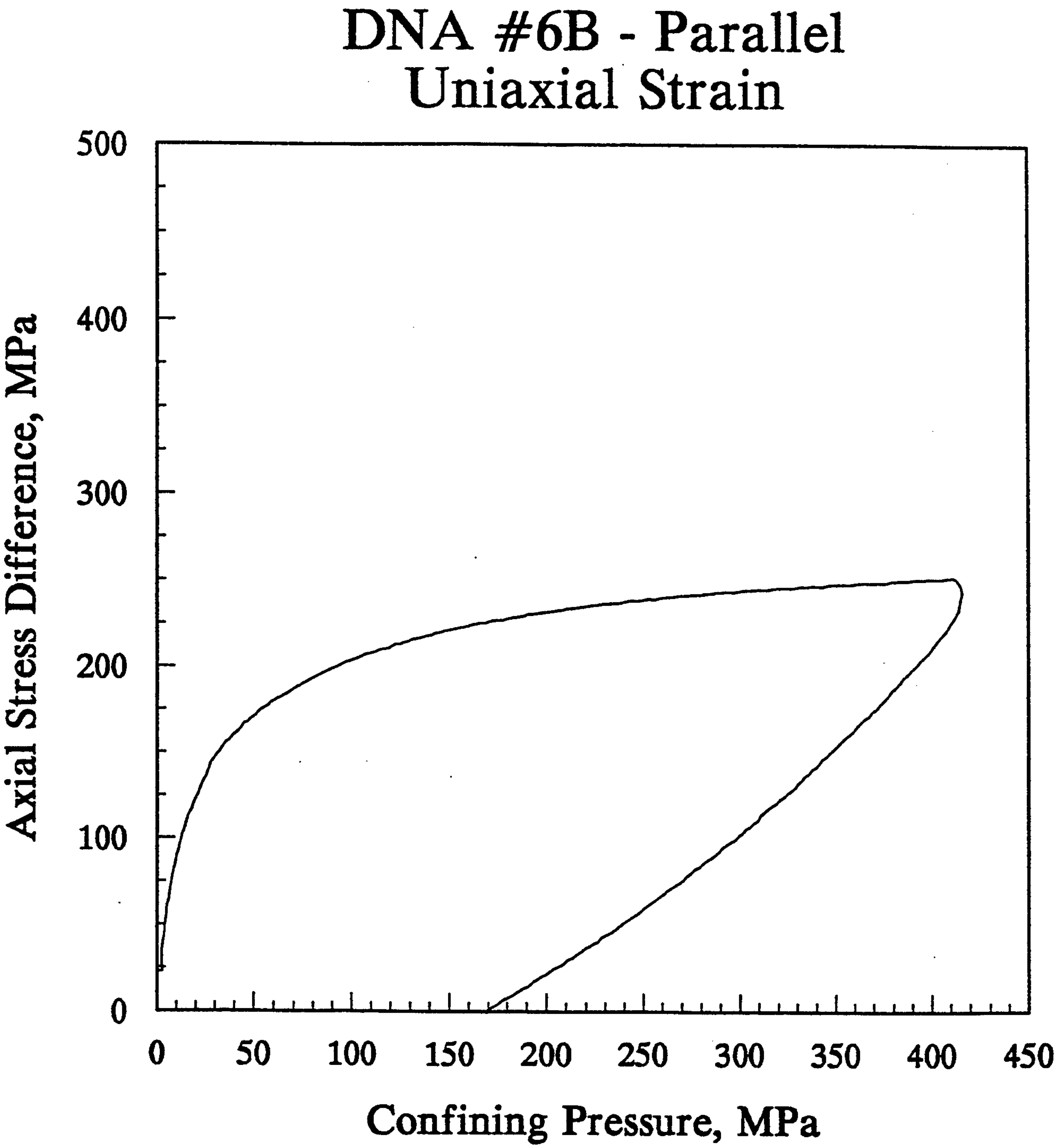

Figure D-62. Axial stress difference versus confining pressure under uniaxial strain conditions for sample #6B - Parallel.

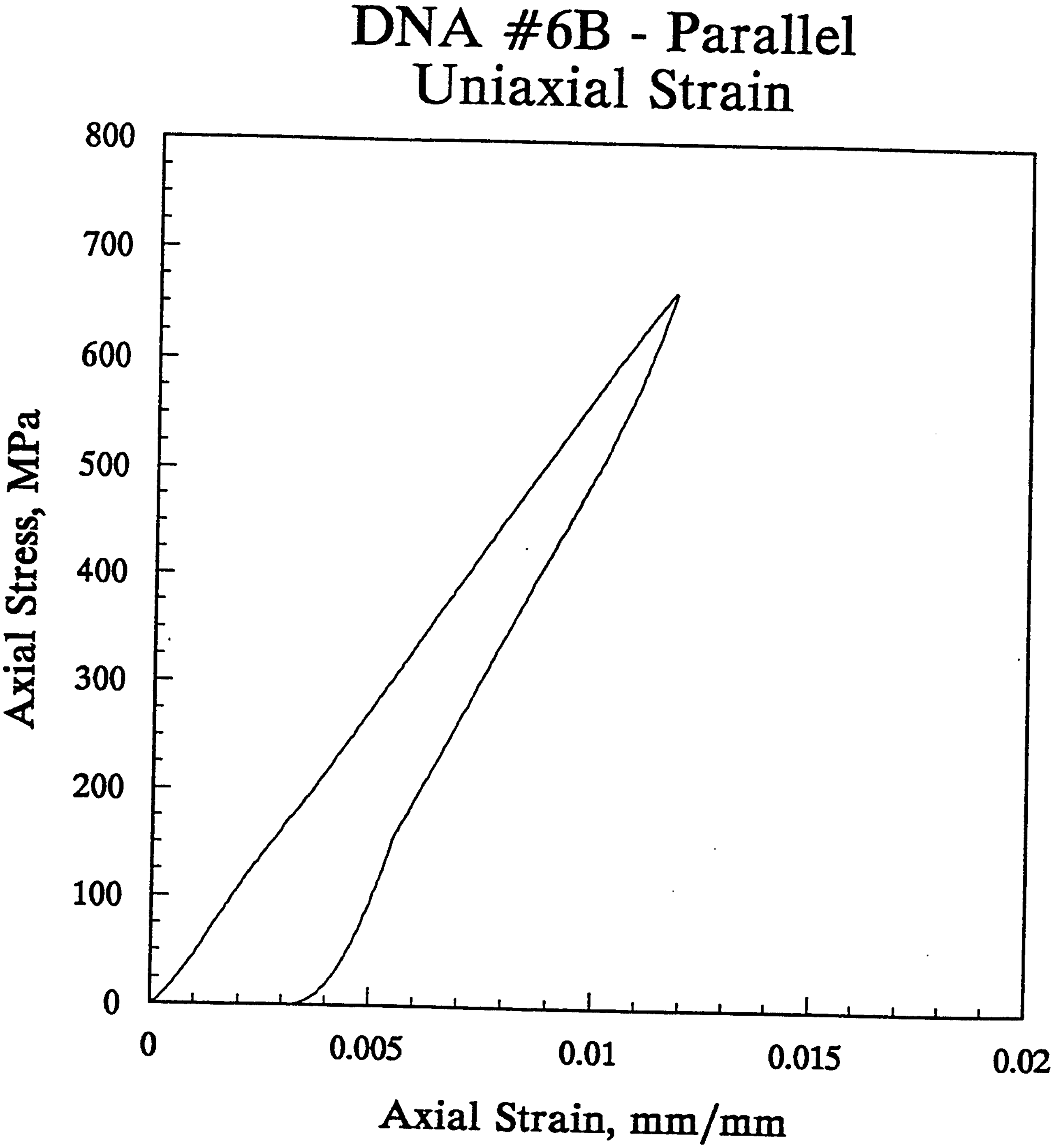

Figure D-63. Axial stress versus axial strain under uniaxial strain conditions for sample #6B - Parallel.

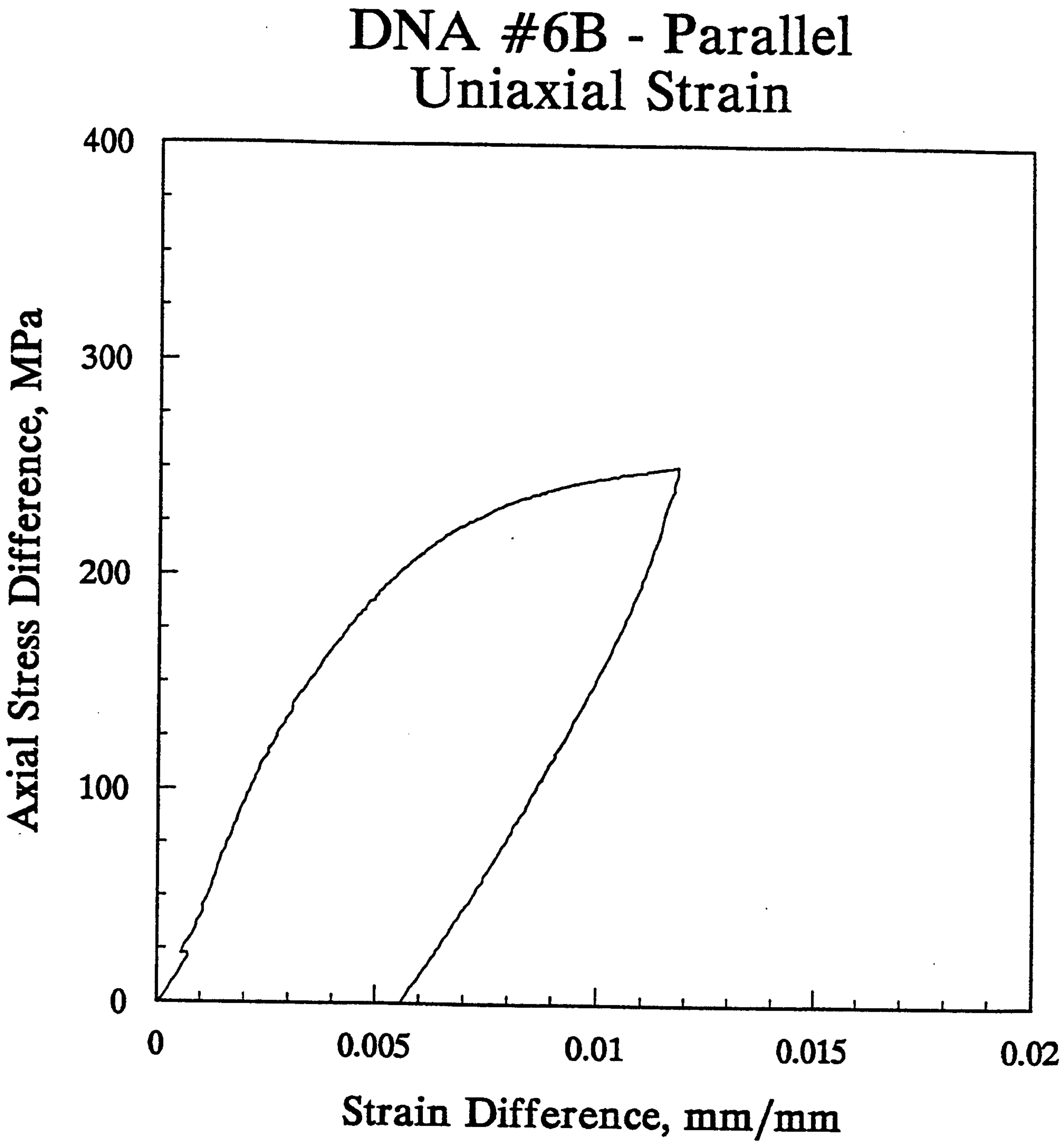

Figure D-64. Axial stress difference versus strain difference under uniaxial strain conditions for sample #6B - Parallel.

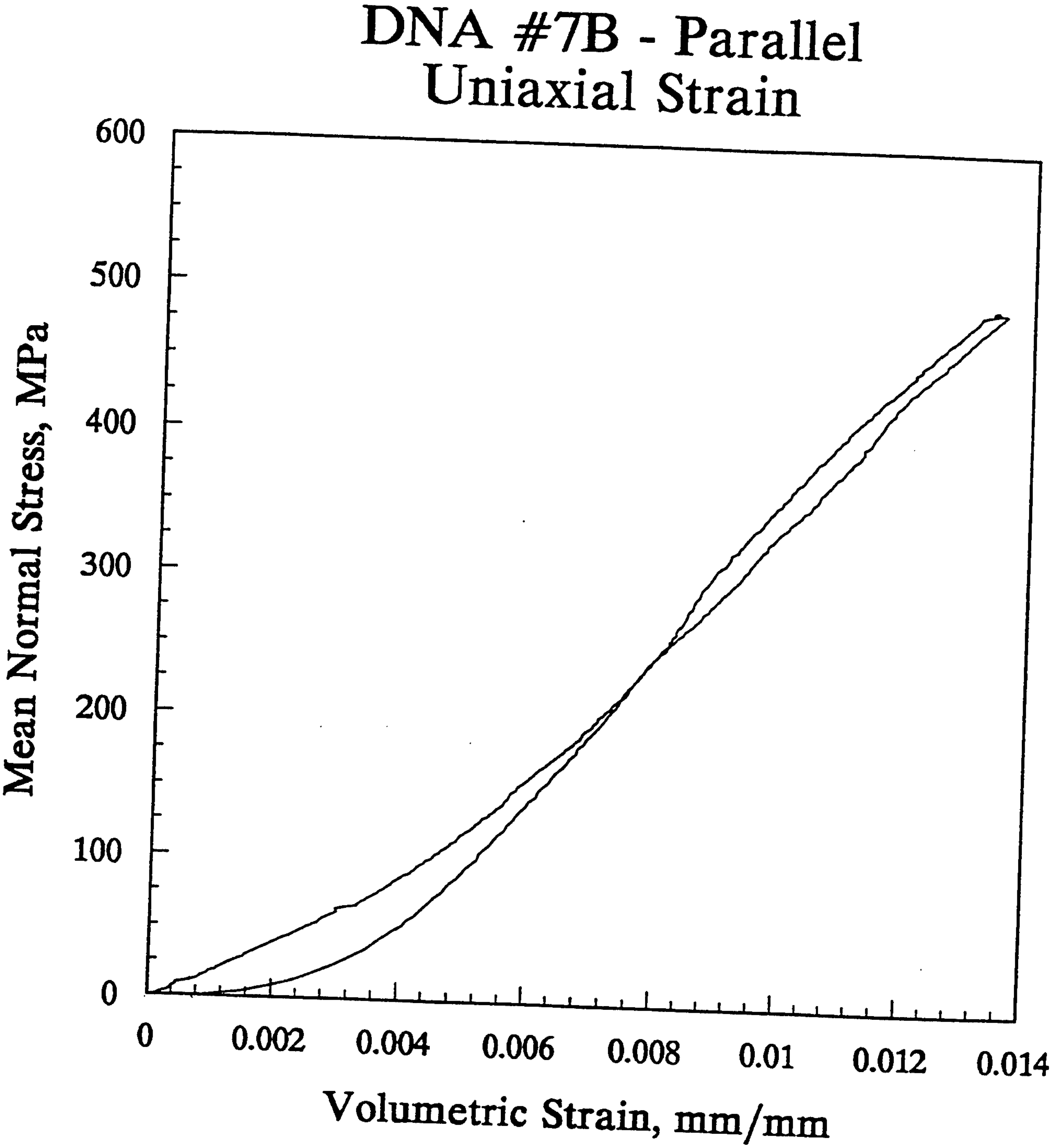

Figure D-65. Mean normal stress versus volumetric strain under uniaxial strain conditions for sample #7B - Parallel.

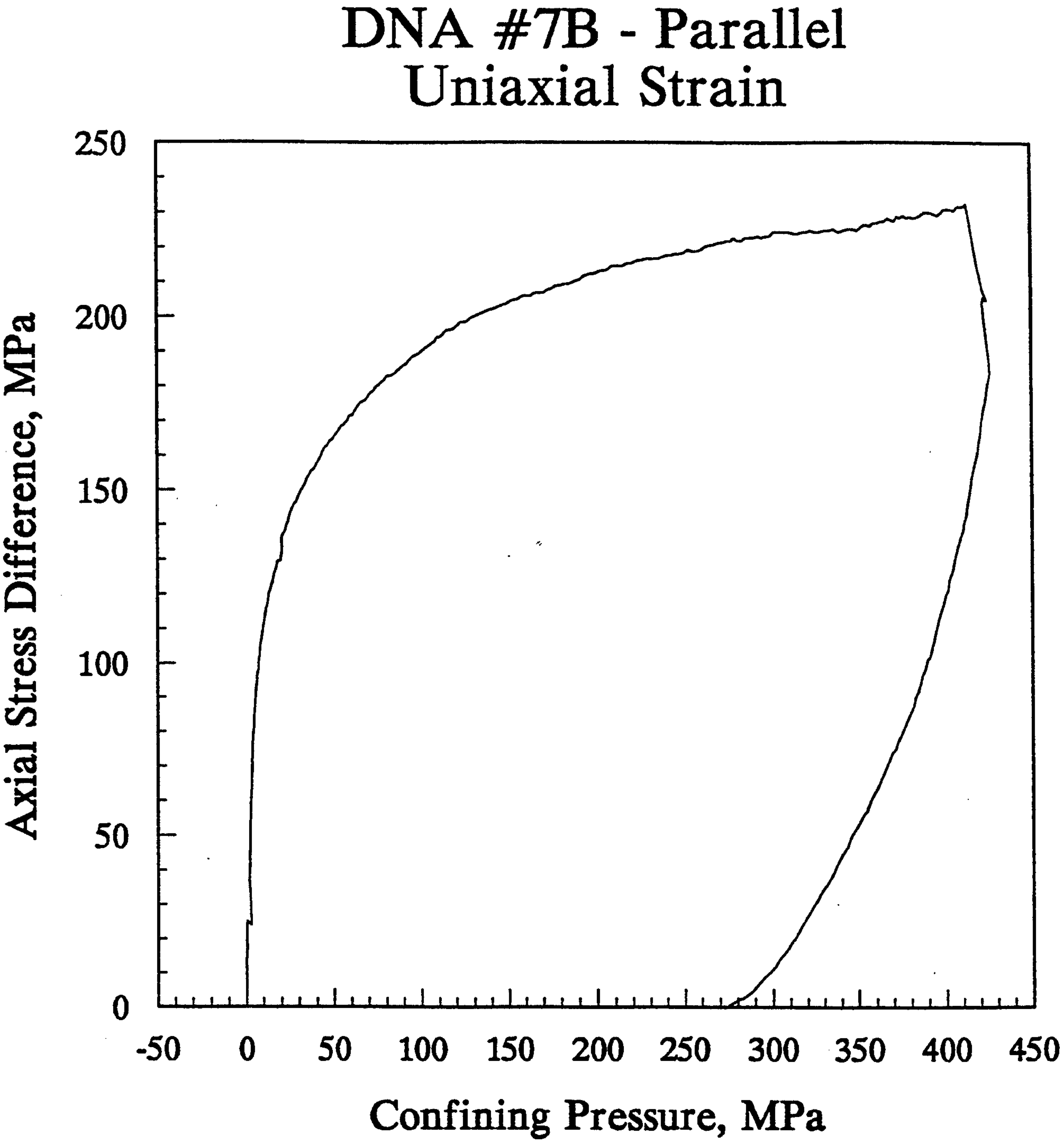

Figure D-66. Axial stress difference versus confining pressure under uniaxial strain conditions for sample #7B - Parallel.

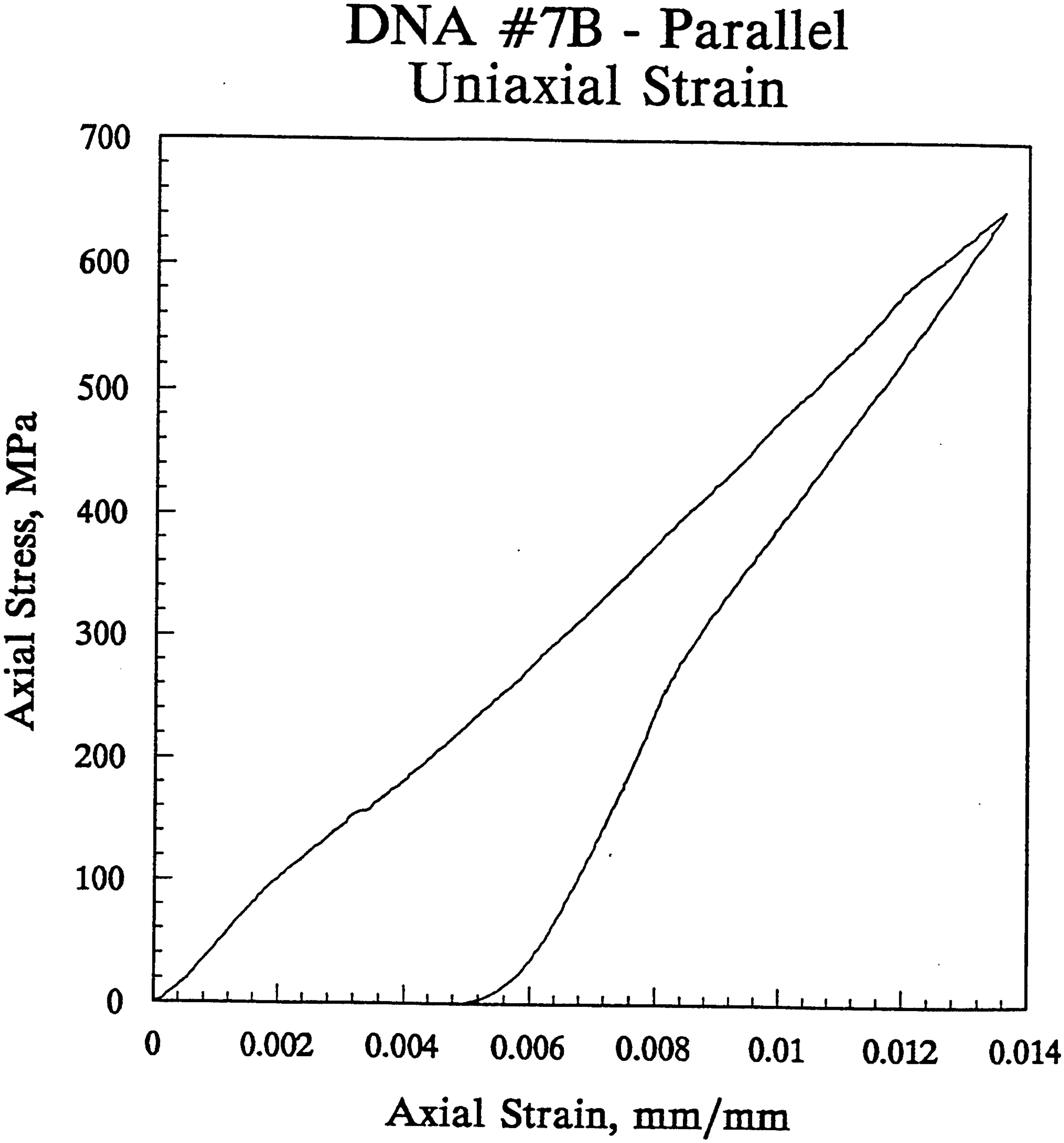

Figure D-67. Axial stress versus axial strain under uniaxial strain conditions for sample #7B - Parallel.

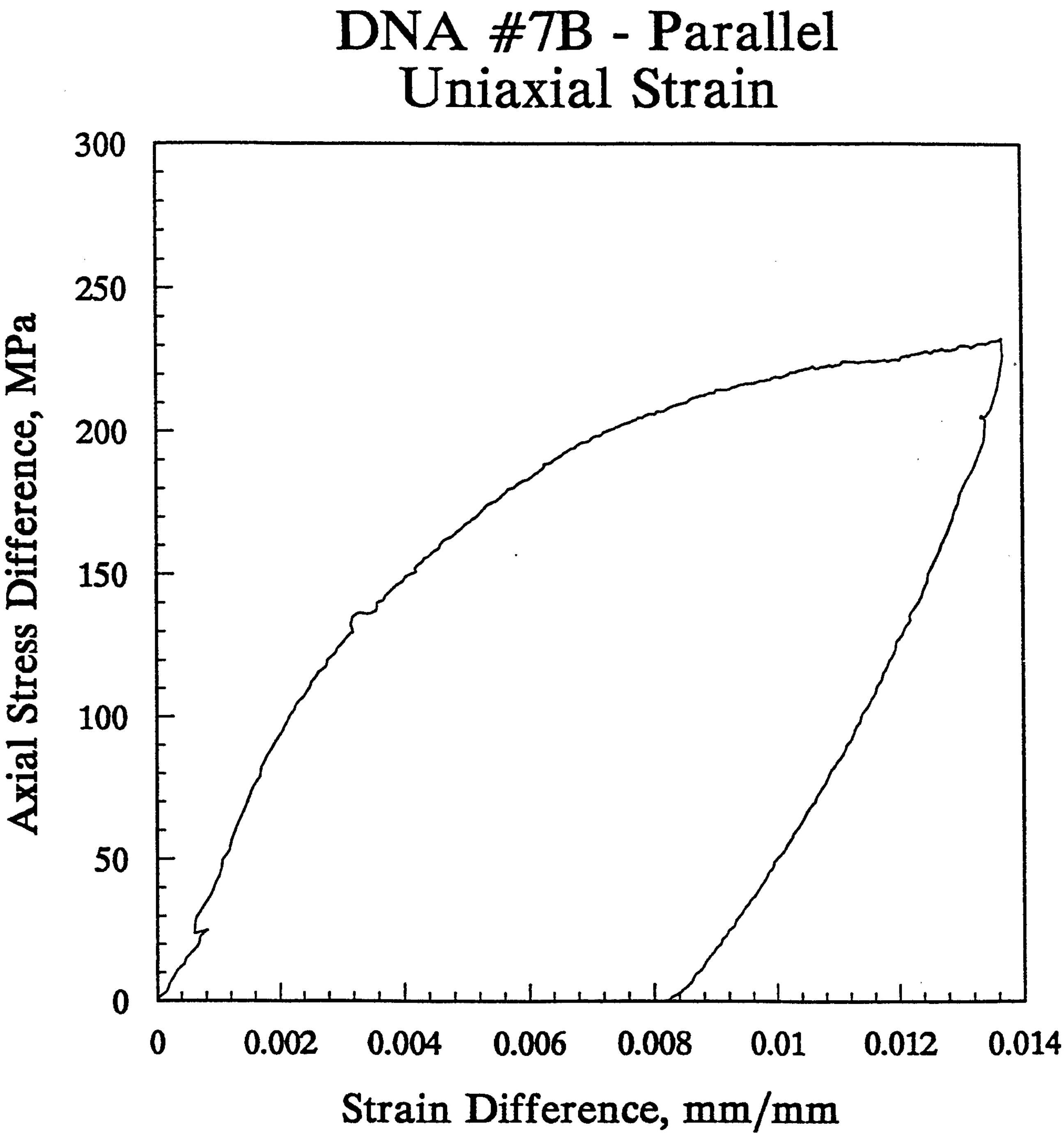

Figure D-68. Axial stress difference versus strain difference under uniaxial strain conditions for sample #7B - Parallel.

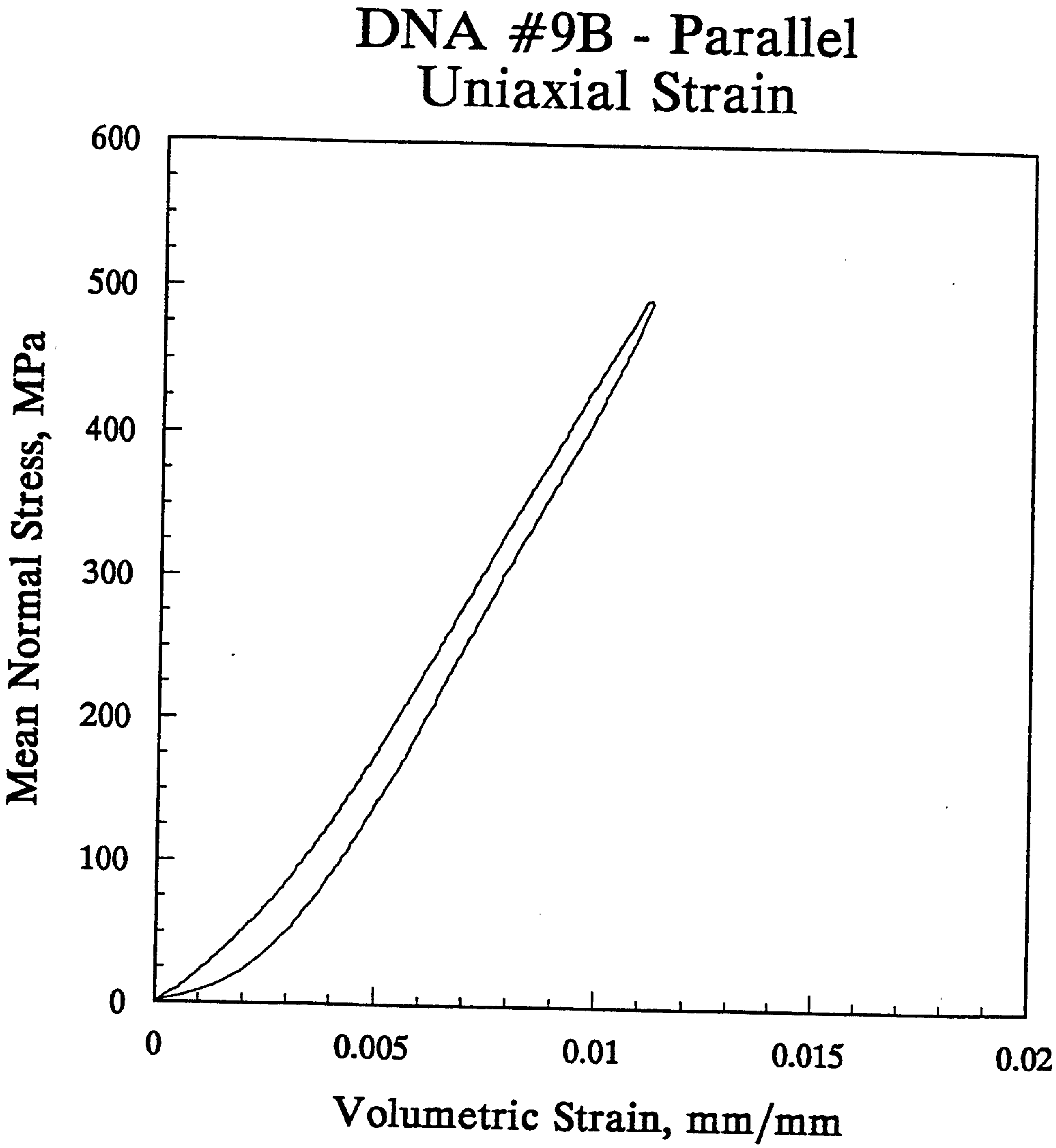

Figure D-69. Mean normal stress versus volumetric strain under uniaxial strain conditions for sample #9B - Parallel.

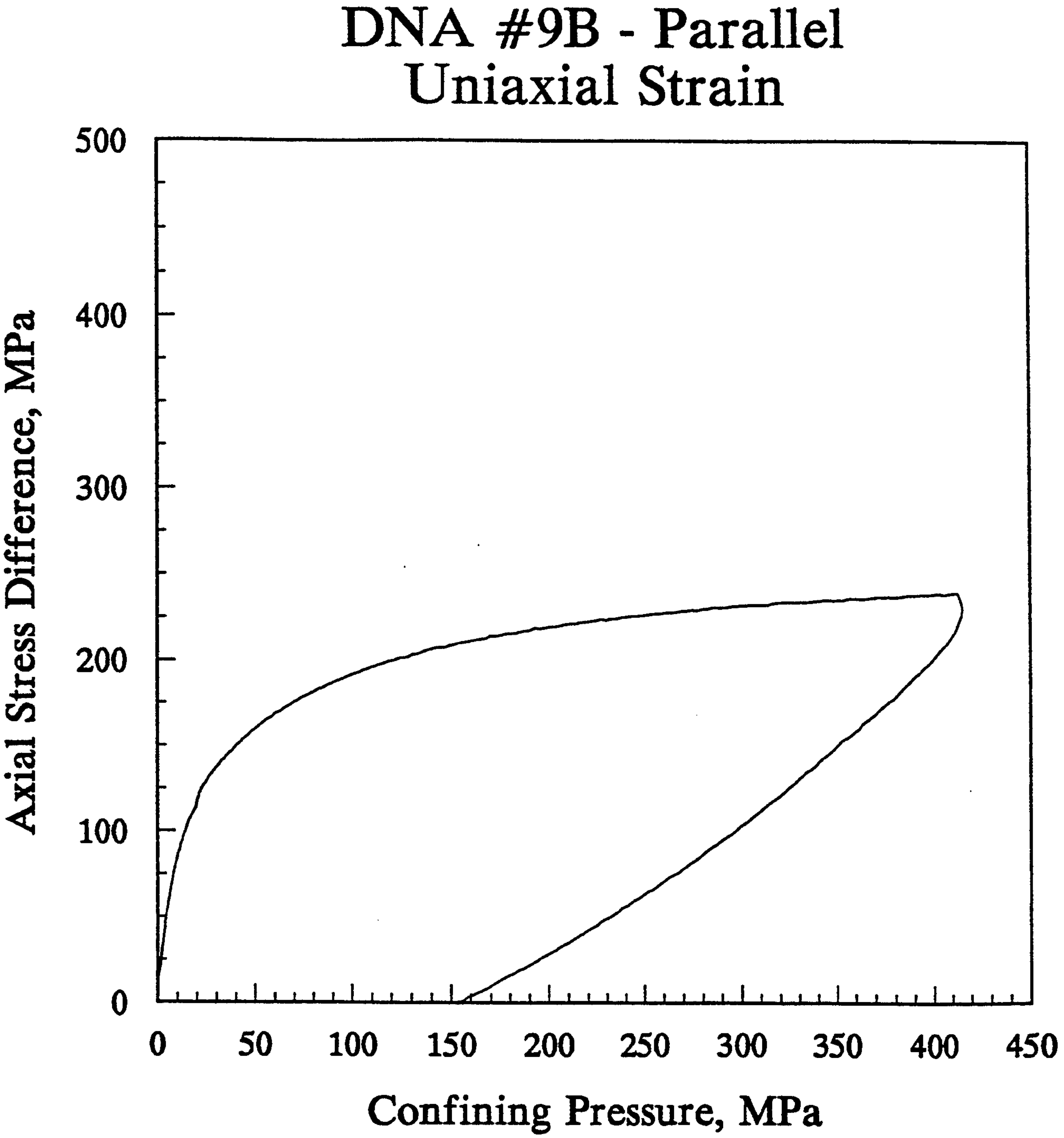

Figure D-70. Axial stress difference versus confining pressure under uniaxial strain conditions for sample #9B - Parallel.

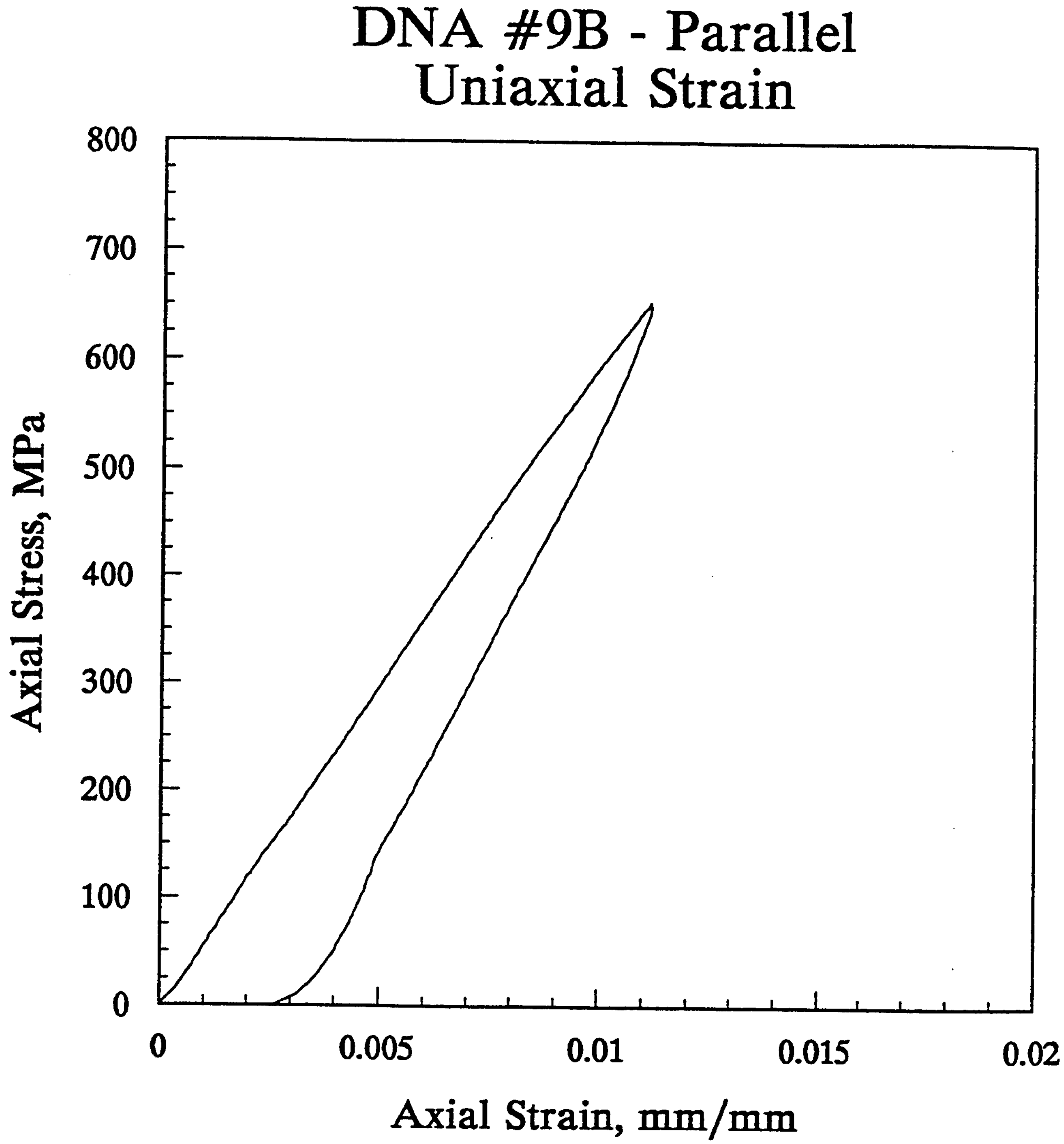

Figure D-71. Axial stress versus axial strain under uniaxial strain conditions for sample #9B - Parallel.

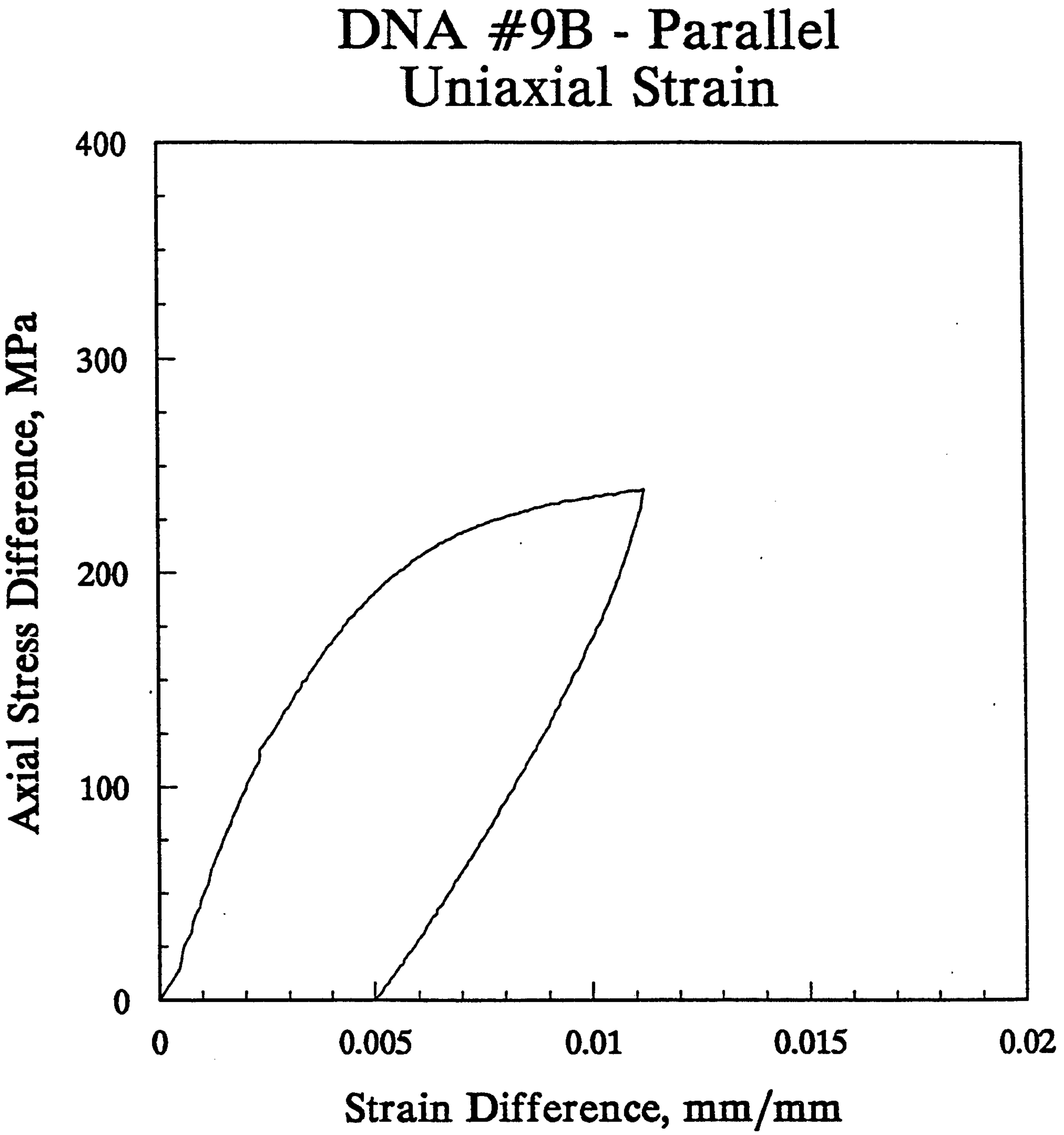

Figure D-72. Axial stress difference versus strain difference under uniaxial strain conditions for sample #9B - Parallel.

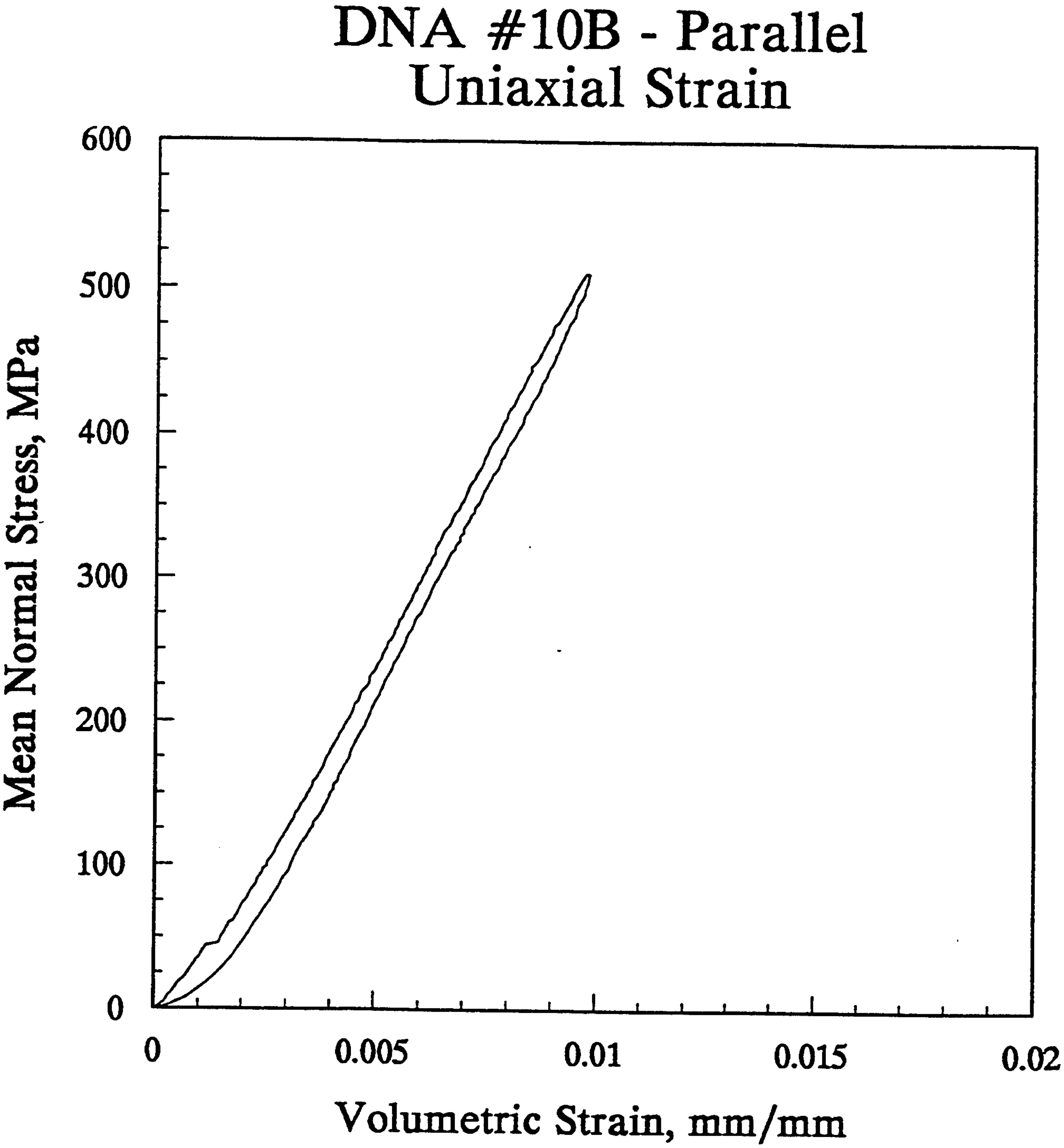

Figure D-73. Mean normal stress versus volumetric strain under uniaxial strain conditions for sample #10B - Parallel.

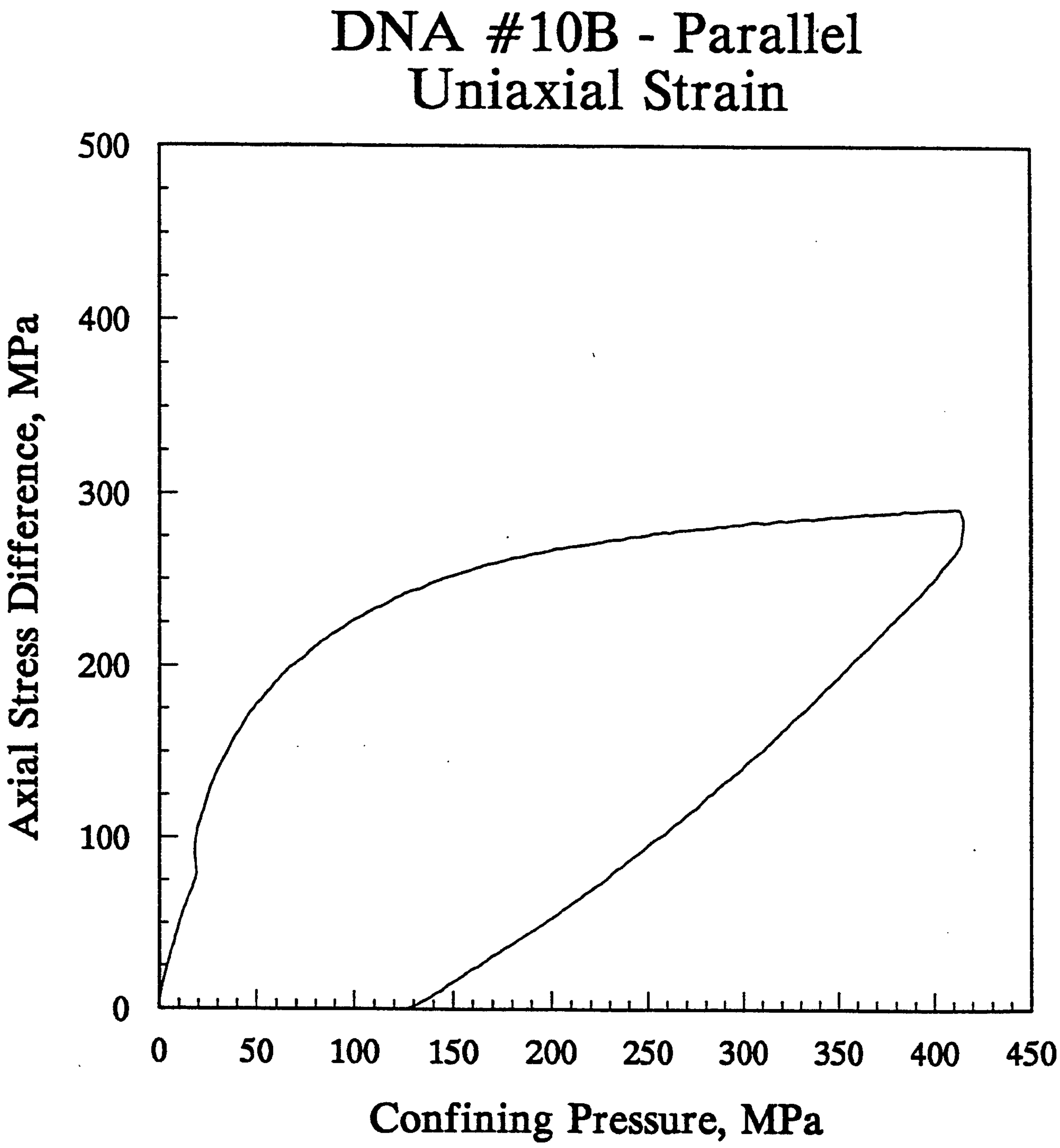

Figure D-74. Axial stress difference versus confining pressure under uniaxial strain conditions for sample #10B - Parallel.

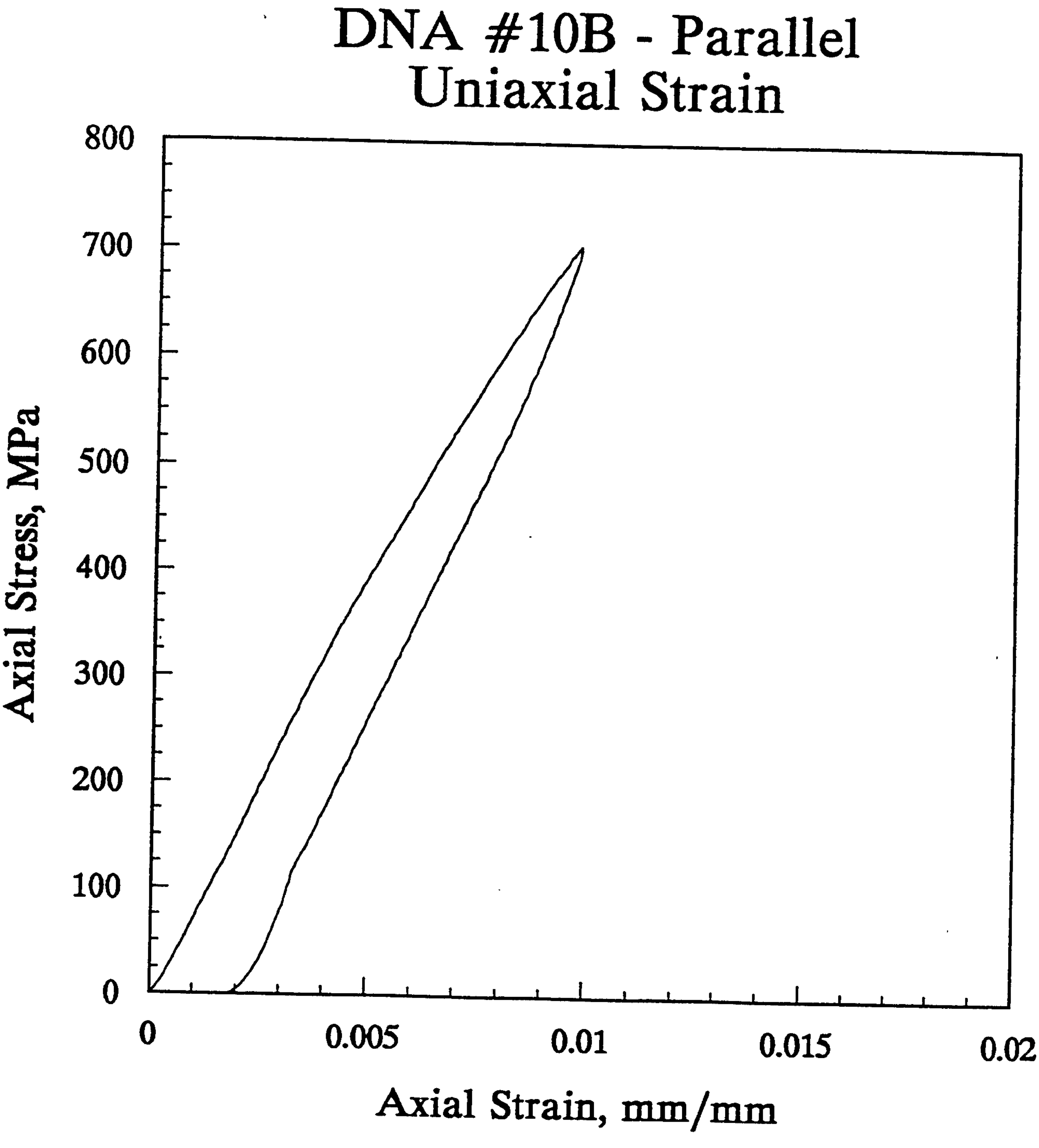

Figure D-75. Axial stress versus axial strain under uniaxial strain conditions for sample #10B - Parallel.

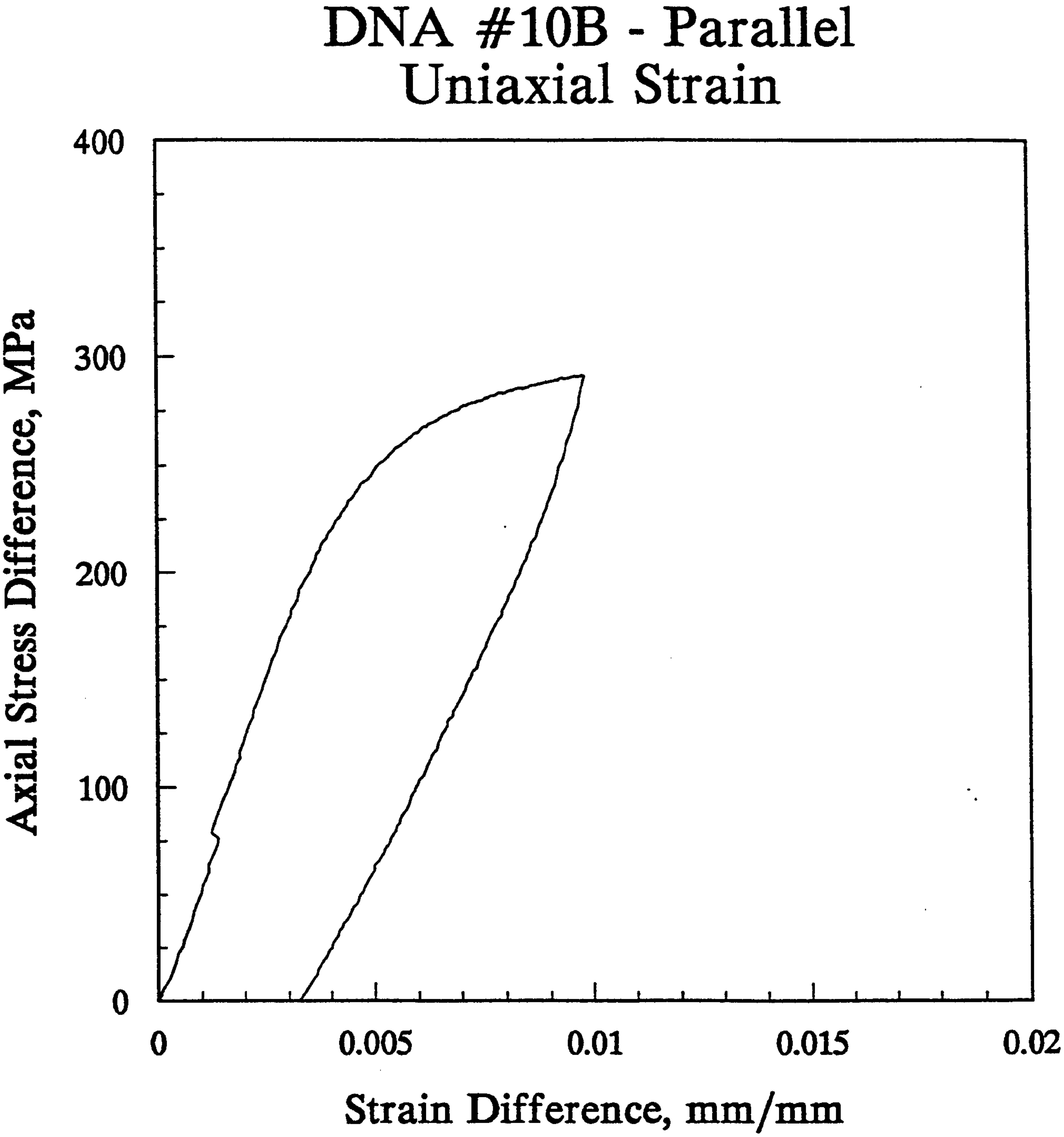

Figure D-76. Axial stress difference versus strain difference under uniaxial strain conditions for sample #10B - Parallel.

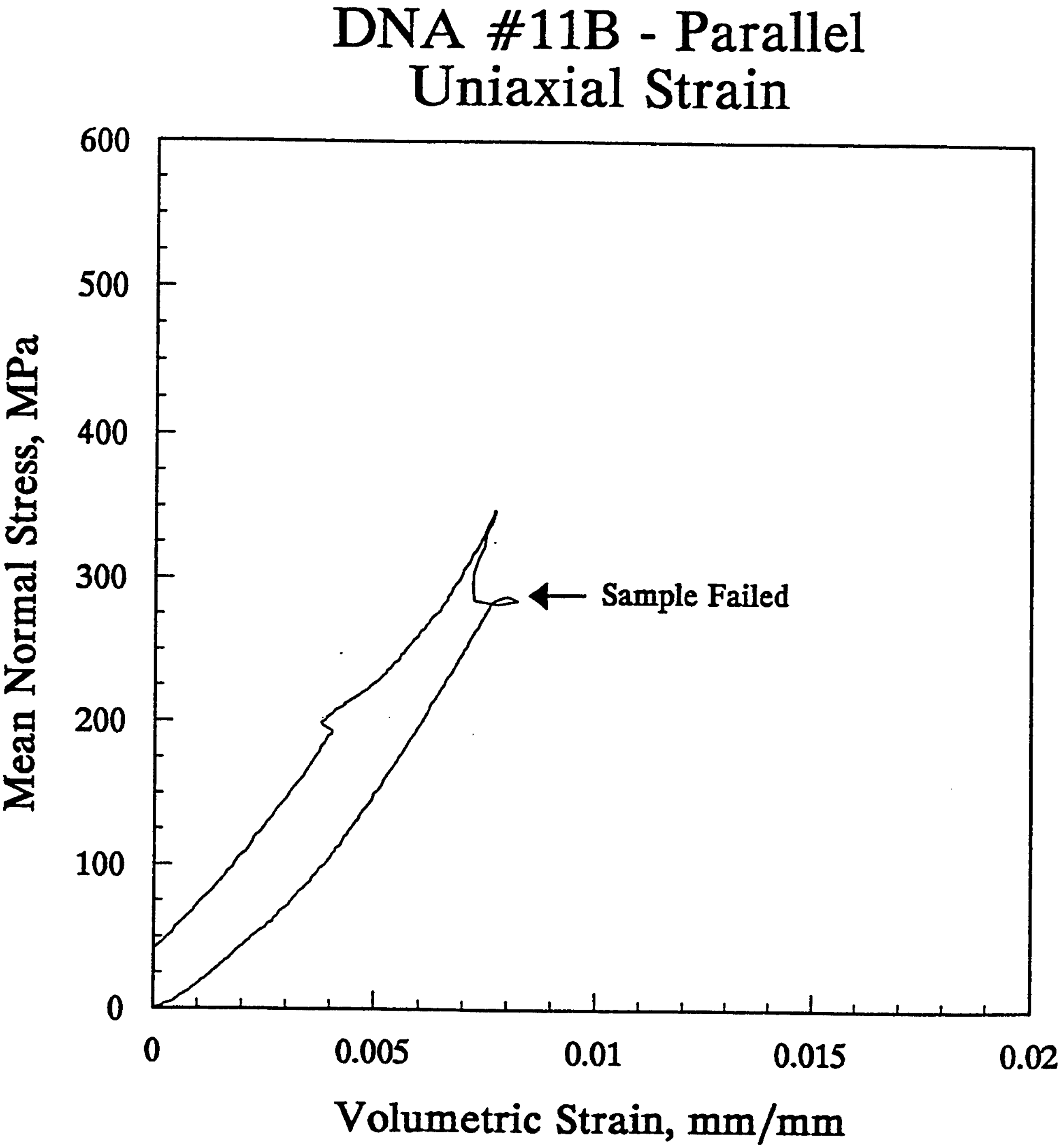

Figure D-77. Mean normal stress versus volumetric strain under uniaxial strain conditions for sample #11B - Parallel.

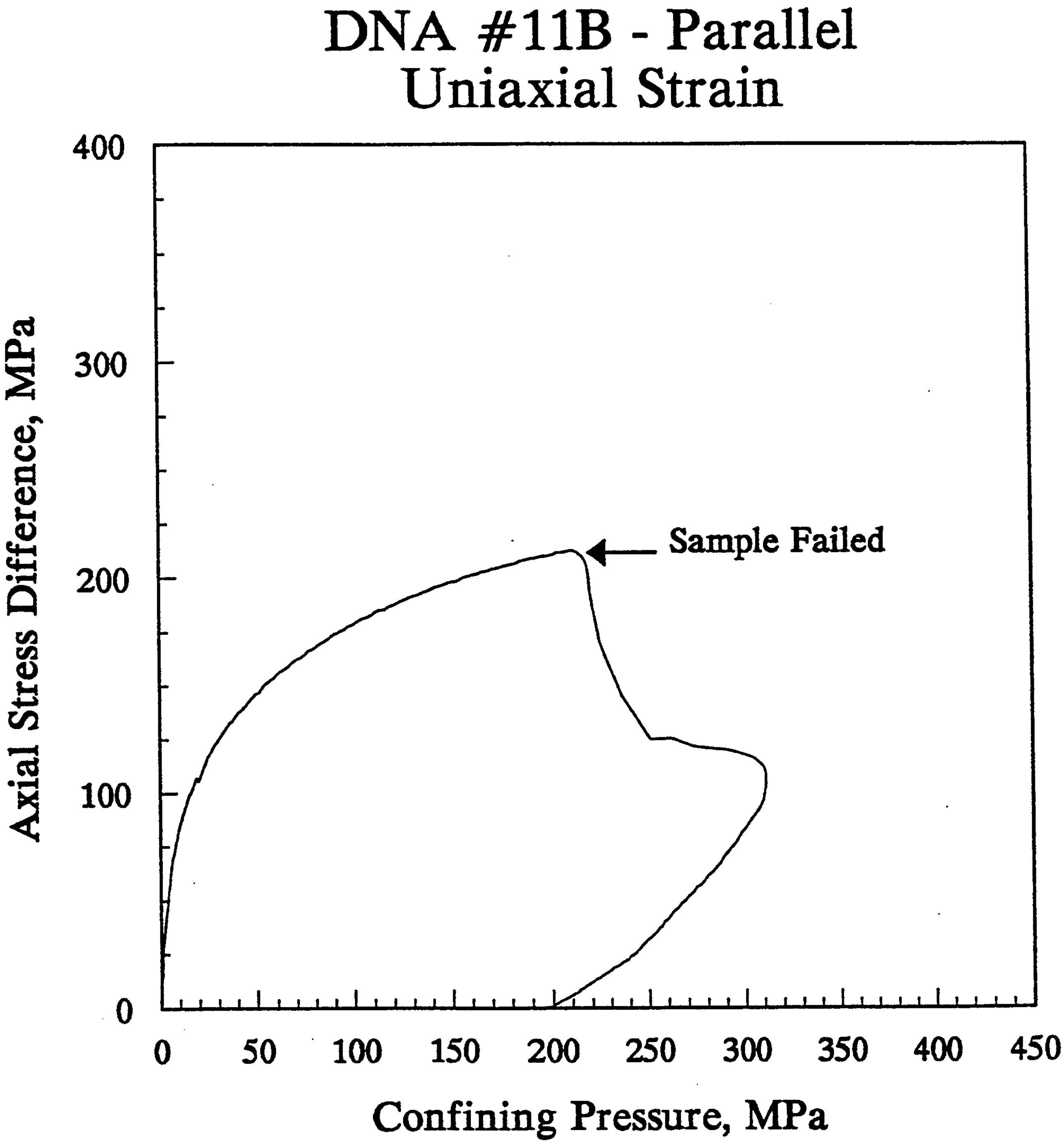

Figure D-78. Axial stress difference versus confining pressure under uniaxial strain conditions for sample #11B - Parallel.

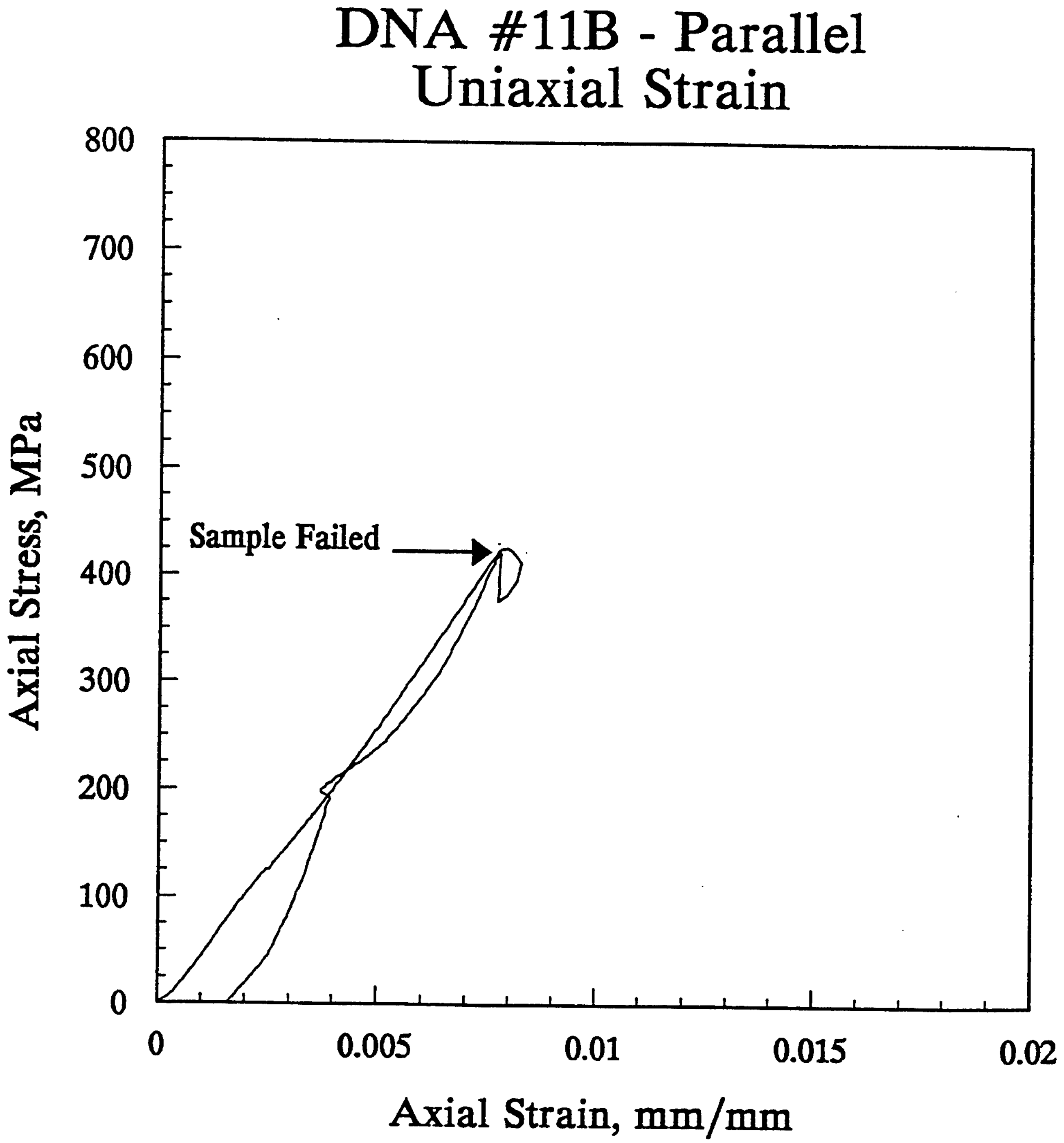

Figure D-79. Axial stress versus axial strain under uniaxial strain conditions for sample #11B - Parallel.

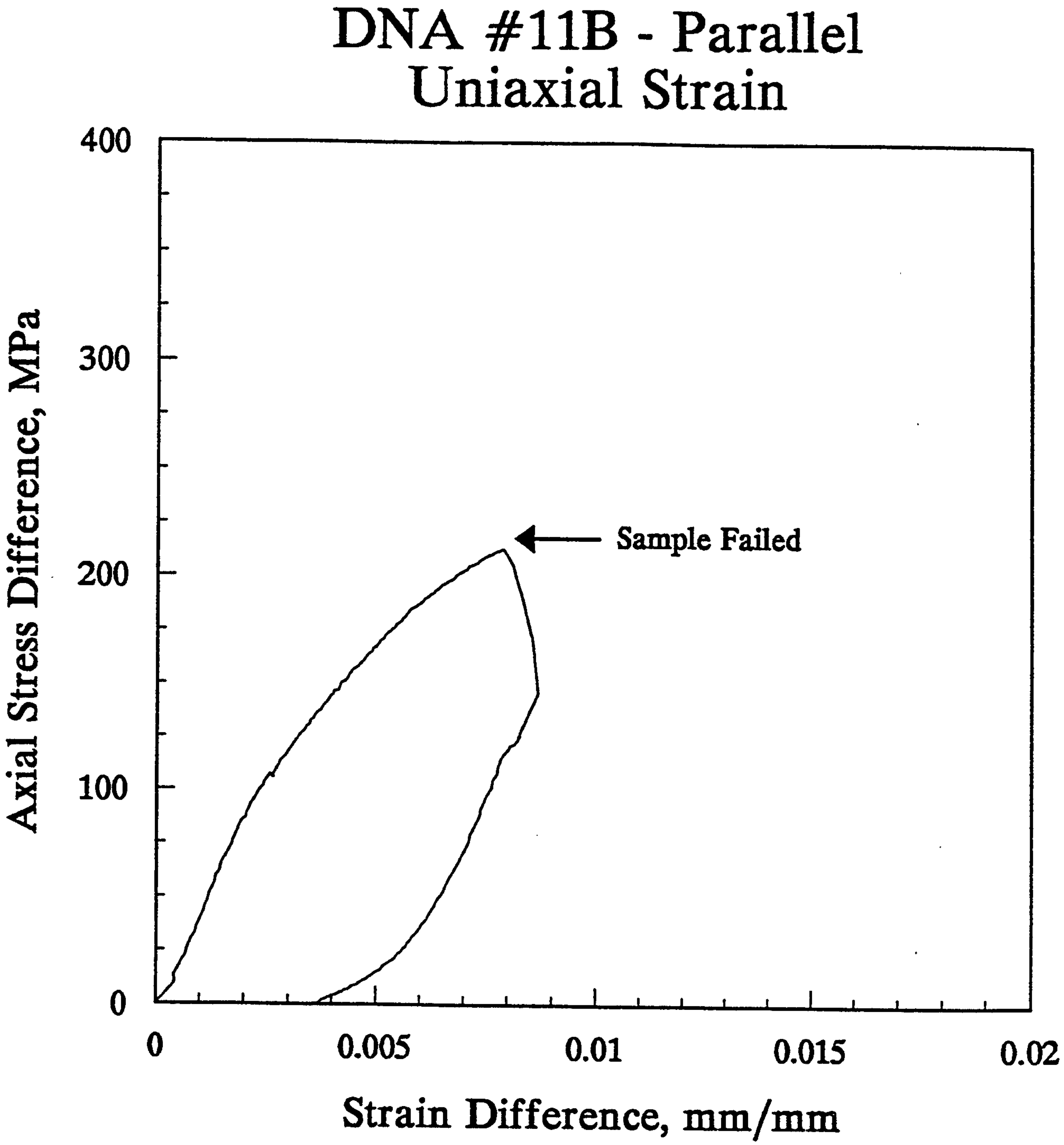

Figure D-80. Axial stress difference versus strain difference under uniaxial strain conditions for sample #11B - Parallel.

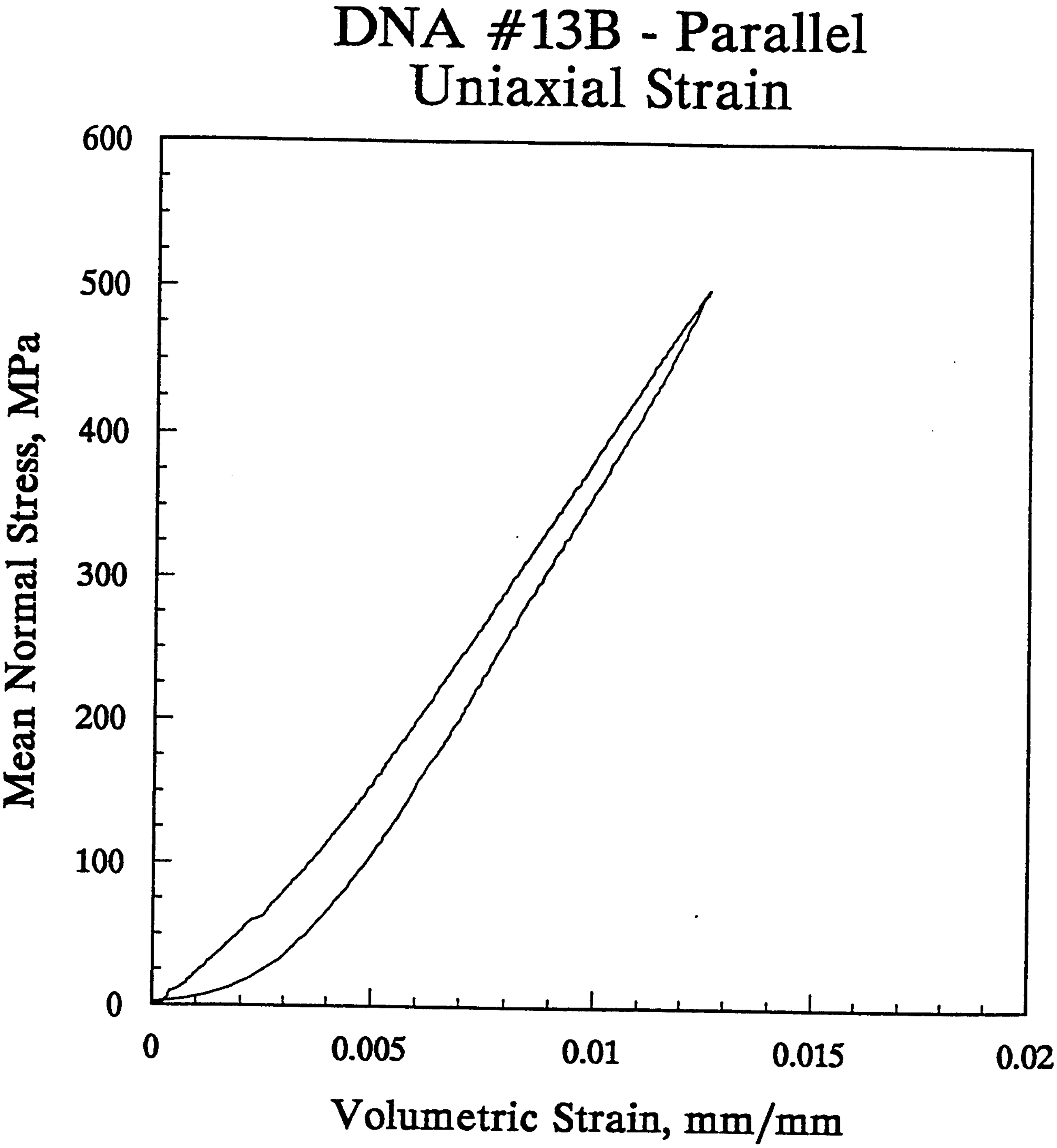

Figure D-81. Mean normal stress versus volumetric strain under uniaxial strain conditions for sample #13B - Parallel.

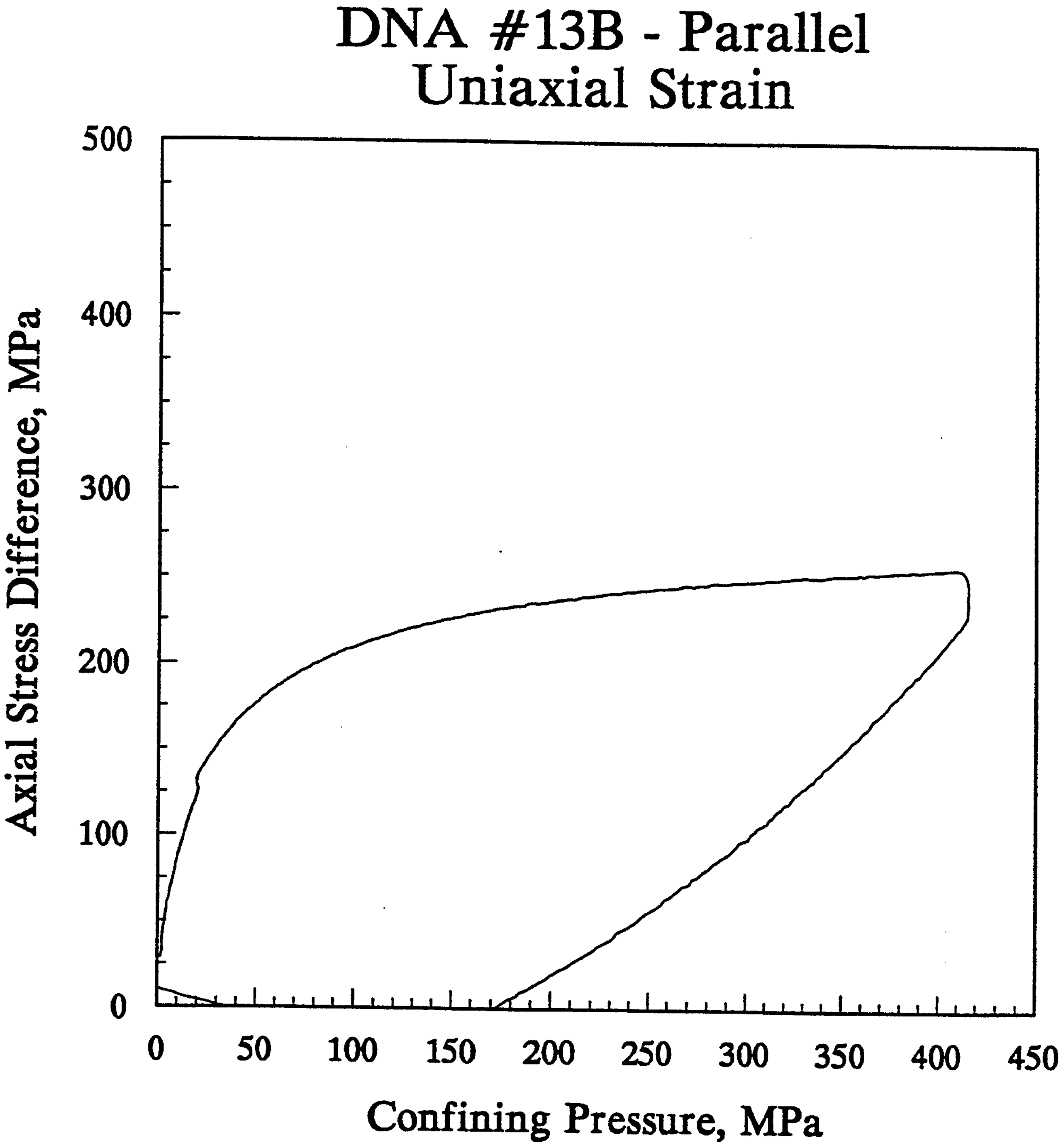

Figure D-82. Axial stress difference versus confining pressure under uniaxial strain conditions for sample #13B - Parallel.

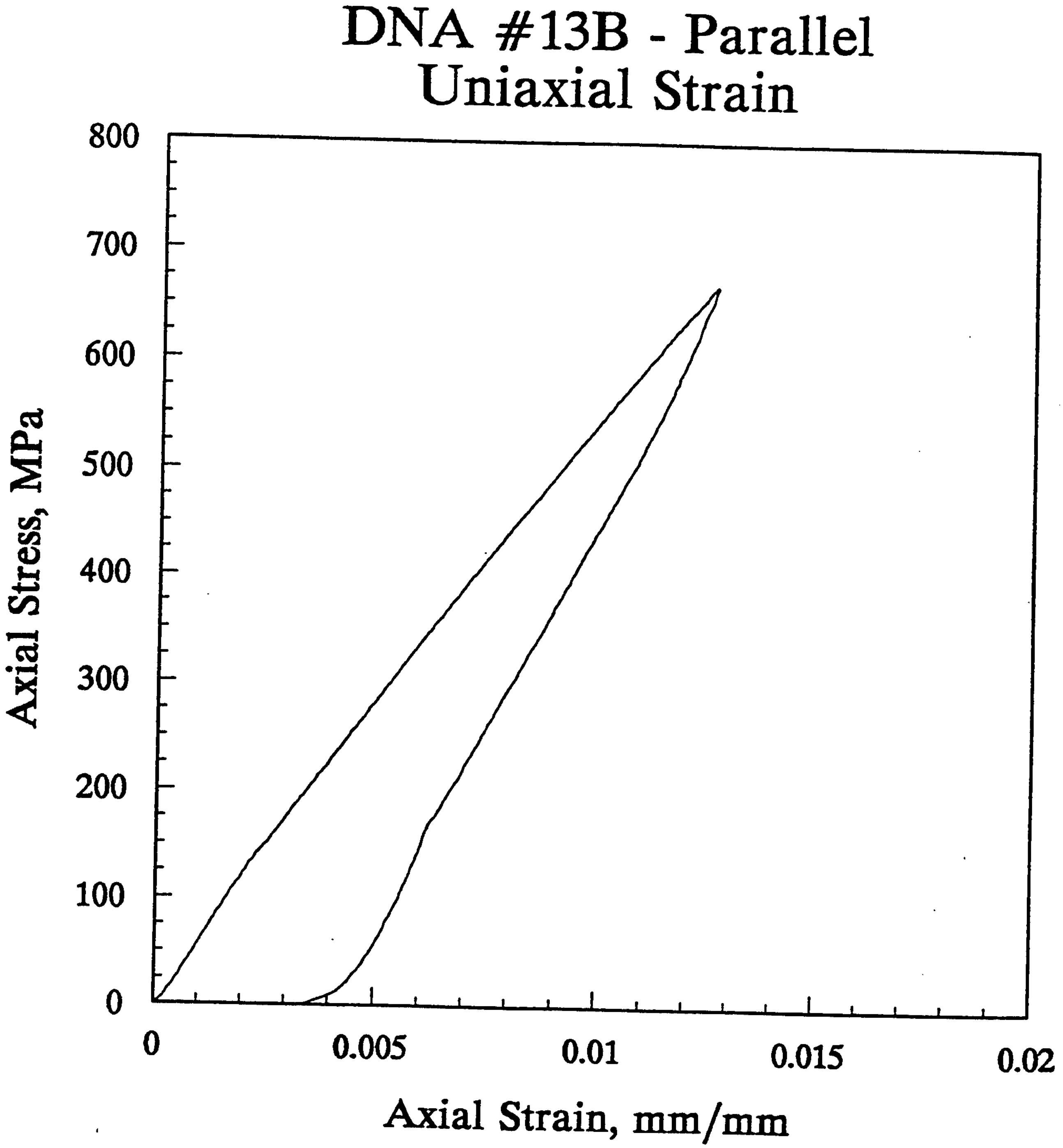

Figure D-83. Axial stress versus axial strain under uniaxial strain conditions for sample #13B - Parallel.

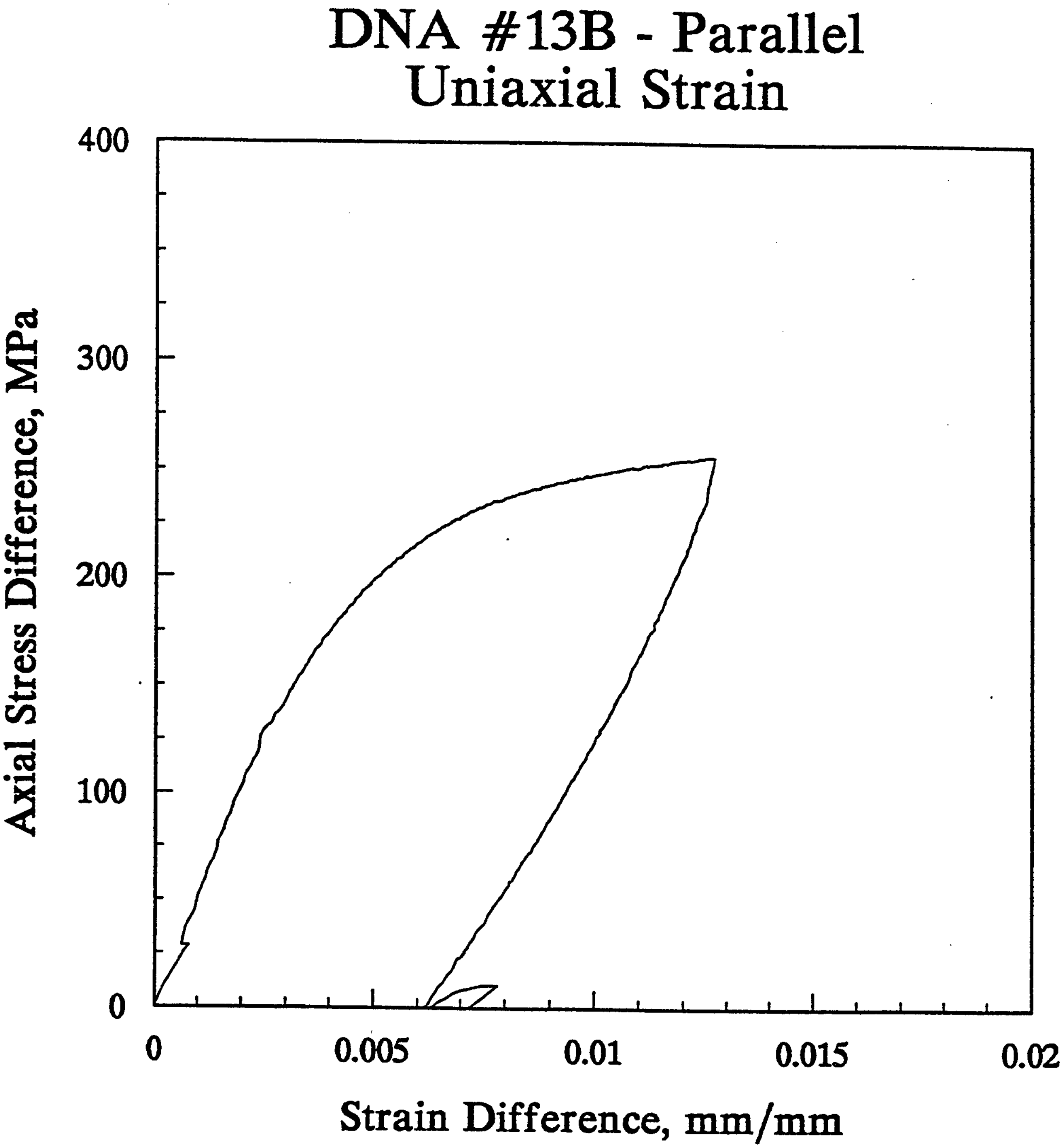

Figure D-84. Axial stress difference versus strain difference under uniaxial strain conditions for sample #13B - Parallel.

DISTRIBUTION LIST

DEPARTMENT OF DEFENSE

DEFENSE TECHNICAL INFORMATION CENTER
8725 JOHN J. KINGMAN ROAD, SUITE 0944
FORT BELVOIR, VA 22060-6218
ATTN: DTIC/OCP

DEFENSE THREAT REDUCTION AGENCY
6801 TELEGRAPH ROAD
ALEXANDRIA, VA 22310-3398
ATTN: CP, D LINGER
ATTN: CPF, M SHORE
ATTN: CPWPT, TRC

DEFENSE THREAT REDUCTION AGENCY
ALBUQUERQUE OPERATIONS
1680 TEXAS STREET, SE
KIRTLAND AFB, NM 87117-5669
ATTN: CPT-D, DR G. BALADI
ATTN: CPTI, G. LU
ATTN: CPTIE E PERALES
ATTN: CPTIE, R. KRUETZIAN
ATTN: CPTN, E. RINEHART
ATTN: CPTN, M. OBRIEN
ATTN: CPTP, A. KERSUL
ATTN: CPTP, DR B. RISTVET
ATTN: CPTP, J. LEVERETTE
ATTN: CPTP, P. THOMPSON
ATTN: CPTP, R. REINKE

DEFENSE THREAT REDUCTION AGENCY
ATTN: ATC/SRF, 3RD FLOOR
6801 TELEGRAPH ROAD
ALEXANDRIA, VA 22310
ATTN: A. BELL
ATTN: R. STEELE

DEFENSE THREAT REDUCTION AGENCY
NEVADA OPERATIONS
P. O. BOX 208
MERCURY, NV 89023-0208
ATTN: CPTON, B. HARRIS-WEST
ATTN: CPTON, L. J. GABRIEL,
BUILDING #143

DEPUTY ASSISTANT TO THE SECRETARY
OF DEFENSE NUCLEAR MATTERS
3050 DEFENSE PENTAGON, ROOM 3C125
WASHINGTON, DC 20301-3050
ATTN: DR SMITH
ATTN: F. CELEC, ROOM 3C125

DIRECTOR
JOINT CHIEFS OF STAFF
STRATEGIC PLANS & POLICY (J5)
5000 DEFENSE PENTAGON
WASHINGTON, DC 20318-5000
ATTN: COL J. A. TAYLOR, USA
ATTN: ND, CAPT W. L. NORRIS, USN
ATTN: RNTI ,MG (RET) E. B. GILLER,
USAF

OASD (C3I)
WASHINGTON, DC 20301
ATTN: ISP/NS&S, E. NAWROCKI

OASD (ISP)
DEP ASST SECY, NUC FORCES &
ARMS CONTROL POLICY
THE PENTAGON
WASHINGTON, DC 20310-2600
ATTN: F. C. MILLER

DEPARTMENT OF DEFENSE CONTRACTORS

ENSCO, INC.
P. O. BOX 1346
SPRINGFIELD, VA 22151-0346
ATTN: G. BEASLEY

ITT INDUSTRIES
ITT SYSTEMS CORPORATION
ATTN: AODTRA/DTRIAC
1680 TEXAS STREET, SE
KIRTLAND AFB, NM 87117-5669
ATTN: DTRIAC
ATTN: DTRIAC/DARE

JAYCOR
1410 SPRING HILL ROAD, SUITE 300
MCLEAN, VA 22102
ATTN: DR C. P. KNOWLES
ATTN: T. J. HANNIGAN

KTECH CORPORATION
2201 BUENA VISTA DRIVE, SE, SUITE 400
ALBUQUERQUE, NM 87106-4265
ATTN: F. DAVIES
ATTN: L. LEE

LOGICON INC
LOGICON ADVANCED TECHNOLOGY
P. O. BOX 471
SAN PEDRO, CA 90733-0471
ATTN: C. MO
ATTN: J. LEWIS

LOGICON - RDA
6940 S. KINGS HIGHWAY, SUITE 202
ALEXANDRIA, VA 22310
ATTN: A. POLK

MAXWELL TECHNOLOGIES, INC.
FEDERAL DIVISION
8888 BALBOA AVENUE
SAN DIEGO, CA 92123-1506
ATTN: K. PYATT

SCIENCE APPLICATIONS INT'L CORPORATION
10260 CAMPUS POINT DRIVE
SAN DIEGO, CA 92121-1578
ATTN: D. PATCH
ATTN: J. KLUMP
ATTN: TECHNICAL REPORT SYSTEM

SCIENCE APPLICATIONS INT'L CORPORATION
ATTN: SECURITY CONTROL OFFICE
4001 N. FAIRFAX DRIVE, SUITE 800
ARLINGTON, VA 22203
ATTN: M. W. MCKAY

SCIENCE APPLICTIONS INT'L CORPORATION
P. O. BOX 19057
LAS VEGAS, NV 89119
ATTN: K. SITES

SRI INTERNATIONAL
333 RAVENSWOOD AVENUE
MENLO PARK, CA 94025-3434
ATTN: DR J. GRAN
ATTN: M. GROETHE

TERRA TEK, INC
P. O. BOX 8275
SALT LAKE CITY, UT 84108-8275
ATTN: S. HEROUX
ATTN: W. MARTIN

DEPARTMENT OF ENERGY

BECHTEL NEVADA, INC.
P. O. BOX 98521
LAS VEGAS, NV 89193-8521
ATTN: G. BATES
ATTN: M. TOWNSEND
ATTN: S. DRELLACK

LOS ALAMOS NATIONAL LABORATORY
P. O. BOX 1663
LOS ALAMOS, NM 87545
ATTN: D. KING, P-15, MS D406

SANDIA NATIONAL LABORATORIES
ATTN: MAIL SERVICES
P. O. BOX 5800
ALBUQUERQUE, NM 87185-0459
ATTN: D. GRADY, MS 0819
ATTN: M. D. FURNISH, MS 1168

DEPARTMENT OF THE ARMY

US ARMY RESEARCH &
DEVELOPMENT CENTER
WATERWAYS EXPERIMENT STATION
3909 HALLS FERRY ROAD
VICKSBURG, MS 39180-6199
ATTN: B. GREEN
ATTN: CEWES-SC, D. WALLEY
ATTN: EE-R, K. KONECNY

OTHER GOVERNMENT

CENTRAL INTELLIGENCE AGENCY
WASHINGTON, DC 20505
ATTN: DCI/ACIS/CBIT, RM4W03 NHB

NATIONAL ARCHIVES & RECORDS
ADMINISTRATION, ROOM 3360
8601 ADELPHI ROAD
COLLEGE PARK, MD 20740-6001
ATTN: USER SERVICE BRANCH

NATIONAL SECURITY COUNCIL
OLD EXECUTIVE BUILDING
17TH & PENNSYLVANIA AVENUE, NW
WASHINGTON, DC 20506
ATTN: B. BELL

U S DEPARTMENT OF STATE
320 21ST STREET, NW
WASHINGTON, DC 20451
ATTN: DR E. LACEY, ACDA/IVI,
ROOM 5741
ATTN: MA/NTP, P. CORDEN